Energy and Technology Review

July • August 1989

The State of the Laboratory

Lawrence Livermore National Laboratory

Prepared for **DOE** under contract
No. W-7405-Eng-48

About the Journal

The Lawrence Livermore National Laboratory, operated by the University of California for the United States Department of Energy, was established in 1952 to do research on nuclear weapons and magnetic fusion energy. Since then, we have added other major programs, including laser fusion and laser isotope separation, biomedical and environmental sciences, and applied energy technology. Our most recent major project, for the Strategic Defense Initiative Organization, is research on the free-electron laser. These programs, in turn, require research in basic scientific disciplines, including chemistry and materials science, computer science and technology, engineering, and physics. The Laboratory also carries out a variety of projects for other federal agencies. *Energy and Technology Review* is published monthly to report on unclassified work in all our programs. A companion journal, *Research Monthly*, reports on weapons research and other classified programs. Please address any correspondence concerning *Energy and Technology Review* to Mail Stop L-26, Lawrence Livermore National Laboratory, P.O. Box 808, Livermore, CA 94551.

UCRL--52000-89-7/8

DE90 000994

Energy and Technology Review

July • August 1989

The State of the Laboratory	ii
Defense Systems	1
Laser Technology	20
Magnetic Fusion Energy	38
Beam Research	44
Energy Program	52
Biomedical and Environmental Sciences	60
Supporting Activities	74

Printed in the United States of America
Available from
National Technical Information Service
U.S. Department of Commerce
5285 Port Royal Road
Springfield, Virginia 22161
Price codes: printed copy A04, microfiche A01

UCRL-52000-89-7 • 8
Distribution Category UC-700
July • August 1989

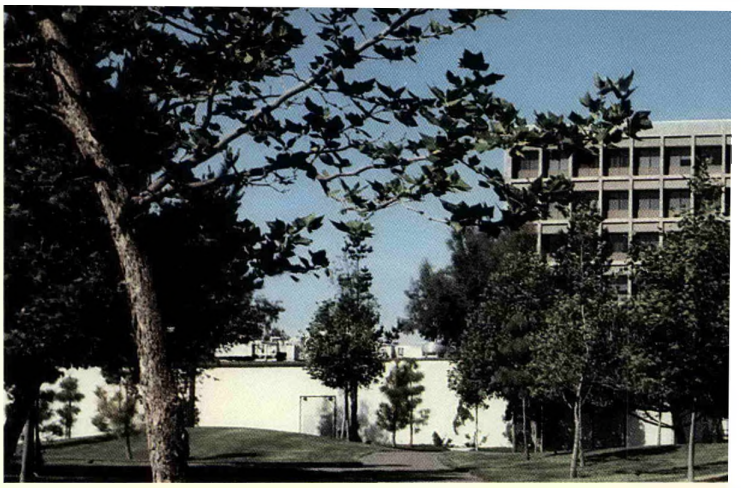

The State of the Laboratory

As we enter the 1990s, LLNL has important roles in meeting four of the nation's great challenges: deterring war, developing clean and affordable energy, preserving the environment, and enhancing this country's economic competitiveness.

Technology and diplomacy continue in partnership to achieve peace. Our work in treaty-verification and weapon technologies will continue to make important contributions to this partnership. In this period of tight federal budgets and remarkable progress in arms-control negotiations, we are challenged to provide effective national defense at a reduced cost and with decreased reliance on nuclear forces. We are addressing this challenge. We are also working to ensure that this nation's nuclear forces are secure and safe. The Laboratory has long been a leader in the development of safety and security technologies for nuclear weapons. During the past year, we greatly increased our efforts to define and meet the highest possible surety standards for nuclear weapons.

National security also depends on developing affordable, plentiful, and safe sources of energy for the 21st century. The preservation of the environment—locally, nationally, and globally—depends in turn on the success of this endeavor. LLNL's fusion programs may provide the key to solving these problems. However, if our understanding of global warming is correct, progress in fusion-energy research must be accelerated if we are to limit adverse climatic changes in the next century.

We must also determine the impact of man's activities on the environment and of the environment on man. The Laboratory's program in biomedical sciences has made important advances in this area. During the past year, LLNL scientists, in collaboration with researchers at the Lawrence Berkeley Laboratory, scored a notable success in the international effort to map the human genome as they obtained images of DNA at resolutions approaching the molecular level.

National security also requires a strong and competitive U.S. economy. The DOE laboratories have been asked to assume leading roles in developing new technologies and transferring them to industry. LLNL's uranium laser isotope separation (LIS) technology is such an example. Beginning in the mid-1990s, LIS production facilities

Building 111 at LLNL, which houses the Director's Office.

could have a substantial cost advantage in a multibillion-dollar-a-year market in fuel for nuclear reactors. Successful development of economically superior fusion reactors would enable the U.S. to dominate a multihundred-billion-dollar-a-year world market in the 21st century.

To meet these difficult challenges, LLNL must substantially increase its capabilities. We are focusing on several areas—including supercomputers, experimental technologies, and state-of-the-art facilities—in which revolutionary advances are occurring. We are also fostering increased openness and building partnerships with the private sector and universities to ensure a strong coupling to the worldwide revolution in science and technology.

Human resources is another area of high potential. We plan to increase substantially our investment in career-long education and training for LLNL employees. We must also further strengthen our recruiting efforts in order to sustain the high quality of the Laboratory workforce in the next decade.

During the past year, our budget and workforce have remained relatively stable. We have focused increased management attention on such institutional issues as the Laboratory's aging infrastructure and local environmental problems. We must accelerate the rebuilding of the Laboratory's physical infrastructure, which has deteriorated as a result of long-term underinvestment by the Federal government. We are also vigorously addressing local environmental problems, both those that the Laboratory inherited and those that it subsequently created. The Secretary of the Department of Energy, James D. Watkins, has committed the DOE to give as high a priority to environmental tasks as it does to mission-oriented tasks.

With our talented and dedicated people, our mission and programmatic focus, and our state-of-the-art facilities, we are in a position to help meet these great challenges.

John H. Nuckolls
Director, LLNL

Defense Systems

The direction of the Defense Systems Program, especially as we attempt to plan for the future, has been markedly affected by recently signed weapon treaties and continuing arms-control negotiations and by the recognition of problems in the nation's nuclear weapons complex. The INF treaty, ratified in 1988, eliminates certain intermediate-range nuclear systems, and the proposed but still incomplete START treaty would significantly reduce the numbers of strategic nuclear warheads. In addition, the U.S. and Soviet Union are discussing further limits on nuclear testing and the need to develop improved methods for verifying the yield limits of the Threshold Test Ban and Peaceful Nuclear Explosion treaties. The most significant problems facing the U.S. nuclear weapons complex are the environmental cleanup needed at a number of facilities and the interruption of tritium production and the effect a resulting tritium shortage may have on the U.S. nuclear stockpile. These issues could seriously affect the character and execution of future development programs and ultimately the characteristics of the weapons in the U.S. inventory.

In the face of this increasing uncertainty in the national weapons program, it is more necessary than ever to maintain the strength of our research, development, and testing (RD&T) efforts. A strong base in research and development is vital if we are to respond quickly and effectively to nuclear force reconfigurations that may be required to maintain deterrence in the face of significant force reductions. In addition, both the potential shortage of tritium and the possibility of new limitations on nuclear testing are placing increased demands on our RD&T efforts.

Modernization of the U.S. stockpile continues to be a high priority. Most of the newer weapons in the stockpile contain insensitive high explosive (IHE) that is almost impossible to detonate accidentally as well as fire safety features to contain the fissionable material in the event of fire. However, many stockpiled weapons were produced before these safety features had been developed. It is important to modernize the stockpile as quickly as possible by replacing these older weapons with modern weapons possessing these improved safety features.

To maintain a stable deterrent, we must ensure that U.S. weapon systems are survivable (i.e., they can survive a first strike and retaliate) in the face of an ever-improving Soviet offensive capability. This is a particular concern for U.S. land-based ICBMs, and increasing the survivability of these weapons is a high priority. There is also increasing recognition of the need to improve the effectiveness of U.S. weapons against ever harder and more mobile targets, and new classes of U.S. weapons may be needed to place these targets at risk.

LLNL has several weapon development projects in progress. The W89, the new enhanced-safety warhead for the SRAM II standoff missile, is in engineering development and is proceeding on schedule. The W87-1, the warhead for the Small ICBM (SICBM), is being

The High Explosives Application Facility (HEAF), completed this year, will provide us with new capabilities for exploring the phenomenology of high explosives.

designed; improved safety and security are prime considerations for this warhead because of the mobile basing mode planned for the system. Should full-scale development of the SICBM be authorized, the mobility of this system should significantly improve the survivability of the U.S. land-based ICBM force.

The W82, a new 155-mm artillery-fired atomic projectile, is in the late stages of engineering development. One of the outcomes of the INF treaty has been to increase the importance of modernizing U.S. shorter-range nuclear systems. The W82 contributes to this effort, as do two proposed new weapon systems—the SRAM-T, a tactical air-to surface missile based on the SRAM II, and the FOTL, or follow-on-to-Lance, a short-range surface-to-surface missile to replace the aging Lance missile system. We are exploring various warhead options for both of these new systems.

Feasibility studies of an earth-penetrating weapon to attack deeply buried targets are also continuing. Such studies for new weapons and new weapon applications have always been an important part of the Defense Systems Program. They are even more important now as new arms-control treaties begin to eliminate entire classes of weapon systems, forcing the U.S. to maintain deterrence with fewer systems in the inventory.

In recent years, the rate of underground nuclear testing has been declining. Our testing opportunities have decreased at the same time our need for data has increased as we strive to achieve a fundamental understanding of the details of the physics involved in the explosion of a nuclear weapon. It is therefore essential that we gather the greatest quantity and highest quality of data possible from each test, and, to this end, we are developing many new instruments and measurement techniques. The Laboratory's Director has set the goal of obtaining ten times more data per experiment than has been possible in the past. To achieve this goal, we will channel more resources and people into this important research area.

As the number of underground nuclear tests decreases, the need for laboratory research facilities increases. Several new facilities are being built at LLNL. The High Explosive Application Facility (HEAF), a multidiscipline explosive science facility, was completed and became operational in April 1989; in this facility, we can test many aspects of high explosives, including the special characteristics of IHE. Also this year, site preparation began for the Nuclear Directed Energy Research Facility (NDERF) and the Nuclear Test Technology Center (NTTC), two facilities that will share the same building site. When they are completed in 1992–93, the NDERF and NTTC will be crucial to our efforts to sustain a quality program in nuclear weapons research, development, and testing.

Contact: W. Scanlin (415) 423-6810.

Weapon Development

LLNL is developing several warheads to modernize U.S. nuclear forces in response to new military requirements.

The Laboratory's Military Applications Program is responsible for developing new warheads that incorporate the latest safety and security features and, when deployed, will improve the survivability and effectiveness of U.S. nuclear forces. The three major elements of our weapon development program are:

- Full engineering development for systems scheduled for deployment (SRAM II, SICBM, and a 155-mm artillery-fired atomic projectile).
- Feasibility studies for systems being considered for deployment (SRAM-T and FOTL).
- Development of new technologies for anticipated future requirements (EPW).

Short-Range Attack Missile

The W89 warhead is being developed for use in the new short-range attack missile (SRAM II), a stand-off missile that will be carried by the B-1B bomber. The new missile will enhance aircraft survivability by enabling the B-1B to attack targets without flying through the terminal defenses deployed in the vicinity of important targets (Figure 1). LLNL has responsibility for the nuclear explosive package for the W89 warhead; Sandia National Laboratory, Livermore, is developing the warhead's nonnuclear components and surrounding structural members, and Boeing Aerospace is developing the SRAM II missile. Full-scale engineering development (Phase 3) of the W89 began in January 1988.

The W89 will use TATB-based insensitive high explosive (IHE). This material is virtually immune to accidental detonation by mechanical or thermal stimuli, such as might occur in an aircraft accident. The W89 is also designed to meet stringent standards for containing molten plutonium when the warhead is exposed to very high temperatures. This feature will reduce the likelihood of dispersing plutonium in an accident involving burning aircraft fuel.

Since the W89 will be deployed in an air-carried missile, it must withstand and operate reliably over a wide temperature range (–54 to 71°C). The different warhead materials expand and contract differently as temperature changes. Guided by calculations and early empirical data, we made small alterations to our initial W89 design to accommodate these temperature effects. The modified design performed well in preliminary thermal cycling tests, and we recently began full-scale thermal tests.

We are also conducting environmental ground tests to demonstrate that the W89 warhead can survive the vibrational and structural loads it will experience during captive-carry flight in the bomber and during missile flight. Early tests of the components believed to be the most vulnerable yielded encouraging results. The environments for which the warhead has been tested were derived from calculations and previous experience with similar weapons. Tests in real flight environments, in which model warheads are flown with data-recording instruments on board, will begin this fall with captive-carry tests in a B-1B bomber, followed by missile flight tests in the fall of 1990. We are now providing hardware to Sandia to support their effort to develop the instrumented flight-test units.

We are working closely with the DOE production plants to optimize the producibility of the W89 design

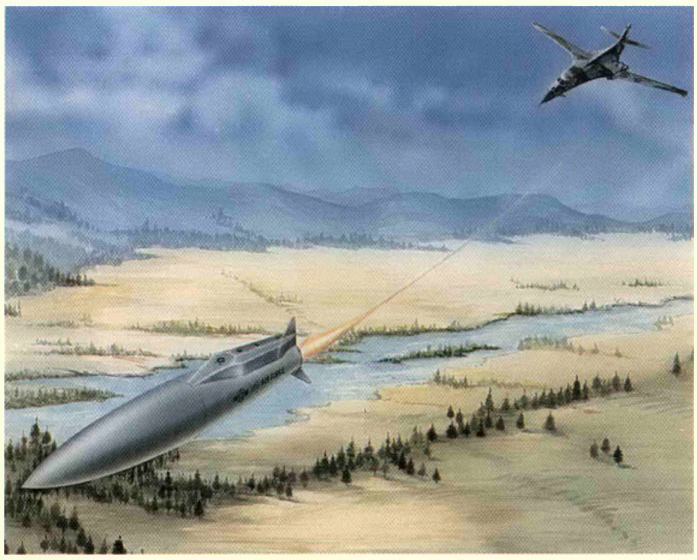

Figure 1. Artist's conception of the SRAM II after release from its delivery B-1B aircraft. This missile, with its W89 warhead, will enhance aircraft survivability by enabling the B-1B to attack targets without flying through the terminal defenses typically deployed near important targets.

and to control cost and schedule. (This warhead will be the first to have its production monitored by the baseline cost accounting procedure mandated by the recent Presidential Blue Ribbon Task Group that reviewed DOE operating procedures.) In October 1988, we provided the plants with a full design description; they used this design to estimate the baseline costs against which the future production program will be measured. We sent out the W89 design definition electronically using the new computer-integrated manufacturing capability being developed by the DOE nuclear weapon complex; the W89 program was the first to use this advanced method of data management and transmission.

To develop the W89, we have relied heavily on materials and production methods proven in previous warhead programs and are maintaining close communications with Sandia, the DOE production plants, and Boeing. This strategy has been very effective. For example, upon review of the initial W89 design, one plant and Sandia each identified a component that would have been very difficult or costly to produce. Using computer modeling and calculations, we were able to alter the design in one case and relax a requirement in the other to allow the elimination of these components without degrading warhead performance. At this point, the W89 nuclear design is almost completely defined and the producibility of the W89 nuclear explosive package is being assured.

Small Intercontinental Ballistic Missile

To improve the survivability of this U.S. land-based ICBM force, two mobile basing modes are being considered—the truck-mobile small ICBM (SICBM), also known as the Midgetman, and the rail-mobile Peacekeeper MX. The LLNL-designed W87-0 warhead is already deployed on the Peacekeeper missiles based in silos. This warhead may be repackaged as the W87-1 for the SICBM (Figure 2), with new use-control features and a higher yield, or as the W87-X, for use in the Peacekeeper rail-mobile system.

To provide rapid and flexible response to Air Force deployment options, we are continuing to provide support for the SICBM and rail-mobile Peacekeeper. We are documenting in detail the end of the W87-0 production (completed in December 1988) so that restarting production for either warhead option would be smooth and rapid. For the W87-1, we are subjecting an instrumented warhead/RV to prelaunch environmental ground testing on a hard-mobile-launcher at Malmstrom AFB, Montana. For the W87-X, a similarly instrumented package will be subjected to railroad-mobility testing at Pueblo, Colorado.

Tactical Short-Range Attack Missile

The recent INF treaty calls for the elimination of the accurate, long-range Pershing II and ground-launched cruise missiles; as a result, modernized short-range, tactical nuclear weapon systems have assumed greater military importance. Air-launched missiles, potential replacements for gravity bombs, can effectively improve the survivability and extend the combat range of tactical aircraft. The Air Force plans to adapt the SRAM II missile, already under development for U.S. strategic nuclear forces, and create the SRAM-T as a cost-effective way to modernize the tactical, air-delivered leg of NATO theater nuclear forces. The SRAM-T would be targeted against theater assets such as airfields, munitions storage depots, and command, control, and communications facilities.

The non-U.S. basing of theater nuclear weapons requires not only enhanced safety features such as IHE but also special warhead use-control

Figure 2. One mobile basing mode being considered for U.S. land-based ICBMs is the truck-mobile small ICBM (SICBM).

features that are not present in the W89 warhead. In addition, adaptation of the bomber-delivered SRAM II missile to tactical aircraft could require further modifications to both the missile and warhead. We are examining these issues and appropriate warhead options in a Phase-2 feasibility study of the SRAM-T.

Two of the principal criteria for tradeoffs are the cost and schedule for producing the SRAM-T missile and its warhead. An important cost decision is whether to modify the SRAM II missile to hold a cheaper but larger warhead or to leave the missile essentially unmodified but build a warhead with new, smaller components. For this option, the number of new components and their production complexity would have to be low enough to permit a relatively compressed development schedule.

We are also assessing the effect of different warheads on the military effectiveness of the system. Range is a high priority with the Air Force and our NATO allies. However, the use of existing components (dictated by cost and schedule) may increase warhead weight and volume and therefore reduce missile range. We are working with the missile contractor to fit candidate warheads into the SRAM-T missile. After the warhead/missile packages are optimized to produce the maximum range, we will compare their relative utility in a number of operational scenarios.

The SRAM-T program is in a competitive feasibility study phase. Two design teams, one from Livermore and another from Los Alamos, examined a number of designs and proposed candidate warheads. This phase was concluded in May 1989, and the DOE is evaluating the proposals.

Follow-on-to-Lance

As a result of the INF treaty, battlefield nuclear weapons are restricted to a small number of nuclear artillery and missile systems with ranges less than 500 km. The aging Lance surface-to-surface missile is the only missile in the current U.S./NATO theater nuclear inventory. The follow-on-to-Lance (FOTL) will provide a greatly needed replacement with enhanced safety and security features as well as improved operational effectiveness. The new FOTL system will require much less manpower to operate and thus should yield long-term cost and logistical advantages as well.

The Army has placed high priority on a FOTL design that could be fielded by the time the existing Lance system is retired. The DOE was urged to ensure early availability by concentrating on designs that would represent only slight modifications of existing warheads. Although the missile design itself has not yet been selected, the choice of a missile launcher bounds the warhead dimensions closely enough that we have been able to begin a Phase-2 study of design options and tradeoffs. Candidate warheads have been identified and the costs and benefits of each are being assessed; a Phase-2 final report was submitted to the DOE in June 1989.

Although the FOTL is intended for use against mobile battlefield targets, whereas the SRAM-T would be used mostly against fixed targets, many of the requirements for the two systems are the same. As was the case for the SRAM-T, range is an important consideration, and thus warhead size and weight must be minimized. Yield, safety and security features, and development schedules are all similar enough for the SRAM-T and FOTL that it is likely that both systems can share a common design with minor modifications. Such an integrated approach would decrease the impact of two new programs on the DOE production complex in a time of severe resource constraints. Our proposals are structured along these lines, and we are studying the potential cost savings that would result from using a common warhead for the SRAM-T and FOTL.

Earth-Penetrating Warhead

An earth-penetrating warhead (EPW) couples a much larger fraction of its explosive energy into ground motion than does a surface-burst weapon of similar yield and thus should be much more effective against a buried target. We are participating in a joint DOD/DOE Phase-2 study to assess the feasibility and requirements of EPW systems that could be delivered by existing weapon systems and by systems in development.

Because the delivery vehicle for an EPW has not yet been selected, we are examining all types of possible carrier systems for an EPW. Other current activities relating to EPWs at LLNL and Sandia include:

- Nuclear effects studies of the propagation of strong shocks through the ground, the structural response of very hard targets, and the effects of various geologies.
- System analyses of tradeoffs among warheads, carriers, and targets.
- Engineering design and tests to certify the penetrator case, the warheads, fuzing and firing components, and new lightweight materials for the penetrator case.
- Nuclear design and tests to ensure that the nuclear device components can withstand the severe deceleration encountered when the EPW strikes the ground and burrows through rock.

A working group has been formed under the auspices of the Defense Nuclear Agency (DNA) to develop a methodology for evaluating the range to effect for an EPW in multilayered geologies. An empirically based, ray-tracing technique was devised with joint participation from the DOE laboratories and the DNA contractors. We have used this methodology to produce isoeffect contours that compare favorably with those obtained from more detailed, first-principles hydrodynamics calculations.

We are using computer modeling to study the response of hardened underground structures to shock waves and to determine the effect of explosion depth (depth of burial) on the coupling of energy into the ground. This work is very challenging because of the complexity of the phenomena involved—different target structures, multilayered geologies, radiation transport in both earth and air, etc. We have compared the effectiveness of EPWs and existing surface-burst warheads against buried targets; we find that even though the EPW is heavier than a surface-burst warhead of the same yield, the enhanced coupling of energy into the ground easily offsets the weight penalty.

We are also conducting experiments to verify penetrator performance. In September 1988, LLNL and Sandia conducted a full-scale EPW impact test with a nuclear-explosive-like assembly at the Tonapah Test Range in Nevada. Figure 3 shows the two-stage Genie rocket, with the penetrator attached, being launched from an Honest John mobile launcher. The first stage of the rocket carried the penetrator to an apogee of 4300 m; after stage separation and turnover, the second stage drove the penetrator into the target at more than 600 m/s. Figure 4 shows the penetrator after the test, scratched but otherwise unaffected.

Figure 3. A two-stage Genie rocket, with the EPW attached, being launched from an Honest John mobile launcher.

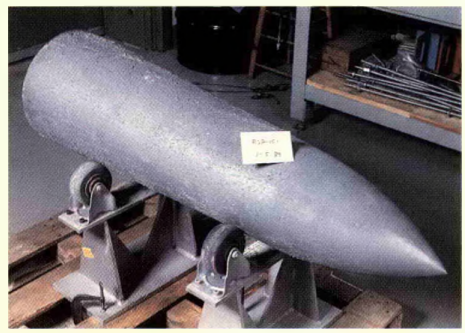

Figure 4. The EPW after the test shown in Figure 3, scratched but otherwise unaffected. When the penetrator was disassembled at LLNL, the mock warhead components were intact and their behavior closely matched our computer predictions.

Warhead structural parts had been developed using the LLNL finite-element codes NIKE and DYNA. When the penetrator was disassembled at LLNL, we found that not only had the mock components survived intact but also that the behavior of the test parts agreed closely with our computer predictions.

Our next goal is to reduce the weight of the EPW. We are evaluating lightweight penetrator case materials and have been testing 1/7- to 1/10-scale models in the Sandia 10-cm (4-in.) gas gun. From the results of these scale experiments, we will select the most promising materials for full-scale testing.

Contact: W. J. Shotts (415) 423-8770.

Military Applications: Evaluation and Planning

Our analyses and evaluations range from specific feasibility and tradeoff studies of new weapon systems to broad considerations of the effect of arms-control agreements on strategic stability to the tactics and consequences of conflict in the European Theater.

The Laboratory devotes much effort to the evaluation and analysis of weapon effects and weapon system capabilities. We participate in joint DOE/DOD feasibility studies to evaluate the military effectiveness and utility of new weapon concepts to fulfill specific missions. Once the military requirements for a new system are specified, we conduct studies of tradeoffs among cost, operational issues, and weapon system characteristics to define a design with the greatest military effectiveness as a function of cost. In addition, we analyze such important issues as the impact of arms-control agreements on strategic stability and the tactics and possible consequences of nuclear and nonnuclear conflict between NATO and Warsaw Pact forces.

Joint DOE/DOD Studies

In this past year, we studied three new weapon system concepts (described in the preceding article). In the hard-target-kill study, we addressed the feasibility of using earth-penetrating weapons to hold at risk some of the Soviet underground targets. For the follow-on-to-Lance, we assessed a longer-range replacement for the aging, short-range Lance tactical missile. The new missile would be armed with a new warhead with modern safety and security features. For the tactical air-to-surface missile, we addressed the design issues of an air-carried nuclear tactical missile that would improve aircraft survivability.

Military-Utility Assessments

Several studies of system concepts for the Strategic Defense Initiative (SDI) were pursued this past year. In one study, Congressman John Spratt (chairman of the *ad hoc* Committee on SDI for the House Armed Services Committee) requested an assessment of the strategic defense architecture described to the Defense Acquisition Board (DAB) in October 1988. We were asked to address (1) the robustness of that architecture against countermeasures (e.g., antisatellite attack, fast-burn boosters, fast buses), (2) the realism of the threat used to evaluate the architecture, (3) the overall performance and integrity of the proposed system, and (4) the cost of this concept compared with the costs of earlier proposed architectures. We were able to respond effectively to the first three issues, but the cost issue is outside our areas of expertise.

We used benchmarked LLNL engagement models along with the threat models presented to the DAB. We expanded the threat to include a higher fraction of fast-burn boosters and fast-bus systems. Finally we made a detailed analysis of the efficacy of an antisatellite (ASAT) attack to assess the architecture's vulnerability to such countermeasures and to determine the effectiveness of some defensive strategies to counter such attacks. We found that:

- The validated threat used in the DAB review was stressing and consistent with intelligence estimates of Soviet boost and deployment features.
- The architecture presented to the DAB is capable of meeting the performance requirements defined by the Joint Chiefs of Staff (JCS), assuming that warhead-decoy discrimination goals can be met.
- Extended Soviet threat projections lower the defense performance below the JCS threshold in some cases. However, this decrease can be compensated for by adding space-based elements or by introducing some advanced weapon concepts (again assuming that discrimination goals can be met).
- The architecture is robust against the postulated ASAT threat. Given current Soviet radar capability, under ASAT attack, the system's performance remains at or just below the JCS threshold. Counter-ASAT strategies decrease overall system performance only slightly.

Strategic Defense Analysis

We have assessed the effects of a U.S. strategic defense system on nuclear deterrence and "crisis stability" (i.e., the likelihood of avoiding nuclear war in times of extreme political tension and uncertainty). We assumed a force

asymmetry by considering only a U.S. strategic defense (no comparable Soviet system). Our goals were to develop quantitative methods for studying these issues and to use these methods to measure the effects of U.S. defenses on deterrence and crisis stability. We also wanted to examine how these effects would change if offensive forces were reduced by a postulated START agreement.

We used two measures to characterize nuclear deterrence, both involving the numbers of military and economic assets that are destroyed in a nuclear attack. The first was the expected damage to U.S. assets from a Soviet first strike, and the second was the expected damage to Soviet assets from a subsequent U.S. return strike.

Our measure of crisis stability was the fraction of military and economic assets a side would save by striking first and absorbing a return strike. This measure assumes that limiting damage to one's own assets is an important strategic goal.

We estimated these quantities using detailed simulations of a Soviet missile attack and the performance of U.S. ground- and space-based interceptor defenses. We assumed that targets for the attacking warheads would be chosen to maximize damage to the other side. The U. S. ground-based defenses were assumed to work preferentially—that is, they would know the target of each attacking warhead and would choose which targets to defend so as to minimize overall damage. The U.S. space-based defenses, on the other hand, were assumed to attack incoming warheads regardless of their targets in an attempt to maximize the number of warheads destroyed. The damage from warheads penetrating the defenses was estimated from the characteristics of each target and warhead. We evaluated overall damage by the value, not number, of assets surviving; these values reflect the fact that some strategic targets are more important than others.

Our major finding is that the effect of capable U.S. strategic defenses like those being considered for early deployment (Phase 1) is very different for proliferated vs START-limited offensive forces (see Figure 1). For example, if Soviet forces are highly modernized and proliferated in response to a U.S. strategic defense system, a Soviet first strike could destroy a large portion of the U.S.'s total asset value, even with a capable Phase-1 U.S. defense; however, a significant fraction of the U.S.'s most valuable targets might be saved. Moreover, U.S. retaliation could still be very effective, assuming our offensive forces have been modernized and our submarines remain invulnerable. Although these results apply only to specific forces and depend on many assumptions, they do suggest that a strategic defense system that meets the Phase-1 performance requirements specified by the JCS might not qualitatively change the results (i.e., massive damage to both sides) of a large, Soviet-initiated nuclear war.

In the case of U.S. defenses and proliferated Soviet offensive forces, crisis stability would be reduced,

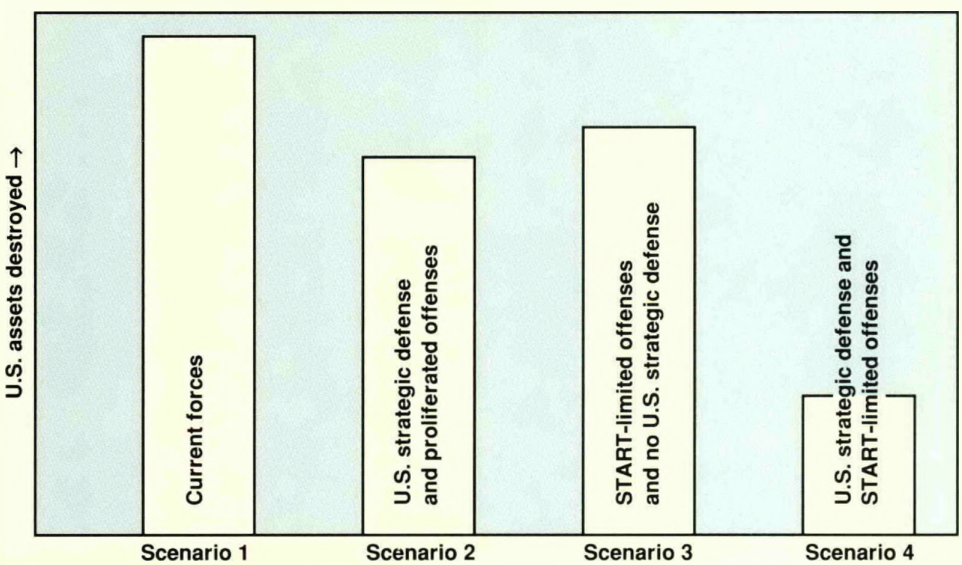

Figure 1. U.S. assets destroyed by a Soviet first strike in several scenarios: (1) current forces, (2) proliferated, modernized offensive forces and U.S. strategic defenses, (3) START-limited offenses and no defenses, (4) START-limited offenses and U.S. defenses. Without offensive arms control, capable U.S. defenses (scenario 2) might allow more assets to survive, compared with current forces (scenario 1); however, the damage is comparable to that with START-limited offenses and no defenses (scenario 3). Offensive arms control and capable defenses (scenario 4) could significantly reduce Soviet ability to destroy U. S. assets.

however, compared to the case with current forces. In a crisis situation, the Soviets might be tempted to strike first to negate any advantage the U.S. could achieve through a first strike. For the scenarios we studied, Soviet retaliation after a U.S. first strike does comparatively little damage to U.S. assets. (This does not mean that damage would be small or "acceptable," only that U.S. war-fighting capability might survive largely intact.) Hence, in a crisis situation, the Soviets might have a strong incentive to execute a preemptive strike first and not risk a U.S. first strike.

With START-limited offenses, in contrast, the same U.S. strategic defenses could have very different effects. In particular, most of the value in targeted U.S. assets could survive a Soviet first strike. (This is not true if we consider the same situations without strategic defenses.) Because of the presence of bombs and cruise missiles in the Soviet stockpile, the U.S. would not be able to reduce damage from a Soviet retaliation much more by executing a first strike. This suggests that, under a START agreement, U.S. strategic defenses could offer significant protection from Soviet attacks and could *increase* crisis stability (contrary to what we found with proliferated offensive forces). The principal difference between this case and current forces is that a strategic exchange would result in more damage to Soviet assets than to U.S. assets. Although the defense deployment results in some increase in crisis stability, deterrence could be weakened from the Soviet point of view, and there could be pressure on the Soviets to redress the imbalance in the capability of strategic forces.

Although these findings apply only to very specific situations and are predicated on many assumptions, they do suggest that the effects of strategic defenses on deterrence and stability could depend heavily on the size of offensive forces. We anticipate that this methodology will be very useful for analyzing other arms-control proposals currently being considered in Washington.

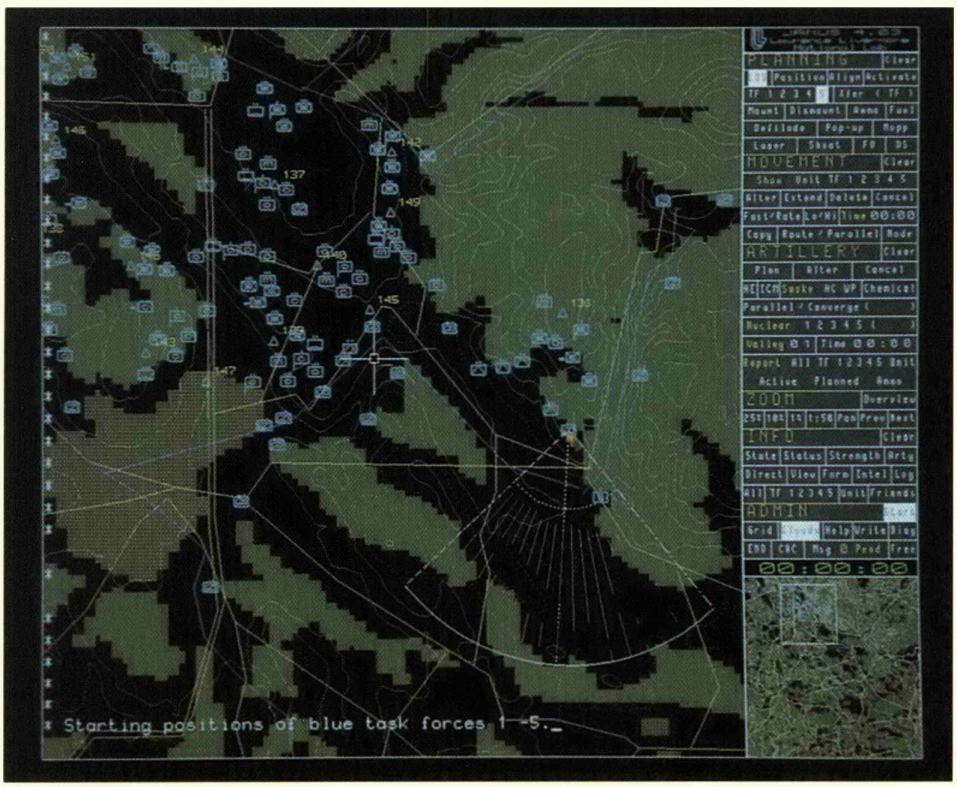

Figure 2. A typical view shown on a Janus workstation, in this case the starting positions of the Blue forces.

Tactical Analysis

In the summer of 1988, the Army's Close Combat Capabilities Analysis (CCCA) made use of our Conflict Simulation Laboratory (CSL) and the Janus system to simulate a defense by a U.S. corps against attack by a somewhat larger Warsaw Pact force in Europe. Janus is a two-sided, interactive combat-simulation system; it models the "physics" of battle (e.g., range and accuracy of the weapons fired, vehicle movement, area of effect) and relies on the human participants to direct the strategy and tactics in real time as the simulation proceeds. For this study, Janus was used to model a counterattack by a U.S. armored division against two second-echelon Soviet divisions—the largest scenario modeled with Janus to date.

The Army set the battle scenario (forces, terrain, missions), weapon system characteristics, and general concept for the counterattack. General unit positions and strengths were derived from a larger Army combat simulation. Army personnel from Fort

Leavenworth, Fort Rucker, Picatinny Arsenal, and the Defense Nuclear Agency joined the CSL staff to conduct the computer battle.

The computerized three-dimensional terrain of the "battlefield" was prepared prior to the Janus exercise. Unit positions were defined down to platoon and section level for Blue (U.S.) forces and to company level for Red (Warsaw Pact) forces. Janus internally further refines the units into individual combat entities. Weapon system characteristics were also entered into the Janus database; this simulation used a total of 4852 weapon systems, close to the current limit of 5000.

Janus allows each side to use several force commanders, each one controlling a subset of the total force. Commands are issued, modified, or cancelled by each commander at his workstation. Each commander can view the terrain of the entire battlefield (60 by 60 km in this case), but he can see only those forces under his command and the enemy forces he has detected through line-of-sight acquisition (a typical view is shown in Figure 2).

Eight "battles" were conducted, spanning scenarios from an engagement with conventional weapons to a battle in the latter stages of NATO's General Nuclear Response, and the outcomes were saved for subsequent analysis. The Janus results demonstrated that simple static measures of effectiveness (commonly used by others in simulation studies) do not adequately capture the essence of the battle. Important cause-and-effect relationships are too easily hidden in the mass of data generated by a simulation. Graphics-aided postprocessing of simulation data (made possible by the Analyst Workstation, developed at the CSL) proved to be invaluable as we interpreted the progression of the battles.

Our results corroborate conclusions from previous studies using other analysis tools, and suggest tactics that should be examined further. In particular:

- The effectiveness of nuclear weapon support to the tactical battle depends more on good planning than on the number of weapons or the aggregate kilotonnage expended. The utility of nuclear weapons is enhanced when their use is integrated into maneuver plans *before* the battle starts.
- Timely target intelligence and decisions to use nuclear weapons are critical for effective support to the close battle. The use of nuclear weapons requires the capability to identify and locate enemy targets quickly and accurately.

Many previous studies have concluded that in a comparable exchange of nuclear weapons between NATO and Warsaw Pact forces, NATO would have been better off if the exchange had not occurred. However, for the scenario examined in our study, this conclusion was not supported. Our results showed that compared to *no* nuclear use, Blue forces fared no worse when nuclear weapons were used, *even* for the case when the nuclear exchange was not comparable (e.g., a massive Red retaliatory strike).

Contact: R. F. Perret (415) 422-8965.

LLNL Efforts in Arms Control

The United States and Soviet Union are working toward agreements on nuclear test explosions; for verification purposes, they have conducted nuclear tests at each other's test sites.

In 1974, the United States and the Soviet Union developed the language of the Treaty Between the United States of America and the Union of Soviet Socialist Republics on the Limitation of Underground Nuclear Weapon Tests (commonly called the Threshold Test Ban Treaty, or TTBT). Two years later, language was developed for a similar treaty, the Treaty Between the United States of America and the Union of Soviet Socialist Republics on Underground Nuclear Explosions for Peaceful Purposes (often called the Peaceful Nuclear Explosions Treaty, or PNET). The intent of both treaties is to limit the yield of nuclear explosions to no more than 150 kt.

Both treaties were signed by the President of the United States and the Secretary General of the Soviet Union, but neither has been ratified by the U.S. However, both the U.S. and the Soviet Union indicated their commitment to abide by the restrictions of the 150-kt yield limit, beginning in 1976.

For a number of reasons, most recently because verification technology was considered to be inadequate, the U.S. did not ratify these treaties. The basic technique available at the time to monitor the yield of Soviet nuclear tests relied on the measurement of teleseismic signals from those tests. Seismic signals, traveling along various pathways around and through the earth, are detected and recorded by sensitive seismometers located thousands of kilometers away. The magnitude of these signals can be interpreted in terms of the intensity of the source—that is, the yield of the nuclear explosion. The signals are affected by uncertainties and variations in the geology near the explosion and in the pathways between the explosion and the seismometers. The accuracy of this technique was generally accepted to be within a factor of two. The U.S. position has been that such accuracy is not adequate to monitor compliance with the TTBT and PNET, and accordingly the U.S. has not ratified either treaty.

During the past decade, the U.S. has developed a new hydrodynamic yield-measurement technology based on very close-in observation of the velocity of the shock wave generated by a nuclear explosion. In this technique, called CORRTEX (for continuous reflectometry radius vs time experiment), an electrical cable is installed in the explosive emplacement hole or in a "satellite" hole very near the emplacement hole. The rate at which this cable is crushed by the shock wave is a measure of the velocity of the shock wave close to the explosive (from a few meters to about 100 m from the explosion); this velocity is a direct function of the explosion yield. For nuclear explosions in relatively conventional configurations, the CORRTEX method is believed to be accurate to within ±30%. The U.S. position is that having the right to use the CORRTEX method will allow effective verification of the PNET and TTBT.

In November 1987, the U.S. and Soviet Union began formal negotiations to develop protocols to the TTBT and PNET, incorporating the improved verification technology considered essential by the U.S. The U.S. delegation was headed by Ambassador Robert Barker (formerly of LLNL) and included delegates from the State Department, the Joint

Figure 1. U.S. and Soviet personnel gathered around the U.S. test canister at the Nevada Test Site during the Joint Verification Experiment (August 17, 1988).

Chiefs of Staff, the Arms Control Disarmament Agency, the Department of Defense, and the Department of Energy (DOE). The delegation's technical advisors, mostly from the Los Alamos and Livermore laboratories, provided expertise in seismic and CORRTEX technology, nuclear testing practice, and nuclear device design physics.

The formulation of U.S. negotiating policy required extensive preparation, and LLNL personnel made a number of important contributions to this process. We reviewed and updated the data that were required under the 1974 TTBT protocol and examined the factors determining CORRTEX accuracy under various conditions. We used this information to suggest revisions to the protocols of the 1974 TTBT and 1976 PNET to provide consistent levels of effective verification for the various testing environments encountered under the two treaties.

Early in the negotiations, the Soviets proposed a joint experiment involving two underground nuclear explosions, one in the U.S. and the other in the Soviet Union, to allow both sides to become more familiar with various characteristics of the verification technologies being proposed by the two sides. Planning for this Joint Verification Experiment (JVE) began immediately, both in Geneva and at the two test sites. To facilitate this planning, the U.S. delegation made a familiarization visit to the Semipalatinsk Test Site early in January 1988, and the Soviet delegation visited the Nevada Test Site a short while later.

Measurements of hydrodynamic yield played a major role in the JVE. For each of the two tests, both sides made hydrodynamic yield measurements in the emplacement hole and in a satellite hole about 11 m from the emplacement hole. The emplacement-hole measurements, unimpeded by any elaborate diagnostic hardware, were taken as "yield standards" for the two explosions. The U.S. carried out CORRTEX measurements in the satellite holes; the Soviets made CORRTEX-like measurements plus a hydrodynamic measurement using discrete "pins" or switches in the satellite holes. The satellite holes at the test sites were drilled by the U.S. with U.S. equipment because of a professed Soviet lack of such capability.

The JVE explosion at the NTS, the Kearsarge Event, took place on August 17, 1988 (Figure 1); it was followed on September 14, 1988, by the Shagan explosion at the Semipalatinsk test site. Both tests were in the yield range of 100–150 kt. Livermore and Los Alamos personnel were heavily involved in fielding the two explosions. Nearly 150 people from the U.S. traveled to the Semipalatinsk test site to participate in various phases of the preparation of that test. On the day of the Shagan explosion, 45 U.S. personnel witnessed the test, standing just 4 km from the location of the explosion.

The JVE also involved the exchange of data related to teleseismic yield determination. Several months of data analysis and exchanges of results followed the two explosions.

In parallel with the planning and preparation for the JVE, the U.S. and Soviet delegations in Geneva worked on language for the protocol to the two treaties, especially the PNET. In November 1988, the delegations arrived at mutually agreed-upon language for the PNET protocol; this protocol has been referred back to Washington and Moscow for review and comment or concurrence by the two governments.

A break in the negotiation process was initiated on December 15, 1988, for holidays and for refinement of the two sides' positions. The negotiations resumed in late June 1989. As in 1988, LLNL is actively supporting the negotiation process, both in Geneva and in Livermore.

In preparation for negotiation of the TTBT protocol, we are continuing to analyze monitoring options, drawing upon LLNL expertise in testing, weapon development, seismic and hydrodynamic monitoring, and statistics and decision analysis. We are examining both the U.S. and the Soviet positions and the implications of the proposals of both sides; the results of these technical efforts are provided to DOE policy makers and to other involved agencies.

Contact: L. Ferderber (415) 423-7789 or R. Ide (415) 422-7378.

Mix Modeling Experiments

We have developed a new mix model that enables us to calculate mix during the evolution of compressible flows. We thus simulate dynamically the interaction of mix with other physical processes such as shock waves.

The mixing of two fluids can be caused by several mechanisms, including shearing motions and acceleration. Current computers cannot accommodate models that cover the extreme range of scales required to calculate accurately the growth of instabilities, turbulence, and mixing and that include the interaction of mix with many other physical processes. To study the interaction of mix with other physical processes in a reasonable time frame, we have simplified certain aspects of the calculation. The resulting model, a two-equation turbulence model, relies on experiments to determine the values of some constants.

The mechanisms that generate mix in one dimension are the Rayleigh-Taylor (R-T) and Richtmyer-Meshkov (R-M) processes. In the R-T process, a heavy fluid is accelerated by a light fluid. In the R-M process, a light-heavy interface is impulsively accelerated in either direction. In both cases, perturbations on the accelerated interface will grow with time, eventually evolving into a layer of fluids that are irreversibly mixed.

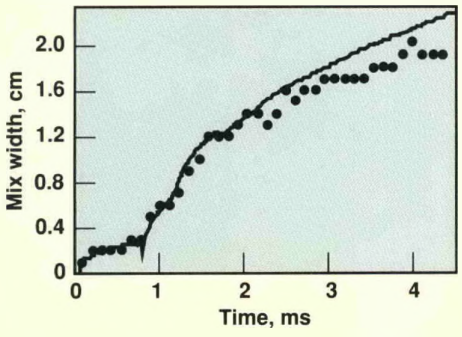

Figure 1. Our computational model (solid line) predicts quite accurately the observed growth of the mixed region at a shocked discontinuous air/SF_6 interface. The driving shock had an initial Mach number of 1.32.

Turbulence models have proved successful in modeling mix in incompressible flows, so we chose such a model as our starting point. We embedded a two-equation, compressible turbulent mix model[1] in a one-dimensional, Lagrangian compressible hydrodynamics code. We have used the resulting model to simulate mix observed in both compressible and incompressible flow experiments.

Our model embodies two new prognostic variables that are associated with turbulence: a specific turbulent kinetic energy k and a variable ϵ that represents the dissipation rate of k. To reproduce the observed phenomena, we chose the parameters in this model to give the same results as those in older, incompressible models, which contain comparable terms. To determine the values of the new parameters introduced by the new compressible terms and to test the predictive capability of the model, we turned to experiments.

Our mix model has been tested against wind-tunnel experiments, shock-tube experiments, laser-driven mix experiments, and rocket-rig experiments. We describe briefly here some results of the shock-tube and laser-driven experiments, with which we are directly involved.

The shock-tube experiments,[2,3] conducted at the California Institute of Technology under contract to LLNL, are done with a specially built, vertical shock tube. Mix behavior is studied in both discontinuous (separated by a thin membrane) and continuous (stably stratified) gases. The driving shock wave is generated in one of the gases (air) and propagates toward the interface with a second gas. The second gas is either sulfur hexafluoride (SF_6), refrigerant 22 (R22), or carbon dioxide (CO_2); in the discontinuous case, we used helium (He) as well. We found that the direction of motion of the air/SF_6 interface reverses after it interacts with waves reflected off the end wall, in contrast to the relatively smooth deceleration of the air/He interface.

Figure 1 shows the observed growth of the mixed region at a shocked discontinuous interface compared with results of our computational model. It can be seen that the mixed region grows rapidly just after the arrival, at 0.8 ms, of the first shock wave reflected from the end of the shock tube. With appropriate values of the parameters, our mix model reproduces the actual behavior quite faithfully. Interestingly, other experiments done with the same gases and a diffuse initial interface show that the asymptotic behavior of the interface depends little on the initial conditions.

The experiments done with the Laboratory's Nova laser[4–8] enable us to extend the range of mix experiments to higher Mach numbers and temperatures. In addition, we are able to study initially discontinuous interfaces without using a membrane

that could affect the results. The laser experiments give us confidence that the results of the shock-tube experiments can be extrapolated to stronger shocks and higher temperatures.

The samples used in the Nova laser experiments consisted of two or three thin layers: a parapropylene sulfide (PPS) ablator, a molybdenum or parylene C foil, and a parylene N tamper (sometimes omitted). Ablation of the PPS produces a shock wave that propagates through the layered materials; the interface between ablator and foil is backlighted and observed with a spectrometer that uniquely identifies the spatial extent and areal density of each material. Figure 2 compares the areal density produced in a high-mix laser experiment with the scaled density distribution calculated by our model. The model reproduces the areal density fairly well but slightly underestimates the amount of mixing. The discrepancy results, in part, from the fact that the one-dimensional mix model does not reproduce two-dimensional distortions of the target edges.

As future experiments provide more calibration data, the fit between model predictions and observed results will continue to improve. Using the improved model, we hope to address several issues associated with mix processes: how turbulence is generated when a shock wave crosses a perturbed density discontinuity, how turbulence is enhanced by the passage of a shock,[7] and the scale on which mix takes place. The last issue involves such questions as whether mix produces large regions that are relatively rich in one fluid and poor in the other, whether two fluids mix on an atomic level, and how the mixed region evolves from one description to the other.

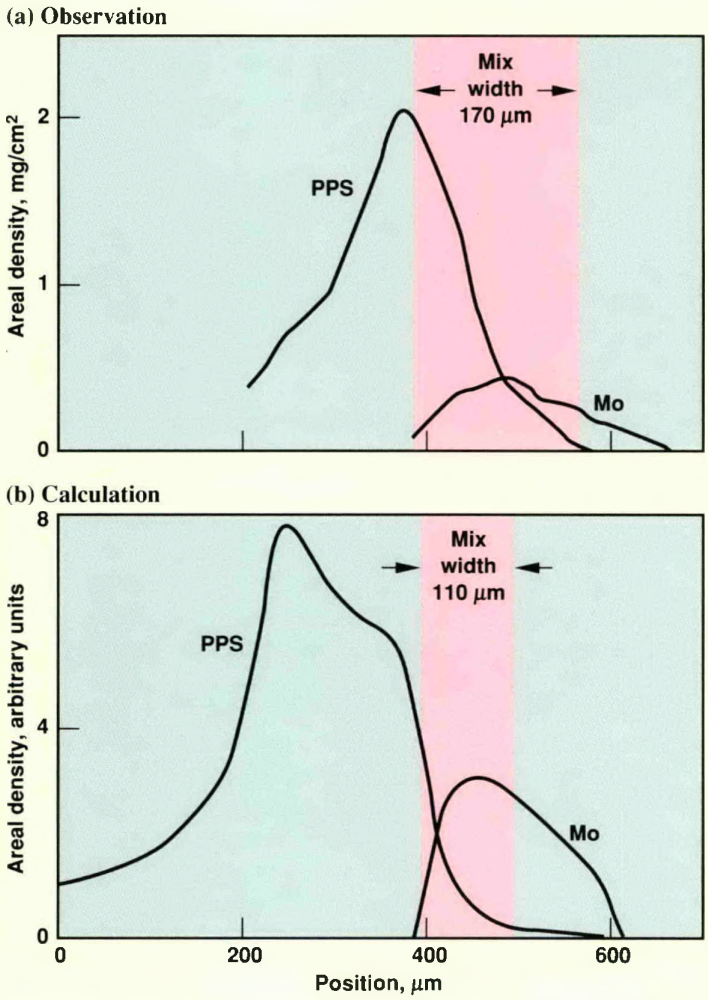

Figure 2. (a) Observed and (b) calculated areal density produced in a high-mix laser experiment. The experiment used a molybdenum foil and a parapropylene sulfide (PPS) ablator. The model slightly underestimates the amount of mixing.

References

1. C. E. Leith, *Two-Equation Turbulent Mix Model*, Lawrence Livermore National Laboratory, Preprint UCRL-96036 (1986).
2. R. Benjamin, "Experimental Observations of Shock Stability and Shock Induced Turbulence," *Physics of Compressible Turbulent Mixing Workshop* (Princeton, NJ, October 1988).
3. M. Brouillette and A. Sturtevant, "Advances in Fluid Turbulence," *Center for Non-Linear Studies Annual Conference* (May 1988).
4. J. Kilkenny *et al.*, "Measurement of Turbulent Mix of Hydrodynamically Unstable Packages," *American Physical Society Plasma Conference* (November 1988).
5. V. Rupert *et al.*, "Calculations of the Nova Mix Experiments Using a $k\epsilon$ Mix Model," *American Physical Society Plasma Conference* (November 1988).
6. P. Skowkowski *et al.*, "Edge Effects in Nova Mix Experiments," *American Physical Society Plasma Conference* (November 1988).
7. V. Rupert, J. Kilkenny, and P. Skowkowski, "Mix Experiments With the Nova Laser," *Physics of Compressible Turbulent Mixing Workshop* (Princeton, NJ, October 1988).
8. P. Fieldhouse *et al.*, "Radiation Driven Planar Foil Instability and Mix Experiments at the AWE Helen Laser," *European Conference on Laser Interaction with Matter* (October 1988).

Contact: W. P. Crowley (415) 422-4667 or V. C. Rupert (415) 422-5403.

Nonnuclear Warhead Development

The Laboratory is developing a number of warhead concepts for nonnuclear application against submarines, armored targets, and hard structures.

As more emphasis is being placed on limiting nuclear weapons, advanced conventional (i.e., nonnuclear) munitions are assuming an increasingly important role. There are many military missions for which conventional munitions are uniquely well suited, including destroying reinforced concrete targets and attacking armored vehicles. We are applying many of the unique skills and facilities developed at LLNL for nuclear weapon research to the development of advanced conventional weapons.

Multistage Munitions

In conventional warfare, many high-value targets are heavily reinforced concrete structures (e.g., command, control, and communications bunkers, bridge piers and abutments, submarine pens). An efficient, cost-effective way to attack these targets is to bury a high-explosive charge in the target and then detonate it. We have worked on a variety of multistage munitions for this purpose for more than a decade.

Our first multistage munition was a large, two-stage, hard-structure munition (HSM), designed and tested from 1973 through 1975. The first stage, or forward charge, is a large shaped charge that detonates when the munition impacts the target, weakening the target and providing a crater-like pilot hole for entry of the follow-through charge. The follow-through charge of bulk high explosive must be packaged to survive both the shock from detonation of the forward charge and the loads from its penetration into the target. The carrying missile's delivery velocity provides the kinetic energy for penetration of the follow-through charge. We successfully tested the HSM against a variety of rugged targets, including a massive block of reinforced concrete, a submarine pen, and a hardened control bunker.

From 1979 to 1982, we developed several versions of a three-stage munition. These munitions consist of a forward charge and follow-through charge plus a velocity-augmenting third stage. The velocity augmentor drives the follow-through charge into the pilot hole created by the forward charge in the target. We designed an explosively propelled multistage munition, called the velocity-augmented munition (VAM), specifically to attack airfield runways. We demonstrated the effectiveness of this munition by cratering a $3 \times 3 \times 0.3$-m slab of 27.6-MPa hardened concrete representative of an airfield runway. During the course of this development program, we learned how to scale this multistage munition

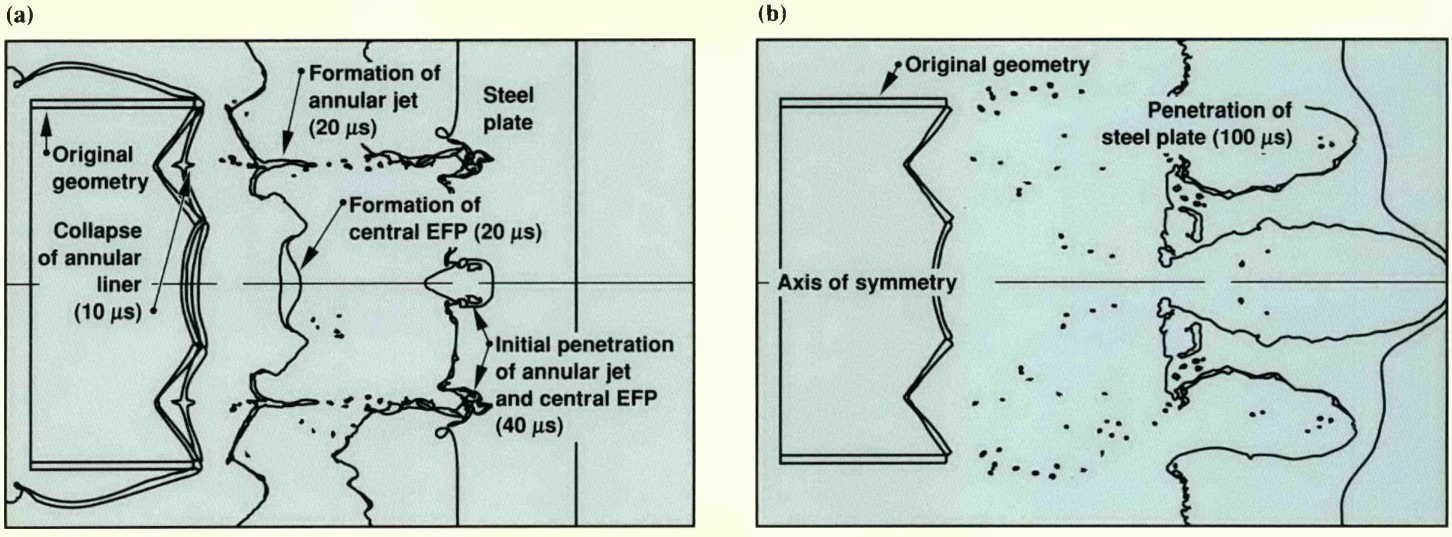

Figure 1. Computer analysis of the penetration of the forward charge of the bridge-pier munition through a 5-cm-thick steel plate representative of the rebar in a reinforced concrete structure. (a) At early times (10, 20, and 40 μs), showing the development of the explosively formed projectile (EFP) and the annular jet, and (b) at 100 μs, showing penetration of the jet.

to a variety of sizes and applications, including a larger, 45-kg version for attacking bridges, roads, and tunnels (known as BRAT).

In 1982, we extended the VAM design by replacing the high-explosive velocity augmentor with a small rocket launcher to create a munition for attacking bridge piers. This 13.5-kg penetration-augmented muntion (PAM) is currently in engineering development; LLNL-developed technologies for this munition have been transferred to the industrial contractors for the Army.

Because the military utility of this munition is lessened by the need to emplace it by hand in between the reinforcing rods in the concrete bridge piers, we are developing a version of this weapon without this limitation that will provide a standoff bridge-pier destruct capability. This new munition will be able to cut a large-diameter hole through rebar-reinforced concrete and immediately inject an explosive charge into the cavity. The injected explosive can be either a follow-through charge or a paste-extrudable explosive (PEX).

For this bridge-pier munition, we have formulated the PEX and have designed the gas-generator-driven piston needed to load the PEX into the cavity. The greatest technical challenge is to design a shaped charge that forms a toroidal jet that can cut through rebar and produce the cavity. Our early design calculations of a variety of shaped-charge configurations are very encouraging (Figure 1), and we will soon begin testing the most promising ones.

Shaped-Charge Warheads

Shaped charges develop a very-high-velocity (8–10-km/s) stretching jet of material as detonation of the explosive causes a conical metal liner to collapse upon itself. This jet can penetrate steel armor plate some 6–8 times the thickness of the original diameter of the shaped charge. For example, a 100-mm-diam charge can penetrate 600–800 mm of steel. Impressive as this is, armors are being developed that can withstand these shaped charges.

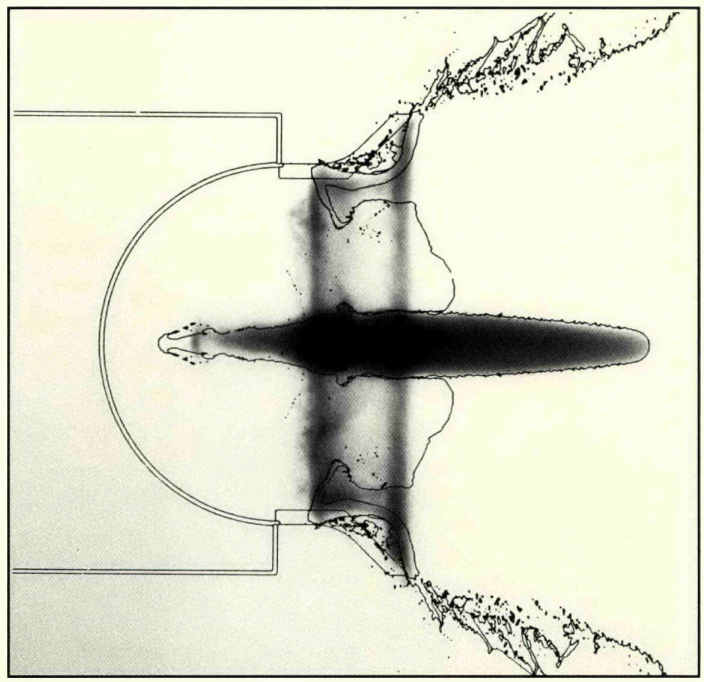

Figure 2. A computer simulation of a shaped-charge jet superimposed on a flash x-ray image at a comparable time, showing excellent agreement between calculation and experiment.

Under the sponsorship of the Defense Advanced Research Projects Agency, we are exploring new shaped-charge concepts and developing base technologies to improve their performance. The many elements of a shaped charge must be precisely designed, fabricated, and assembled. Of particular concern are the initiation system and its location, the quality, safety, and performance of the high explosive, the case configuration and material, the density, purity, constitutive behavior, and metallurgy of the liner, the precision of fabrication and assembly of the charge parts, and the environmental stability of the warhead.

Some of our most significant work has been to relate metallurgical characteristics of liner materials to performance, allowing us to screen proposed liner materials before incorporating them into a design. We use constitutive models from these studies in computer codes to predict the formation of the shaped-charge jet. Figure 2 shows the excellent agreement between a calculation of a shaped-charge jet and a flash x-ray image from a design test. Using an interactive process of computational design and experiments, we have developed an experimental shaped charge that provides much greater penetration than the warheads currently used by the military. We expect that this work will be increasingly important as nuclear arms are limited by current and future treaties and conventional forces and armaments assume greater significance.

Contact: M. Finger (415) 422-6370.

New X-Ray Diagnostics and Sources

Last year saw the development of three new x-ray spectrometers and a new laboratory source of intense x radiation.

X-ray measurements are important to understanding atomic physics processes in nuclear weapons. During the past year, we successfully fielded three new types of spectrometer to observe x-ray emission from underground nuclear tests. We also conducted successful proof-of-principle tests of several prototypes of a new class of high-brightness laboratory sources of x radiation. These innovations represent exciting developments in a continuing string of technological achievements, both at the Nevada Test Site (NTS) and in the laboratory.

X-Ray Spectrometers and Detectors for Use at the NTS

The resolving power of instrumentation used in underground nuclear tests rivals in quality the best available anywhere with respect to measurements of space, time, and energy. Applying sensitive instruments successfully in the rigorous underground environment is a notable achievement in itself; to obtain consistently high-quality data from such experiments is even more remarkable.

During the past year, we performed several programmatically important spectroscopic x-ray measurements at the NTS. These data have deepened our understanding of the ionization balance and atomic kinetics of some critical physical processes. Recently, we fielded for the first time three types of spectrometer to make three fundamentally different measurements in two different spectral regions. Thanks to the success of these experiments, we can now routinely make such measurements on underground tests.

IBEX Spectrometer

The physical basis of both the IBEX spectrometer and the XPOLY spectrometer (discussed below) is curved quartz dispersing crystals that enable x-ray focusing with the 10-μrad precision required in instruments with 10^4 resolving power. We use these spectrometers to analyze radiating sources whose specific intensities are sufficient to heat the crystals during the measurement, significantly changing the lattice spacing on the scales of interest in our experiments. Consequently, we took great care in designing both the x-ray filters placed before the crystal and a sensitive detection system. Prefilters ensure that the flux incident on the crystal produces negligible heating, making it possible to record high-level signals. Filter transmission can change as the filter is heated. Our design ensures that filter properties are understood throughout the measurement period.

The IBEX spectrometer, which operates in the multi-kilovolt region, is designed for high spectral resolution ($E/\Delta E \cong 5000$), moderate sensitivity, imaging in the focal plane, and nanosecond time resolution. The IBEX consists of a spherically curved dispersing crystal with a radius of 100 cm, an imaging detector, and a background-rejection slit. In our experiments, the entrance slit is located 20 m from the crystal; the vertical line-of-sight pipe to the x-ray source serves both as the instrument member defining the slit-crystal geometry and as a vacuum envelope connecting crystal and spectral slit. We verify the alignment to ensure that the position of the dispersion plane is well-specified even if the member should bend. A green phosphor (CdS:In) with a light output of 0.5 ns (FWHM) converts the dispersed x rays to recordable visible light, which is fiber-optically coupled to a streak camera that records one-dimensional spectral information as a function of time.

XPOLY Spectrometer

The XPOLY spectrometer is also used to record spectral information from a source radiating in the multi-kilovolt region. In this case, however, we use a toroidal crystal (modified, unfocused Von Hamos geometry) to achieve high resolution over a limited spectral range ($E/\Delta E \cong 4000$, $E_{max} - E_{min} = 40$ eV). To investigate two separate sources, we place two XPOLY spectrometers side by side. As shown in Figure 1, XPOLY's spectral slit is located 20 m from the instrument, and (as with IBEX) a line-of-sight pipe serves as connecting member and vacuum envelope. Unlike IBEX, however, XPOLY has an active alignment-control system that enables the dispersing crystal to be rotated. As the connecting member could be distorted during the downhole stemming (filling) process and the

spectral range correspondingly shifted, the active alignment system allows the crystal to be rotated to change the central Bragg angle (a characteristic angle at which x rays reflect), thereby correcting the central wavelength. As in IBEX, XPOLY's median focal-plane detector is fiber-optically coupled to a streak camera.

Johann-Geometry Spectrometer

We also developed a spectrometer, based on Johann geometry, to measure bright sources in a different spectral region from that of the other two spectrometers. In conjunction with this instrument, we developed an imaging x-ray detector that is sensitive enough to permit indirect observation of sources by using radiation Rayleigh-scattered from the direct-view line of sight by low-pressure hydrogen gas. The geometry ensures that the diffraction crystal, now located away from the intense radiation beam, is not heated by excessive radiation. The spectrometer uses the diffractive constraints imposed by its geometry to to allow viewing of nearby extended scattering sources. This greatly simplifies alignment of the instrument.

The success of the recent experiment in which we used this spectrometer to observe two different spectral regions was due in large part to the use of the imaging x-ray detector, in which microchannel plates intensify detection of x rays in the underground environment. The spatially resolving detector consists of a photocathode that converts x rays into electrons that are intensified by the microchannel plate, electrostatic focusing electrodes, a fast cadmium-sulfide phosphor that converts the intensified electrons into visible radiation, and an optical-fiber faceplate that preserves the image transmitted out of the detector.

Focusing is designed to compress the electron beam in one dimension, further intensifying and shaping it; in the cross dimension, a spatial resolution of about 350 μm is maintained. The x-ray photocathode consists of a layer of cesium iodide or

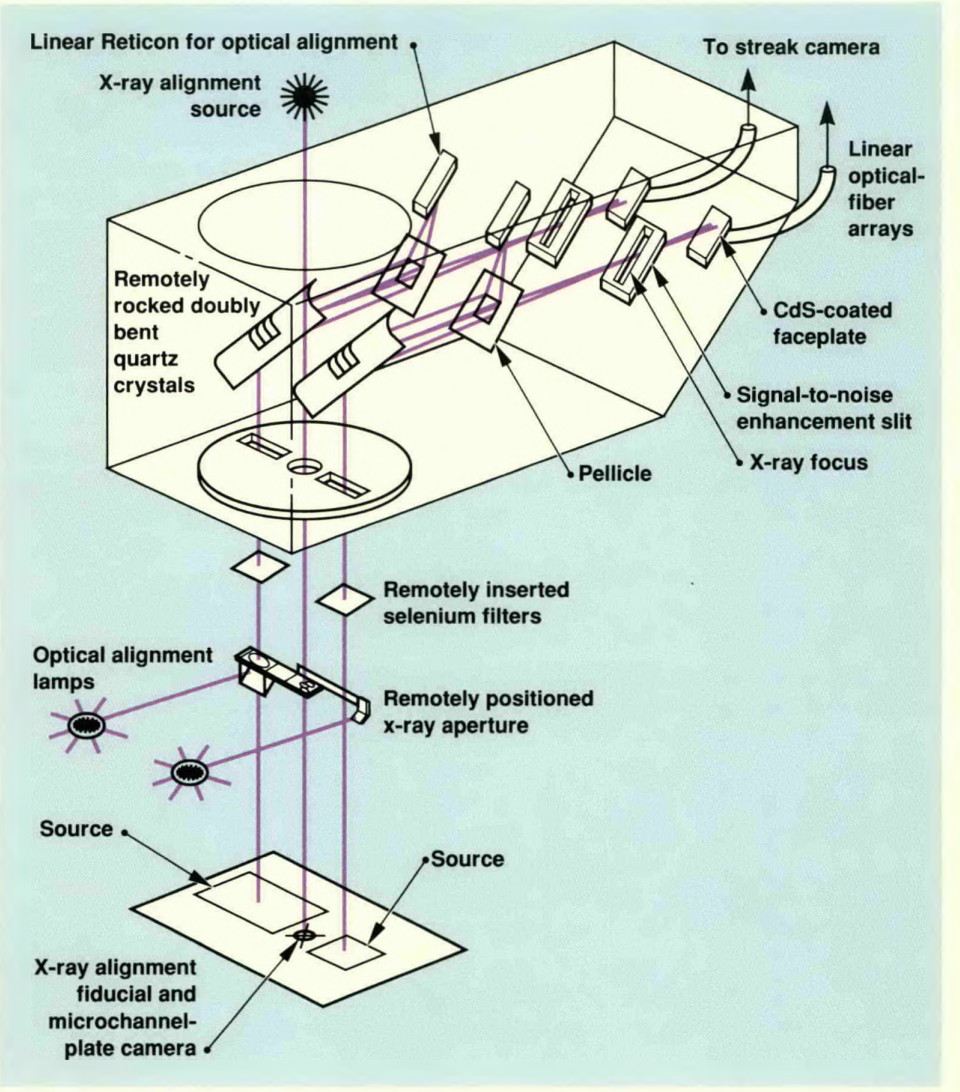

Figure 1. XPOLY spectrometer. A toroidal geometry provides high resolution over a limited spectral area. Tandem XPOLY spectrometers enable us to analyze separate sources. XPOLY's active alignment-control system rotates the dispersing crystal to compensate for distortions in the connecting member. The x-ray alignment point source and the microchannel-plate camera provide an alignment datum for remotely positioned components in the line of sight.

copper iodide vapor-deposited directly on the input face of the microchannel plate. An undercoat of conducting gold accelerates the electrons to produce cascade amplification in the microchannels. The microchannel electron amplifiers, 12 μm in diameter on 15-μm centers, provide the detector's gain. Altogether, the radiant gain of the detector is more than 10^5 times that of the same phosphor detecting unintensified 1-keV photons. This degree of enhancement is essential to observing a hydrogen-scattered source spectroscopically.

Micropole Undulator Insertion Devices: A New Laboratory Source of Intense X Rays

When charged particles are accelerated in a storage ring, either by bending their trajectory in a magnetic field or by creating an oscillating trajectory in a alternating-field wiggler or undulator, they emit synchrotron radiation. Because the energy of the particles can be controlled, and various devices can be used to modify the frequency of the emitted radiation, synchrotron radiation can cover a broad spectrum of precisely tuned wavelengths up to x-ray energies. Tunable, high-intensity radiation from such a source finds use in many types of experiments, from condensed-matter physics to biochemistry.

Wigglers and undulators having alternating magnetic fields with a typical spatial period of one centimeter are currently used on several storage rings. A micropole undulator (MPU) is an insertion device with a submillimeter spatial period. Such devices promise to provide a new class of high-brightness sources of x radiation. Installed on high-energy electron-storage rings, such devices would produce monochromatic x-ray beams significantly brighter than those currently attainable in the laboratory by any other means. Installed on a linear accelerator (linac), an MPU would produce tens of milliwatts of monoenergetic soft x rays, thus providing an x-ray source competitive with the bending magnets currently installed on high-energy electron-storage rings.

As recently as one year ago, the feasibility of scaling undulator devices to submillimeter periods was highly controversial; many in the synchrotron radiation community believed it impossible. However, a strong motive to develop short-period devices emerges when we examine the scaling relations involved. Because the spatial period of an MPU is smaller than that of an ordinary insertion device by a factor f, both the energy and spectral purity ($E/\Delta E$) of the photons it produces in first-harmonic radiation are increased by f. (This relation holds so long as the total length of the undulator remains unchanged and the magnetic-field errors and electron beam emittance are sufficiently small.) In addition, the energy of an electron beam required to produce photons of the same energy as generated in a conventional device can be reduced by $f^{1/2}$. This means that the costs of building and operating storage rings to produce x rays, as well as the associated radiative energy losses, can be correspondingly reduced.

We have investigated theoretically the scaling limits for MPUs. We included the effects of such electron-beam characteristics as positioning accuracy, energy spread, and angular divergence, errors in the undulator's period and in the field amplitude, and the effects of random Fourier components of the magnetic field, cavity interactions, and radiative recoil. In addition, we calculated the effect of an MPU insertion device on the lifetime of a compact electron beam as a result of such factors as gas desorption, Coulomb scattering, image-current interaction, and beam scraping. These calculations were done for a variety of electron machines as a function of undulator period and gap width. On the basis of our calculations and experimental results, we believe that insertion devices with a period of 100 μm ($f \cong 10^2$) and with 10^4 periods are attainable. Installed in synchrotron storage rings, such devices would provide a new class of sources of monochromatic x-ray beams significantly brighter than those attainable in the laboratory today by any other means.

This year, we have focused on developing two distinct prototype designs of an MPU. Each exploits a different technology to address issues in building spatially coherent structures with 10^4 periods. In the first design, the periodic magnetic structure is machined in a single, monolithic block of material. The periodic field, which has zero on-axis amplitude, is created by external, opposite-polarity bias magnets. The principal advantage of this design is that very-short-period structures ($\lambda = 50$ μm) can be reproduced with lithographic accuracy from ion-milled anisotropic materials such as NdFe(B) or $SmCo_5$. Experiments with a prototype on our 150-MeV linac produced the first photons ever from a submillimeter-period insertion device.

This approach considerably simplifies the technical challenge of producing devices with 10^4 periods. Such designs, however, have several shortcomings. First, the amplitude of the magnetic field generated is about

one-half the value of the remnant field in the magnetized field. Second, the bias magnets have relatively high volume, mass, and electrical power requirements. Finally, the electrical energy needed to produce the field must be dissipated by active cooling (we used liquid nitrogen).

We are also investigating a second type of MPU, a laminated design in which each "pole" is a stack of thin, magnetized wafers of alternating magnetic polarity. We assembled a prototype from NdFe(B) wafers having 54 periods of 986 μm (a total of 216 magnets). Since this design requires no bias field or cooling apparatus, and is therefore an independent element, it can be remotely positioned and scanned in vacuum with manipulators having micrometer accuracy, a considerable advantage for tuning with respect to the electron beam. A disadvantage of this design is that it is necessary to handle and characterize a large number of fragile components in which the magnetic force approaches the strength of the magnetic material.

In a series of experiments with our linac, we measured the intensity of 70-eV photons radiated by the laminated MPU design as a function of photon energy and angle (Figure 2). In both prototypes, the frequency, intensity, and angular distribution of radiated photon output were limited by the resolution of the diagnostics and by the characteristics of the electron beam. The measured values agreed with our theoretical predictions for both prototypes.

During this work, we discovered that the strength of the magnetic field in an NdFe(B) wafer decreases when it is less than about 1 μm thick. We attribute this to surface effects caused either by the presence of oxides or by machining. We have found that the phenomenon is qualitatively the same for both laminated and biased-field designs. We used $SmCo_5$, which does not exhibit this property, to fabricate two additional laminated prototypes from wafers 257 μm and 126 μm thick; these devices have 120 and 248 periods, respectively. We found that their theoretical field strength and phase criteria, as well as their measured field strength and thickness uniformity, currently limit the number of coherent periods attainable with 126-μm $SmCo_5$ wafers to about 10^3, or four times that of our largest laminar MPU prototype. At this time, it appears feasible to fabricate coherent devices with 10^4 periods only with the biased-field design.

The electron-beam emittance of our linac is not low enough to adequately test the performance scaling of 250-μm MPUs. To test the radiation characteristics of such devices at x-ray wavelengths, we will either have to upgrade our linac, a project under consideration, or travel to the Bates linac at the Massachusetts Institute of Technology or the Race Track Microtron at the National Institute of Standards and Technology (NIST), under construction. However, low-emittance, low-energy electron beams can be used to characterize these MPUs at optical wavelengths. We are preparing for a collaborative series of such experiments with 1-MeV electrons at NIST in the fall of 1989. It is important to note that either of the two prototype MPUs tested on our linac would produce tens of milliwatts of tunable, narrowband, 10- to 25-keV x rays if installed on the Bates linac, thereby making that facility competitive with high-energy electron-storage rings using bending magnets.

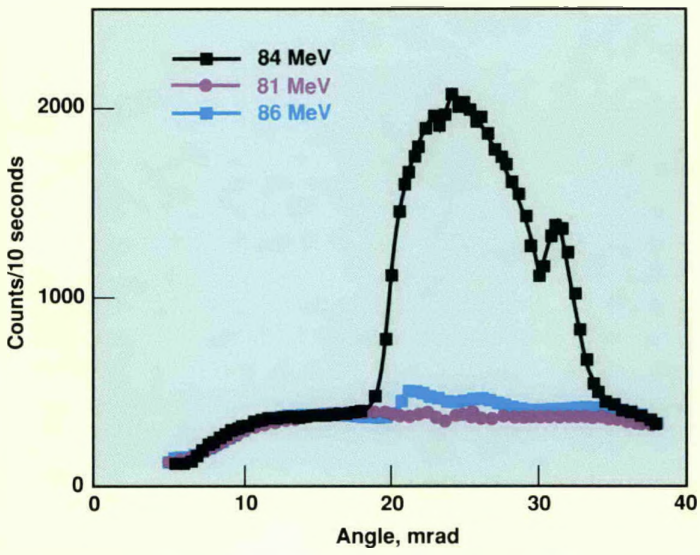

Figure 2. Angular distribution of photons radiated by our prototype NdFe(B), 986-μm-period, laminar MPU at three electron energies. The data show that a ±3% change in electron energy moves the radiated photons out of the diagnostic's bandpass, thereby eliminating the possibility that the photons originate in some other process (bremsstrahlung or channeling radiation).

Contact: R. Fortner (415) 423-7374.

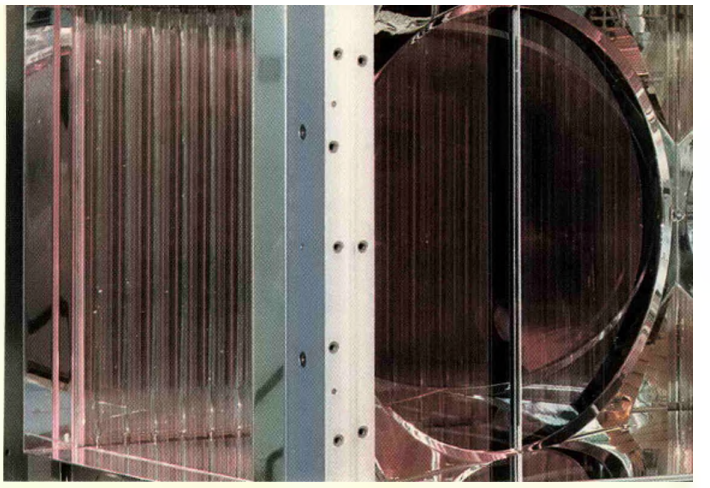

Laser Technology

We have made considerable progress this past year in each of the Laser Program's three programmatic areas: isotope separation and materials processing, inertial confinement fusion, and advanced applications.

The Isotope Separation and Materials Processing (ISMP) Program has two major efforts, the atomic vapor laser isotope separation (AVLIS) of uranium and of plutonium. For the uranium AVLIS process, our principal objective is to prove, by large-scale technology demonstrations, the economic viability of uranium enrichment for commercial reactor fuel. For the plutonium AVLIS process, our objective is the large-scale separation of plutonium isotopes for military applications.

In 1985, the uranium AVLIS process was selected as the future enrichment technology for the U.S. Significant progress was made this past year with the output of the copper vapor and dye laser systems in the Laser Demonstration Facility (LDF). In particular, the LDF was upgraded to double its laser power and triple the operating repetition frequency. The copper laser system now consists of 12 operational chains, many of the lasers operating with a completely solid-state, high-power electrical system. More than 6000 W of laser power was generated for 200 continuous hours in October 1988. The dye laser system has generated more than 1000 W of tunable power for more than 100 hours. This is the highest-average-power, visible-light laser facility operating in the world today. In 1988, the LDF lasers and the Mars separator were involved in a series of 13 large-scale tests of enrichment hardware. Three of these were integrated experiments that combined vapor and laser light to produce enrichment. These tests were the fourth generation of large-scale enrichment demonstrations conducted over the history of the program. At each stage, we have increased the delivered power and the reliability of the lasers, the operability of the separator hardware, and the specific performance achieved. Segregated liquid flows of enriched product and depleted tails, in kilogram quantities, were obtained for times on the order of 10 hours. Extensive diagnostic measurements of many aspects of the process were conducted. The acquisition of such process performance results, together with data on plant economics, will enable the U.S. to make a credible commitment to construct a production plant.

In 1986, the plutonium AVLIS process was selected for future conversion of defense-owned, fuel-grade plutonium to weapon-grade material. Considerable progress was made last year on the Engineering Demonstration System (EDS). We completed the installation of the plutonium-related hardware. This hardware includes gloveboxes and equipment for the plutonium separators, dedicated areas for storage of separator units not in use, and areas for separator assembly and disassembly. The EDS laboratory has been used with surrogate (nonplutonium) materials, and has demonstrated performance consistent with projections. Successful completion of operations with plutonium in this laboratory will support activities on a production plant at the Idaho National Engineering Laboratory in Idaho Falls.

The Inertial Confinement Fusion (ICF) Program continued to study the implosion dynamics of small microspheres with the Nova laser. Well-diagnosed experiments were conducted on the implosion of targets to a high radial convergence ratio of 30 to 1. The achievement of such large convergence ratios requires a high degree of illumination uniformity on the target. This past year, we demonstrated the ability to tune the x-ray drive in a hohlraum to better than 95% uniformity. With these optimized hohlraums, we then showed that high radial convergences can be achieved with a thermonuclear yield close to that predicted by simulations. These results support our calculations of

A Nova 46-cm amplifier with disks of the new, platinum-free laser glass installed.

the drive requirements needed to achieve high-gain implosions in the laboratory.

High-gain implosions with laser drivers require high values not only of radial convergence but also of fuel pressure. To achieve these high pressures requires knowledge and control of the Rayleigh-Taylor instability within the target. Our high-gain target designs rely on the ablative stabilization of the Rayleigh-Taylor instability. We conducted a highly successful series of experiments using x-ray drive from hohlraums driven by the Nova laser to increase our confidence in the modeling of this stabilization approach.

This past year, we completed the replacement of all of the neodymium-doped glass laser disks in the Nova amplifier chain. These new disks are free of the minute platinum particles that were present in the original glass and caused localized damage when subjected to high-fluence laser pulses. Using this platinum-free laser glass, we anticipate an output from all ten beams of Nova of 120 kJ in a 2.5-ns pulse at 1.05-μm wavelength, which will meet the maximum design performance specifications of the laser system.

In advanced laser driver research for ICF applications, we have developed a laser-pumped laser concept that could be used in the 10-MJ single-shot Laser Microfusion Facility. The pump laser is chromium-doped LiCAF which has been made to lase at about 0.78 μm. This laser, operating for about 1 μs, serves as the pump source for a Nd-CaF_2 storage laser. Analysis shows that this laser-pumped laser approach may be more cost-effective than conventional flashlamp-pumped neodymium-doped laser glass.

The Advanced Applications Program is a research and development effort that supports primarily Department of Defense projects. For application in the area of laser communication to submarines, we have invented a quasi-three-level, depletion-pumped solid-state laser. Neodymium is the active ion doped into a crystalline yttrium orthosilicate (Y_2SiO_5) host. To date, we have demonstrated Q-switched operation of Nd:Y_2SiO_5 at 0.911 μm. To obtain higher-efficiency solid-state lasers, we are developing semiconductor diode laser arrays to be used as optical sources for pumping high-average-power solid-state lasers. Our current effort entails the development of an integrated packaging approach that will permit the fabrication of very-high-average-power (~1-kW/cm^2) diode laser arrays.

We also are continuing the development of high-average-power laser sources using both neodymium-doped glass and neodymium in a crystalline host. One example using the crystalline host is our development of the master oscillator for the induction free-electron laser. Approximately one kilowatt of near-diffraction-limited laser output is required for this application. Initial operation of a Nd:GGG (gallium-gadolinium-garnet) slab laser at low pump power yielded laser outputs of 100 W in a few seconds. As a demonstration of the potential of glass lasers to achieve high pulsed energy and high average power, we are developing components and integrating them into a device designed to provide 100 W of 0.53-μm frequency-doubled radiation at a 10-Hz pulse repetition rate.

We are also making significant progress in the development of laser and nonlinear optical materials for use in high-average-power laser systems. This includes devising new crystal-growth methods, testing advanced materials, and prototyping critical components such as Q-switches and frequency doublers.

Contact: J. I. Davis (415) 423-9819.

Uranium AVLIS Program

Large strides have been made this year in the development of plant prototype systems for atomic vapor laser isotope separation (AVLIS) of uranium.

The Laboratory has invested 15 years in the development of atomic vapor laser isotope separation (AVLIS) for uranium. Development and engineering have reached the point that it is now possible to plan for near-term deployment of production plant facilities.

Uranium Enrichment Industry

It is important for the U.S. to retain a major role in the international uranium enrichment market. Such a role contributes to our energy security, technological competitiveness, and positive balance of trade. Evolving market, economic, and technological forces all point to the need for a new low-cost U.S. enrichment capability in the relatively near future.

The international enrichment market remains highly competitive. Foreign suppliers continue to target and erode the DOE's market share, and AVLIS technology is being pursued vigorously in both France and Japan. A long-expected battle for the billion-dollar-per-year, price-sensitive market of the mid- to late-1990s has begun. In addition, the gaseous diffusion plants (this country's present enrichment facilities) are faced with multiple economic, environmental, and regulatory pressures that could make them uncompetitive within the next decade.

Fortunately, the technological status of the U.S. AVLIS effort is ready to face the competition and meet the needs of the marketplace. Last year, integrated laser and separator technologies were tested at LLNL at a scale that confirms the feasibility of deploying an AVLIS uranium enrichment plant in the time frame of interest. A recently completed AVLIS plant design study projects very attractive enrichment costs in the range of $25–50 per separative work unit (SWU), making AVLIS the lowest-cost uranium-enrichment technology known.

Uranium AVLIS Technology Status

The uranium AVLIS technology consists of three major subsystems: lasers, separators, and uranium chemical processing for the interface with the nuclear fuel cycle. Copper lasers optically "pump" tunable dye lasers; the wavelength of the light from the dye lasers is precisely set to photoionize the ^{235}U isotope in the separator (Figure 1). The ^{235}U is collected as product, and the un-ionized ^{238}U is collected as tails. After removal from the separator, the product is chemically processed into a form acceptable for fuel for nuclear reactors.

The modular approach used for the AVLIS system is an essential element of the plant design. One benefit of this approach is the capability of projecting plant costs on the basis of a relatively small number of plant-scale components that can be tested and demonstrated at LLNL. This modular approach also allows for continuous upgrading of the hardware both during the development and demonstration program and later in the production facility. Nearly full-scale, plant-prototype laser and separator hardware has been operated at the Livermore site since 1985, and recent integrated enrichment demonstrations have verified performance predictions.

Nearly 800,000 hours of operation have been accumulated on the copper lasers in 24-hour/day operation over the last three years. In the past year, the operating power of the copper laser system was doubled to greater than 6000 W and the repetition rate of the system was tripled. This is the highest-average-power, visible laser system operating in the world today.

Significant progress has also continued on the uranium separators. Last year, important elements of a separator system were operated at nearly full scale. The demonstrated separator design has the features of modularity and operability that are important for low-cost use in a plant environment.

Integrated laser-separator tests successfully addressed key SWU performance and technology objectives. Our enrichment models were again validated this past year for systems that incorporate the latest design improvements. Recent tests have also provided data that support detailed design of the hardware improvements to be demonstrated in integrated tests of plant-prototype hardware planned for 1991–1992.

Because AVLIS is a metal-based technology, attention must be given to the interface between the separator hardware and the uranium fuel cycle. Presently, the gaseous diffusion plants use uranium hexafluoride (UF_6) gas as the separation medium. However, since AVLIS does not require the conversion of uranium ore concentrate to UF_6, it offers the potential for reduced fuel costs to the

utilities. We have identified several technologies that can lower the cost of interfacing AVLIS into the uranium fuel cycle using concepts that have been well established, at production scale, in the aluminum and chemical industries. When an AVLIS plant begins operation, much of the worldwide enrichment capacity will still be based on uranium hexafluoride gas. Since the transition to an AVLIS economy will take a number of years, a phased approach to the lowest-cost interface with the fuel cycle is planned.

AVLIS Plant Design and Deployment Plan

We have completed a detailed design study for an expandable 3–10 million-SWU/year uranium AVLIS plant. (For comparison, the gaseous diffusion plant in Paducah, Kentucky, one of two operating in the U.S., has a capacity of 11–12 million SWU/year.) Many different criteria may be considered in the selection of the size of an AVLIS plant, including minimizing the capital investment of the initial plant, building the smallest plant to achieve a predetermined enrichment cost, replacing one of the operating gaseous diffusion plants, or aggressively pursuing the price-sensitive market. The inherent features of AVLIS technology (modularity and high throughput) make it possible for the plant design to accommodate the selected criteria for plant size while maintaining a competitive enrichment cost.

The AVLIS plant of the recent design study is deployable in ~3-million-SWU/year increments and covers the market product-assay range of ~2–6%. This plant design contains 63,600 m^2 of building area (10% that of the Paducah gaseous diffusion plant with similar capacity). From a business viewpoint, such a plant is attractive whether it is deployed by the government, by a government corporation, or by a private venture. From the international perspective, it could have a net positive impact of approximately $1 billion/year on the U.S. balance of trade.

The planning schedule for AVLIS deployment follows from consideration of the market situation and AVLIS technological readiness. Initial operation of the AVLIS production facility is timed to compete for the price-sensitive market of the mid- to late-1990s. The major AVLIS enrichment demonstration with full-scale hardware, planned for 1991–1992, supports this planning schedule and is early enough to influence the anticipated decisions by utility companies in the early 1990s for their post-1995 enrichment needs. The deployment plan considers such key issues as the selection of the preferred plant site, coordinated planning with the Nuclear Regulatory Commission, preparation and review of the Environmental Impact Statement, obtaining state and local permits, and resolving domestic and international safeguards issues.

During the next three years, we will demonstrate enrichment performance with full-scale hardware and will compile an engineering/operations database for the specification and design of plant hardware. At this writing, we are focusing on preparations for the 1991–1992 engineering demonstration and completion of the predeployment activities for the start of plant construction in 1992.

Contact: M. L. Spaeth (415) 422-4116.

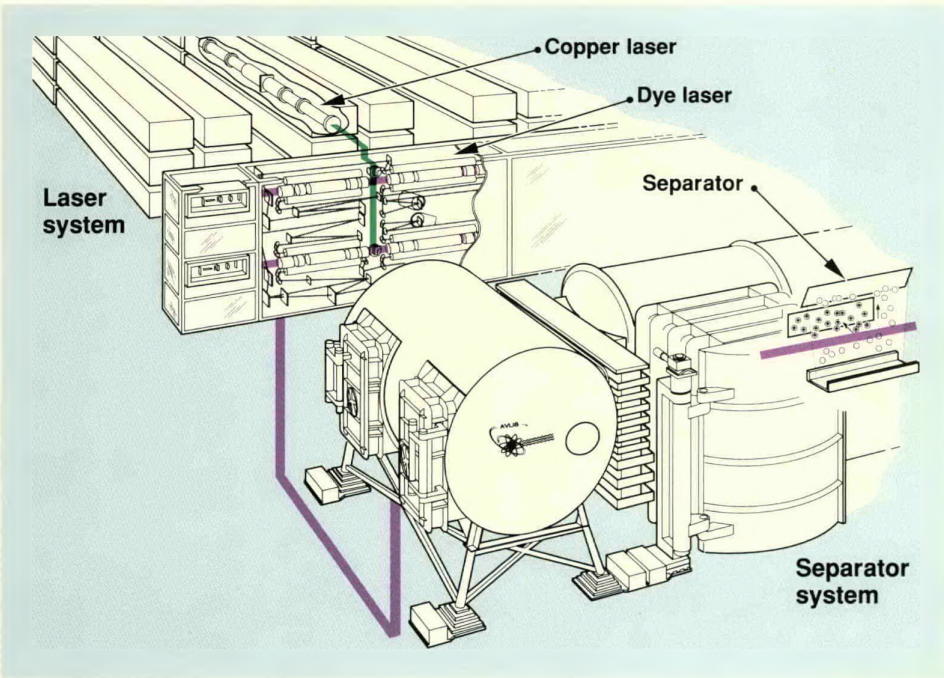

Figure 1. AVLIS laser and separator systems.

Special Isotope Separation Program

Plant prototype systems are now available to demonstrate the readiness to proceed to plant construction.

The Special Isotope Separation (SIS) Program uses atomic vapor laser isotope separation (AVLIS) to transform fuel-grade plutonium to weapon-grade material. The Laboratory has been working for approximately a decade to develop the plant prototypes of the isotope separation and chemical processing equipment. At the present time, surrogate (nonplutonium) material is being used at LLNL to test the hardware and systems that will be used in the planned SIS production plant at the Idaho National Engineering Laboratory in Idaho Falls. Successful completion of these tests will enable facility construction to begin in Idaho in 1990. The final Environmental Impact Statement for the Idaho Falls SIS plant was issued for public review in December 1988, and the DOE Record of Decision was completed in January 1989.

The SIS production plant is important to the DOE because it provides a contingent and flexible supply capability for weapon-grade plutonium with a technical approach that avoids many of the concerns associated with use of production reactors. In today's environment of uncertainty associated with other sources of plutonium, SIS has become increasingly important to national security.

SIS Technology Status

Activities in the SIS program at LLNL include the development and demonstration of all principal technologies required by the SIS production plant, both for the separation process and for plutonium processing. Although we are continuing to refine the designs for the individual technologies, our emphasis has now shifted to the demonstration of the integrated laser and separator systems and planning for plant deployment.

At LLNL, demonstration of integrated laser and separator operation is embodied in tests that utilize the Laser Demonstration Facility (LDF) and the Engineering Demonstration System (EDS), a plutonium separator system installed in the Laboratory's Plutonium Facility. Laser light from the LDF is sent, via mirrors, to the Plutonium Facility through an underground, evacuated beam tube.

The laser hardware in the LDF delivers light that is used by both the uranium and plutonium AVLIS programs. This year, the LDF was upgraded to provide output power at a level more than double that available last year and at a repetition rate that has been tripled.

The EDS hardware and support systems have been installed in the Plutonium Facility. Figure 1 shows the installed EDS linebox, which contains the separator units. This linebox and the accompanying storage, disassembly, and reassembly gloveboxes and their internal transport systems are full-scale, engineering prototypes for production plant hardware.

We recently conducted integrated cold tests that simulate many of the design features important for later application at the production site. High-average-power, multiple-color laser light generated in the LDF was transported 2 km to the EDS through the underground optical system. In the EDS, a surrogate metal was vaporized by an electron beam, the vapor was selectively photoionized, and one of the isotopes of the surrogate material was extracted in a prototype separator unit. Good agreement was achieved between the measured change in isotopic composition and the projected performance. In addition to demonstrating the integration of the laser and separator systems and verifying our physics models, these experiments allowed us to test many of the operating and maintenance procedures important for efficient and safe operations with plutonium.

Plutonium Processing

Successful operation of the future SIS production facility in Idaho also requires handling and chemical processing of the incoming feed material and the outgoing product. The steps necessary for demonstrating these tasks are being developed and optimized at LLNL.

Pyrochemical processes using molten salt solvents are used to prepare metal feed for the AVLIS process from plutonium oxide, the primary form of SIS feed. In the plant, nitrate-based aqueous processes will be used to recycle scrap and recover plutonium from the salts used in the pyrochemical processes. The pyrochemical and other nonaqueous processes, which include calcining, direct oxide reduction, molten salt extraction (to remove ^{241}Am), casting, hydriding/dehydriding, and electrorefining to remove chemical impurities, have

been demonstrated in the Materials Processing Line (MPL). The goals of these demonstrations are to verify that plant requirements for yield, purity, and plutonium utilization can be met. An example of work completed this past year is the demonstration of a superior oxidant for the molten salt extraction of ^{241}Am from plutonium metal.

Use of molten salt solvents is included in the SIS plant design because this approach generates far less waste and involves lower radiation dose hazards to workers than is possible using alternative designs. The use of a molten salt requires that chemical processing be conducted at temperatures typically ~800°C. For several years, SIS personnel have been working on an advanced molten-salt furnace design for direct oxide reduction, molten-salt extraction, and electrorefining. This tilt-pour furnace, as it is called, offers improvements in operability, including reduced worker radiation exposure, reduced waste generation, and increased productivity through shorter cycle times. This year, engineering modifications to the furnace design were completed to further improve its operability; the improved design is presently being built into the MPL for online tests.

Key aqueous processes for plutonium scrap recovery and waste processing are being demonstrated at the Pacific Northwest Laboratory, Hanford, Washington, as part of the SIS Program. These processes incorporate a catalyzed electrochemical plutonium oxide dissolution (CEPOD) process. Developmental CEPOD units have been shown to provide higher yields, reduced aqueous waste generation, and shorter cycle times than conventional dissolvers.

Figure 1. Engineering Demonstration System linebox, which contains the full-scale, production-plant engineering prototype separator.

SIS Plant Performance Verification

The Plant Performance Verification Series, to be conducted at LLNL, is scheduled to begin in 1989 and be completed in 1990. It will demonstrate the integrated performance of major operational elements at or near production batch sizes. Isotopic tailoring will be verified in the EDS with process light from LDF to simultaneously remove all three unwanted plutonium isotopes (^{238}Pu, ^{240}Pu, and ^{241}Pu).

SIS Plant Deployment Plan

Deployment of the SIS technology into a production facility is the first major step in the modernization of this nation's plutonium processing capability. In addition to the unique ability to isotopically tailor plutonium, the SIS plant will incorporate the next generation of systematically combined plutonium pyrochemical and aqueous processes, offering benefits well beyond the specific SIS mission. In order to reach these goals within the environmental and societal constraints that exist today, a major element of the SIS effort has focused on extensive environmental and safety analyses to address both short- and evolving long-term regulatory requirements.

Contact: M. L. Spaeth (415) 422-4116.

The Nova Laser

With its improved amplifier glass, the Nova laser can now operate at its full design specifications of 120 kJ (1.05 μm) and 70 kJ (0.35 μm). Experiments with Nova support research in inertial confinement fusion and weapon physics; the laser also is heavily used to develop sophisticated experiments and diagnostics for comparison with highly evolved simulation codes.

The Nova laser's output energy (60 kJ at 1.05 μm, 25 kJ at 0.35 μm) and power (60 TW at 1.05 μm, 25 TW at 0.35 μm) as well as its extensive diagnostic suite support a wide range of sophisticated experiments. However, since Nova was constructed in December 1984, we have not been able to run it at its design energy output because tiny platinum particulates in the laser glass damaged the amplifier disks at high fluences. Upon discovering this problem, we worked with the glass manufacturers to develop techniques for making platinum-free, damage-resistant glass. New glass for the amplifier disks was delivered and installed this year, and we evaluated the performance of the new amplifiers in an extensive series of experiments. These experiments, discussed in the first section below, demonstrated that the Nova laser can now meet its maximum design performance specifications of 120 kJ at 1.05 μm and 70 kJ at 0.35 μm.

Also this year, we conducted more than 300 target experiments for research in inertial confinement fusion (ICF) and weapon physics. Two examples of these experiment series, studies of the Rayleigh-Taylor instability and of high-convergence implosions, are discussed in the second section.

Experiments with laser-produced plasmas require sophisticated diagnostics to measure optical, x-ray, and particle emissions with temporal and spatial resolutions of picoseconds and micrometers. Much of the recent success of the experimental program with Nova, particularly in implosion physics, is due to the development of such diagnostics. We are now able to measure the physical processes of laser-driven implosions and hydrodynamics to resolutions fine enough to permit detailed comparisons between experimental results and sophisticated simulation codes, such as LASNEX. These comparisons are essential in the development and verification of the predictive capability of our complex modeling tools. Recent progress in advanced diagnostic development is discussed in the final section of this article.

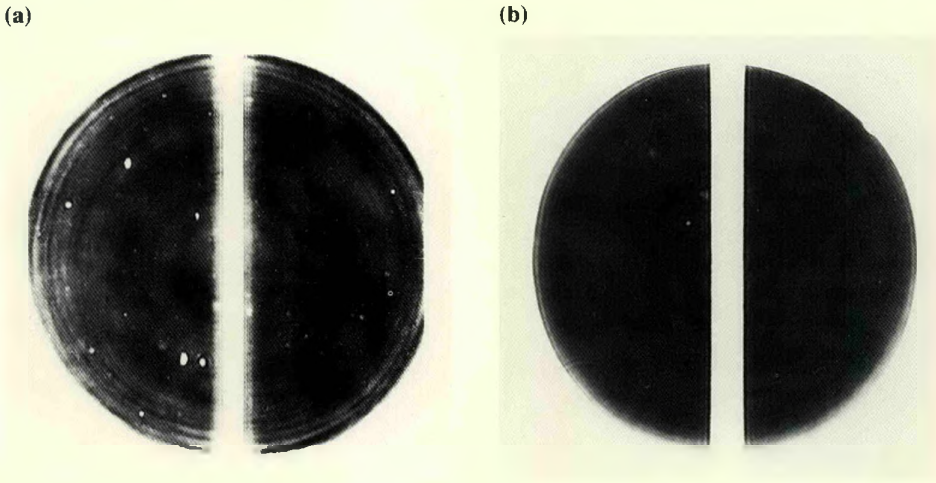

Figure 1. Nova beam profile before (a) and after (b) the new platinum-free laser glass was installed. The spots in the beam in (a) were produced by irradiation damage to the glass amplifier disks at the sites of platinum particles (>10^{-4} cm diam). The very uniform beam profile (b) verifies the absence of platinum inclusions.

New Laser Glass

In December 1988, we completed the replacement of the neodymium-doped glass laser disks in the power-amplifier stages of the Nova laser. The new disks are free of the minute platinum particles that caused high-fluence laser pulses to damage the original glass.[1] Figure 1 shows the Nova output beam profile before and after the glass was replaced.

One beamline was retrofitted with the new disks and extensively tested to demonstrate that Nova can indeed provide high output energy and power at 1.05 μm to the frequency-conversion system without damaging the laser optics. We also wanted to

demonstrate efficient conversion of the beam to the third harmonic at 0.35 μm. We took 450 shots with the retrofitted beamline in 1988 and saw no damage in the new laser glass.

We also conducted frequency-conversion experiments with the prototype beamline. We converted the 1.05-μm infrared light to 0.35-μm blue light using an array of plates cut from potassium dihydrogen phosphate (KDP) crystals. Individual KDP plates are 27 cm square and are arranged in a 3 × 3 matrix to cover the full 74-cm-diam Nova beam. Third-harmonic conversion is done by first converting two-thirds of the 1.05-μm light to 0.53-μm green light in the first KDP crystal. The green light is then mixed with the remaining 1.05-μm light in a second KDP crystal to produce the third harmonic 0.35-μm output. The current scheme in Nova uses polarization mismatch to create the right intensity mix between the first and second harmonics (called type II–type II conversion). One drawback is the sensitivity of this conversion process to the polarization state of the laser; stress-induced birefringence in the laser glass can depolarize the 1.05-μm light and thereby reduce the conversion efficiency to 0.35-μm light.

The third-harmonic conversion efficiency can be increased either by repolarizing the beam or by using a conversion scheme that is less sensitive to polarization. We tested both of these methods using the prototype Nova beam and obtained conversion efficiencies approaching 70% with both methods. Figure 2 compares the third-harmonic energies that were obtained from the standard type II–type II array with those obtained from an array built with the polarization-insensitive conversion scheme, which uses a type I KDP doubling crystal as the first element. In this scheme, angular detuning is used to obtain the correct mix of green and infrared light. With the type I–type II array, we generated up to 8 kJ of ultraviolet light, which exceeds Nova's performance specification of 7 kJ per beamline.

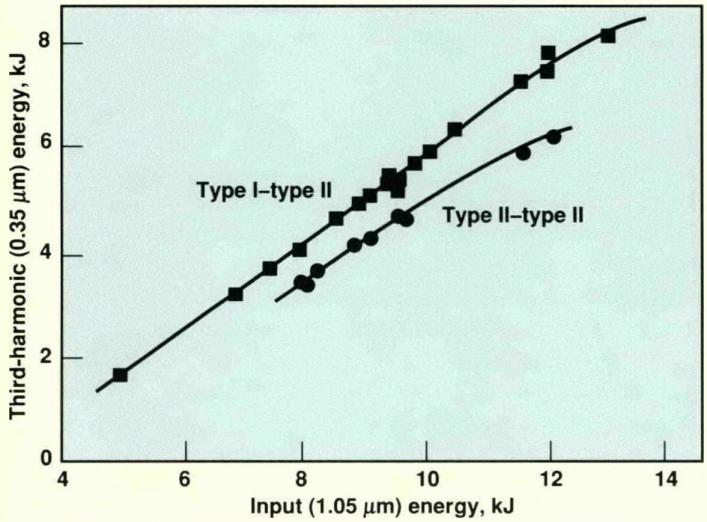

Figure 2. Output third-harmonic energy at 0.35 μm versus input energy at 1.05 μm in 2.5-ns pulses for two frequency-conversion schemes on the prototype beamline of Nova. With the type I–type II array, up to 8 kJ of ultraviolet light was generated, surpassing Nova's design performance specification.

The prototype Nova beamline also provided us with important information on transverse stimulated Brillouin scattering (SBS), a nonlinear optical process that must be understood if the laser is to produce maximum output.

We extensively tested the prototype beamline at high output energies and powers without damage to the components, confirming that the upgraded Nova amplifiers perform extremely well and enable the laser to meet its design performance specifications. The upgraded amplifiers are now installed on all ten arms of Nova, and we are in the process of demonstrating increased performance on all ten beamlines.

Target Experiments

High-Convergence Implosions

High thermonuclear gain from the compression of hydrogen isotopes at energies available from a laser requires radial convergence of ~30. This implies a very uniform ablation pressure over the surface of the target sphere. In the direct-drive approach, this may be achieved by illuminating the surface of the target with many laser beams. Nova, however, achieves a more uniform implosion if the laser light is first converted to x rays in a hohlraum. In this x-ray-drive approach, Nova's ten beams deliver about 20–25 kJ of 0.35-μm laser light onto a high-Z hohlraum. In 1988, we demonstrated that the x-ray drive in a hohlraum can be tuned to the uniformity required for high gain. Using these optimized hohlraums, we showed that a radial convergence of ~30 can be achieved with a thermonuclear yield very close to that predicted by simulations.

To demonstrate the symmetry of x-ray drive, we measured the shape of the implosion core of argon-doped

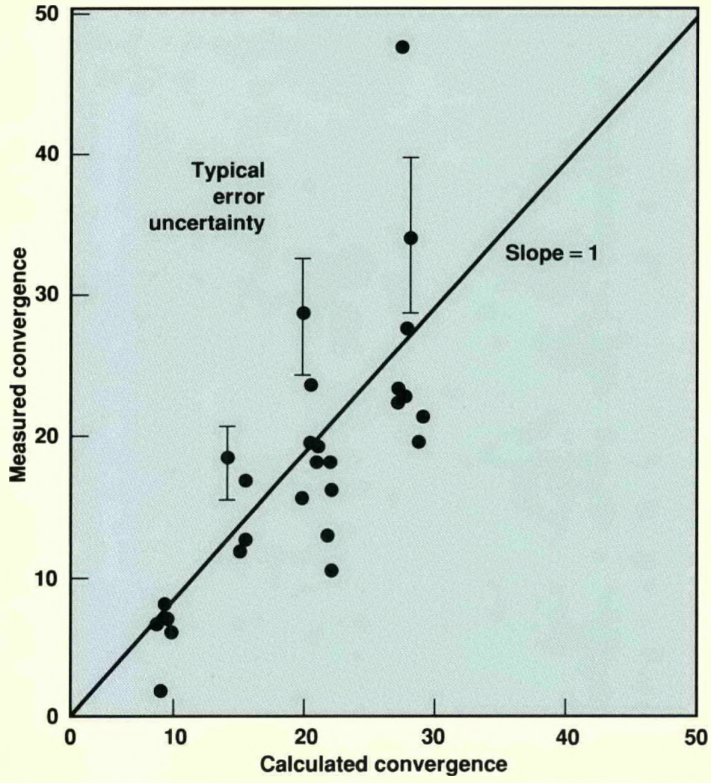

Figure 3. Measured convergence vs convergence calculated from D-D/D-T ratio. Measured convergences were confirmed by the temperature of the compressed fuel and the burn duration. Good agreement was achieved between measured and calculated convergences up to convergences of ~30.

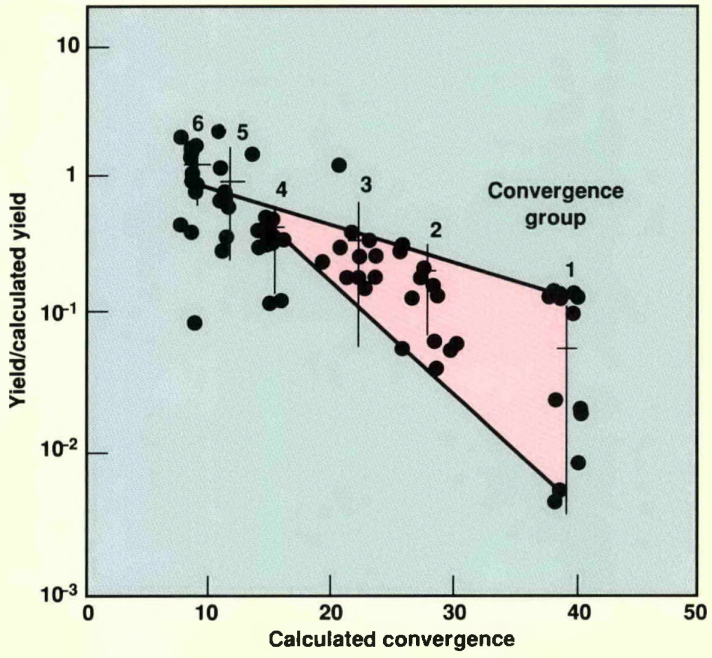

Figure 4. Yields divided by the calculated clean one-dimensional yield. For lower convergences, there is good agreement between measured and calculated yield. For higher convergences, the average measured yield decreases somewhat, a behavior that could be explained by mixing at the pusher/fuel interface (shaded region).

fuel produced from hohlraums of different geometry. A "positively" asymmetric drive gives an elliptic x-ray image, and a negatively asymmetric drive gives a sausage-shaped x-ray image of a compressed core. However, our best hohlraum produced a round compressed core, indicating a drive uniformity required for high gain.

We used the best hohlraum geometry to drive a capsule designed to achieve a radial convergence up to 30–40. The convergence was measured by the ratio of the primary 2.2-MeV neutrons to the secondary 14-MeV neutrons. These D-T neutrons are produced by the tritons from one branch of the D-D fusion reaction interacting with the background deuterium; thus their number is proportional to the areal density (ρr) of the compressed deuterium. The measured convergences were confirmed by the temperature of the compressed fuel and the short duration of the thermonuclear burn. We achieved good agreement between measured and calculated convergences up to convergences of ~30 (Figure 3).

Neutron yield is most sensitive to the quality of the implosions, because the yield is $\rho^2 \langle\sigma v\rangle \tau_b$ where ρ is the density, $\langle\sigma v\rangle$ is the Maxwellian-averaged thermonuclear burn cross-section, and τ_b is the duration of thermonuclear burn. In this temperature range, σv is proportional to $T_i^{5.5}$, and τ_b is determined by thermal conduction cooling, which is strongly dependent on the electron temperature (the classical thermal

conductivity depends on $T_e^{5/2}$). Thus, small errors in T_i lead to large changes in yield.

We conducted a series of experiments in which we measured the yield for various convergences. Figure 4 shows the yields divided by the calculated clean one-dimensional yield (i.e., the yield calculated by a one-dimensional calculation with all physics included without any adjustable parameters). We also calculated an average yield and the variance of the distribution for each of the six convergence groups. For the lower convergences, there is excellent agreement with simple one-dimensional modeling (measured yield/calculated yield = 1). At higher convergences, the average measured yield ratio falls below 1 but is still within a factor of five of an ideal one-dimensional calculation. This small decrease in yield could be explained by mixing at the pusher/fuel interface. A calculation of the effect on yield of mixing at the interface is also shown in Figure 4, showing that yield would be expected to fall slightly at higher convergences, in approximate agreement with the experimental results. At a convergence of 30, the effect of drive asymmetry would also be expected to contribute to some deviation from clean one-dimensional calculations.

Rayleigh-Taylor Experiments

As mentioned above, high-gain fusion with laboratory drivers requires a radial convergence of about 30. To achieve the necessary fuel pressures of 10^{11}–10^{12} Pa from a laser-driven ablator, pressure multiplication by imploding a thin shell is required. Acceleration of the thin shell is limited by Rayleigh-Taylor instability at the interface between the low-density ablating material and the high-density pusher.

Our high-gain target designs rely on the ablative stabilization of the Rayleigh-Taylor instability. To ensure that our modeling of this stabilization is correct, we carried out a series of modeling experiments using x-ray drive from hohlraums driven by the Nova laser. The x-ray drive accelerates a package that is "seeded" with a modulation of a known wavelength. As the target is accelerated, the seed modulations grow and become more opaque to 2-ns pulses of x-ray backlighting. Spatial resolution is obtained from a Wölter x-ray microscope that is time-resolved with an x-ray streak camera. Fluorosilicone is used as the package material because it has a high x-ray opacity in the range of interest.

Figure 5 shows the growth in time of a 100-μm-wavelength initial modulation. The x-ray-backlight timing was set to begin just before the x-ray drive starts. The initial modulation can just be seen at the start (the left of the x-ray record); it becomes more pronounced as the package is accelerated toward the detector. As the perturbation grows, the modulation evolves into a bubble-and-spike shape. This can be seen at late time in Figure 5, where higher Fourier components of the modulation become apparent.

We incorporated an accurate representation of the x-ray drive spectrum and material opacity in the LASNEX hydrodynamic computer code. The LASNEX simulation predicts the growth of the modulations very well (Figure 5). This good agreement between calculated and experimental results is very encouraging.

Advanced Diagnostics

Gated microchannel-plate (MCP) detectors are finding increased use as an alternative to more conventional, electro-optic framing cameras for photon energies from visible light to x rays. The details of these detectors, and their electronic drivers, have been discussed previously.[2,3] Their advantages include sensitivity, compactness, relative simplicity, and low cost. Their disadvantages include limited dynamic range and mechanical fragility. Here we report direct measurements of the framing time attainable with these devices.

In our experiments, the output of a short-pulse (<10-ps), synchronously pumped dye laser is frequency-doubled to 0.29 μm, where it can directly produce photoelectrons from the gold photocathode. The light hits the MCP at an angle to prevent direct light transmission through the channels. The entire system runs at 10 Hz; thus it takes only a few tens of seconds to scan through the response of the MCP. The sampling

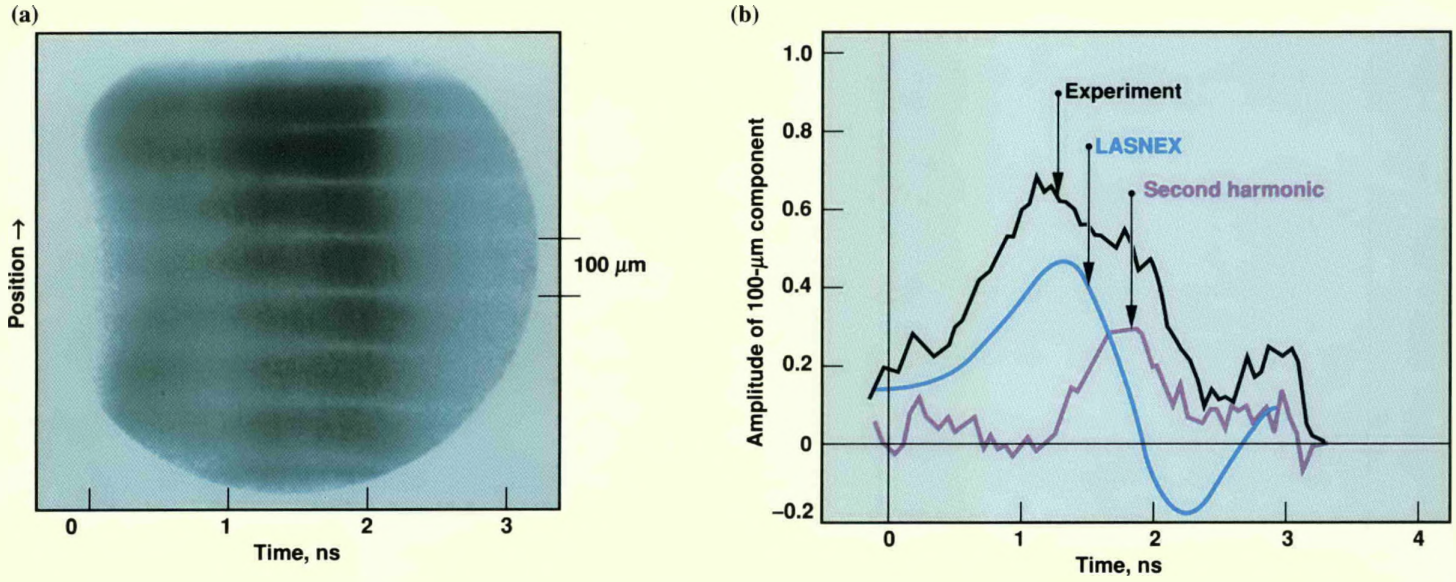

Figure 5. (a) The streaked x-ray image of an accelerating target tagged with a 100-μm-wavelength fluorosilicone marker. The x-ray backlighting was timed to begin just before the accelerating x-ray drive started. (b) The obtained amplitude of the 100-μm component and the LASNEX simulation.

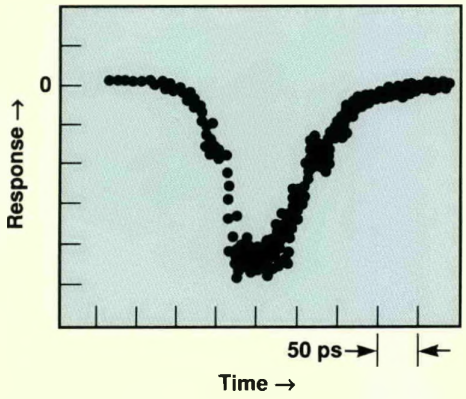

Figure 6. Response of MCP detector to 200-ps FWHM electrical pulse. Such rapid response makes MCP detectors well suited for advanced laser diagnostics.

trigger, instead of triggering a sampling head, is brought out to trigger the high-power pulser. The sampling system slowly varies the timing of the pulser trigger with respect to the time of arrival of the laser light. We typically advanced the pulser trigger 2 ps per laser pulse.

A photomultiplier views the phosphor output through a 2-mm slit. The slit is necessary since the electrical transit time of the pulse across the MCP is longer than the local response time. The photomultiplier output is sent to a gated integrator; the integrator output is displayed on the vertical axis of the scope and the relative sampling time is shown on the horizontal axis.

Figure 6 shows a typical result when using a 200-ps FWHM electrical pulse. The laser amplitude jitter makes for some uncertainty in determining the amplitude. However, the measured FWHM of the signals is between 80 and 100 ps for a 200-ps pulse. We have made no deconvolution for the electronic system response, which is less than 25 ps. When we used a 100-ps pulse, the time response was shortened to 70–90 ps FWHM, but the relative sensitivity was greatly decreased. This decrease in sensitivity is due to the finite electron-transit time through the MCP. We checked the system for linearity by inserting an interference filter into the laser beam. This reduced the signal by a factor of five, in good agreement with the known transmission (22%) of the filter.

We measured the relative gain of the MCP as a function of forward

dc bias, in addition to the pulsed voltage. We also measured the relative sensitivity of the MCP to changes in the amplitude of the pulsed voltage. The MCP relative response was found to be proportional to the voltage raised to the 13th (±2) power, somewhat higher than the usual dc sensitivity variation.

These results have all been "small-signal" measurements. As the laser intensity or forward bias is increased beyond some point, the MCP begins to saturate. The most obvious change observed as a result of saturation is that the FWHM of the response begins to broaden, until, with a 200-ps pulse, the system response is about 150 ps FWHM, or nearly twice as broad as for small signals. Thus care must be used with our current instruments to avoid heavy exposures.

We have used a Monte Carlo computer code to simulate the MCP behavior. In the modeling, a single primary electron is started from the top of the channel. The equations of motion are solved every 1 ps for each electron within the walls. An electron hitting a wall generates a number of randomly directed secondary electrons proportional to the electron's energy. Our algorithm approximately reproduces classical data showing that the secondary production is unity at about 20 eV but allows the secondary yield to continue to increase as the incident energy increases.

This code makes no attempt to calculate the effects on the electric field within the channel due to finite conductivity, a nonunity dielectric constant, or electrons propagating down the channel. The lack of three dimensions and precise information for the true secondary yield in this geometry limits the code's ability to make quantitative predictions for the absolute gain from first principles. However, such theoretical modeling is very useful for examining relative changes as MCP parameters and voltages are varied.

Notes and References

1. These platinum-particle-free disks were fabricated by a new manufacturing technique developed by a broad-based technical and management team at the Laboratory and two commercial companies, Schott Glass Technologies and Hoya Corporation. The glass is still melted in platinum containers, but an oxidizing atmosphere efficiently dissolves any particles into the phosphate-composition glass. The new laser disks also incorporate a unique and inexpensive edge cladding, which consists of absorbing glass strips epoxy-bonded to the edges of the laser disks, to prevent laser oscillation within the disk. Our patented edge cladding was developed by LLNL personnel assisted by Eastman Kodak and Zygo Corporation. The Laboratory shared R&D awards with our commercial partners for the platinum-particle-free laser glass and the cladding, which were selected by *Research & Development Magazine* as being among the 100 most important new commercial products in 1987 and 1988, respectively.
2. J. D. Kilkenny, P. Bell, R. Hanks, G. Power, R. E. Turner, and J. Wiedwald, *Rev. Sci. Instrum.* **59**, 1793 (1988).
3. Z. M. Koenig, *Rev. Sci. Instrum.* **59**, 1813 (1988).

Contact: E. M. Campbell (415) 422-5391.

Advanced Laser Applications

We are developing several advanced solid-state lasers, new laser host and nonlinear optical materials for high-average-power lasers, and semiconductor diode arrays for laser pump sources. We are also applying some of the imaging technologies developed in our laser research to overcome atmospheric distortion and make possible ground-based, high-resolution imaging of man-made satellites and astronomical objects

Much of our work on solid-state lasers involves glass or crystalline hosts doped with ions such as neodymium (Nd), which absorb and store energy from flashlamps or other optical "pumps" and release that energy as laser light when appropriately stimulated. Some large laser systems, such as Nova, deliver only single pulses of laser energy. Other applications require a succession of pulses many times per second; in these cases, the average power of the laser system (that is, the total energy delivered per unit time, averaged over many pulses) is the important feature.

Neodymium ions ordinarily lase at a wavelength of about 1065 nm, in the infrared. Using nonlinear optical crystals like KDP, this light can be converted, by a process known as harmonic generation, into light of other wavelengths that are more suitable for many applications. The harmonics have frequencies two, three, or four times that of the infrared light, so their wavelengths are corresponding fractions of the original wavelength—532, 355, or 266 nm.

Here we report on four major areas of work, including several solid-state laser development efforts, materials development projects for advanced lasers, and a new technique for producing high-power laser arrays for pumping solid-state lasers. We also describe our work on high-resolution imaging of earth satellites.

Solid-State Laser Developments

The compactness and reliability of high-average-power, solid-state lasers suits them for many applications. Neodymium-doped glasses are used if high pulse energies are needed because they can store large amounts of optical energy per unit volume and because they can be cast in large volumes. Neodymium-doped crystals are used if higher pulse-repetition frequencies are needed because they provide high gain and have high thermal conductivity.

High-Power Glass Laser

Since 1984, with the support of the Defense Advanced Research Projects Agency, we have been developing components and technology for high-power glass lasers. By the end of this fiscal year, we expect to obtain 100 W of 527-nm light from a demonstration laser now under construction. This laser (Figure 1) will produce 20-J, 20-ns pulses of 1054-nm light at a 10-Hz repetition rate (an average power of 200 W). It uses a new zig-zag glass amplifier, large-aperture electro-optic switches, an anamorphic image relay telescope, a deformable mirror, and a phase conjugator. All components are designed to maintain high optical quality under the severe thermal and stress loads generated with operation at high average power.

The $1 \times 14 \times 42$-cm amplifier (Figure 1 inset) uses APG-1 phosphate laser glass (described below), efficient solid-quartz flashlamp reflectors, and cooled edge claddings to suppress parasitic oscillations. The development of an evanescent-wave coating and noncontact coolant seals for this amplifier were crucial accomplishments.

The electro-optic switches are of a gas-cooled, transversely excited KD*P design. They maintain a high contrast ratio even under the stresses caused by passing a kilowatt of recirculating average power, and have demonstrated the required optical performance at power loadings as high as 100 W/cm^2. The KD*P frequency doubler has demonstrated conversion efficiencies of about 50% when subjected to 100 W/cm^2 of average laser power.

High-Average-Power Crystal Laser

We are developing a high-average-power crystal laser for use as a master oscillator for the induction free-electron laser, LLNL's concept for a large, ground-based laser for strategic defense. This laser will be suitable for many other applications, including laser radars and tools for cutting, welding, and machining.

To reach our objective of a near-diffraction-limited laser output of about a kilowatt, we need large, high-quality, neodymium-doped garnet crystals, and we must pump them at average powers near their fracture limit. Using a zig-zag slab laser architecture (to minimize beam distortion) and pumping with pulses only a few milliseconds long (to avoid problems with heating), we

observed lasing in a 5 × 70 × 180-mm test slab of neodymium-doped gallium-gadolinium-garnet (Nd:GGG) at our planned pumping powers. Output pulse energies of more than 5 J were obtained at much higher pumping powers.

We mounted the slab in an amplifier housing and made continuous-pumping experiments using two Vortek arc lamps, each rated at over 100 kW of continuous (unpulsed) pumping power. Operation at low pumping power yielded 100-W laser outputs in runs of a few seconds. We are now measuring wavefront and gain uniformity over the laser's output aperture. This information will help us validate our design codes and improve the designs of the laser amplifier and pump cavity.

In cooperation with Allied-Signal Corp., we are growing large boules of neodymium-doped yttrium-aluminum-garnet (Nd:YAG). Nd:YAG can deliver higher power than Nd:GGG because of its higher cross section and material strength and its better thermo-optical properties.

Ground-State-Depletion Laser

The Navy plans to establish a laser-transmitter system for communicating with submarines. The receiver's cesium resonance filters selectively pass light at 455 or 459 nm (near the optical transmission maximum in seawater), while rejecting background noise from scattered sunlight at other wavelengths. The development of efficient, compact, lightweight laser transmitters capable of operation at either of these wavelengths has been the goal of much research.

We are designing a ground-state-depletion (GSD) laser transmitter operating at 911 nm, so that a simple frequency doubling will yield a 455-nm output; its efficiency, size, weight, and cost should make it suitable for deployment. Laser action

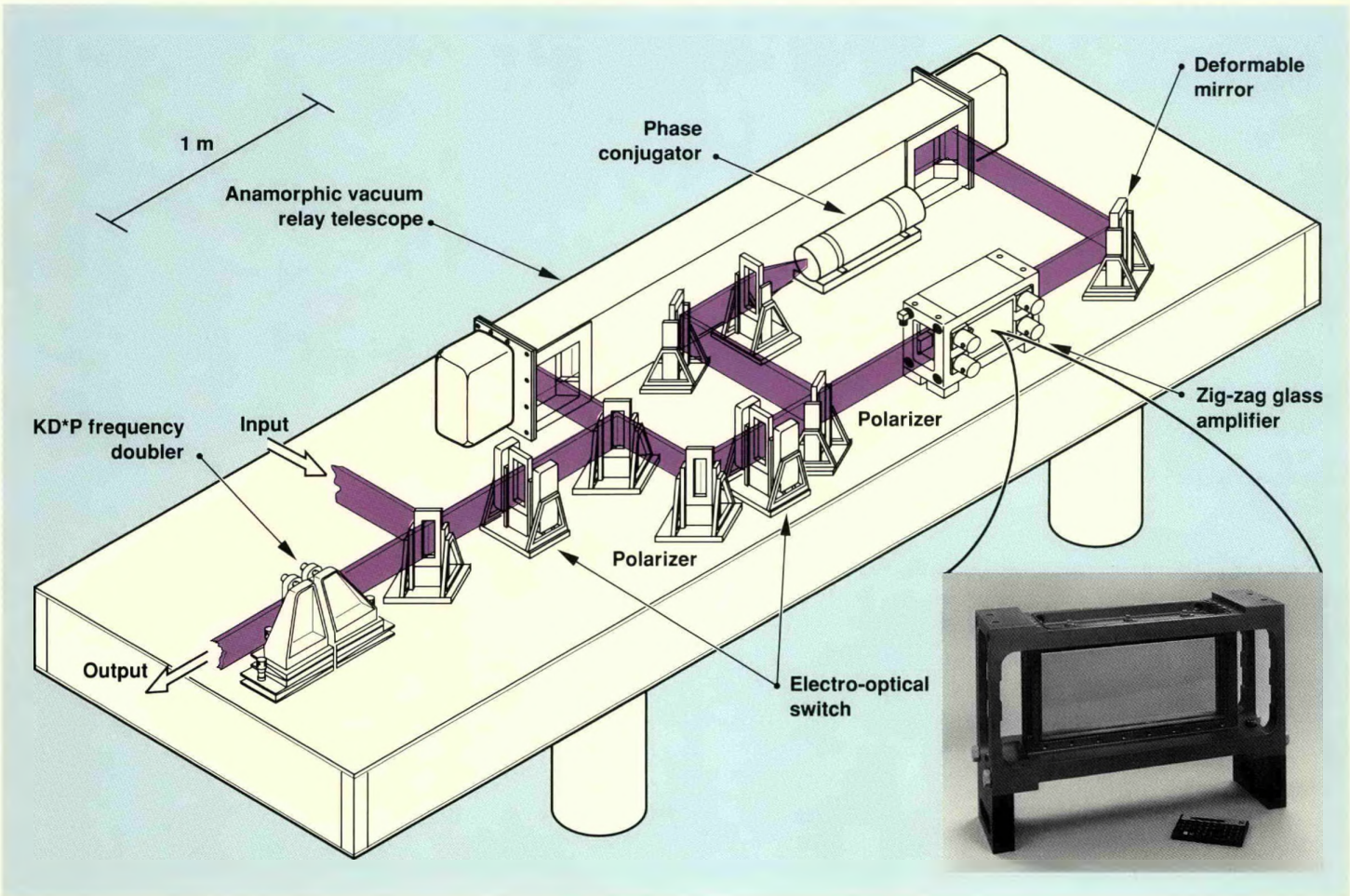

Figure 1. Demonstration high-average-power glass laser and the zig-zag slab amplifier of APG-1 phosphate glass (inset).

is generated by depletion-pumping of the ground state of neodymium ions in a crystalline yttrium orthosilicate (Y_2SiO_5) host. We obtained 911-nm output from this laser, suppressing the more readily obtained gain at 1065 nm; we demonstrated Q-switched operation, which is required for efficient frequency doubling. Gain and loss were satisfactory, and we are working to raise the damage threshold of the laser crystal.

We plan next to construct a GSD laser pumped by an alexandrite laser. This will be a relatively inexpensive way to demonstrate the feasibility of laser pumping with efficient diode arrays (discussed below). Our goal for the alexandrite-pumped laser will be single-shot outputs of 0.5 J at 455 nm.

Materials Development

We are devoting considerable effort to the development of new materials for advanced lasers. We are searching for improved laser host materials and for efficient, damage-resistant nonlinear optical materials for frequency conversion. Such new materials are essential if we are to construct the large, high-power lasers needed for fusion at reasonable cost.

Laser Materials for High Average Power

We are developing and improving two crystalline materials for high-average-power laser applications: Nd:Cr:GSGG for high efficiency, and Nd:YAG for high repetition rates. We are working with Allied-Signal Corp. to grow low-absorption boules of Nd:Cr:GSGG over 20 cm long and 10 cm in diameter. As we reduce absorption, however, we must maintain high optical quality and low scattering. We have achieved absorptions of less than 1.5% per centimeter in small samples by using melt additives such as cerium. We have further reduced the absorption to an acceptable 0.5% per centimeter by postgrowth heat treatment; in large boules, however, heat treatment leads to defects that scatter light and thus degrade beam quality.

The useful volume of conventionally grown Nd:YAG boules is limited by beam depolarization and bending in a high-stress region, called a core, that forms along the boule's central axis. Core formation can be prevented by rotating the crystal rapidly during growth, forcing the growth interface between the crystal and the melt to be flat (and stress-free), rather than concave as in the standard technique. Our goal is to grow coreless, 75-mm-diam boules of Nd:YAG; we have already grown coreless boules of undoped YAG 75 mm in diameter, and have grown coreless doped boules 30 mm in diameter.

To improve laser efficiency and power, we are working to reduce the impurity-induced absorption of neodymium-doped laser glass. Most of this research is conducted by Hoya Optics and Schott Glass Technologies under contract to LLNL. Optimizing the phosphate glass composition for good laser and thermomechanical properties has doubled the thermal power the glass can tolerate without fracture. Schott has developed and is commercially producing large, platinum-free castings of an advanced phosphate glass, APG-1. (Platinum impurities limit the laser fluence that the glass can tolerate without damage.) Hoya has recently produced castings of glasses with equally good laser and thermomechanical properties.

New Laser Host Material

We have discovered and are characterizing a new laser material, chromium-doped lithium calcium aluminum hexafluoride (Cr:LiCAF). This material lases with high efficiency near 780 nm and thus should be suitable for pumping neodymium-based laser amplifiers. The spectroscopic, laser, and thermomechanical parameters of Cr:LiCAF should also make it suitable for use as a laser pump source.

Advanced Crystal Growth Technology

In support of the laser fusion program, we are developing a technique for growing large crystal slabs, rather than cylindrical boules that must be cut to the desired slab shapes. We are working with contractors to develop a variant of the Bridgman method that will allow us to grow crystals with dimensions of about $2 \times 10 \times 20$ cm from melts at temperatures up to 2100°C.

Our experimental program is supported by computational models that simulate the temperature distribution and fluid dynamics of crystal growth. We obtained very encouraging results in growth studies on Nd:YAG and are now studying the growth of Nd:CaF_2, Nd:SrF_2, and Cr:LiCAF.

This work was funded by the Laboratory's Institutional Research and Development (IR&D) Program.

Nonlinear Optical Materials

We are studying frequency-conversion crystals such as deuterated l-arginine phosphate (d-LAP). This is one of many new nonlinear optical materials, based on organic acids, that may provide more efficient frequency conversion than KD*P. Our work on d-LAP has validated our approach to discovering and developing practical frequency-conversion materials.[1]

D-LAP is particularly interesting for high-average-power applications because calculations predict and our experiments appear to confirm that it can operate efficiently over a wide

range of temperatures. We are working with our contractors to reduce optical absorption in d-LAP so as to reduce thermal stresses at high average power.

Another interesting crystal is deuterated l-arginine acetate (d-LAAc). It looks to be especially attractive for third-harmonic (355-nm) generation with neodymium lasers. We have grown crystals of d-LAAc as large as $5 \times 3 \times 2$ cm and will soon begin optical and mechanical tests.

Semiconductor Laser Array Packaging

With support from the IR&D Program, we have developed an approach to the fabrication of arrays of laser diodes (such as GaAlAs) that should be able to deliver average powers as high as a kilowatt from 1-cm^2 diode-array surfaces. Such arrays can be used as pump sources for very-high-efficiency, solid-state lasers.

Semiconductor lasers have been developed with high efficiency (>50%) and high peak power (>1 kW/cm^2), attributes that make them suitable for many applications. Overheating, however, limits their average power output, reduces their efficiency, and shortens their lifetime. A temperature rise of 20°C is about the limit for long-lived, efficient operation at high average power. In a structure generating 1 kW of waste heat over an area of 1 cm^2, this corresponds to a thermal resistivity of less than 0.02°C·cm^2/W.

To achieve resistivities this low, we have combined microchannel cooling technology with high-conductivity array architectures. The microchannels minimize the thickness of the coolant boundary layer—the greatest obstacle to obtaining high thermal conductivity—by providing very narrow, smooth channels for coolant flow while requiring low power for coolant pumping.

We etched channels as small as about 17 μm wide by 60 μm deep into silicon wafers and bonded these to coolant-distribution structures. These coolant structures were then bonded to metalized, synthetic-diamond-chip carriers that were also bonded to AlGaAs semiconductor laser bars assembled as one- and two-dimensional packages. The best one-dimensional structures have resistivities of less than 0.02°C·cm^2/W. Bars measuring only 3 mm long and exhibiting only 25% efficiency have nevertheless delivered more than 5.5 W of average power (Figure 2); the highest average power delivered by commercial bars is 5 W over 10-mm apertures. We constructed two-dimensional packages from which some 30 million quasi-continuous-wave shots were fired over 50 hours of uninterrupted operation. We are working to increase lifetimes to greater than 1000 hours.

We obtained irradiances of 111 W/cm^2 from a two-dimensional semiconductor laser array, exceeding the previous state of the art by a factor of 10. The efficiency of this device was 25%. Integrated cooling architectures usable in all semiconductor laser architectures will soon be assembled and tested.

High-Resolution Imaging

National security requires that the U.S. determine the nature of the many earth satellites already in orbit and of new satellites as they are launched. This in turn requires a low-cost technology for rapid, ground-based, high-resolution imaging. Resolving 10-cm features on satellites at altitudes of 1000 km demands telescopes with apertures of about 12 m, and telescopes with 100-m apertures will be required to obtain 40-cm resolution at 40,000 km.

High-resolution imaging will have many benefits in astronomy as well. Telescopes with 10-m apertures could resolve features on the surfaces of supergiant stars; 100-m telescopes could resolve active galactic nuclei; and 1-km telescopes could resolve planets around nearby stars.

If we could observe objects in space from above the earth's atmosphere, angular resolution would

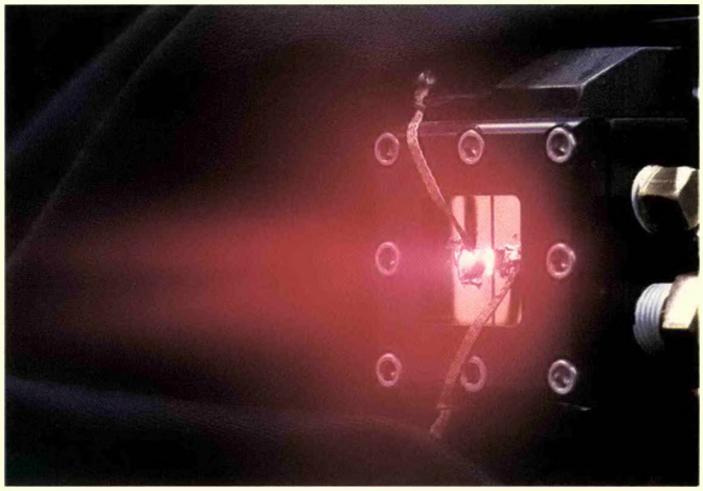

Figure 2. This phase-locked, microchannel-cooled, semiconductor laser bar emitted 5.5 W of average power at 770 nm. Phase-locking is responsible for the double-lobed nature of the emission.

be limited only by the diffraction of light. At wavelength λ, we could just resolve point objects with angular separations of λ/D radians. (All the resolutions quoted above refer to this so-called diffraction limit.) However, thermal distortions in the earth's atmosphere limit the angular resolution of ground-based telescopes to λ/r_0, where r_0 (typically about 10 cm) is the so-called coherence length of the atmospheric distortions—roughly speaking, the size of the smallest uniform blobs of air through which objects are viewed. Thus, despite its great light-collecting capability, the resolution of the 200-in. (5-m) Mt. Palomar telescope is no greater than that of a 10-cm telescope.

It is known, however, that information with angular resolution up to the diffraction limit is present but scrambled in images taken through the atmosphere. For example, if we image a point source of light, such as a star, with a telescope whose aperture D is considerably greater than r_0, we get a spot whose diameter corresponds to the angular resolution λ/r_0. If we increase the coherence length of the light by using a narrowband filter and freeze the atmospheric distortions by taking exposures no more than a few milliseconds long, we find that the large spot is actually composed of a random array of small spots, called speckles, of angular width λ/D.

Our experiments and computer simulations show that we can recover a diffraction-limited image, under conditions comparable with those to be expected in satellite imaging, from a set of speckle images. We use the standard technique of separately estimating the Fourier magnitudes and phases of the image's spatial-frequency components. Combining these two estimates gives us the reconstructed, diffraction-limited image. The 1.2-km path in our experiments (between Mt. Diablo and a nearby hilltop) was long enough to give atmospheric turbulence levels equal to those encountered when looking up through the entire atmosphere. Using a 0.5-m telescope, we imaged targets of various sizes, shapes, and brightnesses. We obtained several gigabytes of data, indicating that large-scale use of this technique will generate an immense computational load.

Figure 3 shows some before-and-after images from these experiments, typical of the results we can expect from satellite imaging at altitudes of about 1000 km. The reconstructed image is clearly much better than any single frame, and future improvements in our technique should yield even better images.

It would, however, be prohibitively expensive to implement these techniques with conventional telescopes. For example, the Keck telescope, which will have a single, segmented aperture of 10 m, will cost about $100 million. The costs of such telescopes scale as the cube of their apertures, so a 20-m telescope would cost $800 million, and a 40-m telescope would cost $6.4 billion! Obviously, completely new designs are needed if we are to obtain apertures of 100 m and more at reasonable cost.

We can greatly reduce cost by arranging many small telescopes in a

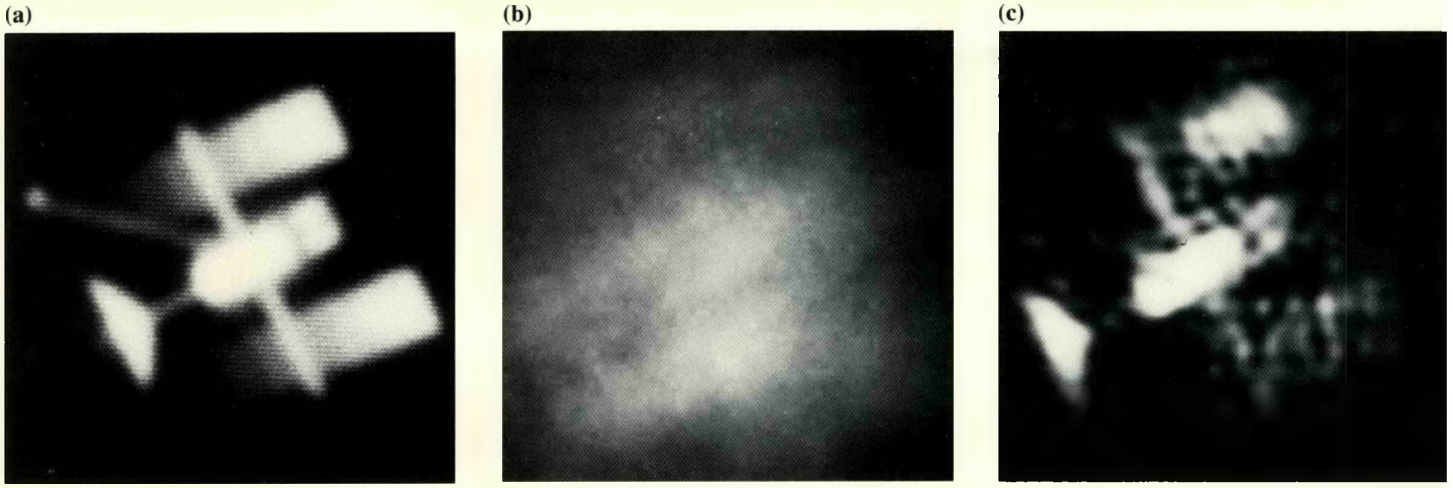

Figure 3. (a) Image as would be obtained with a perfect telescope through a vacuum, (b) single-exposure image obtained through 1.2 km of turbulent air, and (c) reconstructed image at light levels equivalent to 10-cm resolution at 1000 km.

nonredundant pattern, rather than completely filling the aperture, and then combining their outputs coherently at a single image sensor. Dimensional tolerances in such a system can be more relaxed than in conventional telescopes because the light path lengths must be matched only to within the coherence length of filtered light, not to a fraction of a wavelength as in conventional white-light imaging.

We have designed such a telescope; Figure 4 shows a design with a 20-m aperture that uses twelve small telescopes. The telescope will be supported on a central gimbal so it can be controlled by "alt-alt" tracking, a technique that is well suited to following fast-moving objects overhead. The thinness and compactness of the telescope structure increase its stiffness enough that the telescope can operate in the open, without the need for an expensive dome. An inflatable cover can be used during the day and in bad weather.

All our observations will be done in the visible, so we can take advantage of the lower costs associated with operation at sea level. We have identified a site on the northern California coast that has superb "seeing" (that is, large r_0 values).

Figure 4. Model of a 20-m, twelve-aperture version of the low-cost speckle-imaging telescope.

We will continue to assess system performance in numerical simulations and terrestrial experiments during fiscal year 1989. We are preparing a detailed design for a 10-m telescope system from which we hope to obtain a cost estimate accurate to within 20%. (This work is supported by LLNL's IR&D Program.)

References

1. See "Characterizing D-LAP for Fusion Applications," in the July-August 1988 issue of *Energy and Technology Review* (UCRL-52000-88-7-8), p. 43.
2. T. W. Lawrence, J. P. Fitch, and D. M. Goodman, "Image Processing Using the Bispectrum," *Proc. 22nd Asilomar Conf.* (1988).

Contact: J. Holtz (415) 422-4117.

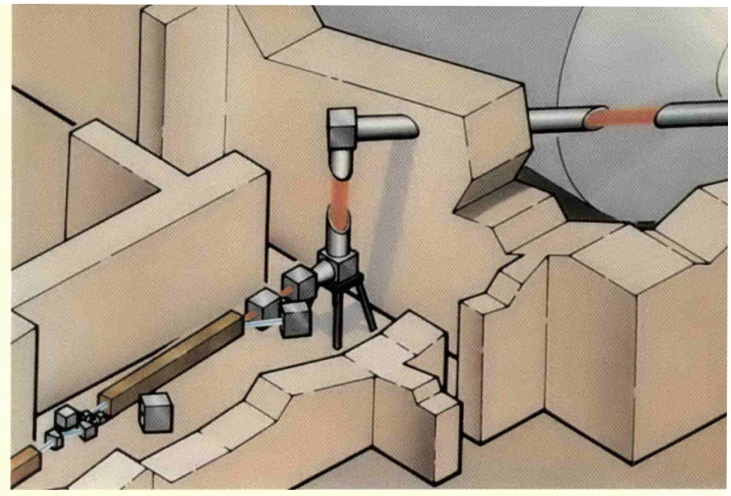

Magnetic Fusion Energy

Following the termination of the magnetic-mirror program at LLNL in 1987, Laboratory magnetic fusion researchers have turned their attention and expertise to the challenge of tokamaks. The goal of magnetic-mirror devices and tokamaks is the same: to heat and magnetically confine a plasma long enough for fusion to occur and energy to be released. We are conducting two new research projects here at LLNL and are collaborating in two important projects with colleagues in the U.S. and abroad.

The Microwave Tokamak Experiment (MTX) is being constructed at the Laboratory (see the article on p. 40). It will test the feasibility of using free-electron lasers (FELs) to heat electrons and drive plasma current in a high-field tokamak similar to the Compact Ignition Tokamak (CIT) that is to be built at Princeton University by 1996. The goal of the CIT is to demonstrate ignition in a deuterium-tritium (D-T) plasma. The MTX will provide a key test of whether or not FELs can be used to heat the D-T plasma in the CIT.

The MTX has recently achieved routine operation with ohmic self-heating ($T_e \approx 1$ keV, $n_e \geq 2\text{–}3 \times 10^{14}$ cm^{-3}). The first pulses of intense microwaves from the FEL of the ETA II facility are expected early this summer. Initial experiments will concentrate on plasma absorption of high-power pulses (gigawatts at 140 GHz), to be followed by heating experiments with long trains of pulses at higher powers and frequencies (≥10 GW peak power, 2 MW average power, at 250 GHz).

The objective of the Compact-Torus Accelerator Project (also being conducted at LLNL) is to accelerate, compress, and focus plasma rings confined by compact-torus magnetic fields (see the article on p. 42). One of the motivations for this work is to develop a low-cost driver for inertial confinement fusion. Another possible application would be to inject accelerated plasma rings into a larger tokamak plasma to fuel the tokamak and to drive current by inductive pulses carried along with the magnetic flux contained in such compact plasma toruses.

We are also participating in important collaborative research, both with General Atomic Technologies and with the international team of researchers designing the International Thermonuclear Experimental Reactor (ITER).

We are collaborating with General Atomic Technologies, in San Diego, on experiments using their DIII-D tokamak. The DIII-D device is a uniquely flexible, large tokamak with many features in common with the CIT and the ITER designs. It has an elongated cross section with a divertor (i.e., a magnetic field configured to divert or eliminate unstable edge plasmas), uses high-power neutral-beam injection and microwave plasma heating, and has extensive diagnostics. These features allow us to use the DIII-D to understand the effects of plasma β (the ratio of plasma pressure to the magnetic energy density), energy confinement, edge physics, microwave heating, and noninductive current drive.

Studies are being conducted to obtain an understanding of the physics of plasmas in the outer edge of the tokamak and to develop a predictive model of these plasmas. In a diverted tokamak like the DIII-D, these edge plasmas are in direct contact with the walls of the device; our experience in the operation of mirror fusion devices is of great value to these studies. We have developed and installed diagnostics to measure the heat load of escaping plasma in the DIII-D divertor; the measurements made with these instruments are among the first of their kind and are essential to the design of ITER-type devices. We have also installed diagnostics to determine the spatial profile of the visible light emission from the neutral hydrogen atoms in the tokamak. These measurements are crucial for determining the radial profile of the particle source strength and, from that, understanding the factors that affect particle confinement. We are in the process of developing a detailed model of the behavior of this plasma and will benchmark the model with our measurements.

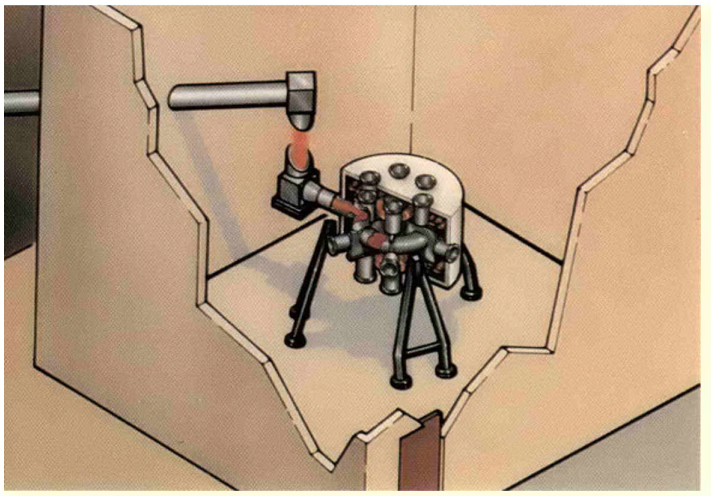

The Microwave Tokamak Experiment facility will be used to study the interaction of intense microwave pulses with plasma confined in a tokamak.

We are also investigating the use of electron cyclotron heating (ECH) in a tokamak plasma. Because of its localized nature, ECH can be used to control plasma instabilities that are driven by pressure gradients within the plasma; short bursts of ECH can also be used to deposit energy locally in the plasma. These studies with the DIII-D are applicable to the use of ECH on the MTX. From these experiments, we have been able to devise an improved confinement mode (H-mode) using ECH only. The DIII-D was the first tokamak to achieve this result.

In addition, we are studying the physics of noninductive current driven by ECH and neutral-beam injection. The DIII-D has 14 MW of neutral-beam power, which is used both to heat the plasma and to provide noninductive current drive. These beams have been used to heat high-density plasmas to a world-record plasma pressure (6.8%). Laboratory researchers have been instrumental in these current-drive studies and have achieved plasma currents of 300–400 MA. The sustained current is consistent with the value expected from classical processes. We are developing a diagnostic to measure the poloidal magnetic field in the DIII-D to better understand the effects of noninductive current drive.

Work is also being done on the many "peripheral" systems required to operate a tokamak, including neutral beams, ECH, vacuum, diagnostics, and cryogenics. Much of our experience with magnetic-mirror devices is applicable to tokamaks.

On the international level, LLNL has been awarded the responsibility for leading the U.S. effort to design, research, and develop the ITER. We are coordinating research activities at LLNL and other U.S. fusion laboratories with the work being done in Europe, Japan, and the Soviet Union. The goal of this international project is to produce a tokamak reactor design by 1990, together with sufficient development of the necessary supporting technologies, so that the participating nations will be able to decide whether or not to construct such a reactor. The technical goal of the ITER is to demonstrate the scientific and technological feasibility of fusion power. The ITER is to achieve controlled ignition and extended burn of a D-T plasma, with steady state as the final objective. It is also to demonstrate the supporting technologies essential for a fusion reactor.

In May–October 1988, an international team of ITER researchers gathered in Garching, near Munich, to define the ITER design. The U.S. sent eleven team members, of whom five plus an administrator were from LLNL. The specified design is for a tokamak 5.5–5.8 m in major radius and a current of 18–22 MA in the plasma. The magnets confining the plasma are to be superconducting, with a peak field near 12 T and a pulsed capability to inductively start the plasma current. Auxiliary plasma heating components (e.g., negative ion beams, klystrons, gyrotrons, FELs) are to be included to assist the plasma current startup, if needed, and to sustain steady-state operation.

About 70 other scientists and engineers in the U.S. are working as the "home team" in support of the ITER team members assembled in Garching. We are coordinating this effort. A new electronic mail system, linked by the LLNL National Magnetic Fusion Energy Computer Center (NMFECC), allows team members in the U.S. and in the other nations to exchange messages, reports, and data files. A computer-aided design system was recently installed in Garching and linked with the NMFECC to permit the exchange of drawings as well.

The likelihood of success in the ITER project is greatly enhanced by the international collaboration of world-renowned experts in magnetic fusion. We hope that the ITER will establish the precedent for international cooperation on other projects with worldwide benefits.

Contact: G. Logan (415) 422-9816.

Microwave Tokamak Experiment

We have brought a new tokamak facility into operation this year to investigate the interaction of intense microwave pulses with plasmas and the resulting heating.

The Microwave Tokamak Experiment (MTX) is designed to investigate plasma heating and confinement. This experiment uses a free-electron laser (FEL) to generate short pulses of gigawatt-level, millimeter-wavelength radiation that interacts resonantly with electrons in plasma at their cyclotron frequency. Our new facility combines two major experimental devices: the Alcator-C tokamak previously used in the fusion program at the Massachusetts Institute of Technology (MIT) and reinstalled at LLNL during the past two years, and a new FEL recently built at the Laboratory. Our initial experiments, beginning in mid-1989, will concentrate on wave transmission and plasma heating by microwaves.

In 1983, MIT researchers used the Alcator-C tokamak to achieve record plasma confinement. This device is now fully operational at LLNL. The accelerator for the FEL, called the Experimental Test Accelerator (ETA II), is described in more detail on p. 48. We are using the FEL for high-frequency, high-power microwave amplification by simultaneously passing the accelerated electron beam and a low-level microwave signal through a wiggler. The FEL is a unique and exciting technology that is being applied to magnetic fusion research for the first time at LLNL.

Since the completion of tokamak installation in September 1988, we have generated plasmas with densities of $>10^{20}$ m^{-3} by passing a 100- to 300-kA electron current through low-pressure hydrogen or deuterium gas in the toroidal vacuum chamber. Our extensive diagnostics to determine the plasma characteristics include measurement of plasma current with a Rogowski loop, electron density with a far-infrared interferometer, and electron temperature with Thomson scattering and electron cyclotron emission. Figures 1a through 1c show time histories of plasma current, electron density, and electron temperature, respectively, from these diagnostics. Figure 1d shows the radial profile of electron temperature in the plasma. This profile is determined from the submillimeter-wavelength emission from plasma electrons in the nonuniform magnetic field of the tokamak.

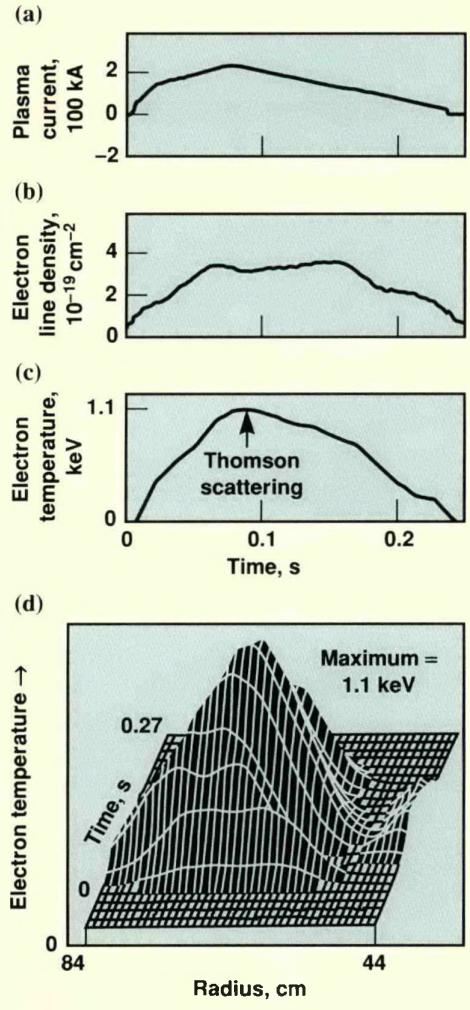

Figure 1. Time histories of (a) plasma current, (b) electron density, and (c) electron temperature. (d) A radial profile of electron temperature in the plasma.

These parameters compare well with those obtained previously at MIT, confirming that we have achieved the high-density and high-temperature plasma needed for our studies of microwave heating.

Figure 2 shows the wiggler, which we will use for single-pulse amplification. In experiments conducted a few years ago, this device generated pulses of high-power microwaves at 35 and 140 GHz. We rebuilt the wiggler and have installed it for our initial MTX experiments at 140 GHz. Following these experiments, we will exchange this wiggler with one that operates in a steady-state mode to produce a long train of pulses. The new wiggler, called the Intense Microwave Prototype (IMP), will be used initially for generating 140-GHz pulses at a 5-kHz repetition rate and later for experiments at 250 GHz. At this repetition rate, we expect we will be able to produce 2 MW of average power.

Although electron cyclotron heating has been used in several previous experiments, the FEL

represents a major step forward in the technology of microwave generation. Theoretical calculations indicate that the interaction between microwaves and electrons will be nonlinear, yielding different absorption coefficients than those for low-power wave interactions. Some backscattering by wave processes is also possible. We will measure absorption by determining the power transmitted through the plasma to a calorimeter. We will then compare the results with an analysis that accounts for wave refraction by plasma density gradients and for nonlinear effects.

Although nonlinear effects will limit absorption in our initial experiments, the predicted mechanisms involve trapping of electrons in the microwave field and can be used to enhance absorption. In particular, this trapping, if experimentally verified, offers opportunities for strong absorption by energetic electrons. Such absorption is needed to drive noninductive current in the plasma. Therefore, our initial experiments will attempt to verify the absorption mechanism and its magnitude.

Last year, the DOE formally ratified an agreement on the MTX with the Japan Atomic Energy Research Institute (JAERI); this agreement amends the U.S.–Japan Supplementing Agreement on Fusion. Scientists from JAERI are working with us as we study heating in the high-density plasma in the MTX tokamak, and they are providing microwave and plasma diagnostics. The first two such diagnostics, which are already installed on the tokamak, will provide a fast (submicrosecond) measurement of x rays from the heated electrons and a fast (10-ms) measurement of neutron emission from ions heated by interaction with the electrons.

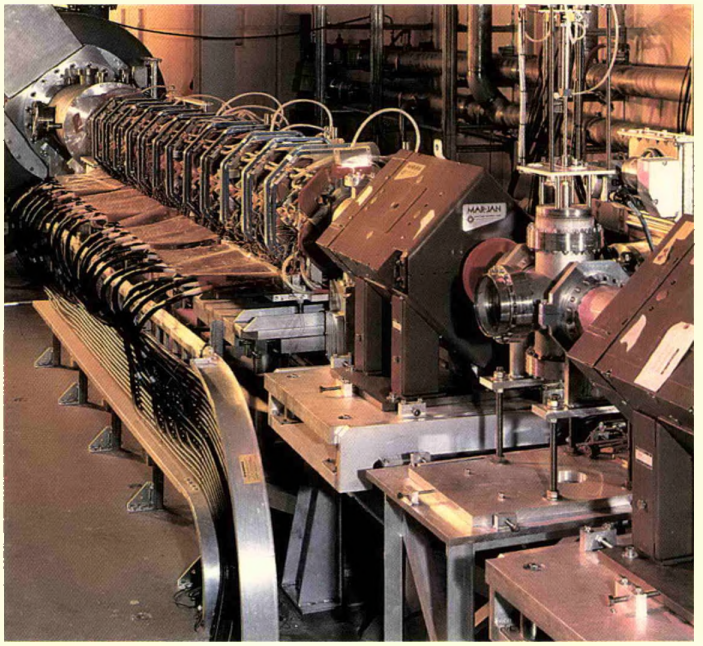

Figure 2. The wiggler, consisting of a periodic array of magnets used for single-pulse amplification at 140 GHz. As an electron beam moves across the magnetic field, each electron wiggles in response to a force at right angles to both the magnetic field and the direction of motion. This device will be replaced in the future with the Intense Microwave Prototype (IMP), which will operate in steady state.

Additional diagnostics have been constructed by the MTX team in collaboration with investigators at several other research laboratories, including UCLA, the University of Maryland, and General Atomics (GA). A fast polychrometer designed and now being constructed by Maryland researchers will measure submillimeter-wavelength electron emission. We will combine the results of this device with the JAERI x-ray measurement to help determine the electron energy distribution following heating. The energy range of our Thomson scattering diagnostic will permit us to search for the light scattered from the energetic group of electrons predicted by heating theory. We will evaluate magnetic perturbations resulting from the rapid heating using magnetic probes constructed as part of our collaboration with GA.

Our MTX experiments are about to begin in this new heating regime. Our initial goal of evaluating the heating mechanism will provide the basis for future work, which will include studies of plasma energy confinement as part of a national initiative to provide a better basis for extrapolations to a reactor, tokamak noninductive current drive, and plasma stability control by microwaves.

Contact: B. Hooper (415) 423-1409.

Compact-Torus Accelerator

Our plasma ring acceleration experiments demonstrate qualitative agreement between predicted and measured internal structure, and show that focusing and soft-x-ray generation are possible.

In the Compact-Torus Accelerator Project (also known as RACE, for ring accelerator experiment), we are attempting to accelerate, compress, and focus plasma rings confined by compact toroidal magnetic fields. We are studying ways to use these focused rings, such as to generate intense pulses of soft x rays for simulating the effects of nuclear weapons in the laboratory. (This work is funded by the Laboratory's IR&D Program.)

In 1987, we accelerated plasma rings in straight coaxial electrodes and obtained good agreement between predictions and measurements. In 1988, we extended these experiments in various ways. In particular, we studied how acceleration affects the ring shape, developed techniques to focus and compress the plasma rings, and explored ways to generate intense, short, soft-x-ray pulses.

Using improved instrumentation, we confirmed that the ring structure is preserved during acceleration and showed that high acceleration fields (B_θ) change the ring's axial distribution from a bell shape to one with steep gradients at the rear (see Figure 1a). This change in ring structure, which qualitatively agrees with calculations using the HAM magnetohydrodynamic (MHD) code, indicates that the accelerator current flows at the back of the ring, revealing that the ring forms a high-conductivity moving short circuit.

Figure 1b shows the observed line-averaged electron density n_e and the axial magnetic field B_z at the outer electrode, 124 cm from the plasma gun. Since no electron density was detectable after the ring passed, very little plasma followed the ring or evolved from the electrodes by interactions with either the ring or the accelerating field. The data in Figure 1b also qualitatively agree with MHD calculations.

Two features of this agreement, consistent with a varying acceleration field, are the tendency of B_z at the outer wall to trail n_e and for the n_e profile to be shaped by acceleration. The trailing B_z results from an axial shift of the ring's back flux surfaces in response to the radial variation of the accelerating B_θ field. The shape of n_e, shown most clearly in the code calculations, results from the way the accelerated plasma tends to "slump" to the rear of the ring. The degree of slumping depends on plasma temperature, which can differ significantly between experiment and simulation.

We continued studies of ring focusing with 2- and 3.75-m-long cones attached to the 4-m-long straight acceleration section, using magnetic field probes along the straight and conical outer electrodes for diagnostics. The head end of the ring reached to about 509 cm; the peak-field point traveled 486 cm. This compressed the ring radially by a factor of 2.35, boosting the peak field by a factor of 2.6.

During the 1988 fiscal year, we evaluated the compact-torus accelerator as a soft-x-ray generator for simulating nuclear weapons effects. When a hypervelocity ring plasma full of heavy ions hits a solid surface, the ions are shock-heated by conversion of kinetic energy. At sufficient focused plasma density, during shock time, the ions collisionally heat the plasma electrons, stripping the ions to high charge states that efficiently radiate line spectra along with plasma bremsstrahlung.

At focused ring speeds of 500 to 2000 km/s (achieved in our experiments), kinetic energy is on the order of gigajoules per gram. Thus the electrons may be heated to about 10 keV to radiate 10–30% of the ring's kinetic energy with a spectrum that peaks at 5–10 keV. To produce enough total radiated energy for testing whole weapon systems, we estimate that a compact-torus accelerator would need an input energy of about 100 MJ.

Preliminary tests of shock-heating and radiation-production tests in RACE experiments with unfocused rings partially confirm the radiation process. Onset of the radiation pulse and arrival of the compact torus at the stopping plate coincide; the observed fluences are consistent with modeling, and the output time scale is about as long as the shock heating time (5–10 μs).

Using straight electrodes with a stopping plate near the far end of the accelerator, we produced comparatively heavy and slow but

well-localized plasma rings (about 1 mg of plasma moving at about 100 km/s), mainly with carbon and oxygen ions. Modeling indicates that these ions have about the right mass for efficient conversion of compact-torus kinetic energy into x rays for this set of ring parameters.

We are adding a single "snipper" coil at the gun muzzle to magnetically block trailing plasma from entering the acceleration region. After acceleration tests with the coil, we will install a new accelerator electrode set to test the effects of precompression. A cone at the start of the accelerator electrode will roughly triple the radial plasma ring compression.

In theoretical work, we made LASNEX calculations of the radiation that compact-torus accelerators may produce at various accelerator-bank energies. According to our calculations, a 100-MJ accelerator would produce about 22 MJ of total radiated energy concentrated in a 10–20-ns pulse. We have calculated that for our RACE experiment accelerating argon plasma rings, outputs comparable to those of state-of-the-art soft-x-ray generators can be obtained.

We used the ring acceleration code RAC to examine the scaling of compact-torus accelerators, calculating the ring trajectory in straight and conical coaxial electrodes, electrode heating by radiation, eddy-current dissipation, and the effect of various energy flows (radiation, ohmic heating, compression, and the like) on the ring's properties. In each case, we had to avoid exceeding the expected limits on acceleration and ring decay. We assumed a precompression phase that couples the accelerator efficiently to the low-voltage capacitor banks and shortens acceleration. Precompression increases the peak fields in the straight acceleration region to 300 kG for 10- and 100-MJ accelerators. A 100-MJ accelerator would be 20 m long. The costliest electrical item in such an accelerator is its capacitor bank. Given the long discharge time (10 μs) and low capacitor voltage (<500 kV), relatively inexpensive off-the-shelf capacitors achieve significant economies of scale. Thus, a 100-MJ, 500-kV bank would cost about $35 million, or $0.35/J.

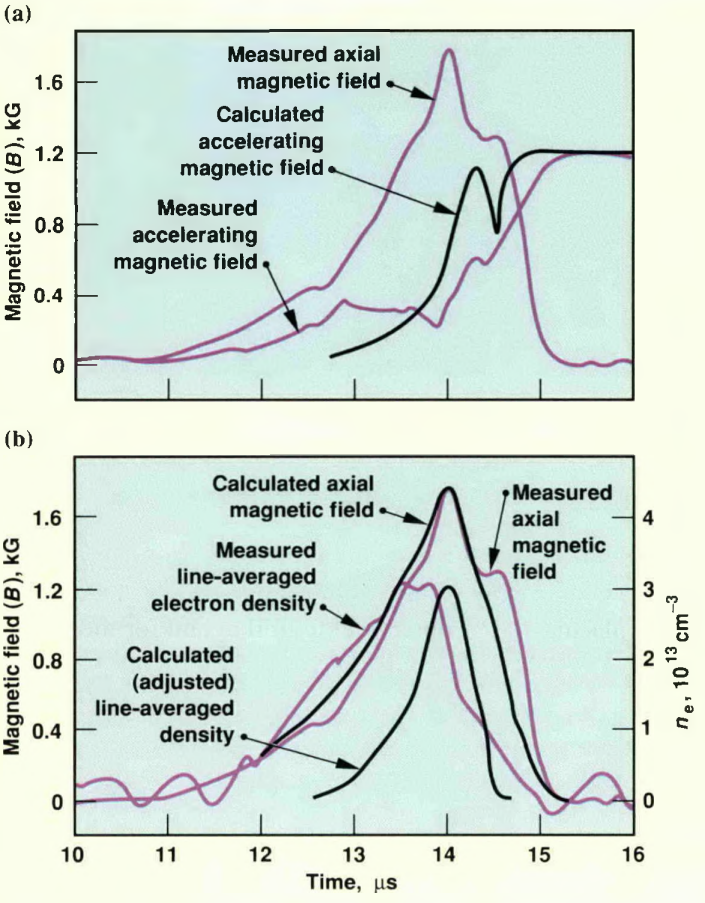

Figure 1. Comparisons showing the agreement between magnetic field B and plasma measurements, at the outer accelerator electrode (124 cm from the breach of the accelerator), and values for the same quantities calculated with the HAM two-dimensional MHD code. (a) Measured axial (B_z) and accelerating (B_θ) fields (color) and the calculated B_θ field (black). (b) Measured (color) and calculated (black) values for B_z and line-averaged electron density.

Contact: C. Hartman (415) 422-1568.

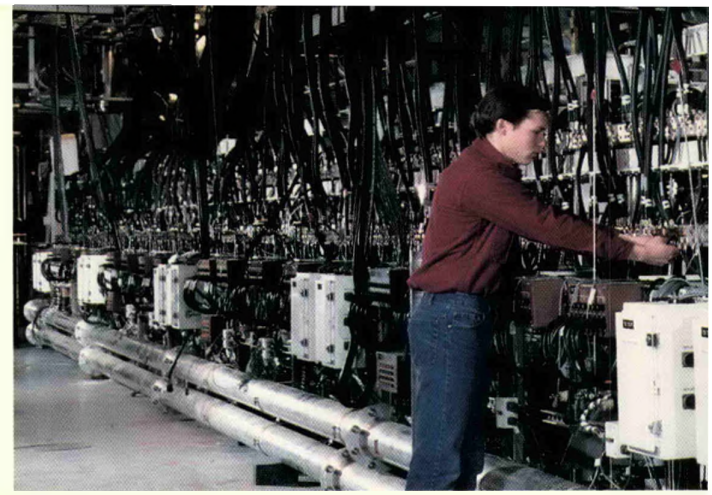

Beam Research

The Beam Research Program has made substantial progress during the past year in its three areas of research: free-electron lasers (FELs), induction electron accelerators, and the propagation of intense electron beams in air.

Together with our industrial partner, TRW, Inc., we have developed designs for a major FEL experiment to operate at the White Sands Missile Range in New Mexico. This experiment, managed by the U.S. Army Strategic Defense Command for the the Strategic Defense Initiative Organization, will use a 1-μm-wavelength FEL at high average power to gather information on how the atmosphere affects transmission of laser light.

In research preliminary to designing and developing the high-power ground-based laser for the White Sands experiment, we have been conducting a 10.6-μm FEL experiment, called Paladin, at the Advanced Test Accelerator at Site 300. In November 1986, we achieved amplification of light in Paladin using a 5-m-long wiggler. By October 1987, we demonstrated exponential gain in a 15-m-long wiggler. In August 1988, we used the full-length 25-m-long wiggler to produce high gain and saturation in an untapered configuration. We are currently tapering this wiggler to determine experimentally the extraction efficiency and optical quality of the beam. Results of the Paladin experiment, together with our extensive theoretical and computational efforts, are crucial to the design of a visible-light FEL for strategic defense applications.

As part of our research on high-power optical FELs, we have developed a new induction accelerator, ETA II, at the Livermore site. This machine, which became operational in late 1987, is designed to generate and accelerate high-brightness electron beams at high pulse-repetition frequencies and at high average power, producing an electron energy of 10 MeV and a pulsed beam of up to 3 kA at a pulse repetition rate of 5 kHz. The design brightness of the electron beam in ETA II is 2×10^9 A/m^2·rad^2, a value that has been demonstrated and exceeded in 2.5-MeV tests. We are now testing a larger cathode that will give higher beam currents and are extending the brightness measurements to the end of the 60-induction-cell machine. We will then be able to increase the repetition rate incrementally to 5 kHz.

We have installed a pulsed electromagnetic wiggler at ETA II that will allow microwave FEL operation at 140 GHz. The 4-m-long wiggler will produce microwave

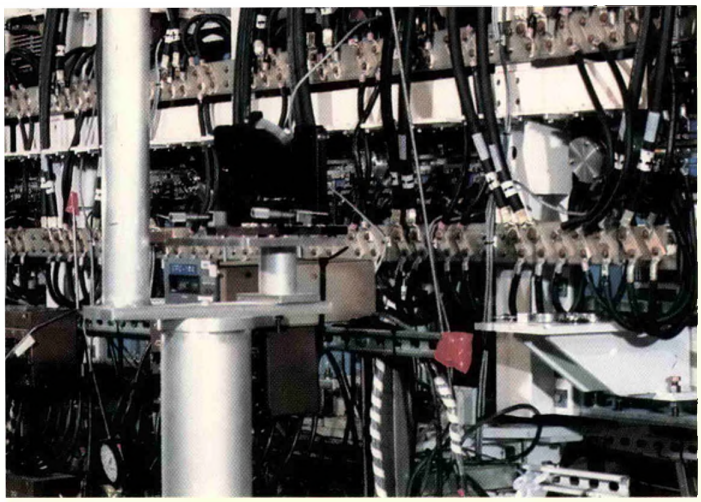

The full-length 25-m-long wiggler for the Paladin experiment.

power at 2 GW in 50-ns pulses. This FEL will be used to supply microwave power to the Microwave Tokamak Experiment (MTX) for cyclotron heating of the fusion plasma. Later, we will install a new-generation wiggler capable of operating at 250 GHz and generating peak powers up to 10 GW.

We are continuing our work on relativistic klystrons as power sources for compact, high-energy accelerators. A relativistic klystron is a device that converts the high peak power in an intense electron beam from an induction accelerator to radiofrequency (rf) power. This rf power can be used to power a high-gradient electron accelerator to achieve very high energies with modest accelerator lengths.

Experiments performed with the Lawrence Berkeley Laboratory and the Stanford Linear Accelerator Center during the past year have concentrated on some of the basic physics issues involved in combining linear induction accelerators with relativistic klystron cavities. We have achieved 170 MW of rf power at an efficiency of about 30%, with an output wave shape that is suitable for driving a high-gradient structure.

In addition, we have designed a new, smaller induction cell for use at the Accelerator Research Center at LLNL that will allow higher-energy electron beams for klystron research. Our goal is to determine whether shorter, lower-cost induction accelerators can be produced for this and other applications.

Finally, we are continuing investigations on the propagation of high-power electron beams in air. In particular, we are developing compact accelerators that may be needed for future weapon systems, an effort that complements our efforts at the Accelerator Research Center on relativistic klystrons. We are also developing the capability to extend the range of electrons in air by propagating them in a series of beams. Our computational modeling research indicates that the range of a high-power electron beam can be extended by propagating it in the reduced-density channel produced by a preceding beam. During the next year, we will conduct experiments at the Advanced Test Accelerator to launch multiple beams in air at a high repetition rate to verify this prediction.

Contact: S. Eccles (415) 422-5083.

Paladin Optical FEL Amplifier

We have been conducting free-electron laser (FEL) experiments at 10.6 μm using the Paladin single-pass amplifier. We have measured the exponential gain and saturation levels of the amplifier and are identifying the parameters that will increase the performance of this FEL amplifier.

The free-electron laser (FEL) is a device that directly converts part of the kinetic energy of a relativistic electron beam into coherent radiation (light). The electron beam couples to the electromagnetic radiation in a device called a wiggler. The wiggler creates a periodic magnetic field oriented transverse to the motion of the electron beam, and this magnetic field imparts to the electron beam a periodic, transverse momentum aligned with the electric field of the radiation. If the proper phase is maintained between the electron beam and the radiation, then the beam will bunch and radiate coherently. Energy is extracted from the electron beam in the form of light.

We have been conducting FEL amplifier experiments at LLNL using the electron beams produced by linear induction accelerators (LIAs). This type of accelerator produces electron-beam pulses with peak currents of a few kiloamperes and with pulse lengths of tens of nanoseconds. The beam energy depends on the number of acceleration modules on the accelerator; typical beam energies range from a few to tens of mega-electron volts. The pulse format of the LIA makes it ideally suited for use in single-pass FEL amplifiers, where each optical pulse passes through the wiggler only once. A seed signal from a master oscillator is injected with the electron beam into the entrance of the wiggler (Figure 1); it is then amplified in the FEL. After passing through the wiggler, the electron beam is diverted to a beam dump, and the amplified radiation signal propagates out of the FEL.

Paladin is a single-pass FEL amplifier. This device uses a several-hundred-ampere, 45-MeV electron beam from the Advanced Test Accelerator (ATA) to amplify an input signal provided by a conventional CO_2 laser operating at a wavelength of 10.6 μm. The magnetic field in the 25-m-long wiggler has an 8-cm period produced by an array of electromagnets.[1] Every two periods of the wiggler are energized by their own power supply. The wiggler can be tuned to resonate either as a whole or in sections to change its effective length.

For the Paladin experiment shown in Figure 1, we accelerate an electron beam of approximately 2.5 kA to 45 MeV; the beam is then passed through a filter, or beam-conditioning system, which removes electrons that have too much random perpendicular motion. This process reduces the peak current and the pulse width. A 0.5- to 1.0-kA beam typically emerges from the filter with a pulse length of 10 to 20 ns. After the filter,

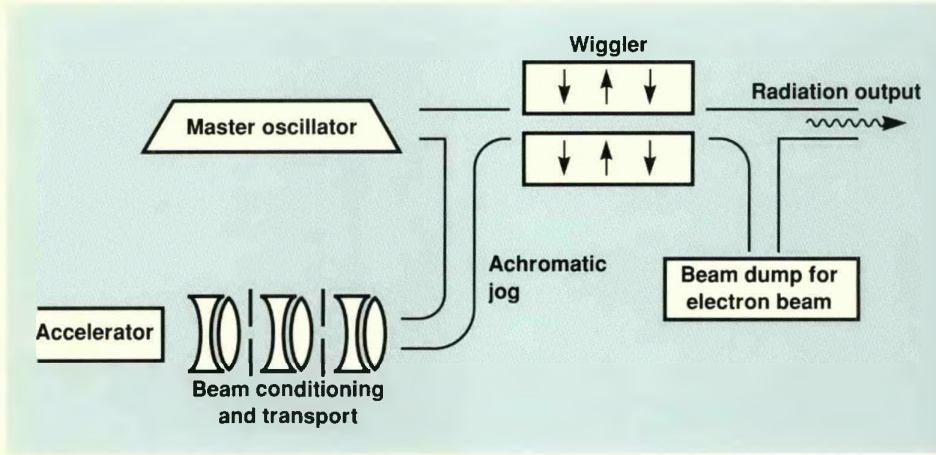

Figure 1. Paladin FEL experiment. An electron beam of ~2.5 kA is accelerated to 45 MeV; it then passes through a filter that removes electrons with excess random perpendicular motion. The electron beam is then transported to a parallel, offset beamline in a series of dipole magnets, called an achromatic jog. Offsetting the electron beam allows us to match the optical-input signal with the electron beam as it enters the wiggler. After the wiggler, the electron beam is swept out of the beamline by a dipole magnet, and the optical signal is transported to a diagnostic area for measuring peak power, total power, total energy, and mode profile.

the electron beam is transported to a parallel, offset beamline in a series of dipole magnets, called an achromatic jog. The purpose of offsetting the electron beam is to provide for matching the optical-input signal with the electron beam as it enters the wiggler. After the wiggler, the electron beam is swept out of the beamline by a dipole magnet, which was designed and calibrated as an electon-beam spectrometer. The optical signal is then transported to a diagnostic area, where we measure peak power, total power, total energy, and the mode profile.

The input signal to the FEL is provided by a CO_2 laser, consisting of an oscillator and an amplifier. Using the oscillator only, we can inject an 18-kW signal into the FEL; with the CO_2 amplifier turned on, we can inject 3.6 MW. The purpose of injecting signals with different amplitudes is to study the onset of saturation. Figure 2 shows the results of gain measurements (output power as a function of FEL amplifier length) for the two input-signal amplitudes. To obtain these data, we kept the 25-m-long wiggler at a uniform magnetic field and varied the entire wiggler field to determine the peak of the FEL resonance. When this magnetic-field level is determined, the effective wiggler can be systematically shortened by tuning sections of the wiggler far from resonance. We then analyze the amplified signal at each effective wiggler length.

In both of the experiments shown in Figure 2, the amplifier was

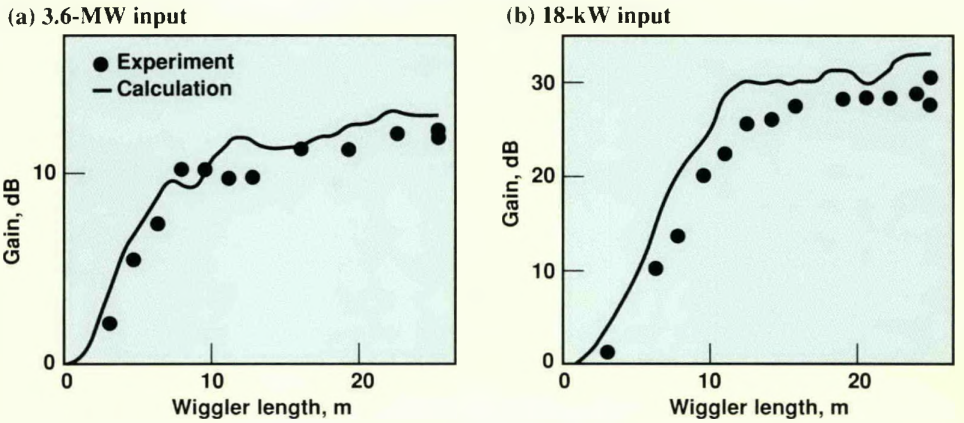

Figure 2. Signal growth through the wiggler for input signals of (a) 3.6 MW and (b) 18 kW. The wiggler field is 1.96 kG. In both experiments, the amplifier is saturated: that is, no more energy can be extracted from the electron beam beyond a certain length. In (a), the signal grows at approximately 1.7 dB/m and saturates between 7 and 8 m into the wiggler. In (b), the signal grows at a rate of 2.6 dB/m and saturates 12 m into the wiggler. Agreement between experimental results and simulation with the computer code FRED is quite good.

saturated; that is, for the conditions of the experiment [electron-beam current, energy, quality (emittance), and other parameters], no more energy could be extracted from the electron beam beyond a certain length. With the stronger input signal of 3.6 MW (Figure 2a), the signal grows at approximately 1.7 dB/m and saturates between 7 and 8 m into the wiggler. The 18-kW signal (Figure 2b) grows at a rate of 2.6 dB/m and saturates 12 m into the wiggler. With the 3.6-MW input, saturation was reached at 60 MW; with the 18-kW input, saturation was achieved at 15 MW.

We have modeled the performance of our FEL amplifier using the three-dimensional FEL code FRED. Figure 2 also shows the results of our simulations using realistic values for the parameters of the electron beam. The agreement between experiment and simulation is quite good.

To improve the performance of the Paladin FEL, we must improve the quality of the electron beam. That is, we need to reduce the random, transverse momenta of individual electrons in the electron beam from the accelerator. Our future experiments will concentrate on increasing electron-beam quality by upgrading the beam source and improving beam transport through the accelerator.

Reference

1. See the article "The Full-Length Paladin FEL Wiggler," in the July-August 1988 issue of *Energy and Technology Review* (UCRL-52000-88-7-8), p. 54.

Contact: T. Orzechowski (415) 422-6709.

High-Brightness, High-Current Operation of ETA II

Using the Experimental Test Accelerator, we have produced a high-current electron beam with sufficient brightness to drive a short-wavelength (1-μm) free-electron laser (FEL). At LLNL, we will use this beam to drive a microwave FEL to heat the fusion plasma in the Microwave Tokamak Experiment.

The Experimental Test Accelerator (ETA II) is uniquely able to produce high-brightness, high-current electron beams at high average power. We are using the ETA II to demonstrate the feasibility of using an induction accelerator to drive a high-power, short-wavelength (1-μm) free-electron laser (FEL) and to drive a microwave FEL (140–250 GHz) for plasma heating in the Microwave Tokamak Experiment (MTX). The 1-μm FEL requires a beam with high brightness [>2 GA/(m·rad)^2] at moderate current (~1.5 kA); the microwave FEL for the MTX requires a beam with moderate brightness [>0.1 GA/(m·rad)^2] at high current (~3 kA). A 1-μm FEL would require further acceleration to high energy (170 MeV); this configuration has been proposed for the experiment at the White Sands Missile Range in New Mexico.

The ETA II consists of a 1.2-MeV, 3-kA injector followed by 80 acceleration cells with a nominal gap voltage of 110 kV. The 10-MeV, 3-kA electron beam will have a peak power of 30 GW produced in 50-ns flat-topped pulses. With a 33% conversion efficiency from electron-beam to microwave energy, peak microwave power will be 10 GW, about an order of magnitude greater than that achieved in earlier experiments. Operating at a 5-kHz repetition rate, the time-averaged microwave power will be approximately 2 MW. Table 1 summarizes the ETA II design parameters (determined largely by FEL requirements) and performance levels; we expect that design performance for all parameters will be achieved by the end of fiscal year 1990.

In the past year, we have made several important achievements:

- Using the injector and 20 acceleration cells, we achieved an electron beam brightness of 4 GA/(m·rad)^2 with a beam current of 1.5 kA and a beam energy of 2.7 MeV.
- Using the injector and 60 acceleration cells, we accelerated a ~3-kA beam to ~6 MeV.
- We demonstrated reduction of thyratron switch jitter using multiple thyratrons operating in parallel.
- We developed a low-energy electron probe technique to align the magnetic centerline to within ±100 μm over the length of 10 acceleration cells.
- We completed the installation of the ELF II wiggler and began fabrication of the IMP wiggler.
- We installed a 18-kV, 1-MJ capacitor bank that will allow 5-kHz, 50-pulse, burst-mode operation.

Our most important achievement was the high beam quality characterized by a beam brightness of 4 GA/(m·rad)^2 through the first 20 cells of the ETA II (see Figure 1). This is more than double the design requirement for a 1-μm FEL, and is the highest-quality beam produced by an induction linear accelerator to date. Figure 1 also shows earlier measurements of intrinsic cathode brightness. For currents of 1.5 kA or less, the ETA II brightness of 4 GA/(m·rad)^2 is about three times less than the intrinsic cathode brightness, which is an upper bound for the accelerator. We will soon extend these brightness measurements

Table 1. ETA II parameters and performance.

Parameter	Design goal	Achieved to date
Brightness, GA/(m·rad)^2	>2	4
Current, kA	3	3.2
Beam energy, MeV	10	6
Energy sweep (head to tail)	±1%, 50 ns	—
Energy stability (pulse to pulse)	±1%	—
Flux line alignment, μm	±100	±100 (10-cell block)
Repetition rate, Hz	5000	few Hz
Duration, ms	10–500	—

of the electron beam after acceleration through 60 cells.

The power-conditioning chain that feeds the accelerator is critical to producing a high-power electron beam. In the ETA II, thyratron modulators are used to charge an intermediate energy storage (IES) capacitor to 25 kV in 120 μs. The IES capacitor is then discharged in 3.5 μs into the input stage of a three-stage magnetic compression modulator that further compresses the pulse (to 70 ns FWHM) and produces an output voltage of 120 kV into a matched transmission line. A single power-compression chain then drives the electron injector or 20 cells of the accelerator.

To achieve good FEL efficiency, we must lengthen the beam-pulse flat top. In turn, this requires that the jitter of the IES thyratron switch be minimized. Originally, our goal was one standard deviation (1σ) jitter less than a few hundred picoseconds. We have found that jitter decreases with the number of thyratrons operating in parallel on a pulsed-power chain. We are planning experiments to measure the total system jitter and the interaction of jitter with beam energy sweep.

To control corkscrewing on the accelerated electron beam, alignment of the solenoidal magnetic flux used to guide the beam must be maintained. To align the central magnetic flux line on the ETA II, we developed a low-energy electron probe (4 kV, a few milliamperes) to trace the central flux line referenced to a mechanical axis that is defined by a co-propagating laser. Sine/cosine correction coils force the central flux line to coincide with the mechanical axis at the end of each acceleration cell. The probe detects the low-energy electron beam and laser reference beam, together with the *x,y* positions of the central flux line mapped through a 10-cell acceleration block. Except near the ends, where field magnitude decreases rapidly, we have been able to hold the flux line deviation to within ±100 μm. Problems with the stability of the laser reference beam should soon be corrected as modifications are made to provide feedback stabilization of the reference beam. We should then be able to extend this technique to the entire length of the accelerator.

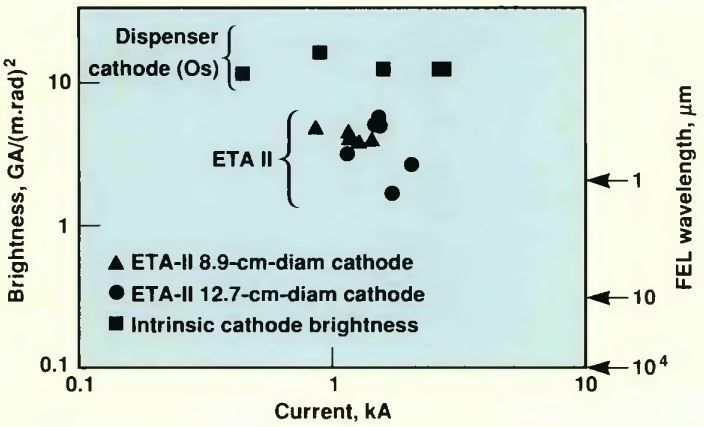

Figure 1. ETA II brightness vs electron beam current. These experiments used the injector and the first 20 cells of the accelerator, a 2.7-MeV beam energy, and an osmium alloy dispenser cathode.

We are building new wigglers for the microwave FEL experiments. For our initial 140-GHz, single-shot microwave experiments, we have rebuilt the electromagnet wiggler used previously in the Experimental Laser Facility; this wiggler, called ELF II, has been installed at the end of the ETA II. For multiple-pulse, 5-kHz operation at 140 and 250 GHz, we are building the Intense Microwave Prototype (IMP) wiggler using an advanced hybrid electromagnet–permanent magnet design.

To date, ETA II accelerator experiments have been conducted at a few hertz with a 600-kW power supply. Because FEL applications require a high repetition rate, we recently built an 18-kV, 1-MJ capacitor bank that will allow 5-kHz, 50-pulse operation. To verify the performance of the new capacitor bank, we operated a complete pulsed-power chain, identical to those on ETA II but mounted on a separate test stand, at 5 kHz for a 300-pulse burst. We are confident that we will be able to extend 5-kHz operation to several seconds.

In conclusion, we have made significant progress toward our goal of using the ETA II to demonstrate the accelerator technology required for a short-wavelength FEL, and we will soon begin microwave FEL experiments for which the 10-MeV energy is a good match.

Contact: W. Turner (415) 422-7976.

Relativistic Klystrons

We are developing relativistic klystrons as power sources for compact high-energy accelerators.

Large linear electron-positron colliders, compact accelerators, and free-electron laser sources all require a new generation of high-gradient accelerators. To keep accelerator length within acceptable limits, we need accelerating gradients of 100–200 MV/m; to keep peak and average power requirements and beam loading reasonably small, we require frequencies of 10-20 GHz; and to drive a traveling-wave structure in the desired frequency range with desired gradients, we must have a peak power of about 1 GW/m with a short pulse length of 50–100 ns.

To meet these power and pulse-length requirements, we are investigating the use of induction accelerators, which routinely produce several-MeV beams with a few kiloamperes of current in 50-ns pulses. In the required frequency range, a straightforward mechanism for converting the high peak power in the intense electron beam to radiofrequency (rf) power is the relativistic, or high-energy, klystron (an electron tube that amplifies microwaves). The goal of the high-energy research community to build inexpensive, efficient high-gradient accelerating structures matches that of the Laboratory's Beam Research Program to build compact accelerators for defense and industrial applications; this work is supported by the IR&D Program.

In a conventional klystron, an rf drive cavity imparts a velocity modulation to an electron beam. The beam is allowed to drift until the velocity modulation bunches the beam; intermediate cavities can be added to increase bunching and to raise the gain of the device. The bunched electron beam finally passes through an output cavity that extracts rf power from the beam. Attempts to scale existing electron tubes to the required frequency and power levels have revealed the need for higher-energy beams.

During the past year, we have continued our collaborative efforts with the Stanford Linear Accelerator Center and Lawrence Berkeley Laboratory to study basic physics issues involved in combining linear induction accelerators with relativistic klystrons. We have obtained results with three experimental relativistic klystrons at LLNL's Accelerator Research Center (ARC): an 8.6-GHz multicavity klystron, a two-cavity subharmonic buncher relativistic klystron (SHARK) with a 11.4-GHz output, and an 11.4-GHz multicavity klystron (SL4) designed to operate with high efficiency and high gain in a 1-kA, 1.2-MV beam. In experiments with these klystrons, a peak rf power of 200 MW was achieved, but only with an rf flat top much shorter than the beam pulse. The maximum reasonably flat rf pulse achieved in our initial tests was only 70 MW.

We have since built and are testing several variants of SHARK and SL4. Specifically, we have:

- Introduced cavities with iron magnetic shielding and slotted noses to combat multipactor (i.e., resonant buildup of emitted secondary electrons in the rf cavities).
- Added a penultimate cavity to SHARK to improve gain and efficiency.
- Replaced the single output cavity of a relativistic klystron with a six-cell, traveling-wave output structure to reduce electric fields.

We are conducting experiments with these variants, using ~1.2-MeV, ~500-A beams, to explore the phenomena related to pulse shortening and to find a way to achieve longer pulses.

In one experiment, using a high-gain relativistic klystron tube with three intermediate-gain cavities and a traveling-wave output structure (Figure 1), we achieved 160 MW of rf power, a gain of about 52 dB, and

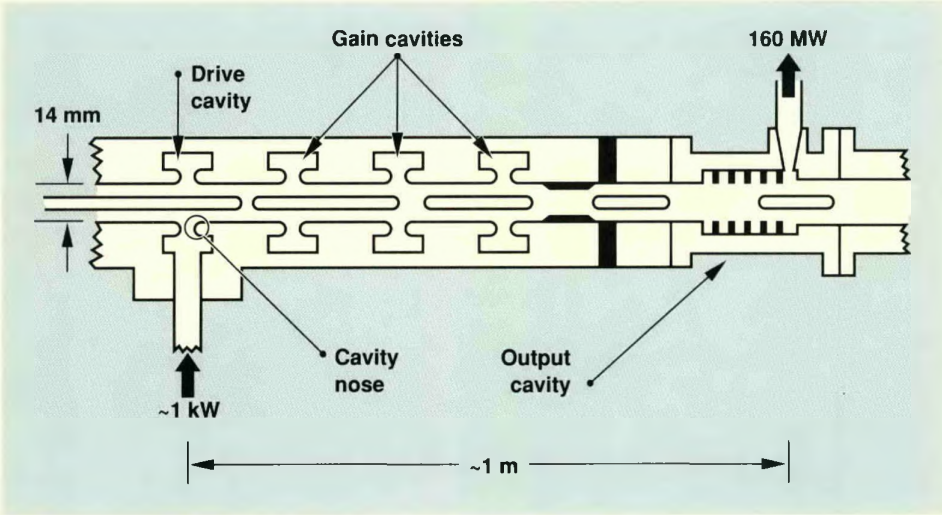

Figure 1. Schematic of the high-gain 11.4-GHz SL4 klystron.

an efficiency of about 30%. Phase-stability measurements indicated that the output pulse was satisfactory for driving a high-gradient rf accelerator. With the problem of pulse shortening evidently alleviated, our next challenge is to develop higher-energy klystrons and multicavity extraction devices and to reduce the cost and improve the efficiency of relativistic klystrons.

To complement these klystron experiments, we have built a 26-cm-long section of a 11.4-GHz accelerator structure operating in the $2\pi/3$ traveling-wave mode. The shortened 200-MW peak rf pulses from the SL4 tube have been coupled to the accelerator structure; this drive power corresponds to an accelerating gradient of 140 MV/m. In our first tests of this structure, however, appreciable dark current (field-emitted electrons from the copper surfaces), an undesired phenomenon, was observed at accelerating gradients above 90 MV/m. Additional tests will be performed shortly using the wider pulses that SL4 can now produce in an attempt to achieve higher accelerating gradients. This high-gradient structure will form part of a second beamline to accelerate an electron beam with much lower average current to a much higher energy than the primary drive beam.

In addition, a higher-energy klystron, called a chopper, has been built and is now ready for testing at the ARC (Figure 2). The chopper is designed for a beam voltage of 3 MeV and 1 kA of current. At energies above about 3 MeV, velocity modulation (as used in tests to date) no longer efficiently bunches the electron beam. The chopper uses a transverse deflector cavity and a slit to modulate the currents (hence its name). The system is immersed in a magnetic field to minimize beam degradation. Two traveling-wave structures extract the rf power; each structure converts part of the beam's power to rf power. This design should produce 500 MW of rf power at 11.4 GHz.

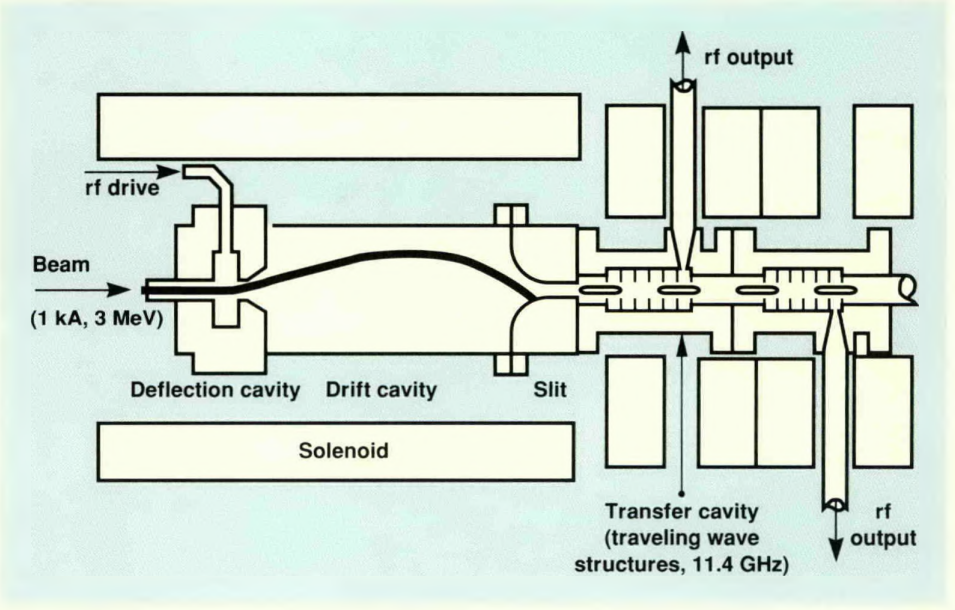

Figure 2. Diagram of the relativistic klystron design called the chopper, a high-energy beam tube using rf deflection to modulate the beam current.

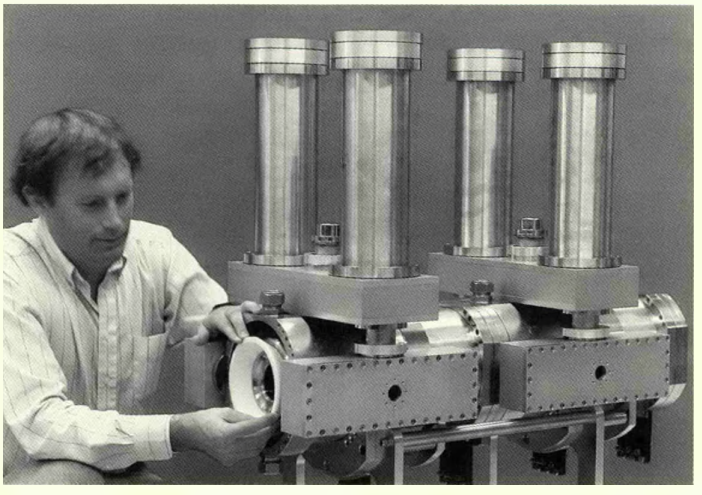

Figure 3. New induction accelerator cells under construction for testing.

We are building several smaller induction accelerator cells (Figure 3) with which we will be able to test klystrons at higher energies at the ARC and determine whether the cost of induction-driven klystrons can be reduced. The new accelerator cells are designed for lower beam currents and a shorter overall pulse length than present accelerators at LLNL. We are also building a klystron with four output structures coupled to four high-gradient structures; this system will have its own electron gun. The second beamline in this system is designed to accelerate electrons to 100 MeV within about 1 m.

Contact: G. Westenskow (415) 423-6936 or S. Yu (415) 422-7876.

Energy Program

Adequate energy supplies are critical for securing this nation's prosperity in the future. For decades, the Laboratory has conducted research and development in energy fields that promise to enlarge supplies, improve utilization, mitigate environmental problems, and lower costs. It is important that the government continue its research into advanced processes and fundamental principles to overcome technical problems encountered in developing alternative and renewable energy sources.

Fossil Energy

One of our major research goals is to develop underground coal gasification as an economic, environmentally benign way to gasify deep coal seams and extract energy otherwise not exploitable. The gas produced can be upgraded to pipeline quality or used as a synthesis gas for liquid fuels. We are analyzing the results of recent field tests of an underground coal gasification process conducted near Hanna, Wyoming. We are acting as DOE's technical representative to several foreign countries considering use of this process. We are also investigating methods to strip hydrocarbon fuels from coal through "mild gasification" (pyrolysis) and then to use the remaining char as a solid fuel, perhaps to generate electricity.

In addition, we are working on an efficient, aboveground, fluidized-bed coal combustor that minimizes emissions of deleterious oxide gases. Destruction of in-bed, heat-exchanger tubes has long been a problem with this technology. The conventional solution has been to replace the tubes frequently or to protect them from particulate and gas flow; we are finding that a more economic alternative may be to treat the molten steel used eventually for the tubular products.

In a related program, we are working to gain a better understanding of the granular flow of materials. In almost all conversion processes involving solid fuels (coal, oil shale, and tar sands), plant design and operation are hampered by an imperfect understanding of the granular flow of these materials. Scaling up from laboratory to pilot-plant-size operations is frequently attended by unexpected, complex problems related to the flow of materials—problems requiring time-consuming and costly empirical solutions. Using complex modeling of interacting solid spheres, we have developed a three-dimensional computer code that successfully describes particle behavior and interactions. We have used this code to model rapid shearing flows of systems with various shear rates and solids packing with various elasticities, size, sorting, and frictional properties. As we learn more about flow behavior, we continually upgrade these models; currently, we are adding more complex boundary conditions. Our goal is to develop these models to the point that they can deal with multiphase flows with interstitial fluids. These models provide essential direction to researchers working to improve the conversion processes.

Our oil-shale program has directly benefited from the insights provided by these models of the granular flow during the retorting process. In addition, this year, we have focused on scaling up the size of our reactor and on building a cooperative program with industry to exploit our new-found understanding.

In the general fields of oil and gas, we have made considerable progress in understanding the chemical processes in both freshwater and marine environments whereby organic debris is transformed into conventional oil and gas. Nine oil companies are supporting this work, which should eventually help them to locate oil and gas. Once we know the thermal and structural history of sedimentary basins that may contain oil, we can predict both the degree of transformation of the organic material into oil and gas and the most likely location of commercially exploitable quantities within the basin.

Another program is to improve the supply of conventional fuels. We are applying advanced remote-sensing techniques to evaluate procedures that enhance

The Rocky Mountain underground-coal-gasification test facility near Hanna, Wyoming.

our ability to recover oil. These processes should enable us to recover part of the large quantities of oil left underground when we use standard recovery procedures. These improved techniques currently account for 7% of domestic oil production, and this percentage is growing.

The nation's Achilles' heel in the energy field is a long-term shortage of transportation fuels; usage is very high, and there are currently few viable fuel alternatives. To meet this challenge, we are investigating methods for converting methane directly to a liquid hydrocarbon using novel catalysts. One method is to use an understanding of natural bacterial processes that consume methane through enzyme catalysis to design new, nonenzymatic catalysts that mimic enzymatic action. The final product can be upgraded to a conventional fuel or mixed with petroleum and used in refineries.

Tackling the problem of liquid fuels from another direction, we are making substantial progress in improving the efficiency of the internal-combustion (IC) engine by developing a basic understanding of the chemical process of engine knock, which robs the engine of power. We are analyzing the fundamental combustion properties of a direct-injected, stratified-charge IC engine by modeling the flame process. This work holds promise of developing a highly efficient alternative to the IC engines now in use.

Conservation and Renewable Energy

Our principal program to improve renewable energy is focused on geothermal technology. We are developing methods to locate seismically new geothermal reservoirs by identifying the locations of magma bodies and related hydrothermal systems in the earth's upper crust. We have conducted experiments at the Medicine Lake volcanic field and The Geysers in California and at the Newberry Volcano in Oregon. We are field-testing geophysical techniques to evaluate their use in monitoring the movement of brine injected into geothermal systems, including electromagnetic tomography, resistivity, self-potential microseismicity, and pore pressure response to solid earth tides. We are also providing technical assistance to the DOE in analyzing and interpreting field data in a Hawaiian experiment to design and test fiber-optic instruments and cryogenic gravimeters, some developed here at LLNL.

Nuclear Energy

A national goal in the field of nuclear energy is to close the fuel cycle by disposing of nuclear waste in a safe and acceptable manner. An objection to nuclear reactors on the part of the general public is the lack of an immediate solution to waste disposal. To accelerate progress on the disposal of nuclear wastes, Congress passed the Nuclear Waste Management Policy Amendments Act of 1987, which designated the Yucca Mountain site in Nevada as the sole site to be characterized for suitability as an underground repository for civil radioactive solid waste. LLNL is the lead organization for designing the package for nuclear wastes that will meet requirements for emplacement, storage, and possible retrieval.

In this role, we are characterizing materials, developing detailed process models to predict material behavior, and characterizing the environment near the waste package. We use the powerful geochemical modeling code EQ3/6, developed at LLNL, to simulate the geochemical environment of the proposed facility. We are also developing simulator codes for coupled hydrologic-thermal mechanical processes and for reactive transport of radionuclides, developing experimental field techniques, improving geochemical databases, and supporting international programs for technical interchanges.

Contact: R. Schock (415) 422-6189.

Reducing Tubing Wastage in Fluidized-Bed Coal Combustors

We have identified chemical composition and tube microstructure as metallurgical variables that seem to influence resistance to tubing wastage (metal loss). Correcting wastage problems will enhance the operation of environmentally clean, coal-fired electrical generating plants.

Fluidized-bed combustion offers a commercially attractive means for using the vast U.S. coal resources without incurring the environmental penalties associated with many of the other combustion methods. In this process, pulverized coal is burned efficiently in the presence of sorbents, such as crushed limestone or dolomite, which chemically convert sulfur dioxide from the combustion process into solid gypsum. Sulfur remains within the combustor; it does not contribute atmospheric pollutants. Similarly, because the combustion temperatures are lower than in conventional coal-fired boilers, fluidized beds produce only minimal amounts of nitrogen oxides—principal ingredients of photochemical smog.

One problem of fluidized-bed combustion units, however, is that their carbon-steel evaporator tubes have been afflicted with materials wastage (loss). Total loss rates have averaged as much as several millimeters per 1000 h of operation. A typical wastage profile in an evaporator tube from the Tennessee Valley Authority (TVA) 20-MW atmospheric fluidized-bed combustor (AFBC) pilot plant in Paducah, Kentucky, is shown in Figure 1.

The reasons for such metal loss have been perplexing, since temperatures of the tubing rarely exceed 400°C and gas-stream velocities are well below those required for metal loss by classical erosion. Steps to control this loss have included adding studs, fins, and other types of shielding to the vulnerable lower surfaces of the tubes. However, these "fixes" are not practical long-term solutions for commercial-scale units.

In collaboration with DOE's Morgantown Energy Technology Center, we have identified the principal wastage mechanism as mechanical exfoliation of the normally protective oxide scale along the tube undersides. Exfoliation occurs as the bed particulates impinge on the undersides of the tubes and scour away the protective scale as rapidly as it forms. Continued scale loss and its re-formation at the expense of tubing wall can lead to high rates of localized metal loss. Vertical gas streaming probably also contributes to accelerated exfoliation as particulate velocities and closure pressures in the wakes of passing bubbles produce locally aggressive conditions at the fireside surface of the tube wall.

The consensus in the industry has been that any solution to this problem probably involves modifying fluidization conditions or protecting the tubes from exfoliating effects of bed materials. Unfortunately, however, such measures often result in combustion inefficiencies and deterioration of other operating characteristics. Because the affected tubes are made of ordinary carbon steel, the metallurgy of the tubes was considered to be essentially a constant and, therefore, not a factor that could be improved. Nevertheless, we are continuing our efforts to understand more clearly the wastage phenomenon, including reasons why an early tube bank at a TVA pilot plant resisted wastage for thousands of hours while apparently similar tubes wasted rapidly under similar conditions. From these studies, we have identified metallurgical

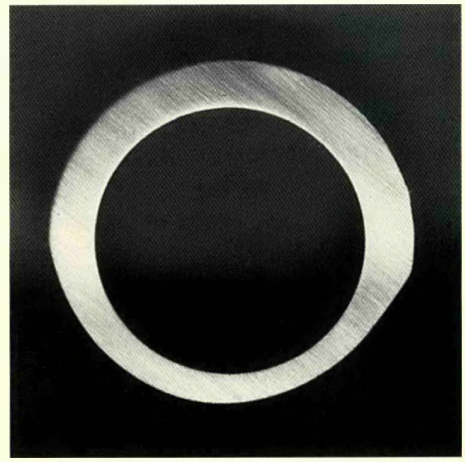

Figure 1. Cross section of an evaporator tube from the TVA 20-MW AFBC pilot plant showing wastage profile (actual size). The wasted region corresponds to the 5:00 to 7:00 o'clock position as the horizontally oriented tubes are located in the combustor.

variables that, contrary to prevailing opinion, apparently do have an effect.

The chemical composition and microstructure of the tubes seem to correlate with the wastage response. Laboratory oxidation tests on samples of metal removed from actual evaporator tubes, carried out in still air at combustor tube-wall temperatures, have confirmed these indications. The presence of trace amounts of alloying residuals (possibly a reflection of the steelmaking process used) seems to influence alloy homogeneity and its resulting microstructure, scale-growth kinetics and possibly scale resilience and adherence, and the exfoliating effects of the combustor environment.

For example, we found that steel from tubes that resisted wastage had lower indentation hardness at elevated temperatures than did tube steels that were susceptible to wastage. This is possibly related to the deoxidation practice used in making the steels, as those showing evidence of aluminum deoxidation were among those exhibiting greatest resistance to wastage. The steel with the most resistance also showed an enrichment of chromium at the scale/substrate interface, traceable to what is believed to have been an inadvertent residual in the steel. Such steel formed an oxide scale that appeared different and thinner in laboratory tests than did steel without this and other residuals (Figure 2). Also, the microstructure of the

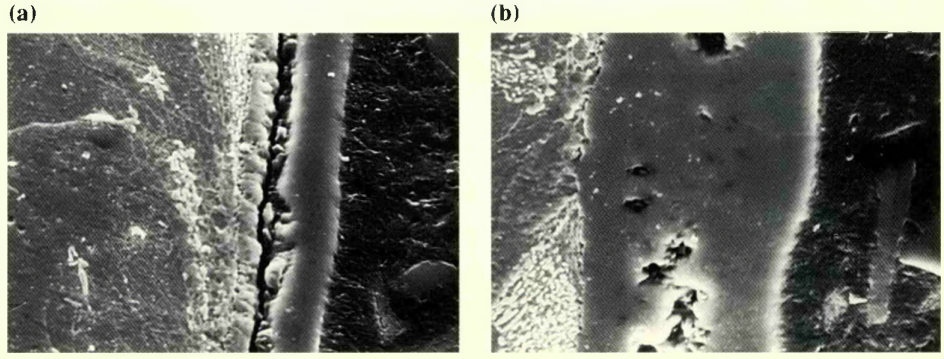

Figure 2. Scanning electron micrographs (steel substrate at left) of cross sections at the scale/substrate interface, showing scales formed on evaporator tube steels in 100-hour laboratory oxidation tests at 450°C. (a) Sample containing residual elements; (b) sample with low elemental residuals (3000× magnification).

wastage-resistant steels was more homogeneous, with less pearlite banding and segregation, than was that of the wastage-susceptible steels. It appears then that by optimizing the steelmaking procedures, with proper control over deoxidation and microalloying residuals, it may be possible to produce carbon steels that can resist these aggressive combustor environments.

To verify this, the next step is to make a systematic study of microalloying effects upon the scale-forming kinetics of carbon steels under fluidized-bed combustion conditions. For this, we are preparing a series of experimental steels using the recently installed alloy development and metal preparation facilities at LLNL. If initial examinations of these steels in laboratory-scale oxidation tests support earlier findings, full-scale sections of evaporator tubing will be prepared and tested under actual fluidized-bed coal combustor conditions approaching commercial-scale operation. The Tennessee Valley Authority and the Electric Power Research Institute have expressed interest in these Laboratory developments, and negotiations for testing our experimental steels are under way for possible implementation later this year or as combustor operating schedules permit.

Contact: C. Witherell (415) 422-8341.

Modeling Petroleum Generation and Expulsion

We have developed new chemical kinetic models of vitrinite reflectance and petroleum generation and expulsion that will help locate petroleum deposits.

Traditional petroleum exploration has used geophysical techniques to locate traps (reservoirs) where petroleum (oil and gas) may have accumulated. We are trying to increase the odds on finding oil by predicting whether a given trap is likely to contain oil.

Oil generated from organic material that has been buried for more than tens of millions of years can be expelled either by accumulation in a trap or by convertion to gas as it undergoes further burial. This year, we made significant advances in predicting when and where oil is generated, migrates, and accumulates. First, we developed an improved chemical kinetic model of vitrinite maturation and reflectance that better constrains thermal-history models of sedimentary basins. The thermal history is required to calculate if, when, and where the oil is generated. Second, we incorporated fluid equations of state, a simple mechanical model of source rock compaction, and a pseudo-one-dimensional calculation of mass transport into our detailed chemical kinetic model of oil and gas generation and destruction. This is required to determine if expulsion from the source rock occurs at the right time and geometry to fill a trap, which may be formed before, during, or after expulsion by crustal folding, faulting, or erosion and redeposition.

Deriving a thermal history for all sedimentary layers at locations throughout a basin involves steady-state heat-flow calculations at all historical times using inferred sedimentary thicknesses. Many approximations are required and there are many possible sources of error, so it is necessary to have some way for checking the calculated thermal history. The reflectance of light from vitrinite (a major constituent of coal and a minor constituent in many other sediments) is the most common indicator used to constrain geothermal histories, but there has been a long-standing disagreement on exactly how vitrinite reflectance depends on time and temperature.

We have developed an improved method for calculating vitrinite reflectance from thermal histories. Our model builds on the well-known correlation between vitrinite reflectance and its composition, particularly its hydrogen-to-carbon ratio. As vitrinite becomes more graphitic (containing more carbon), its reflectance increases. We derived a simple chemical kinetic model that reproduces changes in vitrinite composition (and hence its reflectance) for both geological and laboratory maturation. This model assumes that maturation proceeds by four independent reactions that eliminate water, carbon dioxide, oil, and methane from the vitrinite structure; each reaction is described by a distribution of activation energies. We then use data from the literature to derive improved correlations between composition and reflectance. Combining these

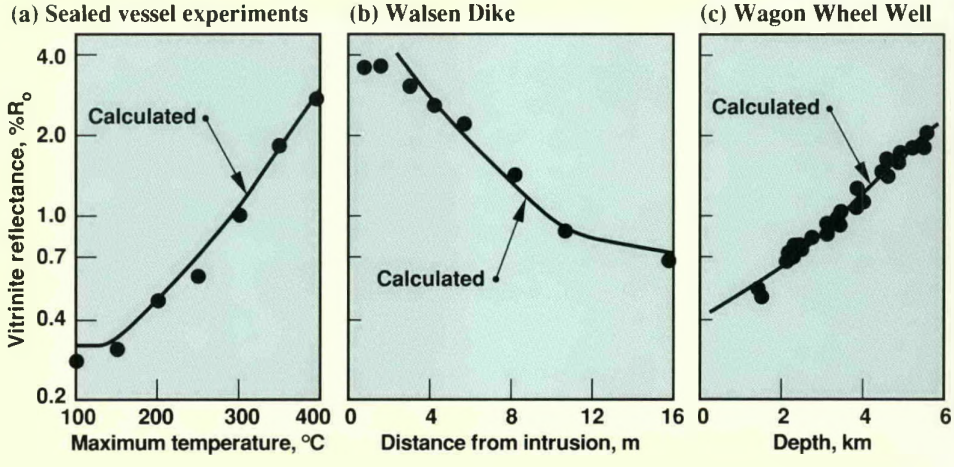

Figure 1. Comparison of measured and calculated vitrinite reflectance values for three drastically different time-temperature regimes: (a) sealed-vessel pyrolysis experiments for samples heated at 1°C/week, (b) temperatures of 200–450°C experienced over 50,000 to 500,000 years as heat dissipates from a volcanic intrusion (assuming 1143°C magma) near Walsen Dike, Wyoming, and (c) normal sedimentary heating to 180°C over 80 million years caused by deposition and subsidence (geothermal gradient of 24°C/km) near the Wagon Wheel Well, Wyoming.

two aspects allows us to calculate reflectance for maturation at time scales from hours to millions of years. Figure 1 compares measured and calculated reflectance values at three different time scales.

Once a thermal history for each sedimentary layer has been calculated and checked, it can be used to calculate the timing of oil generation in various parts of the basin. The most crucial question is not when oil was generated, but when it is expelled from the source rock so that it can migrate into a trap. While oil is in the source rock, it is continually cracked to lower-molecular-weight oil and gas, so the delay between generation and expulsion has a strong impact on the oil-to-gas ratio expected in a given trap.

To model this process, we must understand the chemical kinetics of oil cracking, how oil and gas volumes depend on temperature and pressure, how the decrease in rock porosity (compaction) depends on overburden pressure, how expulsion depends on porosity and pore-fluid pressure, and how compaction is inhibited by pore pressure. To calculate the volumes and compositions of the oil and gas phases, we added corrected Redlich-Kwong-Soave equations of state to our chemical kinetic model. We assumed that the equilibrium porosity decreases exponentially with the difference between the lithostatic pressure and the excess pore pressure (pore pressure in excess of hydrostatic). We further assumed that the rate of expulsion was proportional to an effective hydraulic conductivity estimated from the porosity. We also added a "pressure relief valve" so that the pore pressure cannot exceed lithostatic pressure, which simulates the process of natural hydrofracturing. In Figure 2, we show a calculation of generation, expulsion, pressure, and compaction curves for an idealized segment of

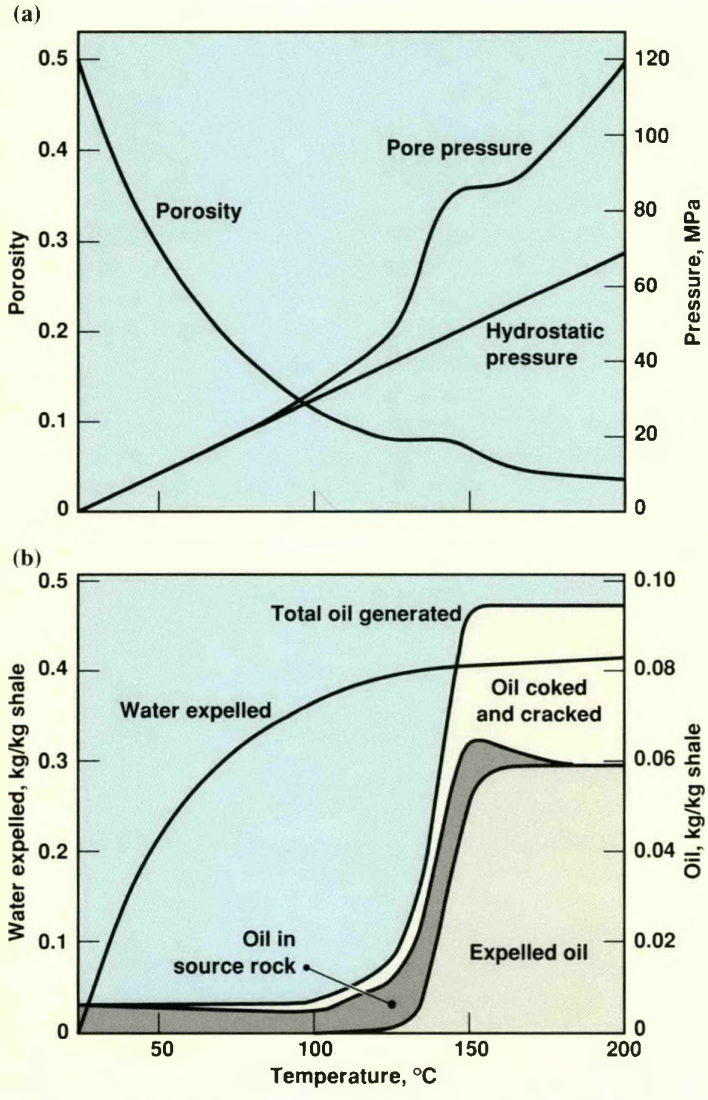

Figure 2. Simulation of compaction, pressures, oil generation and degradation, and oil and water expulsion for Green River shale. The shale initially contained 10% organic carbon and was heated at 3°C/million years, and the effective geothermal gradient was 25°C/km.

rich source rock that is heated at a rate of 3°C/million years in a geothermal gradient of 25°C/km. We chose the proportionality constant for leakage so that the excess pore pressures were similar to those observed in the oil window of the Uinta Basin, which we had described previously.[1]

It can be seen that oil expulsion is delayed from generation by about 10°C (3 million years), during which time about 30% of the oil is degraded to gas and coke. Other parameter studies show that the amount of oil cracking prior to expulsion is much larger for a source rock with less organic matter. These predictions are qualitatively consistent with general observations. Quantitative testing will be a major part of our further work. We will also use this model to test simpler models under development that could be used more routinely.

Reference

1. "Modeling the Generation of Oil and Gas," May 1987 *Energy and Technology Review* (UCRL-52000-87-5), pp. 21–30.

Contact: A. Burnham (415) 422-7304.

Conversion of Methane to Liquid Hydrocarbons

We are developing new catalysts and catalyst-based processes that may enable us to convert ample U.S. natural-gas resources into hydrocarbon liquids that can be used as transportation fuels.

Transportation fuels are a critical energy commodity that affects most sectors of this country; they account for 27% of U.S. energy consumption and 63% of U.S. oil needs. Thus, there is great interest in finding processes to economically convert other domestic fossil-energy resources to hydrocarbon liquids that can be used as transportation fuels.

Natural gas is a readily available resource, with U.S. reserves located on the Alaskan north slope, the outer continental shelf, and offshore in the Gulf of Mexico and extensive proven reserves worldwide. If these reserves can be processed to a liquid hydrocarbon, a 100-year worldwide supply of transportation fuels will be available.

The future for natural-gas processing depends on the development of catalyzed routes that convert methane, the major component of natural gas, directly to liquid hydrocarbons. The reaction that transforms methane (CH_4) to higher hydrocarbons is an oxidative process requiring the use of a catalyst to facilitate the reaction. The key to upgrading methane to liquid fuels is the controlled catalytic activation of the C-H bond of methane to prevent over-oxidation to carbon monoxide and carbon dioxide.

Using funds from the IR&D Program, we have concentrated our efforts on developing new catalyst materials that facilitate reactions for converting methane to liquid fuels. We are linking traditional catalysis research with the emerging field of biotechnology by studying biocatalytic systems, derived from living microorganisms, that perform desired chemical transformations of methane. We will use the knowledge obtained from studies of these biocatalytic systems to develop new types of "traditional" catalysts.

One area of current traditional catalysis research is the study of reactions involving partial oxidation (which form methanol and formaldehyde) or oxidative coupling (which form ethane and ethylene) of methane in the presence of oxygen. We are working to describe the gas-phase reactions of methane and oxygen that lead to methane oxidation and to develop new catalysts that select and accelerate the partial oxidation or coupling reactions.

We have used a chemical kinetic model called HCT (hydrodynamics, chemical kinetics, and transport), developed at LLNL, to describe such homogeneous gas-phase reactions that lead to the oxidative coupling of methane. We have tested this model against a series of experimental reactions, comparing the effects of reaction parameters such as temperature, residence time, and feed gas composition. Figure 1 shows the results of one such experiment in which the model calculations and

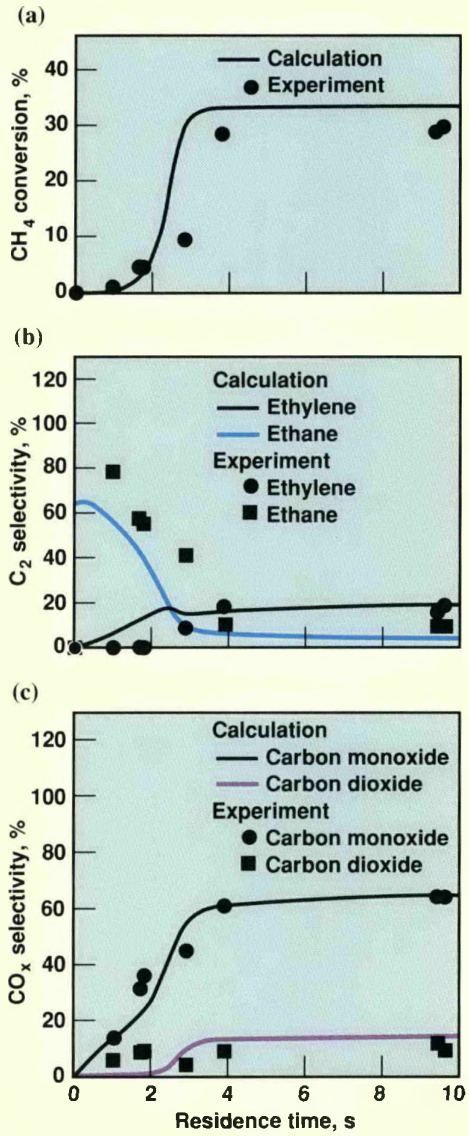

Figure 1. Comparison of model calculations and experimental results for methane conversion and product selectivities at various residence times (800°C, 3:1 methane-to-oxygen ratio).

experimental results for methane conversion and product selectivity are compared as a function of residence time. Our calculations successfully predict both the trend and the numerical values of the experimental data. Thus, the HCT model allows us to predict, quickly and accurately, the magnitude of the background reactions and to begin to separate the thermal gas-phase chemistry from the actual catalytic chemistry.

We are also studying the synthesis and reactions of new catalyst materials. These catalysts consist of an inorganic oxide matrix, such as SiO_2, in which transition and lanthanide metal ions are incorporated into the oxide coordination environment of the matrix. We have synthesized new catalysts containing niobium, lanthanum, and mixed niobium-lanthanum. Characterization studies have elucidated the bulk properties of the catalysts and determined details of the metal ion coordination environment. Reactor studies testing these catalysts for methane partial oxidation reactions are in progress; the results will be correlated with both the characterization data and the chemical kinetic modeling of the thermal reactions of methane and oxygen.

A select group of aerobic soil/water bacteria called methanotrophs can efficiently and selectively use methane as the sole source of their energy and carbon for cellular growth. The first reaction of methane in the organism, catalyzed by the enzyme methane monooxygenase (MMO), forms methanol, a product of the partial oxidation of methane and a useful fuel or fuel precursor. We hope to discover new catalysts modeled after the enzyme and/or to use stabilized protein components derived from the organism itself to develop processes for the conversion of methane to methanol. We are studying selected, naturally occurring bacterial systems that consume methane and catalyze the conversion of methane to methanol to determine the fundamental chemistry used by the enzymatic system for this process. We are investigating three areas: (1) microbial growth studies to maximize the cell mass yield and MMO activity in a selected methanotrophic microorganism, (2) MMO isolation and fundamental biochemical studies, and (3) MMO catalyst active-site identification and catalysis mechanism studies.

We are examining the influence of cell-culture parameters on the intracellular location, form, and stability of the MMO enzyme. This work will lead directly to the large-scale production of the bacteria using a state-of-the-art fermentation bioreactor. Future experiments will involve the isolation of the enzyme-protein from broken-cell extracts for probing the metal-ligand structure, reactions, and other properties of the catalytically active site in the enzyme.

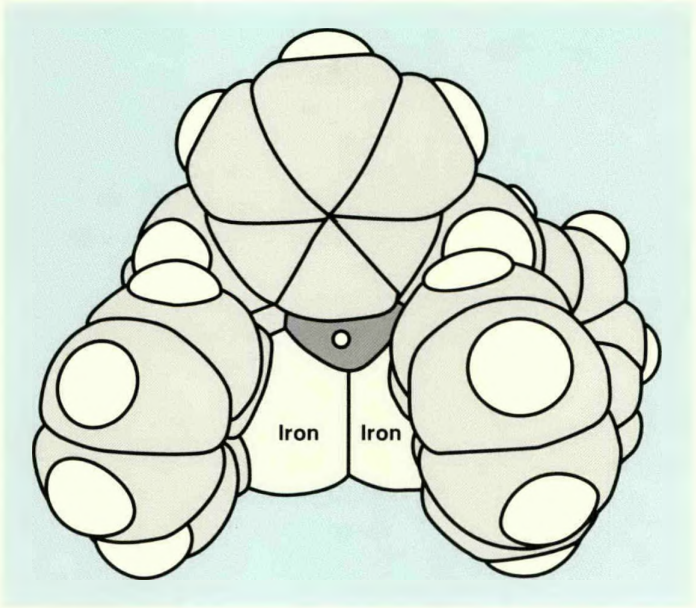

Figure 2. Space-filling model of binuclear metal complex showing the coordination of metal ions (iron) and reaction "pockets" formed by the organic chelating ligand. White circles represent hydrogen atoms; dark shaded segments represent carbon atoms; nitrogen atoms are hidden.

We are also trying to develop "bioinorganic" (nonbiological) catalysts that mimic MMO enzymatic action. Our approach is to synthesize inorganic chemical models of the biocatalyst active site that mimic the function of the biocatalyst. We are preparing discrete complexes in which metals of interest, such as copper and iron, are coordinated to atoms or molecules that may resemble components of the enzyme. Figure 2 is an example of a complex we have prepared that binds two metal ions using imidazole groups in a fashion thought to be similar to that found in the native enzyme. Using such complexes as a starting point, we can systematically modify them by monitoring both the physical properties and reactions until we obtain a good correspondence to the action of the native enzyme. In this way, we can study in detail the events of the catalytic reaction and develop an active catalytic material that performs a desired transformation of methane.

Contact: M. Droege (415) 422-0155.

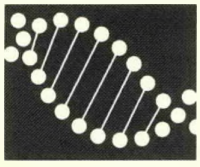

Biomedical and Environmental Sciences

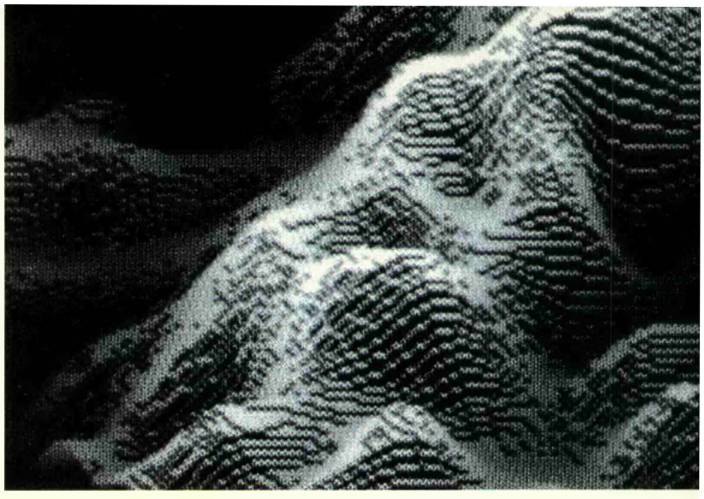

The Biomedical and Environmental Sciences Program at LLNL is conducting research in a number of very exciting areas of great significance to mankind. These projects combine traditional aspects of biological and environmental science with advanced diagnostics, instrumentation, computer modeling, and analysis.

One of the most exciting projects in current biomedical research is the international effort to characterize the human genome by ordering its DNA, mapping its genes, and eventually sequencing and interpreting its genetic information. Our primary focus has been to construct chromosome-specific libraries of human DNA and to organize the fragments of DNA (of roughly 45,000 base pairs) from specific chromosomes into overlapping, contiguous regions. To do this, we use an automated method of analyzing the fluorescent footprints of the DNA fragments. This work will eventually enable us to unlock the genetic code of man.

In a related and particularly dramatic development this past year, we were able to image double-stranded DNA at atomic resolution. We used a new imaging method called scanning tunneling microscopy. These images represent a major scientific breakthrough and signal a new era in molecular biology and high-resolution imagery.

We also made progress in our chromosome analysis work using the technique of fluorescent *in situ* hybridization. With this method, we can label DNA fragments with fluorescent compounds and then use these labeled fragments to locate and mark their homologous counterparts in cells and chromosomes. This technique provides a rapid and easy means of detecting abnormal numbers of chromosomes in nonmitotic (i.e., nondividing) cells and will become an important tool for the prenatal diagnosis of genetic disease.

We are also applying a novel method for measuring mutations in human red blood cells. This work combines Laboratory expertise in monoclonal antibodies with LLNL-developed high-speed flow cell sorters. We obtained and analyzed blood samples from survivors

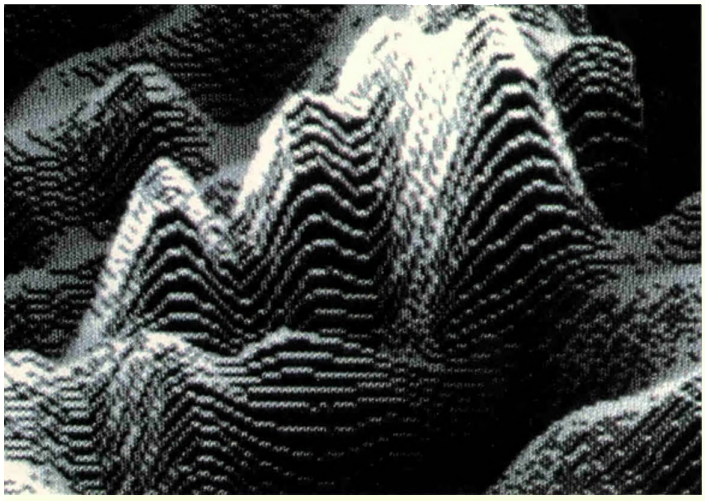

Scanning tunneling microscopy image of DNA (<10^6 bases) from calf thymus; the spiraling, right-handed structure of DNA is clearly visible.

of the Chernobyl nuclear reactor-accident and of the accident in Brazil involving a damaged ^{137}Cs radiotherapy source. These new data confirm our earlier findings on the mutational dose response in survivors of the atomic bombs of Hiroshima and Nagasaki. We have also applied this technique to blood samples from people with deficiencies in the repair of their DNA. These individuals show clear elevations in the number of red-blood-cell mutations that are consonant with their increased risk of cancer. This work will enable doctors to detect small increments of genetic damage caused by exposure to environmental mutagens long before an individual develops cancer or some other disease due to DNA damage.

Our environmental research has similarly broad and significant application. We are developing optical-fiber technology for the remote detection of chemicals in the environment. The coupling of optical fibers to surface-enhanced Raman spectroscopy (SERS) offers great potential for sensitive environmental chemical sampling. Although the SERS method is still in its infancy, it is attracting much attention because of the sensitivity and richness of the signals it provides from many environmentally important chemicals.

We are continuing our work in atmospheric and geophysical modeling. This research requires the combination of advanced computer modeling and detailed understanding of the chemistry and behavior of gases. We are modeling the distribution of nitrogen oxides and other manmade pollutants on a global level to determine their impact on the atmosphere (e.g., the depletion of ozone and the greenhouse effect). We are also modeling the behavior and dispersion of dense gases on scales of a few meters to a few kilometers, taking into account the effects of local terrain. This modeling ability has application in the event of potentially toxic releases of gaseous chemicals (e.g., a train accident involving tanker cars of liquefied natural gas) to help emergency-response crews plan their cleanup efforts and determine whether populated areas need to be evacuated.

Contact: M. Mendelsohn (415) 422-5765.

The Human Genome Project

We are mapping human chromosome 19 using new techniques, including fluorescent DNA fingerprinting, as part of an international effort to decipher the genetic code of man.

Human genetic material—deoxyribonucleic acid (DNA)—contains about three billion nucleotides, which are bits of chemical information that code for an estimated 100,000 genes. The products of these genes are proteins that determine the functions of cells and the body's physical structure. Only about 4% of all human genes have been identified to date, and less than 0.1% of human DNA has been sequenced.

The goal of the Human Genome Project is to develop a complete understanding of human DNA—its organization, its sequence, and the functions encoded by that sequence. The project is international and multidisciplinary; the Laboratory's Biomedical Sciences Division, with funding from the IR&D Program, is a major focus in this effort. We have established a core research group to develop and apply new technologies in chemistry, molecular biology, computations, and instrumentation to decipher the genetic code of man.

This effort has been divided into two steps. First, the human genome will be broken into small fragments, perhaps as many as a few hundred thousand. These fragments will be mapped relative to one another and to known genes and then reassembled in a computer. Next, certain fragments, perhaps those containing important genes, will be selected and sequenced. Because such fragments are small and represent only a minute portion of the human genome, instrumentation and methods that increase the efficiency of DNA mapping and sequencing are a high priority. Our efforts have focused on cloning, mapping, and reassembling DNA fragments obtained from chromosome 19.

We first purify chromosome 19 from human cells using high-speed flow sorters. DNA is then isolated from the purified chromosomes, broken into small pieces, and inserted into cosmid vectors (special DNA molecules that can join with human DNA to form a recombinant DNA clone). Each recombinant DNA clone contains a fragment of chromosomal DNA about 40,000 base pairs long (about 0.001% of the whole genome) and is grown and reproduced in bacteria. To ensure that all the DNA of the chromosome is available, we must clone a five- to tenfold excess of fragments. For chromosome 19, this represents about 8000 such clones. These 8000 clones are then ordered into a linear array of about 1500 clones, the minimal set of fragments that spans the entire human chromosome 19. Each fragment is about the size of a gene and is stored individually in a numbered vial. Using standard methods in molecular biology, genes are then localized on individual fragments. With the fragment and gene in hand, it becomes possible to determine the underlying genetic code (the DNA sequence) and to understand the role of that gene.

We have developed a fast, semiautomated method to reassemble the cloned DNA fragments, called fluorescent DNA fingerprinting (Figure 1). We are currently exporting the chemistry and software required to perform this analysis. In the past year, we have made substantial progress in reassembling DNA fragments from parts of two human chromosomes, 14 and 19, and in identifying and mapping genes on chromosome 19. We created recombinant DNA clones (libraries) for a region of chromosome 14 containing 600,000 base pairs and for all of chromosome 19, which contains 60 million base pairs. For the cloned region of chromosome 14, we constructed sets of overlapping cosmids that span nearly all of this region. To do so, we selected 92 clones at random, fingerprinted each one using our fluorescent fingerprinting method, and reassembled them using our software into six contigs (sets of overlapping cosmids) spanning nearly the entire 600,000 base pairs. The shortest contig consists of two cosmids and the longest has 58.

We applied several techniques to map the location of four genes in chromosome 19: branched chain transferase 2 (BCT2), creatine kinase, muscle form (CKMM), and two DNA repair genes (ERCC1 and ERCC2). Gene BCT2 makes a protein used in the metabolism of amino acids; defects in this gene are associated with seizures, failure to thrive, and mental retardation. Gene CKMM makes a protein used in the generation of chemical energy for muscles. The two DNA repair genes, ERCC1 and ERCC2, make proteins involved in removing and replacing

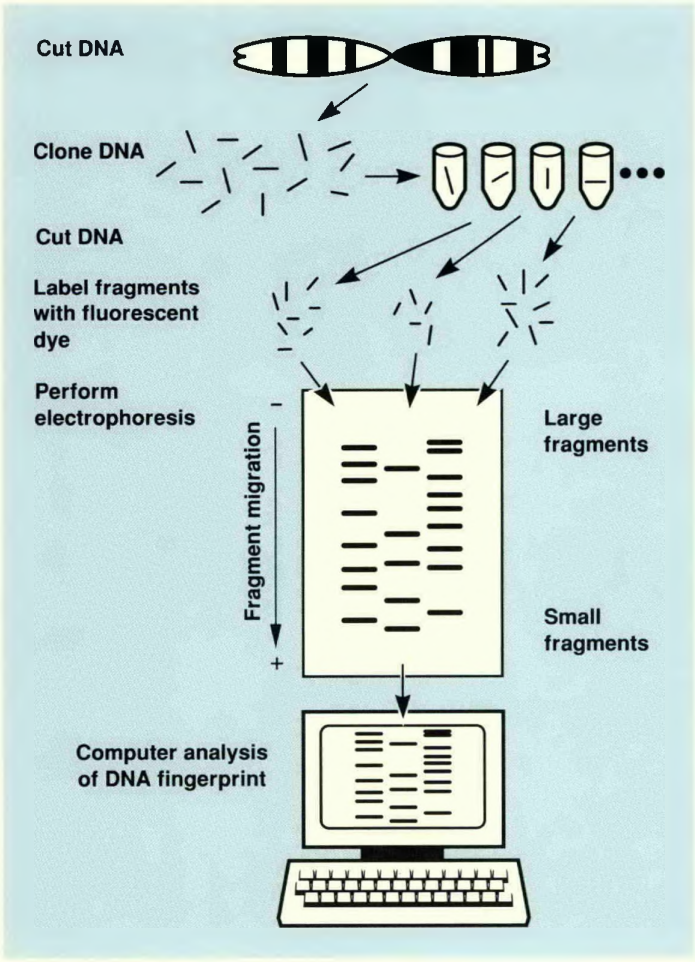

Figure 1. DNA is isolated from purified chromosomes, cut into small pieces, and inserted into vectors to form a DNA clone. Each clone is broken into smaller fragments in a reproducible manner. The ends of the fragments are labeled with a fluorescent dye and separated by size via electrophoresis. The dye is excited by a laser, and the fragments are visualized on a computer monitor in real time as they migrate in an electric field applied to a gel. The sizes of the fragments from each clone form a fingerprint. Clones with similar fingerprints can be shown to overlap and, hence, form a linear array along the chromosome.

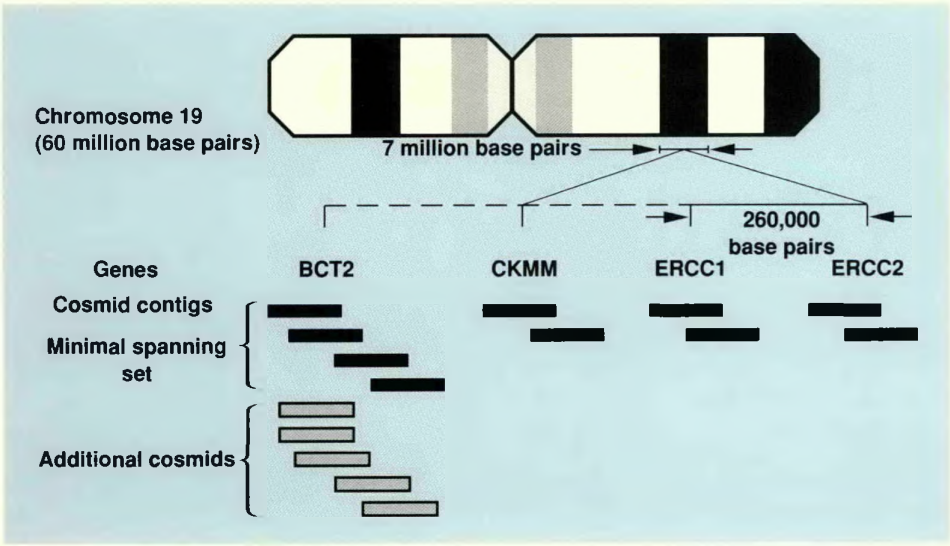

Figure 2. The location of four genes on chromosome 19. The genes BCT2, CKMM, ERCC1, and ERCC2 lie in a region of this chromosome containing about seven million base pairs; genes ERCC1 and ERCC2 lie within 260,000 base pairs of one another.

DNA damaged by exposure to radiation or chemicals. Using techniques of *in situ* hybridization, we found that the four genes are localized in a single region on chromosome 19 containing about seven million base pairs, or about 10% of the chromosome (Figure 2). Other mapping methods revealed that the ERCC1 and ERCC2 genes lie within 260,000 base pairs of each other.

Next we isolated these genes on specific clones from our chromosome-19 cosmid library. We screened the chromosome-19 cosmid library using probes for four genes previously mapped to the chromosome. The gene probes identified approximately 50 cosmids from our library, and these cosmids were then "fingerprinted" to establish contigs for each of the genes. Each gene was found to be associated within a unique contig; the contig for BCT2 contains nine cosmids, and the CKMM, ERCC1, and ERCC2 contigs each have two cosmids. (Figure 2 shows the minimal spanning set of cosmids as black boxes; other overlapping cosmids are shown by gray boxes.) Thus, in a rapid procedure, we established a set of cosmids that spans four genes of interest and probably some of the intervening DNA. It is highly likely that these cosmids contain all the genetic information necessary for making the associated proteins.

Our quest for a map of the human genome and the structure of DNA is both scientifically stimulating and of great potential benefit to mankind. The information obtained will be important for the diagnosis of genetic disease, the production of pharmaceuticals by recombinant DNA methods, and, perhaps in the future, for replacement gene therapy.

Contact: A. V. Carrano (415) 422-5698.

DNA Sequencing and Atomic Imaging

We are using an air-operated scanning tunneling microscope to analyze biological materials at the atomic level of resolution.

The recent development of the scanning tunneling microscope (STM) and demonstrations of its capabilities for imaging molecular structures with atomic resolution provide tremendous promise for future studies in molecular biology. The main difference between the STM and all other microscopes is that it uses no free particles; consequently, there is no need for lenses and special light or electron sources or any elaborate apparatus to provide a vacuum in which particles can travel freely. Instead, the instrument exploits the movement of bound electrons that exist in all conducting materials.

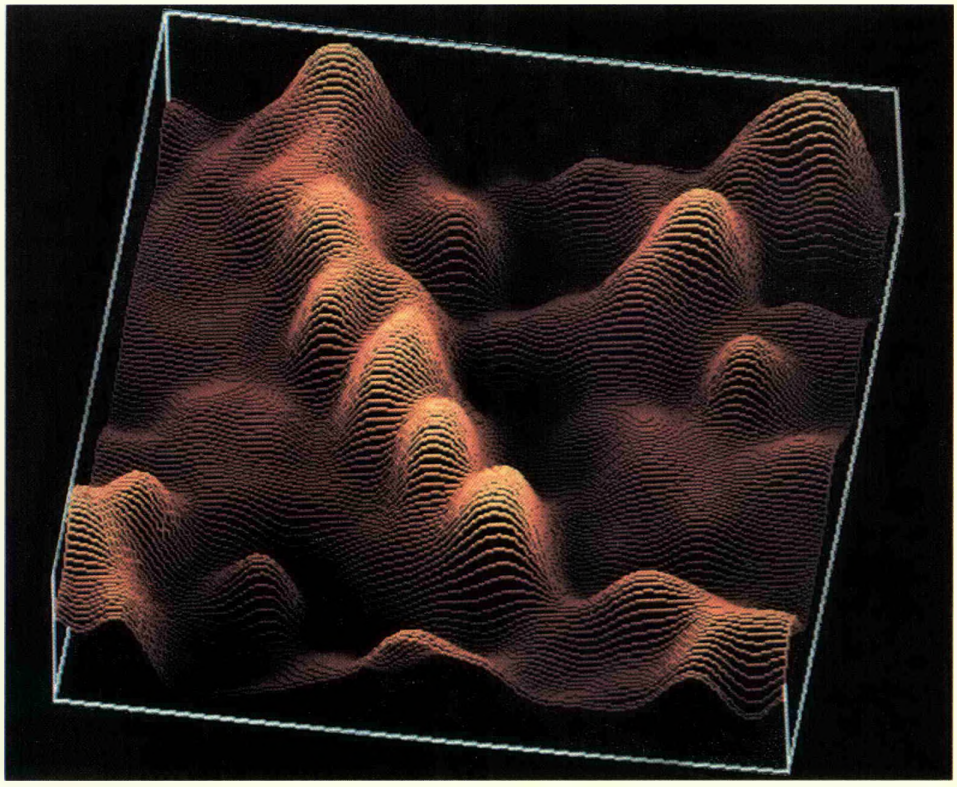

Figure 1. STM image of calf thymus DNA obtained from the Worthington Biochemical Corporation (Freehold, New Jersey). Highly polymerized thymus DNA was dissolved overnight in aqueous 10-m*M* KCl (4.5 mg/ml). Aliquots of stock DNA solution were diluted with 10-m*M* KCl to a working concentration of 1 mg/ml. We then evaporated one droplet in air on a freshly cleaved, pyrolytic graphite substrate, which provides a conductive surface with crystal planes atomically flat over hundreds of nanometers. This 34 × 34-nm image shows a DNA molecule with convolutions on the surface such that the spiraling, right-handed DNA structure is clearly visible.

To understand the operation of our STM, imagine one atom at the end of an atomically sharp metallic needle located close to the surface of a conducting material to be examined. For gap distances of 0.5 nm, an applied bias of several tens of millivolts induces current flow in the nanoampere range. Electrons are said to "tunnel" or flow across the gap because of the quantum-mechanical tunneling effect. Because electrons do not migrate into free space, the instrument can operate in any nonconducting medium, such as air, water, or oil.

We have used three operating modes: constant current, constant height, and local-barrier height. In the constant-current mode, for example, the needle is scanned across a surface laterally while its distance from the surface is adjusted to maintain a constant tunneling current. The current typically decreases by one order of magnitude for every 0.1 nm in gap spacing. Our scanner provides a maximum tip range of 100 nm in all directions with displacement control to better than 0.001 nm. We obtain a topographic image of the surface in the recorded trajectory of the tip as electrons tunnel across the gap from the outer electronic surface of a sample's atoms. We can acquire pictures of such samples that are 10 nm on each side in less than one minute.

At the outset of our project, the only biological samples that had been examined with the STM were virus particles and isolated, double-stranded DNA. Such studies, however, did not provide images even approaching the atomic level of

resolution. Our primary goal was to prepare biological samples relevant to ongoing studies in the Biomedical Sciences Division and to devise methods for imaging the atomic structure of these samples using the STM constructed by researchers in the Chemistry and Materials Science Department. We also sought to identify and solve special problems that might arise in imaging samples on conventional graphite surfaces. This work has been supported by the Laboratory's IR&D Program.

We prepared samples for analysis that varied in both size and complexity, including a single-stranded fragment of DNA, a folded protamine molecule containing 50 amino acids, high-molecular-weight double-stranded DNA, and a sperm chromatin particle several micrometers long and two micrometers wide. The bulk of our effort, however, was directed toward imaging the atomic structure of double-stranded DNA. We realized that once the capability for imaging the nucleotide subunits of DNA was attained, an entirely new electronic approach for sequencing DNA could be developed, automated, and applied to the analysis of very long DNA fragments.

We used a simple approach for drying DNA on the surface of graphite to prepare double-stranded DNA for scanning tunneling microscopy. We have now successfully scanned these samples using a tapered, atomically sharp probe (Figure 1). Although we have only begun to learn what factors control optimal sample and tip preparation, our current methods have produced images of DNA at near-atomic resolution (Figure 2) that are the best in the world. In future efforts, we expect to provide enhanced images at the atomic level of resolution and to couple the tunneling phenomenon and spectroscopy to identify individual DNA base pairs.

Contact: R. Balhorn (415) 422-6284.

(a) Calf thymus DNA

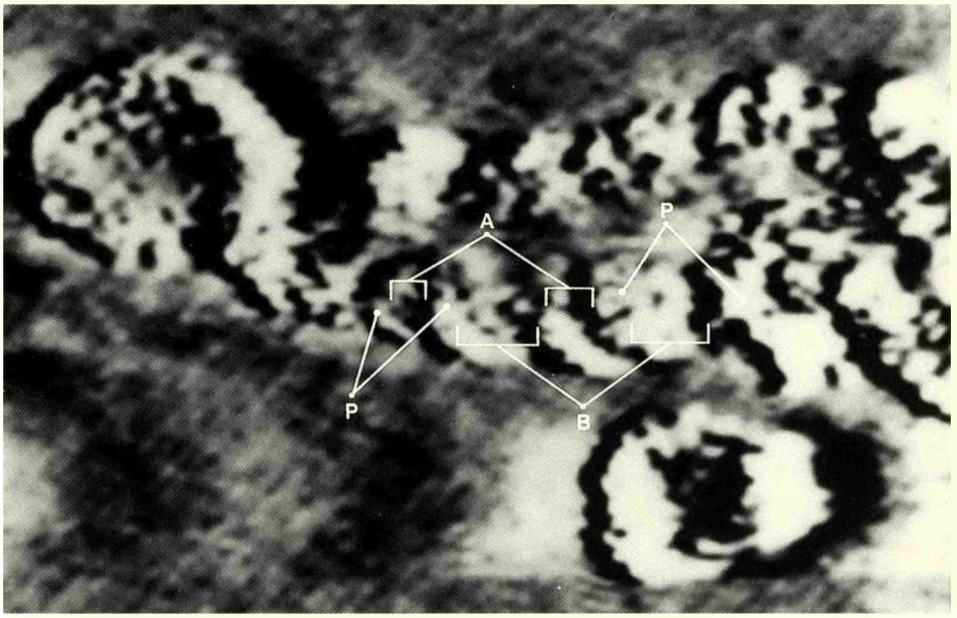

(b) DNA helix

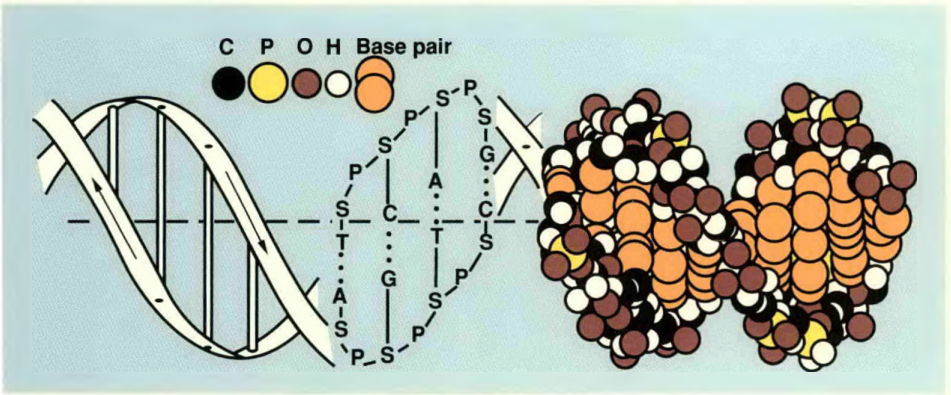

Figure 2. (a) Image of calf thymus DNA obtained with the STM. This image clearly resolves the two individual phosphodiester strands (P) of DNA as well as the minor (A) and major (B) grooves produced by the helical coiling of the two strands. (b) Schematic of the DNA helix for comparison.

Fluorescence *in situ* Hybridization

We are using new, highly specific nucleic-acid probes in the prenatal detection of disease-linked chromosomal aberrations, such as that seen in Down syndrome.

The classification of chromosomes using banding analysis is now applied routinely for the prenatal detection of numerical and structural aberrations in chromosomes that are associated with genetic disease. Some of the most common numerical aberrations analyzed in this manner are Down syndrome (caused by an extra copy of chromosome number 2; trisomy 21), Edwards syndrome (trisomy 18), Patau syndrome (trisomy 13), Turner syndrome (only one X chromosome and no Y chromosome), and Kleinfelter syndrome (two X chromosomes and one Y chromosome). Examples of important disease-linked structural aberrations include retinoblastoma (loss of a portion of chromosome 13), Prader-Willi syndrome (loss of a portion of chromosome 15), and Wilms tumor (loss of a portion of chromosome 11).

Banding analysis is the visual classification of dividing (mitotic) cells that have been stained so that different chromosome types carry unique patterns of bands along their lengths. Such analysis allows us to accurately detect most chromosomal aberrations; however, the technique suffers from several important limitations. The procedure is labor-intensive and time-consuming, and requires a highly trained analyst. In addition, it can only be applied to cells that are dividing. Thus, actively dividing cells, such as amniocytes, must be obtained using invasive procedures, and several weeks may elapse before a sufficient number of mitotic cells can be produced for analysis. Finally, banding analysis does not allow the detection of structural aberrations involving fewer than 3 to 15 million bases of DNA, depending on the nature of the aberration and the resolution of the specific banding technique.

We have now developed a technique called fluorescence *in situ* hybridization (FISH) with chromosome-specific nucleic-acid probes as a way of overcoming these limitations. The FISH procedure allows us to intensely and specifically "stain" selected chromosomes or subregions according to their DNA sequence. In this approach, DNA in the target cells or chromosomes is denatured (heated so that the DNA, which is normally a double helix of complementary strands, melts and the strands separate). The target DNA of interest is then incubated with chemically modified and denatured nucleic-acid probe sequences that are complementary to DNA sequences in the chromosomes to be stained. The incubation conditions are such that the probe binds only to target DNA sequences that are complementary. The bound probe is made visible by treatment with a fluorescent reagent that is able to bind with high affinity.

The key to our chromosome staining approach is in obtaining the chromosome-specific probe. The most important sources of such probes are the recombinant DNA libraries that have been made by the National Laboratory Gene Library Project at the Livermore and Los Alamos laboratories. Separate libraries have now been produced for each of the 24 different types of human chromosome by this project. Each library contains many sequences that are uniquely present only in one chromosome type and others that occur repeatedly on many (or all) chromosome types. Chromosome-specific staining is achieved by removing the nonspecific, repeated sequences from each library or by blocking their binding.

A major advantage of FISH with chromosome-specific probes is that it permits intense staining of selected chromosomes in interphase (nondividing) cells. The need for expensive and time-consuming cell culture is thereby eliminated. Because chromosomes are tightly localized in interphase nuclei, the hybridization regions are visible as bright spots, called hybridization domains, in such nuclei (Figure 1).

We can detect abnormal DNA content (called aneuploidy) and targeted chromosomal subregions in interphase nuclei simply by counting the number of hybridization domains. Normal cells, for example, typically display two domains when they are hybridized with a composite probe for chromosome number 21. Cells from a fetus with Down syndrome, on the other hand, often display three domains.

We have tested the diagnostic utility of our approach in the prenatal detection of Down syndrome during a collaborative study with the Prenatal Detection Program at UC San Francisco. In this investigation, we analyzed interphase fetal cells in a blind study of 20 cell cultures. These cells were left over from cultures established from cells obtained using amniocentesis or chorionic villus biopsy for routine cytogenetic

analysis. After completion of the study, and for purposes of comparison, data were also partitioned according to whether the cells were normal or trisomic for chromosome number 21 by conventional cytogenetic analysis.

Figure 1 shows the domain frequencies we measured for the two populations. Normal cells uniformly showed about 70% of the nuclei with two domains, about 30% with one domain, and about 1% with three domains. The Down syndrome cells showed about 45% of the nuclei with three domains, about 45% with two domains, and about 10% with one domain. These data indicate that samples can be easily classified as either normal or Down syndrome by counting the number of interphase domains.

It also appears likely that our approach can be extended to the detection of other important abnormalities in DNA content, including segmental duplications and deletions, in uncultured cells within one or two days after collection from a fetus. One exciting possibility is that our assay may eventually allow cytogenetic analysis of interphase fetal cells isolated from a few milliliters of maternal blood.

Contact: J. Gray (415) 422-5610.

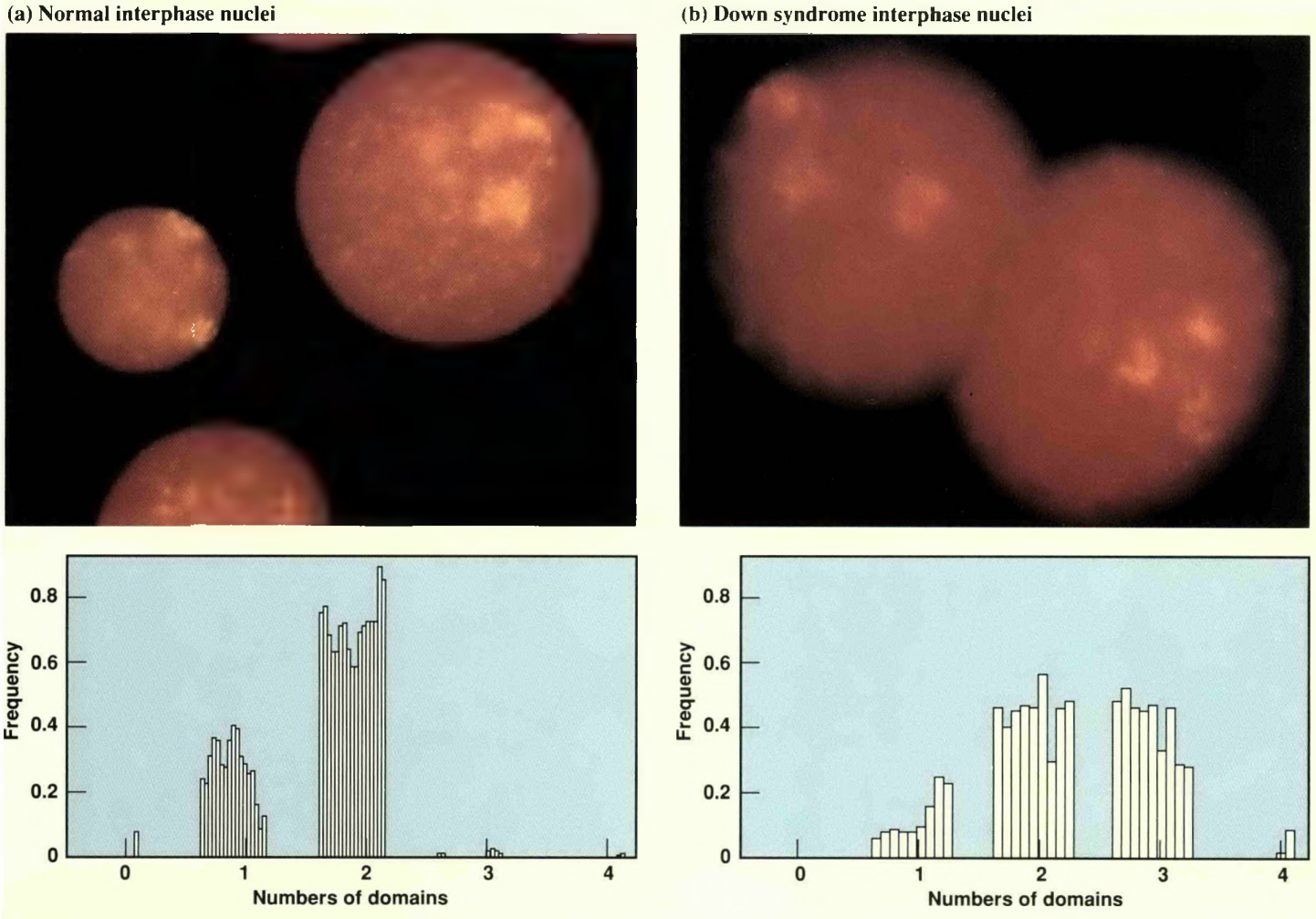

Figure 1. Application of fluorescence *in situ* hybridization (FISH) in the detection of Down syndrome. (a) Top: In the interphase nuclei of cells from a normal individual, the number 21 chromosomes stain bright yellow whereas other chromosomes stain red. Bottom: Such normal cells typically display two yellow domains. (b) Top: Interphase nuclei of cells from an individual with Down syndrome. Bottom: Such cells from fetuses with Down syndrome typically display three yellow domains. In a collaborative study with researchers at UC San Francisco, all prenatal samples were correctly classified as either normal or trisomic for chromosome number 21 by the FISH analysis.

Measuring Human Mutations

We are using a new technique to estimate somatic-cell mutations in Chernobyl and Brazilian radiation-accident victims and to detect the high levels of spontaneous mutations in cancer-prone individuals.

We have developed a new assay to estimate the level of genetic injury in human cells. Our method determines the frequency of circulating red blood cells with alterations in the expression of the cell-surface protein antigen called glycophorin A (GPA). The frequency of variant cells is a measure of the level of genetic damage that has occurred within the GPA genetic locus of bone-marrow cells that give rise to peripheral red blood cells.

We apply our assay to blood samples from genetically appropriate individuals whose red blood cells normally contain two different forms of the GPA protein, GPA(M) and GPA(N). The DNA of these individuals contains single copies, called alleles, of the two genes that code for the two forms of GPA. A nonlethal mutation in a bone-marrow cell that inactivates one of the GPA alleles will ultimately result in the production of a clone of red blood cells lacking one form of GPA. In our assay, we can identify such cells by simultaneously immunolabeling the red cells with a pair of monoclonal antibodies, one of which specifically recognizes and binds to GPA(M) and the other to GPA(N). The two antibodies are tagged with fluorescent dyes, one of which fluoresces green and the other red.

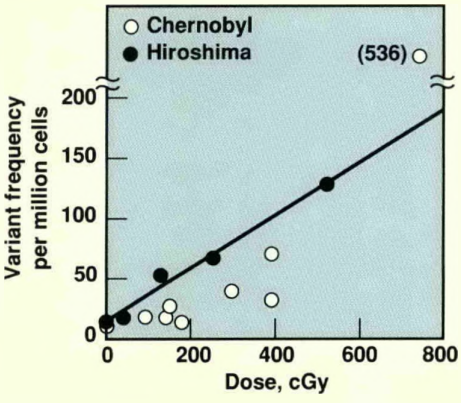

Figure 1. GPA hemizygous variant cells per million in blood samples from individuals exposed to radiation. The frequencies of variant cells are plotted as a function of estimated radiation doses for pooled groups of Hiroshima survivors and individual victims at the Chernobyl accident. The straight line represents a linear fit of the data from Hiroshima survivors.

Normal cells derived from bone-marrow precursor cells with functional GPA(M) and GPA(N) alleles contain both forms of GPA and bind to both monoclonal antibodies. These doubly labeled cells fluoresce both green and red. However, the variant cells lacking expression of one of the GPA alleles are singly labeled and fluoresce only one color. We count these rare, single-color variant cells using a flow cytometer that is capable of analyzing a million cells in a few minutes. The cytometer quantifies the fluorescent signal from every red blood cell and characterizes each one as belonging to one of the three following categories:

- Normal red blood cells, which express both GPA(M) and GPA(N) alleles.
- Mϕ or Nϕ hemizygous variants, which are cells that have lost expression of one of the two GPA alleles and express the remaining allele as a single copy.
- MM or NN homozygous variants, which are cells that lack expression of one GPA allele and express the other at a two-copy level.

We tested the hypothesis that the frequency of variant cells reflects the amount of mutagenic damage at the GPA locus of the precursor cells of individuals. To do so, we applied the assay to blood samples from cancer patients undergoing chemotherapy with mutagenic drugs and from survivors of the Hiroshima atomic bomb who were exposed to whole-body ionizing radiation. We observed elevated frequencies of hemizygous variant cells in the cancer patients during and immediately following therapy. In the Hiroshima survivors, we obtained dose-dependent increases in the frequencies of hemizygous variant cells. It is important to keep in mind that our analysis of Hiroshima survivors was done 40 years after exposure. Our results indicate that radiation-induced GPA mutations can be stably integrated into long-lived precursor (stem) cells.

We have recently begun to study the responses to ionizing radiation in blood samples from individuals who were exposed as a result of the Chernobyl accident in 1986 and a ^{137}Cs accident in Brazil in 1987. Figure 1 shows the results of an initial survey of nine MN blood samples obtained from emergency personnel and reactor workers exposed at Chernobyl. Some of the samples revealed significantly increased levels of hemizygous variant cells. These variant frequencies are plotted as a function of estimated radiation dose (in units

of cGy) provided by Soviet scientists, based on clinical symptoms and cytogenetic measurements. The estimates suggest that the power-plant workers and general population immediately surrounding Chernobyl received significant radiation doses and, thus, constitute a unique group for studying *in vivo* radiation effects. Approximately 50,000 people received a dose of at least 50 cGy, and 4000 people may have received an average of 200 cGy. Under the auspices of the International Atomic Energy Agency, we are now making collaborative arrangements with Soviet researchers to discuss applications of the GPA assay to this population. For comparison, Figure 1 also includes a summary of the dose response observed in the Hiroshima survivors.

We have established a collaboration with Brazilian researchers to study blood samples from individuals associated with a 1987 radiation accident. This accident resulted from damage to a ^{137}Cs radiotherapy source, leading to exposure of at least 100 people. We know that 29 individuals received doses exceeding 50 cGy, 21 received more than 100 cGy, and eight received more than 400 cGy. To date, we have analyzed blood samples from three people with hemizygous variant-cell frequencies ranging from a normal background level of 6 per million cells to a high of 76 per million cells. We will soon receive a complete set of blood samples from this exposed population for GPA analysis. GPA studies of the Chernobyl and Brazilian populations will be important in validating our results from the Hiroshima survivors and will provide additional data to compare with other measures used in estimating biologically relevant radiation doses in humans.

We have recently applied the GPA assay to study cancer-prone individuals and their families. The patients in this research were diagnosed with either ataxia telangiectasia (AT) or Bloom's syndrome (BS). Both of these heritable conditions result in high spontaneous rates of chromosome instability thought to be indicative of genetic abnormalities in DNA metabolism and/or repair. Our measurements of GPA somatic-cell mutations in Figure 2 show that AT patients also exhibit a mean spontaneous level of hemizygous variant red blood cells that is about ten times normal. The elevation in such levels for patients with BS is even more dramatic, with a mean of over 70 times normal. Nearly all unaffected family members, many of whom are carriers of these two diseases, display normal frequencies of GPA variant cells. A unique finding is that patients with BS also show high frequencies (about 70 times normal) of homozygous variant cells. Such cells arise by additional mutation mechanisms recently shown to be significant in the process of cancer induction. Such measurements in cancer-prone individuals demonstrate a link between genetic defects in DNA function and cytogenetic instability, somatic-cell mutation, and susceptibility to cancer.

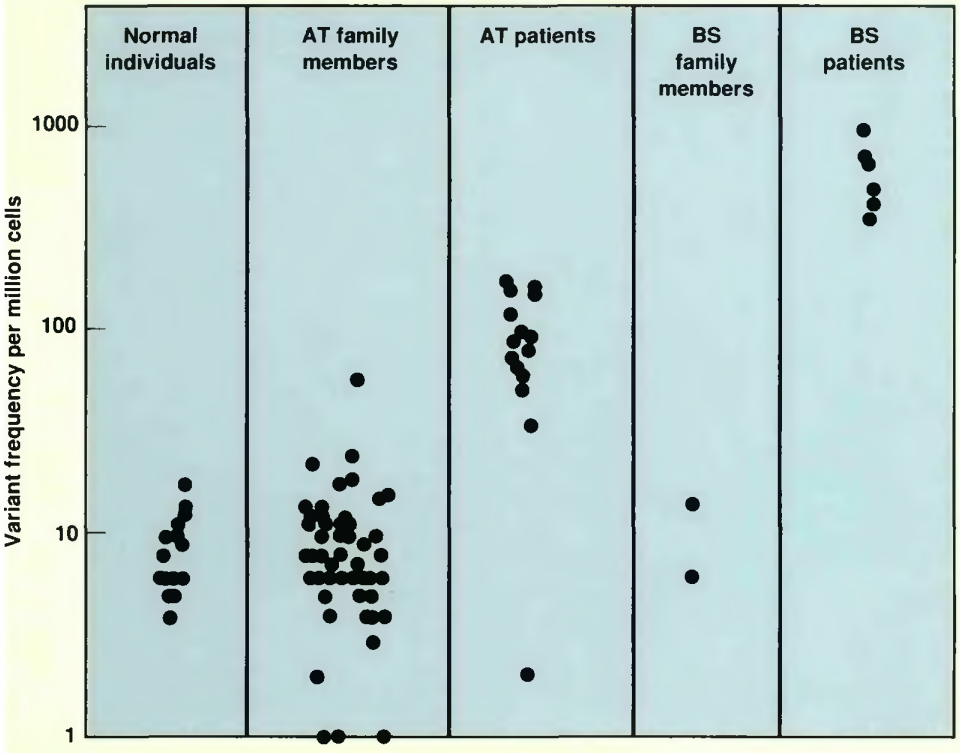

Figure 2. GPA hemizygous variant cells per million observed in blood samples from 16 normal individuals, 56 AT family members (including grandparents, parents, aunts, uncles, brothers, and sisters of affected persons), 15 AT patients, 2 BS family members (both parents), and 7 BS patients. Note that the scale for variant cell frequency is logarithmic. Both AT and BS patients show elevated spontaneous levels of hemizygous variant red blood cells whereas unaffected family members display normal frequencies of GPA variant cells.

Contact: W. L. Bigbee (415) 422-5682.

Near-Infrared Surface-Enhanced Raman Spectroscopy

By incorporating a near-infrared technique into surface-enhanced Raman spectroscopy, we can use a less costly, semiconductor diode laser excitation source and fiber optics for remote spectroscopy.

We are developing a near-infrared (NIR) technique of surface-enhanced Raman spectroscopy (SERS) for use with long optical fibers to make remote, sensitive measurements of groundwater contaminants. NIR SERS allows the use of inexpensive semiconductor diode lasers as the excitation source and eliminates problems encountered with sample fluorescence. This research is funded by the Laboratory's IR&D Program.

The NIR SERS Technique

In SERS, enhanced Raman signals are observed for molecules adsorbed onto microscopically roughened metal surfaces. Most SERS studies have used visible-light excitation sources. For certain types of molecules, SERS can be very sensitive, and because SERS is a vibrational spectroscopy, a SER spectrum contains much molecular information.

The introduction of Fourier-transform (FT) Raman instruments has made possible the use of NIR excitation sources, which eliminates problems with sample fluorescence and photoreactions usually encountered in Raman spectroscopy. We have recently extended the range of NIR Raman techniques to include FT SERS and NIR SERS.

NIR SERS has physical significance. Since this wavelength range differs significantly from the visible range used in most SERS studies, calculation of NIR SERS enhancement factors may help to refine current theoretical explanations of the SERS phenomenon.

NIR SERS is well suited to remote spectroscopy using fiber optics. NIR excitation is efficiently transmitted by optical fibers; it significantly reduces the fluorescence background signals that come from the optical fiber and sampling region and reduces the intensity of interfering fiber-optic Raman bands.

This technique can also be used to monitor highly luminescent molecules, such as those used in biological and environmental research. For example, by using NIR SERS instead of resonance Raman spectroscopy, one can avoid problems associated with the luminescence of the target molecules, molecular complexes, changes in binding resulting from electronic excitation of the molecules, and spurious results from photoreaction products.

The initial goal of our SERS research was to determine whether we could indeed use NIR-wavelength excitation to obtain SER spectra and then to quantitatively compare the magnitude of the effect with that of visible-wavelength excitation. We used an FT Raman spectrometer with an Nd:YAG laser. In experiments with pyridine, we found that copper and gold electrodes both give very large SER enhancements, comparable in magnitude to reported enhancements using visible-wavelength excitation. We also found that copper and gold colloids both give very large NIR SER enhancements with many different types of molecules.

To develop the NIR SERS technique for environmental applications, we began by studying very simple monosubstituted aromatic compounds. Spectra obtained for mixtures of these compounds reveal that the SER spectrum of any one compound is often affected by other substances in solution. Because contaminated groundwater usually contains mixtures of related compounds, it is essential that we determine what factors affect the SER spectra of mixtures.

Diode Laser Excitation Source

Semiconductor lasers are ideal excitation sources for spectroscopy; they are inexpensive, small, easy to use, long lived, they require little maintenance, and they can be battery-powered for field use. The diode laser is very small (see Figure 1a); some systems are no larger than a small camera, even with their power supply and collimation optics. However, because powerful single-mode lasers are available only at NIR wavelengths, the use of diode lasers for Raman spectroscopy has only recently been considered. We have demonstrated NIR SERS using a conventional Raman spectrometer

and the 785-nm line of a GaAlAs diode laser as excitation source.

The 785-nm wavelength is transmitted very efficiently by optical fibers and thus is ideal for measuring SER spectra of highly luminescent compounds with visible absorption bands. This wavelength is far removed from most electronic absorption bands and therefore produces little or no fluorescence. Also, since a typical Raman spectrum using 785-nm excitation is within the range of photomultiplier tubes, diode lasers can be used with conventional spectrometers.

Despite the low output power of the GaAlAs diode laser, we easily obtained SER spectra of a variety of compounds on silver and copper electrodes. For 0.1-*M* pyridine on a silver electrode, typical signal levels were 10,000 counts/s. The SERS enhancement with 785-nm excitation was about 10^5–10^6, about the same as with visible-light excitation, for both silver and copper electrodes.

Using the GaAlAs diode laser, we were able to eliminate sample luminescence and measure SER spectra of tris(2,2′-bipyridine) ruthenium(II), RB3, in bulk solution. RB3 is an interesting compound because of its unique excited-state properties, but its intense visible luminescence makes luminescence-free Raman spectra difficult to obtain. Figure 1b shows the diode-laser-excited SER spectrum of 6-m*M* RB3 solution on a silver electrode. Remarkably, we obtained this spectrum in bulk solution with no evidence of luminescence or attenuation of the laser beam, even though 1 cm of solution was on the excitation and collection sides of the electrode.

Optical Fiber Length

Measurement of SERS is straightforward if short optical fibers (about 10 m) are used. However, for longer optical fibers, the fiber background can be larger than the SER signal itself, because the SERS substrate reflects the Raman and fluorescence background signals generated in the fibers back into the collection fibers.

We built a prototype fiber-optic SERS probe using miniature graded-index optics to eliminate fiber background signals; we successfully measured SER and Raman spectra over 250 m of optical fiber without background subtraction. The prototype probe uses a small AgCl-coated silver wire as the reference electrode and a small platinum electrode to control the current flowing through the SERS substrate (electrode). With this arrangement, we have regenerated the SERS substrate *in situ* many times by performing repeated oxidation-reduction cycles. Although not truly reversible, the SERS substrate can be used many times before it must be replaced.

Conclusion

We have made much progress toward developing a fiber-optic system using the NIR SERS analytical technique for sensing and monitoring environmental contaminants in groundwater. We have developed the NIR SERS technique, introduced the use of semiconductor laser sources for Raman measurements, and successfully measured SER spectra over very long optical fibers without the need for background subtraction. On the basis of these achievements, we expect to be able to construct a practical, fully portable, highly selective remote sensor using NIR SERS.

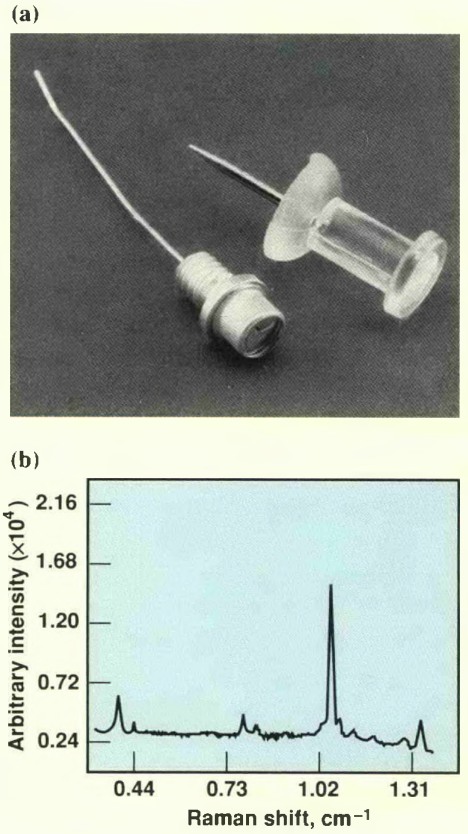

Figure 1. Raman spectroscopy with a diode laser. (a) An NIR-emitting diode laser similar to the one described in the text. (b) Spectrum of 6-m*M* tris(2,2'-bipyridine) ruthenium(II), on a silver electrode measured by NIR SERS using a 4-mW, 785-nm wavelength diode laser.

Contact: S. M. Angel (415) 423-0375.

Modeling of Atmospheric Chemistry and Toxic Gas Emissions

We are developing global and local models of gaseous emissions to help us understand complex atmospheric phenomena.

Our work on modeling gaseous emissions in the atmosphere is vital to our efforts to understand such important topics as the behavior of air-borne pollutants and the dispersal of toxic gases. We are building a three-dimensional chemistry version of our GRANTOUR model to simulate dispersal and mixing processes in the atmosphere. We are also using the FEM3 and SLAB codes to model hazardous dense-gas releases.

Effect of NO_x Emissions on Atmospheric Chemistry

We use GRANTOUR to simulate the global nitrogen oxide (NO_x) distribution, and our results help define how fossil-fuel and other anthropogenic emissions influence NO_x abundances worldwide. NO_x has multiple effects on atmospheric chemistry; it determines the abundance of ozone (O_3, a gas that contributes to the greenhouse effect), the concentration of hydroxyl (OH, a gas that helps cleanse the atmosphere of pollutants), and the deposition of nitric acid (HNO_3, a constituent of acid rain). In areas of high NO_x concentration, a photochemical reaction sequence produces O_3; in areas of low NO_x concentration, the sequence destroys O_3. NO_x can also destroy OH, thereby indirectly determining how rapidly pollutants can be removed from the atmosphere.

Fossil-fuel combustion is the main source of NO_x; other sources include soil microbial activity, lightning, biomass burning, and transport from the stratosphere. Previously, transport from the stratosphere was thought to contribute most of the NO_x found over the oceans. However, studies with GRANTOUR indicate that such transport is by far the smallest source. Our results suggest that anthropogenic sources, like the burning of fossil fuel, are the major contributors to the abundance of NO_x observed in remote areas. Conceivably, then, NO_x emissions from fossil-fuel combustion are perturbing the global abundances of O_3 and OH.

NO_x reacts in the atmosphere with OH to form HNO_3, a major constituent of acid rain. When deposited in the oceans, HNO_3 is also a nutrient for phytoplankton. Our model predicts that anthropogenic emissions of NO_x will substantially increase the supply of HNO_3 to the oceans. For example, GRANTOUR predicts that current NO_x emissions have caused HNO_3 deposition in the southern Pacific Ocean to increase by 24% over natural levels. (In the southern hemisphere, biomass burning is responsible for most of the anthropogenic NO_x emissions.) Increased HNO_3 to the oceans may be enlarging the phytoplankton population, and since phytoplankton contribute a variety of gases to the atmosphere, there may be further impacts on atmospheric chemistry.

These studies are helping us to understand the global consequences of anthropogenic NO_x emissions. We plan to use GRANTOUR to examine the atmospheric chemistry of carbon monoxide, methane, and nonmethane hydrocarbons and to investigate how these gases affect O_3 and OH concentrations. We hope that once we can predict the abundances of O_3 and OH, we can calculate how atmospheric chemistry affects global climate.

Modeling Toxic Gas Emissions

The 1984 accidental release of methyl isocyanate in Bhopal, India, which killed and injured thousands of people, forced the widespread realization that similar accidents, though improbable, could occur in the U.S. and other industrialized countries. To develop methods for predicting the consequences of an accidental release of toxic chemicals into the atmosphere, we have applied two gas-dispersion models, FEM3 and SLAB. These codes use mathematical descriptions of the physics of heavy-gas dispersion, including gravity spread, density stratification effects on turbulence mixing, ground heating, and phase-change effects from entrained aerosols.

FEM3 simulates the dispersion of a released gas by solving the time-dependent, three-dimensional conservation equations of mass, momentum, energy, and species along with the ideal gas law for the equation of state. Because it is fully three dimensional, FEM3 can treat gas flow over variable terrain and

around obstructions and can reproduce complicated cloud behavior (e.g., gravity-flow-induced vortices and channeling caused by sloping terrain). FEM3 also contains a submodel for phase change. This submodel has two versions: one for atmospheric water and the other generalized for a variety of hazardous liquids. Both versions assume that the mixture components (air in the gas phase, liquid material, and material vapor) are always in thermodynamic equilibrium.

We have used FEM3 to analyze experimental results. In one experiment, we released a large volume (66 m^3) of liquefied natural gas into a vapor fence (a containment structure 44 m by 88 m by 10 m tall) and measured the gas both in the structure and downwind. The FEM3 simulations are in excellent agreement with data taken 250 m downwind of the fence (Figure 1), confirming the ability of FEM3 to accurately simulate complex events.

Because FEM3 is more detailed than needed for many problems, we developed SLAB, a simpler, one-dimensional model. SLAB solves averaged forms of the equations for conservation of mass, species, downwind and crosswind momenta, and energy as well as the ideal-gas-law equation of state. The dispersing gas cloud is modeled as a steady-state plume, a transient puff, or the two combined when the release is of finite duration. Because it also calculates the cloud dimensions, SLAB is quasi-three-dimensional, conserving total mass, energy, species, and momentum.

SLAB can simulate the formation and evaporation of liquid droplets and can treat three types of sources: a ground-level evaporating pool, an elevated horizontal jet, and an instantaneous release. Two species are allowed to form droplets:

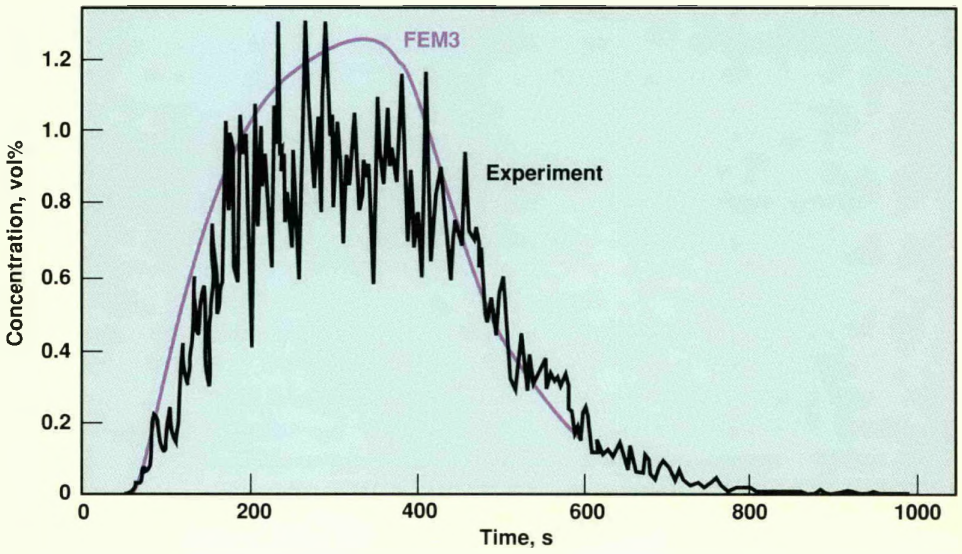

Figure 1. Comparison of FEM3 simulation with gas concentration data from a release of liquefied natural gas measured 5 m above ground and 250 m downwind of the vapor fence.

ambient water vapor that enters the cloud, and the released material. The thermodynamics of liquid droplet formation and evaporation is treated by assuming local thermodynamic equilibrium. SLAB treats the transport of the vapor-droplet mixture as a single fluid and neglects gravitational settling and ground deposition of the droplets.

SLAB and FEM3 use conservation principles to treat gravity effects. FEM3 does so by solving the three momentum-conservation equations, including the buoyancy term and variable density; SLAB solves two layer-averaged momentum equations and uses the hydrostatic approximation. Because SLAB is one-dimensional and FEM3 is three-dimensional, they handle turbulence differently. SLAB uses the somewhat artificial concept of entrainment across the cloud-air interface and does not explicitly treat turbulence within the vapor cloud. Mixing between the cloud and ambient atmosphere is assumed to occur at the interface and is governed by an entrainment velocity that depends on the local properties of the two regions. FEM3 assumes that turbulence can be described as a diffusion process and uses a continuous diffusion coefficient that depends on the local properties of the dense-gas cloud.

We are incorporating the SLAB model into the Atmospheric Release Advisory Capability (ARAC) emergency response system and the FEM3 heavy-gas physics package into the ARAC three-dimensional transport and diffusion models. With these improvements, ARAC will be able to respond to accidental toxic gas releases as well as to nuclear emergencies and will be the only system that can accurately calculate the dispersion of a dense, toxic gas plume under a range of conditions, including complex terrain with variable winds.

Contact: J. Penner (415) 422-4140 or R. Koopman (415) 422-7381.

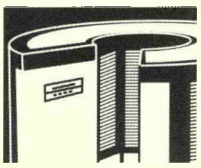

Supporting Activities

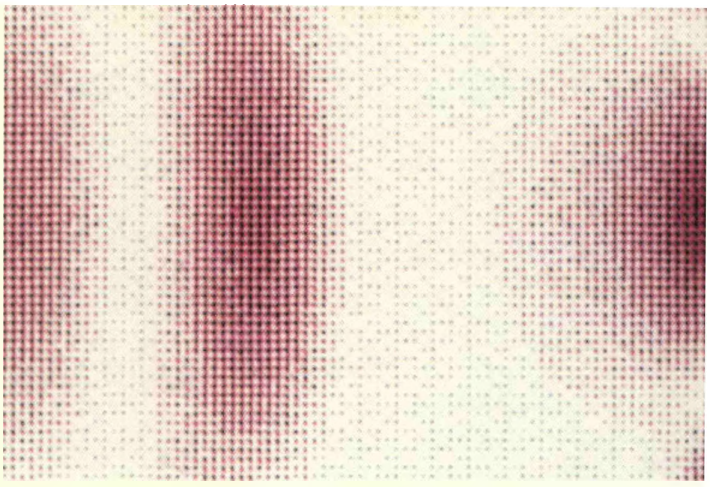

The primary function of the scientific and technical organizations at LLNL is to provide the expertise and research capabilities that can support Laboratory programs and contribute to the general base of scientific knowledge needed to fulfill Laboratory and national needs in the near and distant future. Researchers from chemistry and material science, engineering, physics, computations, and earth sciences continue to advance the state of the art in their respective disciplines. Cross-fertilization and collaboration are increasing and the boundaries among the disciplines are blurring as we apply the diverse tools, techniques, and knowledge of the appropriate fields.

The Laboratory benefits in many ways from activities within and across the disciplines. Advantages include testing the feasibility of projects before large portions of program budgets are committed, anticipating and developing advanced capabilities that will be of future program use, furthering technologies to satisfy urgent national needs, creating a stimulating environment that will continue to attract high-quality, research-oriented staff members, promoting collaboration with colleagues at universities (especially in the University of California system), laboratories, and industrial concerns, and contributing to the general base of scientific knowledge.

Our scientific and engineering activities contribute to the effective functioning of Laboratory programs. In our list of significant accomplishments this year, we include the products of selected projects in the Administration and Operations Directorate. These projects have enhanced our ability to function in a safe and secure manner while minimizing any negative impacts on the environment. They have contributed to the restoration or improvement of our surroundings and have enhanced nuclear safety on the national level.

LLNL promotes research and innovation through several institutional mechanisms. Most notable at the Laboratory-wide level is the Institutional Research and Development (IR&D) Program, which was established in 1984 to foster exploratory work in a variety of scientific fields and long-term interdisciplinary research to support our national energy and defense missions. The IR&D Program is funded at 2% of the Laboratory's operating budget; the primary criteria for supporting IR&D research are furthering innovative ideas in LLNL's areas of expertise and developing new areas of expertise in the national interest.

The IR&D Program supports three categories of research: Exploratory Research promotes pioneering work in the disciplines, the Director's Initiatives focus on a small number of larger projects selected by the Director, and the Individual Awards support promising research outside the usual programmatic channels that offers scientific excellence, potential impact, and leverage for future funding. The IR&D Program has had a far-reaching impact, as is evidenced by our references throughout this document to projects supported by IR&D funds. It cuts across the entire programmatic structure of the Laboratory and further enhances our ability to perform basic and applied research of institutional and national importance. The IR&D Program has also supported the University of California Institutes, in which we participate in the nation's academic and research establishment and collaborate with researchers from the University of California campuses and other universities nationwide.

LLNL's scientific and technological contributions in supporting roles have been outstanding this past year. Our physicists, engineers, chemists, and computer scientists have provided the science and technology, instruments,

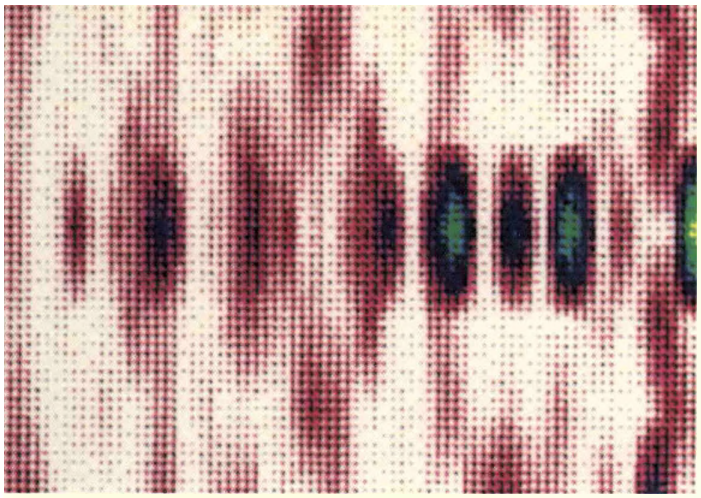

Field intensity calculated for a localized-wave-transmission (LWT) pulse; pulses with LWT characteristics may find application in remote sensing, communications, and directed-energy weapons.

facilities, and overall environment for the efforts crucial for the Laboratory's work. In this section, we review some of these accomplishments and highlight their interdisciplinary nature.

Chemistry and materials science activities at LLNL are producing results on the leading edge of the technology. Research is focusing on surface chemistry, the modeling and development of new materials and characterization techniques, and the mechanical properties and phase transitions of metals. Chemistry research complements this work with efforts to synthesize new materials, develop new analytical techniques, and investigate transport processes. Important advances have been made in studying high-temperature superconductors and developing characterization methods based on scanning tunneling microscopy and x-ray microtomography.

Engineering continues to emphasize a broad range of technologies vital to the future goals of the Laboratory, as represented by its eight thrust areas: computational electronics and electromagnetics, computational mechanics, diagnostics and microelectronics, fabrication technology, materials engineering and science, microwave and pulsed power, nondestructive evaluation, and remote sensing, imaging, and signal engineering. Important research outputs in these thrust areas include the experimental verification of localized wave transmission and the development of improved techniques and sensors for measuring straightness.

Physics research concentrates on work essential to LLNL's long-range energy and defense programs, including computational, theoretical, and experimental aspects of the entire spectrum of physics. Notable examples of results achieved in this past year are benchmark measurements with electron-beam ion traps, the development of improved x-ray calorimeters, a theoretical investigation of high-energy-density matter, and research into a novel computation approach that uses aspects of physical systems that lend themselves to efficient parallel computation.

In basic and applied earth sciences, we have made advances in geochemical modeling, rock mechanics, seismology, reservoir analysis for new resource-recovery technologies, and the containment of underground nuclear tests. The studies of seismicity and fluid flow through fractures find significant application in treaty verification work and nuclear waste containment.

Environmental protection is always a top priority at LLNL. Significant progress was made this past year in groundwater cleanup and wastewater discharge control. A gas sampler was developed to provide constant analysis of sulfur hexafluoride. Research is continuing on the evaluation of seismic safety margins for nuclear power plants.

Computations and information systems scientists are increasing the Laboratory's capabilities for high-speed, numerical scientific computing. Major accomplishments this year include providing world-class supercomputing facilities for unclassified work in the Open Computing Facility and developing and implementing a computer security monitor that can be used with any host computer system to generate an audit trail.

Safeguards and security work has led to notable hardware developments now in use at LLNL and being transferred to industry. These include the Secure Interactive Livermore Alarm System (SILAS), the Controlled Access by Individual Number, Phase II (CAIN II) system, and an improved central security console.

Contact: A. J. Poggio (415) 422-8557.

Materials Science, Technology, and Fabrication

Our work in materials science, technology, and fabrication is wide ranging and supports almost every Laboratory program.

Almost all Laboratory programs require research in some aspect of materials science. Metallurgy and knowledge about the behavior of exotic materials under extreme conditions are essential in weapon design and testing. Magnetic fusion requires research into the properties and performance of superconducting materials; laser fusion needs optical components for the x-ray and extreme-ultraviolet portion of the electromagnetic spectrum. Precision-fabricated components are required in both defense and fusion applications. The research described below illustrates the breadth and depth of our work in this discipline.

Superconducting Properties of Substituted High-T_c Oxides

Although some progress has been made in understanding the complex physics of recently discovered materials that become superconducting at relatively high transition temperatures (T_c), much work remains before their properties can be predicted with confidence. We are using a variety of experimental and theoretical techniques to study the effects of substituting various elements in extremely pure high-T_c oxides. Our goal is to elucidate the basic mechanisms of high-T_c superconductivity. (This work is supported by the IR&D Program.)

We are focusing on four systems with unusual properties:

1. $Y_{1-x}Pr_xBa_2Cu_3O_{7-\delta}$.
2. $YBa_2Cu_3O_{6.2}Br_y$.
3. $Nd_{2-x}Ce_xCuO_{4-y}$.
4. $Ba_{1-x}K_xBiO_3$.

Substituting Pr for Y in $YBa_2Cu_3O_7$ allows us to study the effects of magnetism on superconductivity, while substituting Br for O enables us to probe the role of charge transfer. In $NdCuO_4$, substituting Ce for Nd adds electrons to the system, allowing us to compare the properties of superconducting oxides in which electrons are the charge carriers with the other oxide superconductors in which the carriers are holes. In the $Ba_{1-x}K_xBiO_3$ system, we can study the properties of a high-T_c oxide that does not contain Cu.

During this past year, we collaborated with the Department of Physics at UC Davis to synthesize extremely high-quality polycrystalline samples of the four materials. Particularly important insights were obtained from studies of the upper critical field (H_{c2}), which is the value of the magnetic field that destroys superconductivity, and from Raman spectroscopy, which samples the vibrations of atoms in the lattice and is sensitive to the coupling of electrons to the lattice vibrations (a key aspect of superconductivity). On several Raman spectroscopy samples, we collaborated with Sandia National Laboratory, Livermore. Here we summarize our results for $Y_{1-x}Pr_xBa_2Cu_3O_{7-\delta}$ and $Ba_{1-x}K_{1-x}BiO_3$.

In the $Y_{1-x}Pr_xBa_2Cu_3O_{7-\delta}$ system, superconductivity is destroyed when x is greater than 0.5; this is in contrast to the other rare-earth substitutions (Nd, Sm, Eu, Gd, Dy, Ho, Er, Tm, Yb, Lu), which remain superconducting at a T_c of ~90 K. The $Y_{1-x}Pr_xBa_2Cu_3O_{7-\delta}$ system has an undesirable tendency to separate into phases consisting of $YBa_2Cu_3O_7$ at a T_c of 90 K and $Y_{1-x}Pr_xBa_2Cu_3O_{7-\delta}$ (where the value of x varies) at a lower T_c. Although such phase separation can be clearly identified in field-cooled, magnetic-flux expulsion measurements (known as the Meissner effect), it does not show up in x-ray diffraction measurements. We have overcome this problem by developing appropriate preparation techniques.

We discovered in this work that two of the Raman-active modes change significantly as a function of Pr concentration. In going from $YBa_2Cu_3O_7$ to $PrBa_2Cu_3O_7$, the ~500-cm^{-1} mode hardens (increases) by some 15 wavenumbers while the ~340-cm^{-1} mode softens (decreases) by nearly 40 wavenumbers. The ~500-cm^{-1} mode results from vibration along the c-axis of the oxygen atom bridging the Cu-O "chains" and the CuO_2 "planes," and the ~340-cm^{-1} mode results from the out-of-phase vibration along the c-axis of the oxygen atoms in the CuO_2 planes. It has been shown that the ~500-cm^{-1} mode is strongly coupled to the electronic continuum. Comparison of our results with the Raman frequencies observed for the other rare earths indicates that the dominant cause of this change is the larger size of the Pr ion relative to that of the Y ion. Most important, we observed no abrupt changes at the critical concentration $x = 0.5$.

Lattice vibrations as a function of Pr concentration are well-behaved, an observation that leaves unresolved the question of why the T_c of the

system decreases when it is doped with Pr but remains constant when it is doped with other rare earths. Our explanation is that the magnetic fields induced by Pr ions break up the electron pairs that promote superconductivity. The most convincing evidence for magnetic interaction comes from our new results for the behavior of the upper critical field H_{c2}. Figure 1 shows the temperature dependence of H_{c2} in samples of $Y_{1-x}Pr_xBa_2Cu_3O_{7-\delta}$ with various values of x. For all samples in which x is greater than 0.3, $H_{c2}(T)$ is smoothly bell-shaped and the initial slope, $(dH_{c2}/dT)_{T=Tc}$, decreases rapidly with increasing x.

In conventional superconductors, the critical field increases monotonically with decreasing temperature. It is well-established, however, that in certain cases the presence of magnetic pair-breaking interactions can impose a maximum value on the critical-field curves as a function of T. This occurs as the strength of the internal fields generated by the magnetic ions increases dramatically at lower temperatures. The critical field curves shown in Figure 1 exhibit this bell-shaped behavior for x greater than 0.3, indicating the importance of magnetic interactions in this system.

It is interesting to compare Cu-based superconducting materials (La-Cu-O, Y-Ba-Cu-O, Bi-Ca-Sr-Cu-O, Tl-Ca-Ba-Cu-O, and their derivatives) with Bi-based materials (Ba-K-Bi-O and Ba-Bi-Pb-O). While the Cu-based materials exhibit superconducting transition temperatures (T_c) approaching 125 K, the T_c of the $Ba_{1-x}K_xBiO_3$ systems is about 30 K.

We compared samples of $Ba_{1-x}K_xBiO_3$ prepared by two different synthesis techniques: a sintering process (developed in collaboration with UC Davis) that produces low-density samples, and melt processing, which produces high-density samples (we obtained ours from Argonne National Laboratory).

Figure 2 illustrates the Raman spectra obtained from high-density $Ba_{0.6}K_{0.4}BiO_3$ samples at temperatures between 295 and 4 K. Most interesting is the evolution of

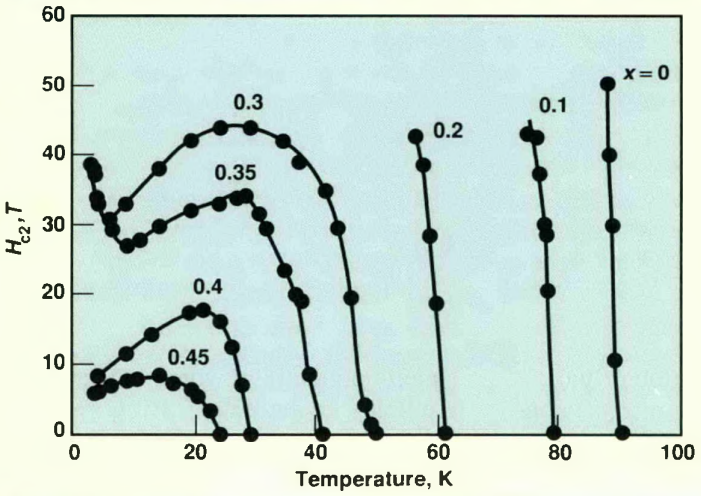

Figure 1. Measured upper critical field, H_{c2}, of $Y_{1-x}Pr_xBa_2Cu_3O_{7-\delta}$ as a function of temperature for various values of x.

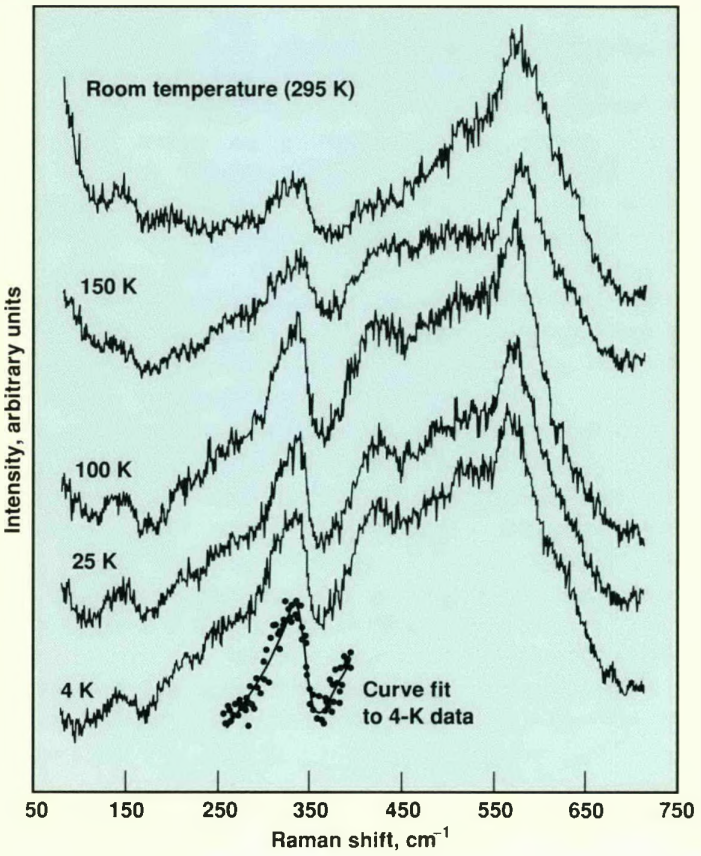

Figure 2. Observed Raman spectra of superconducting high-density $Ba_{0.6}K_{0.4}BiO_3$ samples (T_c = 24 K) between room temperature and 4 K. (The absolute scaling of all spectra is the same; they have been linearly offset here for clarity.) The partial spectrum (small, smooth curve at the bottom), the least-squares fit to the Fano line shape, is compared with data points from the 4-K experiment.

the peak centered around 325 cm^{-1} as temperature drops. When the sample is cooled below room temperature, the peak develops the distinctive Fano line shape; that is, the peak is highly asymmetric, with the intensity dropping off sharply on the high-frequency side. On the high-frequency side, the peak penetrates below the background, which increases in intensity roughly linearly with increasing Raman shift. The Fano line shape occurs when scattering from an electronic continuum interferes with scattering from a discrete phonon (quantized lattice vibration). Observation of a Fano line shape is convincing evidence for strong coupling between the phonon and electronic states. The frequency of the Raman peak at 348 cm^{-1} (43 MeV) that exhibits the distinctive Fano line shape as a result of electron-phonon coupling is similar to that of the O vibration in YBa_2Cu_3O at about 340 cm^{-1}, discussed above, which also exhibits electron-phonon coupling.

To summarize, we have developed techniques for making extremely high-quality polycrystalline samples that allow us to study the roles of magnetism, charge transfer, electrons vs holes, and electron-phonon coupling in the high-T_c superconductors. We have also demonstrated that in the absence of large, single crystals, extremely phase-pure polycrystalline materials can still provide critically important answers in our quest to understand these fascinating oxide superconductors.

Chemical X-Ray Microscopy

The x-ray microscope goes beyond the limits of the optical microscope while avoiding the chief disadvantages of the electron microscope. With our three-dimensional chemical x-ray microscope, we can examine materials in three dimensions in their unaltered state. The process requires a source of parallel x rays (synchrotron radiation) and utilitzes a sample stage, a detector system, and an analyzing computer. In operation, a double-crystal monochromator selects x rays in a narrow energy range from the primary synchrotron beam. The x rays pass through the sample, through a second, magnifying x-ray optic, and then to a converter (scintillator) where they are converted to visible light. The visible light image is magnified and recorded on a low-noise, two-dimensional charge-coupled-device (CCD) detector. The sample is rotated by a small angle, and another two-dimensional absorption image is collected. This process continues until a full 180 deg of sample rotation has been recorded and stored in a computer. Tomographic software converts x-ray absorption profile data into two-dimensional reconstructions of the density distribution in the sample interior. These in turn are rendered into a three-dimensional view using rendering software and high-speed digital image-processing computers.[1]

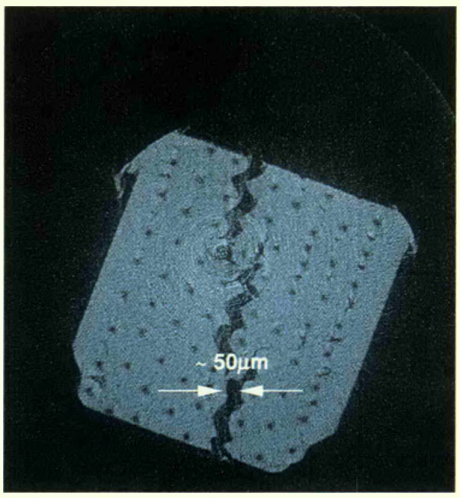

Figure 3. A three-dimensional chemical x-ray microscope image of an aluminum/silicon carbide composite showing a crack running across the sample parallel to the fiber ply. The crack in this image is approximately 50–60 μm wide. Smaller (5-μm) cracks can be seen nucleating at the ceramic-metal interfaces. This figure is a single cross section showing only one of several contiguous slices taken in parallel using our x-ray microscope.

There are similarities between the three-dimensional x-ray microscope and the CT (computed tomography) scanners used in medical and engineering studies. The difference is in the resolution and the chemical and phase sensitivity. Resolution is perhaps 1 mm in conventional computed tomography and 0.1 mm in microtomography. With our technique, we can reach a resolution of 5 μm, which will improve further with the next generation of x-ray optics and synchrotron storage rings.

In addition, if we want elemental or phase-mapping details, we can obtain excellent chemical contrast by subtracting two images recorded at two x-ray wavelengths (usually above and below a characteristic absorption edge). This elemental selectivity is why we call our instrument a chemical microscope. (Conventional CT technology uses a polychromatic beam from conventional tube sources and a single set of exposures, which precludes the possibility of performing quantitative chemical analysis.)

We have applied three-dimensional x-ray microscopy to the study of chemical composition and microstructure in a variety of

materials, including catalysts and ceramic composites. One fruitful area of investigation is the characterization of fiber-composite materials, where random or aligned fibers have been introduced into a material to increase strength. The use of composite materials for primary structural applications requires adequate design margins and lifetimes under all anticipated loading conditions and environments.

It is extremely difficult to isolate fundamental failure mechanisms in composites from the confusion of information created by incidental specimen-to-specimen variations. Present methods used for characterizing damage in composites rely on destructive analysis and cannot readily ascertain the order in which the observed features developed. Serial sectioning, for example, is destructive, extremely costly, and inefficient. Furthermore, in the case of metal-matrix composites, surface relief during polishing tends to obscure any interfacial cracks that might be present in the sample.

A composite material in which a crack had been introduced was recently imaged at the Stanford Synchrotron Radiation Laboratory 31-pole wiggler beamline. In this study, a 1.5 × 1.5 × 10-mm specimen of an Al/SiC composite was examined. An x-ray energy of 21 keV was selected for good sample transparency and x-ray contrast between SiC and Al. Figure 3 shows a single cross-sectional slice of the composite from a larger set of contiguous cross sections obtained with the x-ray microscope. The slice thickness is 2.8 μm and the spatial resolution is 8 μm. Data were collected at 1-deg intervals. This undersampling leads to some loss in image quality; nevertheless, the 33-μm-diam graphite cores and surrounding 140-μm-diam SiC sheaths are clearly visible.

A crack can be seen running across the sample. This crack, (approximately 50–60 μm wide in this slice) does not penetrate the SiC fibers. Instead, the crack propagates by deflecting around the fibers and remains confined within the aluminum matrix. It is interesting that the crack is not continuous across the sample. Instead, the crack moves across the parallel fiber ply, thereby relieving stress at the ceramic-metal interface.

Although similar information can be obtained by serial sectioning, it must be emphasized that these x-ray images have been taken of unaltered interior surface. Because of this, direct observation of crack nucleation and growth is possible throughout bulk specimens during deformation testing. The availability of such data should have a profound effect on modeling the damage accumulation in metal-matrix composites and other advanced materials.

We have redesigned the chemical x-ray microscope to operate in an ultrahigh-vacuum environment, making possible studies in the soft-x-ray region (500–1500 eV). This energy range is essential for many interesting studies in biological materials, which weakly absorb higher x-ray energies. We are also designing *in situ* reaction chambers to examine samples in reactive and hostile environments. We should then be able to study materials processing and failure in real time.

Multilayer Structures for X Rays

Multilayer structures of sufficient quality for optical applications in the x-ray, soft-x-ray, and extreme-ultraviolet (EUV) ranges, where wavelengths are 10 to 10,000 times shorter, have been fabricated only during the past decade. Simple reflective diffraction gratings were developed in the early 1900s and are now a standard dispersive element used in moderate- to high-resolution optics. The in-plane scale of

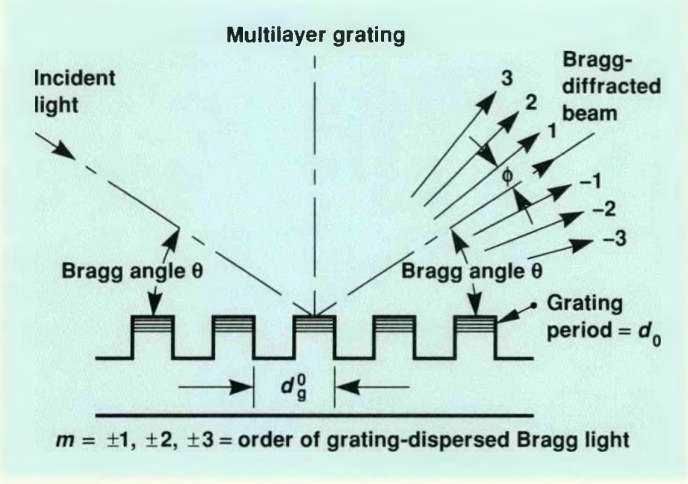

Figure 4. Cross section of a multilayer diffraction grating. Flat-topped grating bars have a width $d_g^0/2$ and a period d_g^0. Multilayers with a geometric period d_0 are deposited onto these bars. Light is incident from the left at a grazing angle θ, typically called the Bragg angle. Diffracted beams are shown on the right.

diffraction gratings ranges from 300 to 5000 nm; in contrast, the in-depth microstructural scale typical of multilayers is 1–40 nm. Our challenge was to design advanced reflective optical elements that focus, disperse, and otherwise manipulate short-wavelength light.

We have used IR&D Program support to prepare multilayer diffraction gratings by multisource magnetron-sputter deposition onto 2000-nm-period laminar amplitude grating substrates. The grating structures were anisotropically etched in (110) single-crystal silicon patterned using standard microlithography techniques. We fabricated multilayers of tungsten/carbon, rhodium/carbon, molybdenum/silicon, and 304 stainless-steel/silicon, with periods of 2.5 to 20 nm, onto these diffraction-grating substrates and characterized them at the Stanford Synchrotron Radiation Laboratory.

Figure 4 is a schematic cross section of a multilayer grating. The grating consists of flat-topped bars with width $d_g^0/2$ and period d_g^0. We deposit multilayers with a geometric period d_0 onto these bars. Light is incident from the left at a grazing angle θ, called the Bragg angle, and is diffracted in a specular manner by the multilayer at an exit angle θ relative to the multilayer in the zero grating order ($m = 0$). Interference of light diffracted by the multilayers on each grating bar results in intensity maxima at angles $m\phi$ relative to the zero order, where $m = \pm 1, 2, 3, \ldots$.

The convolution of diffractive properties of the two periodic structures results in a relation between the grating-order dispersion angles $m\phi$ and the geometric parameters of the multilayer and grating structures. The resulting analytical relation is

$$\sin m\phi = \frac{2md}{nd_g^0},$$

where m is the grating order, d is the refraction-corrected multilayer period, and n is the Bragg order of the multilayer-diffracted light.

Several unique characteristics of multilayer diffraction gratings are apparent from this result. First, the dispersion angle ϕ is constant because it is independent of the angle of incidence θ or the wavelength of light that is Bragg-diffracted by the multilayer. Second, the multilayer grating separates Bragg orders of the multilayer-diffracted light because the dispersion angle ϕ is inversely proportional to n. Third, because angle ϕ is independent of wavelength, the gratings are constant-resolution dispersion elements for a given geometry. Fourth, the specificity of the relations among ϕ, d, and d_g^0 results in design criteria for more complex structures including laminar, blaze, and echelle gratings. Gratings meeting these criteria will, in general, produce Bragg-reflected light that constructively interferes over broad angular and wavelength ranges (being always "on blaze" or "on phase"), greatly extending the range and use of such optical elements. This property makes possible efficient, very-high-resolution dispersion elements in the soft-x-ray and EUV ranges.

We have used a multilayer grating as the second element in a two-parallel-element monochromator to measure the carbon K-absorption edge at 283 eV. The multilayer contained no carbon, was synthesized from 304 stainless steel and silicon, and had a period of 5.5 nm. The period of the grating substrate was

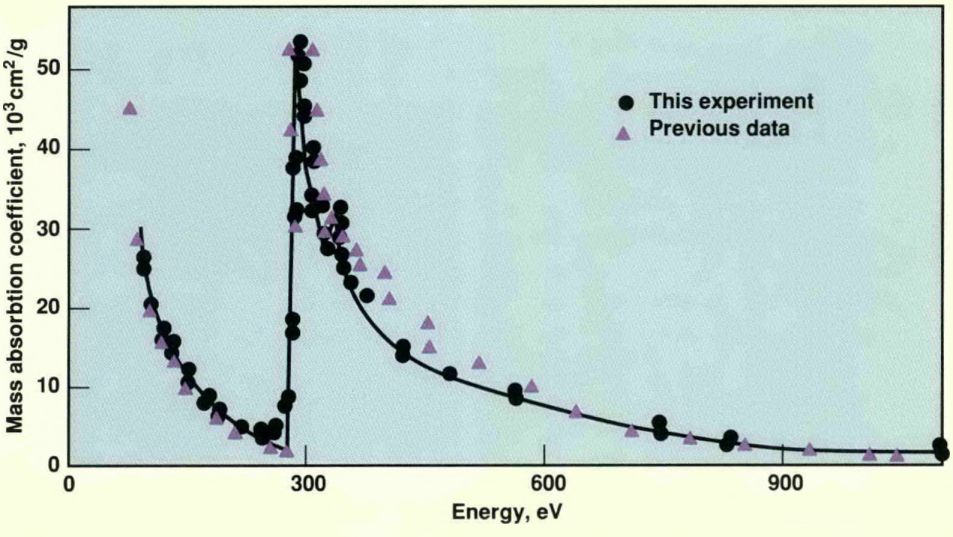

Figure 5. Mass absorption coefficient of carbon measured via a multilayer grating (d_g^0 = 2000 nm) as the second element in a two-parallel-crystal monochromator for energies of 95–1100 eV. The experimentally observed structure at approximately 330 eV probably signifies the presence of small microcrystalline regions in the carbon foil. These are the first measurements obtained with a multilayer/multilayer grating in a simple, two-parallel-crystal monochromator.

2000 nm. We used a 236-nm-thick carbon foil for our transmission measurements. Figure 5 shows our measured mass absorption coefficient for energies of 95–1100 eV compared with previous data from the literature. The agreement is good; however, our experiment reveals structure at approximately 330 eV that is not seen in the previous data. This structure is at the same energy as that observed in crystalline graphite and is believed to signify the presence of small microcrystalline regions in carbon foil. These are the first measurements obtained with a multilayer/multilayer grating in a simple, two-parallel-crystal monochromator. Our data demonstrate the unique capabilities of such advanced optics.

Studies of Premartensitic Behavior in Nickel–Aluminum

Structural phase transformations are of great interest to materials technologists because they are a remarkably effective means to control structure-sensitive properties of metallic alloys and ceramics. We understand diffusional transformations, where material "moves" (where atoms rearrange on sites throughout the crystal lattice), but not diffusionless displacive transformation behavior (where a material undergoes cooperative atomic shifts without lattice site interchange). We must gain an understanding of displacive transformations in order to expand our capabilities for designing materials with optimum properties.

The most common of these displacive structural changes are the martensitic shear transformations that occur in steels and a wide variety of other metallic alloys and ceramics. It is now well established that the crystalline phases that undergo first-order martensitic transformations upon cooling show unusual changes as they approach their transformation temperature *Ms*. We are examining these precursory effects within the parent phases for the light they shed on the crystal symmetry-lowering transformation process itself. Prominent among these effects are tweed-like striations in transmission electron microscopy (TEM) images; these striations are derived from local lattice distortions that develop well above the transformation temperature and become more pronounced with cooling. In addition, there is an anomalous anisotropic "softening" of the parent lattice; that is, certain elastic constants and lattice vibrational modes are unusually low and decrease further with falling temperature.

(a)

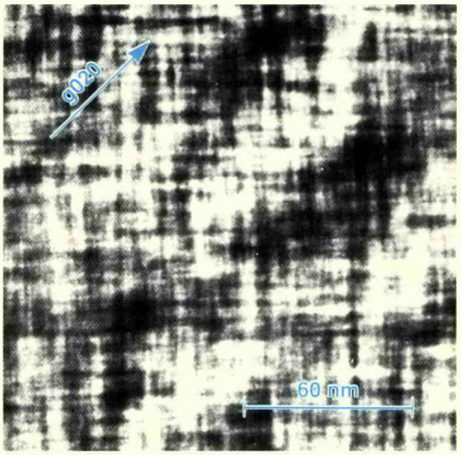

(b)

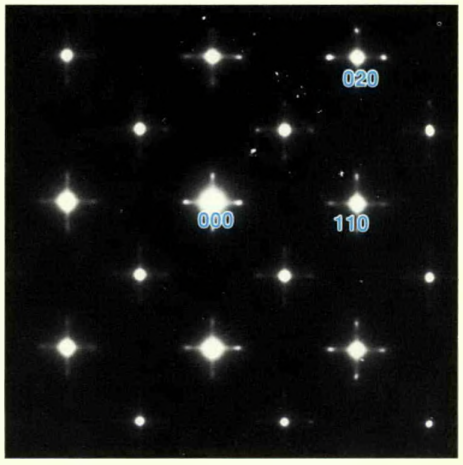

Figure 6. Images of premartensitic nickel–aluminum alloy: (a) CTEM image, and (b) electron diffraction pattern.

We have been studying the metallic alloys Ni_xAl_{100-x} ($50 < x < 65$), some of which display such premartensitic effects rather prominently. We examine samples from high-purity single crystals using conventional contrast TEM (CTEM), high-resolution TEM (HREM), and electron diffraction in conjunction with elastic and inelastic neutron scattering to reveal microstructural evolution and lattice dynamical variations over a range of temperatures down to *Ms*, which is usually below room temperature. The CTEM images display the quasi-periodic tweed strain contrast (Figure 6a); electron diffraction reveals a related diffuse scattering, both streaks and satellites, in the vicinity of parent-phase Bragg reflections (Figure 6b). Contrast amplitude increases and striations become more sharply defined as *Ms* is approached. The diffuse scattering intensities also increase.

Using HREM, we can see the distorted atomic configurations that underlie the tweed contrast. The microstructure is a fine-scale mosaic assembly of variously distorted and modulated domains of fractional nanometer-scale atomic displacements (Figure 7a). Images of the unstrained lattice of this ordered cubic parent phase must be calculated (since the unstrained lattice cannot be retained from elevated temperatures; see Figure 7c). With proper choice of imaging conditions for the crystal orientation of interest, we simulate a

square pattern of repeating white dots that is directly related to the projected columns of atoms of either all-nickel or the mixed nickel–aluminum sublattices of this body-centered structure (see Figure 7c).

Comparison of the observed and ideal unstrained patterns provides insight into the local atomic movements. Within the contiguous domains of 4–6 nm extent, we find a micromodulated substructure. Each three-dimensional domain should contain one of six possible variations of the micromodulation, where only two, roughly parallel to the traces of (110) and ($1\bar{1}0$) lattice planes, would be visible in this (001) viewing plane. The modulation involves 6–7 lattice planes with a wavelength of approximately 1.3 nm and is derived from a sinusoidal displacement wave ("shuffle") superimposed on a homogeneous lattice shear of the form $\{110\}\langle 1\bar{1}0\rangle$, as shown schematically in Figure 7d. Simulation of this distortional pattern can also be made (Figure 7b) and it is in quite good agreement with our observed images.

We used elastic neutron scattering to investigate the functional characteristics of this quasi-static microstructural assembly, and inelastic scattering to probe the lattice vibrational or phonon spectra associated with its development. The latter reveals remarkably anomalous behavior for the $\Sigma_4[\zeta\zeta 0]$ transverse acoustic mode corresponding to displacements of $\{110\}\langle 1\bar{1}0\rangle$-type mentioned above. The entire phonon branch is of extremely low energy and exhibits an unusual dip in frequency at $\zeta \cong 0.16$, which deepens further with cooling as *Ms* is approached. The position $\zeta \cong 0.16$ along the ‹110› direction in reciprocal space corresponds to the location of the diffuse satellites we observe in the diffraction patterns. Satellites flanking Bragg reflections are the signature of a structural modulation and, indeed, their distance from the Bragg peaks is inversely proportional to the micromodulation wavelength in the real space HREM images.

Nucleation and growth of the martensitic product phase is a singular event at *Ms* that interrupts the quasi-continuous process just described. Nucleus formation invariably occurs at heterogeneous sites of stress intensification (e.g., structural interfaces, dislocation tangles) where the stress induces local stabilization of a precursor domain or "embryo." In the nickel–aluminum alloy phase, we find that the amplitudes of the $\{110\}\langle 1\bar{1}0\rangle$ shears and shuffles are increased, forming a distorted orthorhombic martensite nucleus of 7-lattice plane, 1.4-nm periodicity that develops directly from the 1.3-nm micromodulation of an embryonic domain.

With these experimental observations, we have established for the first time a direct relationship between the evolution of the premartensitic microstructure and the anomalous lattice dynamical behavior of the parent phase. Furthermore, we have shown that martensite nucleation is a localized stress-assisted process within this premartensitically modulated lattice. We are now developing theoretical models, based on these unique observations, of the mechanism for martensitic transformation.

Micromechanics of Fiber Composites

Fiber-composite materials are undergoing a rapid expansion in usage because of the extraordinary

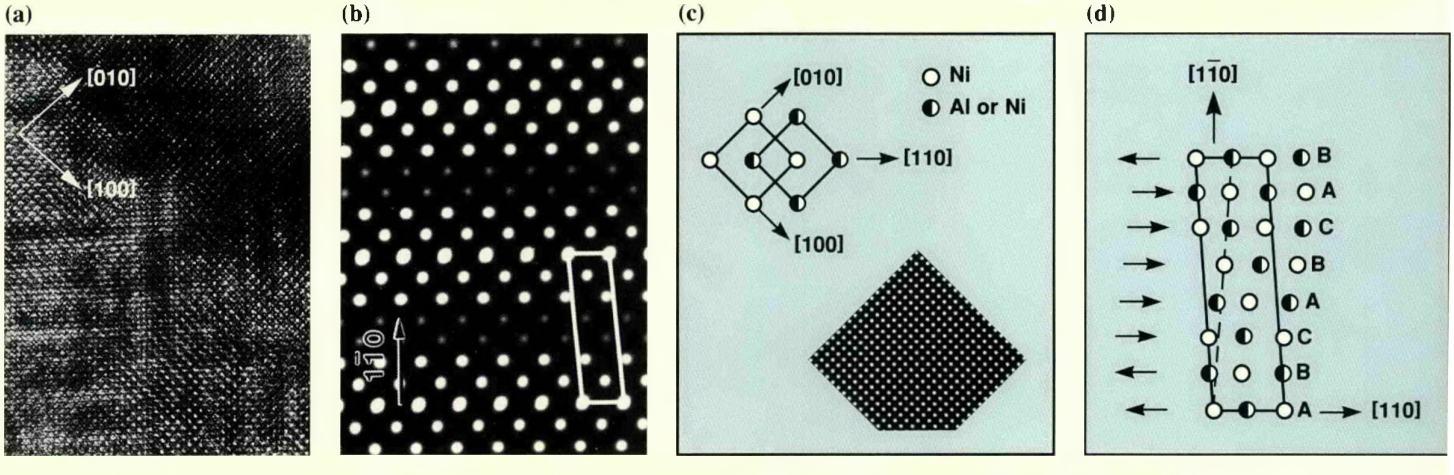

Figure 7. Images of premartensitic nickel-aluminum alloy: (a) HREM image, (b) computed strained pattern, (c) relation of the sublattices an computed unstrained pattern, and (d) model of the premartensitic micromodulation.

properties they offer. For example, the usable strength of composites of Toray T1000 and Hitex 46-9A graphite fibers is in the neighborhood of 1.38 GPa, while bare filaments have tensile strengths of 6.9 GPa. Compare this with a high-performance aluminum (ALCAN 8090), which has an ultimate strength of about 0.517 GPa. Almost all high-technology applications place a premium on light weight. Dividing these strengths by the respective densities gives the specific composite strength as 0.86 Mm^2/s^2 vs the specific strength of the high-performance aluminum as 0.19 Mm^2/s^2. Other properties, such as specific modulus, show a similar advantage for composites. Comparisons with other materials besides aluminum are even more favorable to composites.

High-performance fibers for composite reinforcement are produced from all of the general classes of materials—metals, ceramics, glasses, and organics. Despite this diversity of materials, virtually all fibers are fabricated with a filament diameter of only 10 μm, about one-tenth the diameter of human hair. For most materials, these tiny dimensions are required to achieve the excellent mechanical properties required for composite applications.

Fiber selection is usually based on both performance and cost factors. Metal fibers are rarely used (too heavy). For high-temperature (>1000°C) applications, fibers based on ceramics, such as silicon carbide, are invariably selected. Even glass, which is normally considered a weak and brittle material, can be fabricated at a relatively low cost into high-strength fibers. Organic fibers exhibiting tensile strengths greater than that of steel have been produced from both exotic liquid-crystalline polymers and more common plastics, such as polyethylene. By far, the fibers of choice for high-technology applications in the defense and aerospace industries are those based on graphite. More than 100 types of graphite fibers are now available, constituting a class of materials exhibiting some of the highest tensile strengths (~7 GPa) and highest tensile moduli (900 GPa) ever measured for any structural material.

Composites are almost always used with a polymeric binder phase. If modern fibers in a polymeric matrix phase offer such desirable properties, would not the same fibers in a metallic or ceramic matrix phase be even better? This is an active area of research, but the general answer appears to be no; polymer composites offer the better performance, except at temperatures above 300-400°C. The reasons for this are not completely understood, but they relate to the very complex microscale state of the interaction of the individual filament with its surrounding matrix and the different types of failure modes that are possible on this scale. A relatively compliant polymeric matrix phase provides a more harmonious balance of properties with those of the high-strength, high-stiffness fibers than do other candidate matrix materials. This observation introduces the area of research described here, namely the micromechanics of composite failure.

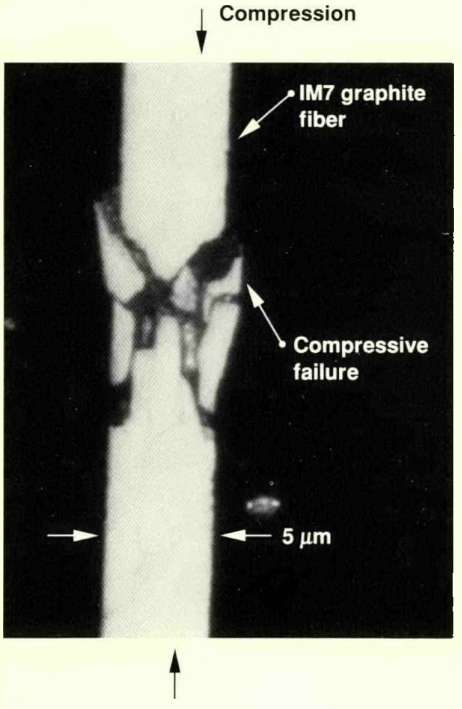

Figure 8. Axial compressive failure in a single Magnamite IM7 graphite fiber.

Aligned fiber-matrix systems at the level of a lamina within a laminate have macroscopic properties characterized by a state of transversely isotropic symmetry, which corresponds to the hexagonal symmetry of crystallography. These laminates have five independent elastic properties, the moduli, whereas a completely isotropic material has two. Our research program on micromechanics has concentrated on the microscale fiber-matrix interactions that contribute to the five macroscopic behavior properties. There are rigorous micromechanics analyses that predict the macroscopic stiffness properties in terms of the properties of the individual fiber and matrix phases themselves. The solutions for the five properties are quite complex, except for the simplest one that we give here to illustrate a fundamental effect. The axial or longitudinal shear modulus μ_L is that in the direction of the

aligned fibers. The micromechanics solution for this property is

$$\mu_L = \mu_m \left[\frac{\mu_f(1+c) + \mu_m(1-c)}{\mu_f(1-c) + \mu_m(1+c)} \right],$$

where μ_f and μ_m are respectively the fiber and matrix shear moduli and c is the volume fraction of the fiber phase. Notice two limiting cases from this expression. As the matrix modulus vanishes ($\mu_m \to 0$), the composite modulus also vanishes ($\mu_L \to 0$). But as the fiber modulus becomes unbounded ($\mu_f \to \infty$), the composite modulus remains bounded, $\mu_L \to [(1+c)/(1-c)]\,\mu_m$. This composite behavior is obviously that of a matrix-dominated property. Of the five micromechanics properties, two are fiber-dominated and three are matrix-dominated. This provides the key to a new methodology.

We are able to derive the stress-strain constitutive relation

$$\sigma_{ij} = \lambda \epsilon_{kk} \delta_{ij} + 2\mu\epsilon_{ij} + (E_{11} - E)\,\delta_{1i}\delta_{1j}\epsilon_{11},$$

where E_{11} is one of the fiber-dominated properties, with axis 1 in the fiber direction. Properties λ, μ, and E are determined both by the other fiber-dominated property and the matrix-dominated properties but most strongly by the matrix properties. This constitutive form provides the bridge to the derivation of the corresponding failure criteria, which forms are essential to all applications of composite materials.

The last term in the constitutive form represents the direct fiber contribution, while the other two terms are effectively matrix-dominated effects. The resulting failure criterion for the composite material retains the micromechanics-induced distinction between fiber- and matrix-dominated effects. In fact, the criterion degenerates into two criteria, one for fiber failure and one for matrix failure, i.e.,

$$\epsilon_f^{(-)} \le \epsilon_{11} \le \epsilon_f^{(+)} \text{ (fiber failure),}$$

and

$$\alpha\epsilon_{kk} + e_{ij}e_{ij} \le k^2 \text{ (matrix failure).}$$

The failure criteria are accessed with only the four failure parameters shown.

We compared our model description with experimental failure data for fiber failure and matrix failure conditions. The agreement is very satisfactory. However, from a materials perspective, it would be desirable to go one step further in our predictive capability toward bridging the gap between constituent (fiber and matrix) properties and composite properties. Predicting ultimate strengths of composite structures based on fiber and matrix properties is presently beyond our reach.

We are studying failure at the level of single fibers, to further our understanding of the relation between micromechanics and macromechanics. In one approach, we are determining the properties of fibers that most strongly influence the ultimate strains for fiber-dominated composite failure. When a composite is stretched in the fiber direction, it fails when the fiber's tensile strength is exceeded. Failure by compression of the composite in the fiber direction is a much more complex process involving several failure modes, including fiber-matrix debonding, fiber microbuckling, and fiber compressive failure. Clearly, the optimum composite compressive strength is achieved when fibers fail in compression rather than buckle or debond from the matrix.

To determine the inherent compressive strength of graphite fibers and thereby set the limit of compressive performance of a composite, we have recently developed a technique for monitoring compression of a single filament. We bond a single graphite fiber to the surface of a polymer compression specimen, and use the fiber as a resistance strain gage. We can measure fiber compression up to failure. Fiber failure strains and failure morphologies vary among the different types of graphite fibers; an example of compressive failure in a high-strength fiber is shown in Figure 8.

We are studying the initiation of compressive failure in experiments on composites with many fibers. We are looking at fiber-fiber interaction and such imperfections as voids and fiber waviness. Our preliminary results show that graphite fiber compressive failure does not occur in real composites and that imperfections and matrix properties play major roles in determining composite compressive strength.

Optics Polishing with *in situ* Metrology

Traditional processes for manufacturing high-quality optical components (e.g., mirrors) require many iterations of polishing and measuring to produce the final surface finish and geometrical figure (i.e., shape or contour). In most cases, the part is polished on one machine, taken off and mounted on a measuring machine, and then remounted on the first machine for

more polishing. The number of iterations and time required depends on material removal rates, which are uncertain, but increases as the accuracy specification for the optical surface become more stringent. Using traditional methods, nearly a hundred iterations may be required to fabricate optics for use at extreme ultraviolet wavelengths.

We have assembled a single machine on which we can both polish grazing-incidence optics and perform metrology. With this new machine, we can identify, define, and implement changes needed in the polishing process to obtain the desired surface quality and figure convergence without transferring the part from one machine to another and back again. Figure 9 shows the machine and its computer-control system. The basic machine is a Moore No. 3 Universal Measuring Machine with an air-bearing spindle for rotating the part, a linear stroking mechanism for mounting the polishing head, and instrumentation for *in situ* measuring of surface finish and figure. The metrology instrumentation currently consists of a Wyko profilometer for measuring surface finish and an interferometric stylus-type transducer for measuring figure. A personal-computer-based system handles data collection and coordinates the positioning of the axes for stroking and spindle rotation as well as the positioning of the measuring instruments.

During polishing, the spindle rotates at a fixed angular speed, and stroking occurs at a specified frequency. The number of strokes per revolution of the spindle is varied to avoid unwanted waviness on the part. After several hours of polishing, the metrology instruments are positioned, and finish and figure are measured.

Figure 9. LLNL's new computer-controlled optics-polishing machine with *in situ* metrology. With this single-machine system, we have eliminated the customary need to move and refixture the part for discrete polishing and measuring operations, thus decreasing the fabrication time and reducing the risk of damaging the workpiece.

The first parts polished using this machine were two telescope mirrors for the Extreme Ultraviolet Explorer (EUVE) experiment of the University of California, Berkeley, Space Astrophysics Group (UCB-SAG). The primary mirror was an interior-surface paraboloid, and the secondary mirror was an exterior-surface hyperboloid.

The aluminum mirror substrates had been accurately machined on one of LLNL's diamond-turning machines and then plated with a layer (about 13 μm thick) of electroless nickel. Our goal was to polish these mirrors to improve their surface finish without distorting their accurate shape. The *in situ* metrology alerted us to any changes in figure so that corrections could be made to the polishing process.

The EUVE Scanner mirrors were delivered to UCB-SAG with a surface roughness of approximately 1.1 nm rms and a half-energy width in the visible (a measure of how well light is focused) of 13 arcsec. These values are well within the mirrors' design specifications. With these mirrors, we clearly demonstrated the utility of a polishing machine with *in situ* metrology.

Reference

1. The three-dimensional chemical x-ray microscope won an *R&D 100* award in 1988. We shared the award with Sandia National Laboratory, Livermore, and Dortmund University, West Germany.

Contact: H. B. Radousky (415) 422-4478 (superconductors), J. H. Kinney (415) 422-6669 (chemical x-ray microscopy), T. W. Barbee, Jr. (415) 423-7796 (multilayers), L. E. Tanner (415) 423-2653 (premartensitic behavior in Ni–Al), R. M. Christensen (415) 422-7136 (fiber-composite micromechanics), or T. T. Saito (415) 422-1553 (in situ metrology).

Experimental Facilities, Devices, and Techniques

The advanced experimental facilities, devices, and techniques discussed in this article enable us to obtain otherwise unobtainable measurements of important phenomena.

The Laboratory is a world leader in the design, development, and use of advanced experimental facilities, devices, and techniques. The four examples presented here—the Electron Beam Ion Trap, Accelerator Mass Spectrometry, x-ray calorimeters, and a free-electron laser alignment technique—make it possible for us to obtain accurate measurements that are unobtainable by any other means.

EBIT Experiments on Highly Charged Ions

During the past year, with funding from the IR&D Program, we have used the Labotatory's Electron Beam Ion Trap (EBIT) to make important measurements on highly charged ions. These measurements have provided benchmark data in three areas: precise wavelengths, electron-ion collision cross sections, and excitation mechanisms for x-ray line emission. The experiments have demonstrated EBIT's ability to produce ionization states that, until now, have been inaccessible. We are using the results to test sophisticated calculations of atomic structure and reactions. Here we focus on our measurements of x-ray line emission.

EBIT works by trapping ions in an extremely narrow, intense electron beam with an energy up to about 30 keV, a radius of about 35 μm, and a current density of as much as 4000 A/cm^2. Once the ions are trapped, the electron beam strips them of electrons and interacts with the ions to produce the x rays we observe. Because the spread of electron energies in the beam is very small, we can tune the beam's energy to generate very pure ionization states and thus selectively excite different processes. This technique enables us to make measurements with EBIT that cannot be done anywhere else.

X-Ray Excitation Mechanisms

The intensity ratios of x-ray line emission from highly charged ions are often used to infer the properties of the medium containing the ions. This is the method used to determine quantities such as electron density or electron temperature in astrophysical and laser-produced plasmas. However, the interpretation of x-ray line emission is often model-dependent, and uncertainties in the atomic models translate into uncertainties in the inferred quantities. A better understanding of the mechanisms of x-ray line emission would help narrow some of these uncertainties. One approach to this problem is to identify the contributions of various mechanisms to the observed spectra.

One emission mechanism is electron cascades from higher energy levels. To study the effect of such cascades on x-ray line intensities, we have begun to investigate the intensity ratios of the x-ray line emission from neon-like barium (Ba^{46+}) as a function of electron beam energy and to compare the results with the predictions of a collisional-radiative model. Figure 1 shows the measured and predicted ratios of the intensity of the $(2p_{1/2}–3s_{1/2})_1$ transition to the intensity of the $(2p_{3/2}–3d_{5/2})_1$ transition in Ba^{46+} at various beam energies. The predicted line ratios are from a collisional-radiative model that includes collisions and radiative decays involving levels of the type $2\ell\, n\ell'$.

We used three variants of the model with different numbers of electron energy levels: 37, 89, and 157. The results indicate that the predicted line ratio grows significantly as the number of levels in the calculation increases. The predictions agree much better with the data if the calculations include either all 89 levels with excited electrons in the $n = 3, 4$ shells or all 157 levels with excited electrons in the $n = 3, 4, 5$ shells. Comparison of calculations and data shows that cascade feeding from high-n levels is a significant population mechanism

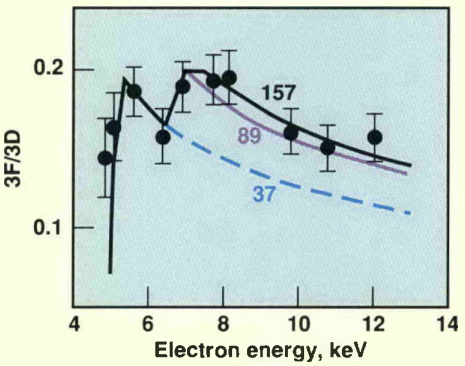

Figure 1. Ratio of intensity of the $(2p_{1/2}–3s_{1/2})_1$ transition to that of the $(2p_{3/2}–3d_{5/2})_1$ transition (abbreviated 3F3D in the figure) in (Ba^{46+}). Data points are from EBIT experiments; the lines represent predictions of three models with different numbers of electron levels.

for neon-like ions and cannot be ignored in theoretical models.

We are studying excitation mechanisms in hydrogen-like and helium-like systems. Figure 2 shows a typical x-ray spectrum of the $n = 2–1$ transition in helium-like iron (Fe^{24+}). We will use a series of such spectra, obtained at various electron energies, to reduce model-dependent uncertainties. X-ray lines from Fe^{24+} are particularly important to understand because they are observed in the x-ray spectra of solar flares.

Future Work

EBIT produces ionization states with purities that exceed those observed in the most advanced tokamaks (toroidal magnetic-fusion machines). To meet the growing demand for research time on EBIT, we are building a second machine. Among improvements implemented in EBIT II are a more energetic, 50-keV electron beam and faster switching of beam energy. Together with the original EBIT, we will use it to extend our measurements to higher charged states and to more chemical elements. We are also building an extraction system that will enable us to remove and analyze all the ions from EBIT.

We have started the design of a new machine, called SuperEBIT, that will generate an electron beam with an energy as high as 250 keV. SuperEBIT will be able to produce completely ionized uranium (U^{92+}) and to trap the ions for hours. These capabilities will inaugurate a new regime of possible experiments. For example, the nuclei of certain isotopes that are stable in their natural, neutral forms can undergo beta decay when their atomic electrons are stripped. The ejected beta particle (electron) is captured in a bound atomic state. This process, known as orbital-insertion beta decay, has never before been observed; we believe we can produce evidence for the decay of dysprosium-163 to holmium-163 by trapping dysprosium ions for as few as four hours.

Accelerator Mass Spectrometry

LLNL's new Accelerator Mass Spectrometry (AMS) facility started operation last year; the AMS facility receives funds from the IR&D Program. AMS can measure extremely low concentrations of an isotope in the presence of large amounts of another, providing an improvement in sensitivity of 10^6 to 10^9 over current mass-spectrometric techniques. Research planned for the AMS facility includes studies in archaeology, geology, biomedical and clinical science, climatology and oceanography, and arms-control technologies. A portion of the construction funding for the AMS facility was provided by the Regents of the University of California (UC), and much of the research will be done collaboratively with UC staff.

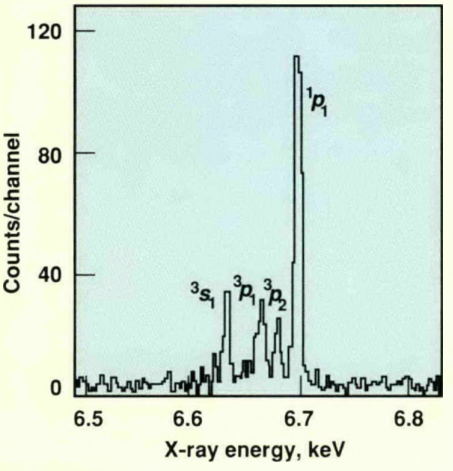

Figure 2. Measurements of transition line ratios in helium-like iron excited in EBIT are used to understand x-ray spectra of solar flares.

The ability to detect rare isotopes at extremely low concentrations promises to become a useful tool in many fields of science. When invented 12 years ago, AMS was first applied to radiocarbon dating of archaelogical artifacts. Subsequent applications have dated deep ocean waters by measuring their carbon-14 content, dated groundwater in arid regions from chlorine-36 content, and estimated annual variations in cosmic-ray flux from the concentration of beryllium-10 in annual snow layers on icecaps. Our AMS research will focus on applications in new fields and on extending the technique to serve LLNL programmatic needs.

Operation of the AMS

Figure 3 shows the principal parts of an AMS system. A sample of an element containing a mixture of isotopes (typically 100 μg to 1 mg) is placed in a hollow in the anode of a cesium sputtering source. The source produces a negative ion beam of the element. The ion beam is injected into a tandem electrostatic accelerator that raises the beam's energy from a few tens of thousands of electron volts to several million electron volts, in the process stripping electrons from the negative ions to produce positively charged ions. By rapidly switching the voltage on the vacuum tank of the injection magnet, we switch the beam being accelerated between the abundant stable isotope and the rare isotope of interest. At the first spectrometer magnet, the beam of the abundant isotope (which may be either more or less massive than the rare isotope) is caught in a Faraday cup at the magnet exit, while the relatively few atoms of the rare

isotope are passed farther along the spectrometer for additional analysis. To ensure identification of the rare isotope, the remainder of the spectrometer measures particle momentum, charge-to-mass ratio, ionizing strength, and total energy. The abundance of the rare isotope may be as low as one part in 10^{15} to 10^{16}, so redundant identification is important.

Calibration Measurements

In December 1988 and May 1989, we checked the performance of the AMS by measuring the ratios of carbon-14 to carbon-12 in standard samples provided by collaborators from Simon Fraser University in Vancouver. Figure 4a is a spectrum of particle energies detected at the end of the spectrometer. The large peak corresponds to counts from carbon-14, present in modern graphite at a concentration of one part in 1.2×10^{12}. The much smaller peak at the left reflects the presence of negatively charged dilithium-7 (Li_2). This molecule is formed at extremely low concentrations from contamination of the cesium sputtering source, and, after being stripped to Li_2^+ ions, is able to pass the momentum and charge-to-mass tests for carbon-14 to end up in the spectrometer detector. In actual data acquisition, the peak will be rejected by measurements of ionization power and total particle energy, but it is useful for calibration purposes.

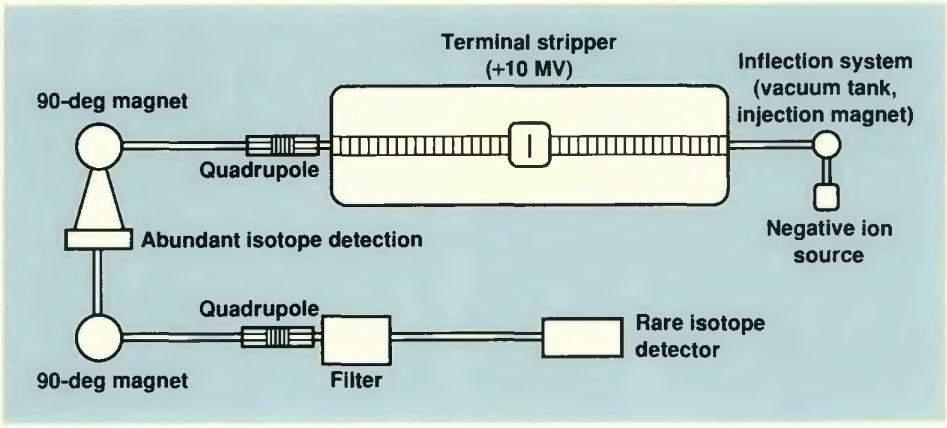

Figure 3. Components of the AMS spectrometer.

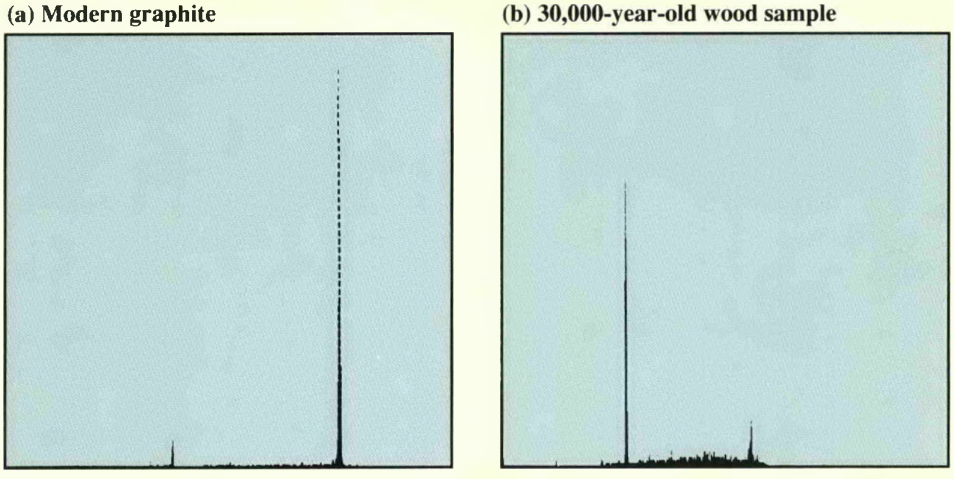

Figure 4. Spectrum of particle energies detected by the AMS. (a) The large peak is produced by carbon-14 in modern graphite. The small peak at the left was produced by negatively charged dilithium-7 molecules, a contaminant in the cesium sputtering source. (b) The same measurement on carbon-14 in a wood sample 30,000 years old produced the peak at the right. As the carbon-14 has decayed to only 2% of the original content, it was necessary to magnify the vertical scale, making the dilithium-7 peak at the left much larger. The concentration of carbon-14 in this sample is only one in 2.4×10^{14} carbon-12 atoms.

Figure 4b is a spectrum from the same measurement performed on a sample of carbon prepared from wood 30,000 years old. The smaller peak at the right, adjusted to amplify the vertical scale, was produced by carbon-14 atoms. The naturally occurring carbon-14 has decayed for 5.5 half-lives, leaving only 2% of the atoms originally present in the wood when the tree died—a relative concentration of one carbon-14 atom in 2.4×10^{14} carbon-12 atoms. The prominent peak at the left reflects the contaminant Li_2 at the same concentration as in Figure 4a but magnified by the change in scale. The noise visible in the spectrum comes from scattered carbon-13 signals, which can be removed by ionization-power measurements.

We are currently completing a sample changer for the ion source that will allow us to measure 60 samples without a vacuum cycle, and are fine-tuning the accelerator and detector for the isotopes we plan to

measure. We are also preparing to install the next generation of detectors and a new data-acquistion system.

X-Ray Calorimeters

Thermal x-ray and particle detectors offer high quantum efficiency and resolving power over a broad energy range. Detection of dark matter in the universe and high-resolution stellar x-ray spectroscopy are two notable examples of their application. We began an experimental effort more than two years ago, using IR&D Program funds, to develop photon-counting x-ray microcalorimeters. Successful use of such a device aboard an orbiting spacecraft will represent a dramatic scientific achievement, making entire classes of galactic and extragalactic x-ray sources available for study. When operated between 100 and 300 mK, a microcalorimeter will offer the broad-bandwidth capability of photoelectric detectors, nearly 100% quantum efficiency below 10 keV, and the superior resolving power of a Bragg crystal.

In principle, a calorimeter may be any material that exhibits a measurable temperature increase after absorbing a single photon or particle. For the temperature rise to be measurable, the material must possess a small heat capacity. This can be achieved below 1 K in crystals with small dimensions because the volume heat capacity of an ideal crystal drops with the third power of temperature.

Monolithic and Composite Calorimeters

Using well-developed infrared bolometric techniques, we have constructed prototype calorimeter refrigeration systems to operate at 1.4 and 0.3 K. We are fabricating and studying the properties of monolithic and composite calorimeters. In monolithic devices, a single material serves as both thermometer and absorber. To date, we have built and tested samples of single-crystal germanium doped via neutron-induced transmutation (NTD). The dopant level defines a well-characterized variation between sample resistance and temperature.

Figure 5a shows an x-ray spectrum obtained with a $0.1 \times 0.1 \times 0.01$-cm monolithic germanium sample using low-noise electronics specially designed for cryogenic calorimetry. The calorimeter was cooled to 0.3 K and irradiated by a radioactive source of americium-241, which produces neptunium L x rays and fluoresces copper x rays from the backing in the source container. The source also contained some iron-55. The 320-eV resolution is within 20% of that predicted for this device and the operating conditions. Energy resolution can be improved by reducing the heat capacity or by selecting a thermistor with a steeper resistance-vs-temperature gradient.

Figure 5b shows a spectrum obtained with a smaller germanium sample measuring $0.025 \times 0.01 \times 0.01$ cm. This spectrum shows the manganese $K\alpha$ and $K\beta$ emission lines near 6 keV, which are produced by a source of iron-55. The resolution of 80 eV is 40% better than the best resolution achievable with a lithium-drifted silicon detector. We are investigating the behavior of resistance with temperature for germanium of varying dopant concentrations and believe an optimal combination of geometry, electric field, and dopant concentrations can yield further improvements in energy resolution at 0.3 K.

The ultimate resistive thermal sensor will be too small for practical use as a monolithic x-ray-absorbing calorimeter. Thus, we are developing methods for connecting thermometers to an x-ray-absorbing material that possesses larger surface area and

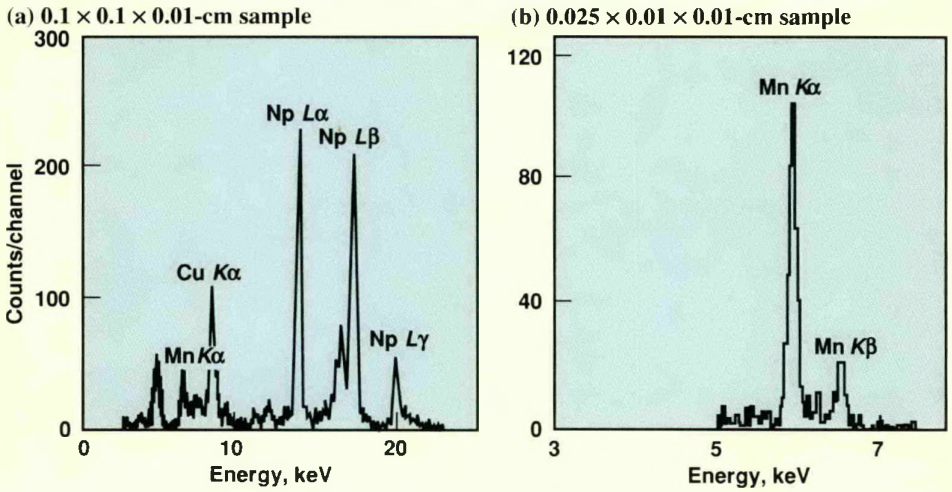

Figure 5. X-ray spectra measured with two monolithic germanium microcalorimeters at 0.3 K. (a) The resolution in the larger device is within 20% of that predicted for these operating conditions. (b) The resolution of the smaller device is 40% better than that achievable with a lithium-drifted silicon detector.

lower heat capacity than the sensor. Candidate materials are sapphire, diamond, and high-purity germanium and silicon.

Dielectric Calorimeters

We have begun to investigate an innovative concept that should virtually eliminate Johnson noise and sensor self-heating. This concept takes advantage of the temperature dependence of the dielectric constant in ferroelectric materials. In a dielectric calorimeter used with a constant dc bias, the output signal can, in principle, be controlled by an applied voltage without elevating the sample's temperature by introducing self-heating. The energy resolution for photon-counting spectroscopy may be improved by at least a factor of three with this device.

We have fabricated a proof-of-principle device from strontium-titanate glass ceramic and have operated it at 1.4 K. We tested this device by measuring the pulses produced when it was irradiated by a short burst of infrared radiation. The pulse response demonstrated that calorimetery with dielectrics is indeed possible. A dielectric calorimeter can potentially provide an energy resolution below 20 eV at 300 mK, an operating temperature that is easy to achieve with conventional helium-3 closed-cycle refrigerators. We have obtained two years of funding from the National Aeronautics and Space Administration's Office of Innovative Research to continue developing this device.

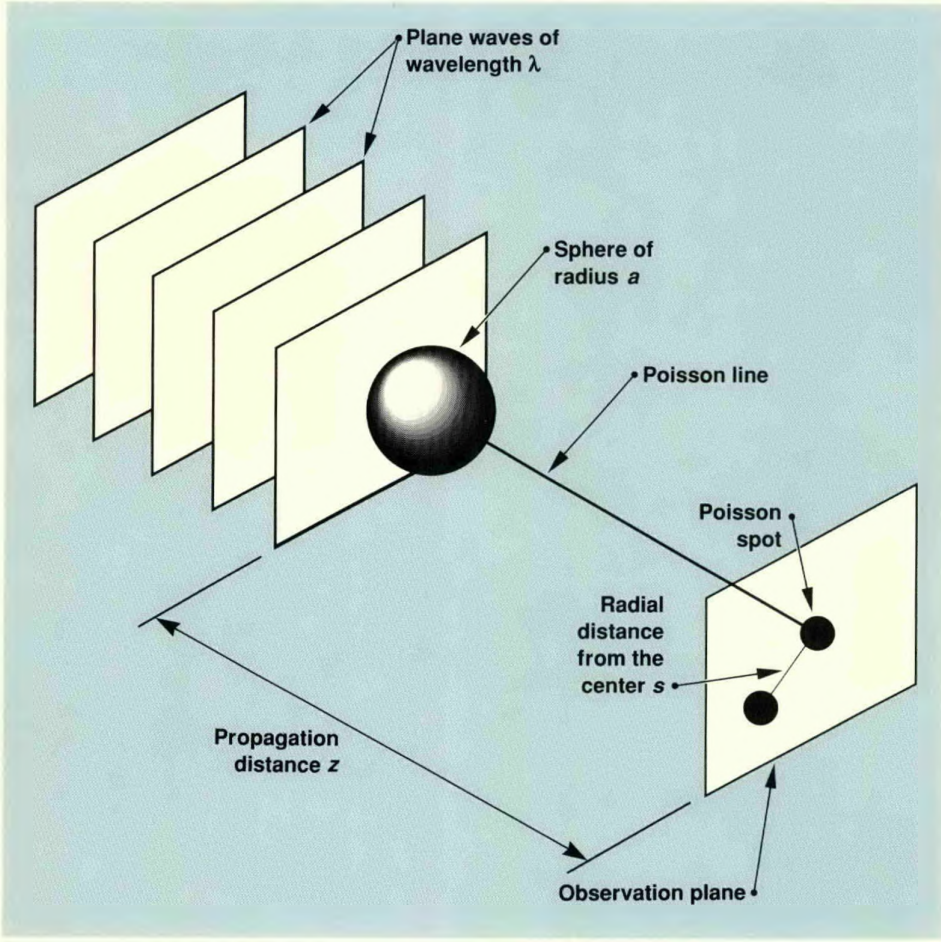

Figure 6. A sphere illuminated by a laser produces a line of light, called the Poisson line, in the shadow of the sphere. The intersection of the Poisson line with an observation plane identifies the sphere's location relative to the laser beam or other spheres in the beam.

Adiabatic Demagnetization Refrigerators

We are constructing adiabatic demagnetization refrigerators to further reduce temperatures. Our system uses ferric ammonium alum as the paramagnetic salt. A salt crystal is sealed with epoxy into a stainless-steel cylinder supported in the magnet bore by nylon microfilaments. To date, we have obtained a temperature of <50 mK. To achieve a temperature stability of <8 μK, we have developed a microprocessor-based servo-control system that adjusts the superconducting magnet current with the desired precision. We have achieved an rms stability of ±3 μK, which is more than twice the stability we require.

Poisson Alignment Reference System

We have developed an alignment technique for use in free-electron lasers (FELs). Aligning the magnetic axes of the various components of an FEL is a three-step process of (1) locating the magnetic centerline

of the component, (2) locating an alignment fiducial relative to the magnetic centerline, and (3) measuring the fiducial position relative to a straight-line reference. We have defined the straight-line reference by using the Poisson line, which greatly facilitates the latter alignment requirement.

The Technique

When an opaque sphere is illuminated by a large-diameter laser beam (a plane wave; see Figure 6), a diffraction pattern forms behind the sphere. The diffraction pattern can be observed by placing a screen or camera perpendicular to the beam at any point behind the sphere. A central bright area in the shadow of the sphere is the Poisson spot, which is the intersection of the Poisson line and the observation plane. Figure 7 shows the normalized intensity for the Poisson spot of a 25-mm-diam sphere at 50 and 100 m from the observation plane. The resolution of the center of the Poisson spot is proportional to the gradient of the intensity.

The Poisson line passes through one fixed point at the center of a sphere; however, to serve as a reference line, the Poisson line must pass through a second fixed point. The center of a quadrant detector (quad cell) serves as the second fixed point. By centering the Poisson spot on the quad cell using a feedback circuit between the quad cell and a mirror that actively steers the incident plane wave, we form the Poisson reference line, which is ostensibly as stable as the two fixed points.

We can align many points simultaneously by placing several spheres in the large-diameter laser beam. With two or more spheres in the collimated beam, some mutual influence of one sphere on the diffraction pattern of an adjacent sphere arises. The altered symmetry of the diffraction pattern causes a shift in the center of the energy of the Poisson spot. We have determined this shift both calculationally and experimentally. In the experimental setup, we align a moving sphere such that its axis of motion causes it to overlap a stationary sphere. A quad cell monitoring the Poisson spot from the stationary sphere is on a calibrated stage that moves parallel to the moving sphere and thus provides a direct measurement of the level of interference. The diffraction rings from the moving sphere have little effect on the stationary (measurement) sphere when the center-to-center separation is greater than about 20 mm.

In our experimental setup, it would have been possible to support the spheres on a glass plate perpendicular to the laser beam. In an FEL, however, sufficiently high radiation levels could darken glass and each plate would result in some shift in the laser beam direction. Thus, we support the spheres on thin (25- or 50-μm) taut wires. If a wire is more than about 10 mm from the edge of a sphere, the wire's movement has a reasonably small (<10-μm) influence on the apparent position of the Poisson spot. More important, once a wire moves between the edges of the sphere, its effects are less than 5 μm for any of the wires we have tested.

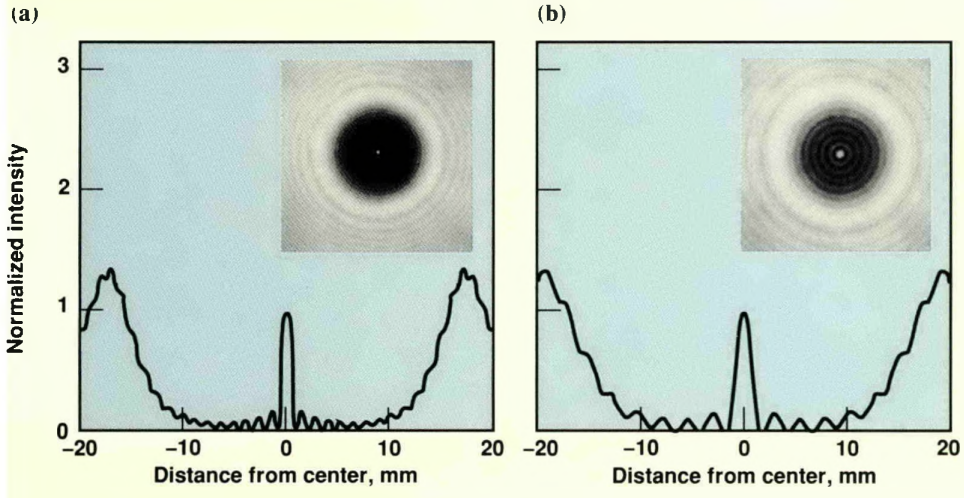

Figure 7. Calculated intensity and images of the Poisson spot from a 25-mm-diam sphere in an observation plane at (a) 50 m and (b) 100 m.

Contact: R. E. Marrs (415) 422-3890 (EBIT), J. C. Davis (415) 423-1414 (AMS), E. H. Silver (415) 422-2244 (x-ray calorimeters) or L. V. Griffith (415) 423-4209 (alignment system).

Mathematics of Wave Propagation

A localized-wave-transmission (LWT) theory that describes the localized, slowly decaying transmission of energy as a function of space and time has been developed. Pulses with LWT characteristics could find application in remote sensing, communications, and directed-energy weapons.

We have developed a localized-wave-transmission (LWT) theory to describe localized, slowly decaying transmission of energy as a function of space and time. (This work is supported by the IR&D Program.) The LWT effect is evident in acoustics (scalar wave-equation systems), guided wave systems (wave equations with boundaries), electromagnetic systems (Maxwell's equations), and particle systems (Schrödinger, Klein-Gordon, and Dirac equations). Acoustic LWT pulses, which are characterized by their high directionality and slow energy decay, are called acoustic directed-energy pulse trains (ADEPTs), and the corresponding electromagnetic solutions of Maxwell's equations are called EDEPTs.

Traditional continuous-wave (cw) solutions to linear systems separate the space and time characteristics of the waves and thus allow immediate application of Fourier analysis. Laser-produced Gaussian beams, for example, are studied in this fashion. Signals from conventional antenna systems, such as uniphase or phased arrays, are driven essentially with cw signals; they begin to spread and decay when they reach the Rayleigh distance, which depends on the nature of the original signal.

In contrast, the space and time properties of LWT pulses are inseparable, giving the LWT effect an extra degree of freedom. As a result, there is no precise value for the Rayleigh distance for the LWT effect because of the broadband nature of the constituent pulses. In fact, LWT solutions can be designed to remain localized over a distance many times that expected from traditional solutions. A comparison of the fields generated by cw- and ADEPT-driven arrays is shown in Figure 1.

We have also developed a new, bidirectional representation of the solutions for these wave systems that reproduces both the LWT and standard time-dependent solutions. This representation is more effective than conventional Fourier plane-wave decompositions for describing LWT pulses and their properties. Moreover, it provides us with a natural basis for

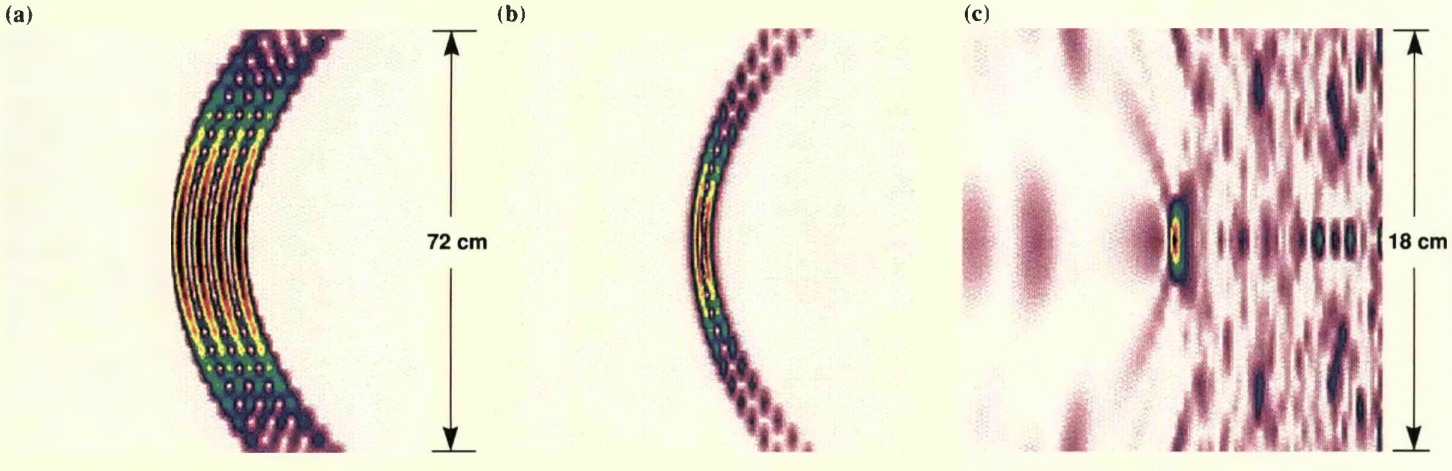

Figure 1. Field intensity at a distance of 10 m resulting from a 6-cm square array driven (a) uniformly by a two-cycle cw pulse with a frequency corresponding to the maximum (1/*e*) point of the ADEPT spectrum, (b) uniformly by the on-axis ADEPT function, and (c) by a modified form of the full ADEPT solution. Field intensity as a percentage of the original level is denoted by color: black = 80–100%, red = 60–80%, yellow = 40–60%, blue = 20–40%, purple = 0–20%. Time increases from left to right. Note that the fields generated from the cw and uniform pulse-driven arrays (a, b) require a 72-cm window whereas the ADEPT field (c) requires only an 18-cm window.

synthesizing pulse solutions that can be tailored to give the LWT effect in a variety of physical systems.

Having uncovered this interesting class of theoretical pulses for describing localized transmission of wave energy, we are now attempting to replicate, both experimentally and numerically, ADEPT/EDEPT fields by a finite set of sources such as a planar array of radiating elements (i.e., an independently addressable, pulse-driven antenna array). In particular, we are making numerical simulations and conducting acoustic experiments to determine the physical likelihood of launching one of the ADEPTs, called the modified-power-spectrum (MPS) pulse because of the form of the weighting functions used to construct it from the basic LWT solutions. The physical characteristics of the MPS pulse are such that it can be optimized so that it is localized near the direction of propagation and so that it maintains its original amplitude out to extremely large distances.

We have shown numerically that the combination of spatial and temporal distributions of ADEPT/EDEPT-driven arrays generates pulses that maintain their localized shape at distances well beyond the conventional Rayleigh distance. Unlike past attempts at enhanced localized transmission (such as super-gain antennas), ADEPT/EDEPT-driven arrays appear to be very robust and insensitive to perturbations in the initial aperture distributions. Although the arrays were not optimized, our results to date indicate that energy can indeed be transmitted from a modest-sized array over long distances without spreading.

These LWT pulses may also affect several fundamental ideas involving the wave-particle duality concept used in quantum mechanics. While investigating the use of the fundamental LWT solutions as a model of the photon, we found that these solutions exhibit both local and nonlocal characteristics usually associated with wave-particle duality. An LWT "wavepacket" can take on either a transverse plane-wave or a particle-like character, depending on the size of the parameters that define it. That is, it exhibits the billiard-ball characteristics associated with macroscopic entities and the wave-like properties of microscopic ones. We are exploring the implications of LWT solutions in ionization, Compton scattering, and photoelectric events.

Pulses that could be designed with LWT characteristics have many potential applications, such as remote sensing, communications, power transmission, and directed-energy weapons. All of these applications raise a number of questions as to the stability and longevity of the ADEPT/EDEPT solutions in dispersing, attenuating, inhomogeneous environments. We are studying these issues and are planning a number of experiments to validate our theoretical predictions. If we are successful and can develop these ideas further, the resulting beams would revolutionize the fields of potential application.

Contact: R. W. Ziolkowski (415) 422-3889.

Highly Parallel Physics Codes

We are developing a family of parallel codes for calculating hydrodynamics and radiation transport, called free Lagrange independent timesteps (FLIT), for use on modern parallel multiprocessor supercomputers.

New computational resources are changing the way experimental science is conducted, but the way computers are used to solve problems has not changed much over the years. For example, the Fortran computer language encourages scientists to represent the physical world as a series of states within a set of data structures with fixed properties. As a result, researchers must decide whether to use an Eulerian or Lagrangian coordinate system for a given problem. Neither system is best for all circumstances, and it is difficult to change from one to the other.

According to the principle of relativity, however, coordinate systems have no intrinsic significance in either time or space, and we should be able to perform calculations without a fixed framework. With the advent of parallel computers, we can finally use this principle to change our style of computation. The new approach to computing considers the relationships among the data to be as important and as mutable as the data themselves. Also, the relationships are assumed to be determinable from knowledge of local conditions. This allows computations to be carried out in many subdivisions of a problem asynchronously (i.e., with no physical necessity for coordinating between the subdivisions).

With support from the IR&D Program, we are developing a family of parallel codes, called free Lagrange independent timesteps (FLIT), that implement these considerations for calculating hydrodynamics and radiation transport. We have tested one of these, FLIT2D, that allows an arbitrary number of processors to be brought to bear on a problem without changing the source code in any way.

Different physics packages can be introduced into FLIT2D with no impact on the details of parallel-processing management. FLIT2D allows various subdivisions of a problem to be scheduled for consideration in parallel. Each region of space can be advanced to a different time. While one region is advancing, other regions that share information with it are restricted to prevent corruption of their information. At no time can any part of the problem advance to a time that would be physically incompatible with other parts. Regions that have no activity are not updated until they actually cause restrictions in active regions. Thus large portions of a typical problem can be run with much larger timesteps than would otherwise be possible.

Using this efficient parallel approach, we have run computations in as little as 10% of the time taken by a standard code; multiprocessing reduces execution time even more. Figure 1 shows the state of an asynchronous computation performed on a multiprocessor.

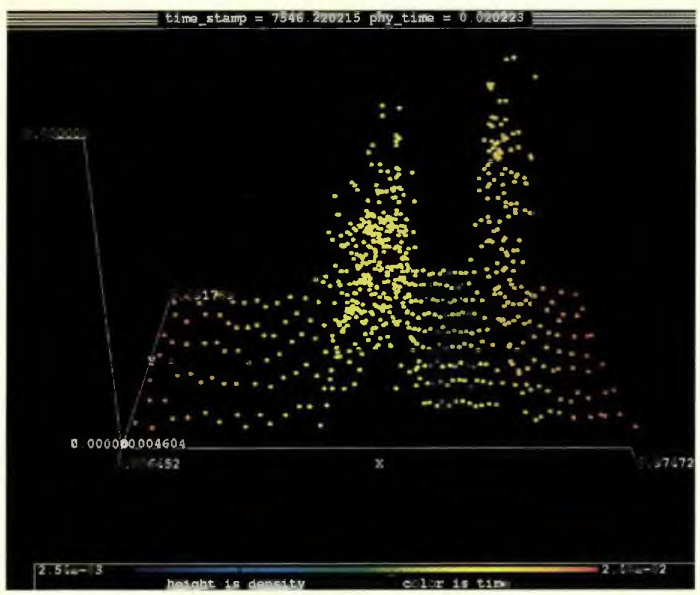

Figure 1. An asynchronous snapshot in two space dimensions of two blast waves approaching each other along the *x* axis. The vertical axis represents fluid density, and color denotes the time to which a variable has been advanced. Active areas have advanced to late times; areas not affected by either wave have not advanced very far.

Contact: P. Eltgroth (415) 422-4096.

High-Energy-Density Matter

We are studying the theoretical properties of shape isomers, a class of isomers that have not yet been found in nature but are predicted to exist in nonfissioning nuclei.

We have been investigating alternative techniques to fission and fusion for the release of nuclear energy. One is to extract nuclear energy from materials that could be made to store it in a high-energy state. Most of the known isomers have extended lifetimes because their angular momenta are quite different from their neighboring nuclear levels (hence the term "spin isomers"), which delays their electromagnetic decay.

We are drawn therefore to the potentially interesting properties of a class of isomers that have not yet been found in nature but are predicted to exist. These isomers are called "shape isomers" because their electromagnetic decay is inhibited by their shapes. Should shape isomers exist in nonfissioning nuclei, they could be candidate nuclear storage states for lasers and high-energy-density materials.

Shape isomers would exist at much higher excitation energies than spin isomers, perhaps around 5 MeV vs 100 keV) per atom. Being at much higher energies, they would be embedded in a "sea" of other nuclear levels to which they might be made to transit electromagnetically, thus initiating the release of their stored energy. They would generally not have an angular momentum greatly different from the nearby nuclear levels, which also would facilitate their release of energy. A shape isomer also would be "collective" i.e., have a large electromagnetic strength); it would have an electromagnetic strength of perhaps 50 or 100 single particle units, whereas an ordinary spin isomer has at best a strength of 1 single particle unit. This collectivity would facilitate the production of shape isomers and, under the right conditions, also their release of energy.

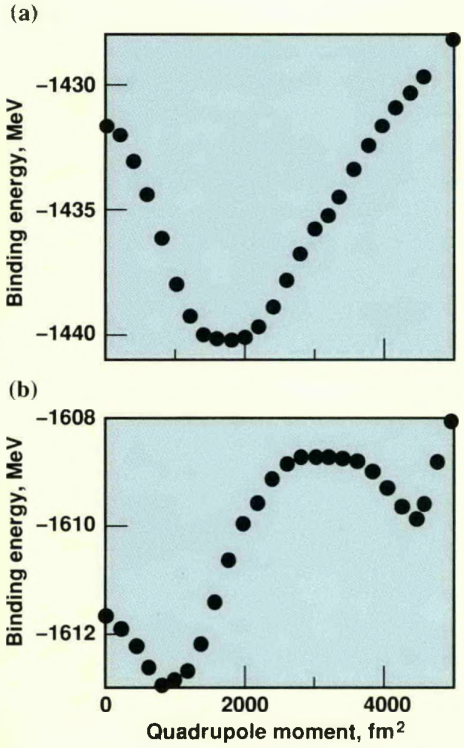

Figure 1. Energy curves for (a) the "normal" ^{180}Os, with one minimum corresponding to the observed nuclear ground state, and (b) ^{210}Os, which has a second minimum corresponding to a state predicted to be a shape isomer.

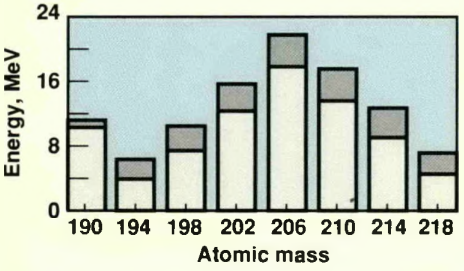

Figure 2. Excitation energies (light gray) of the predicted shape isomers for mercury isotopes and the well depths (dark gray) of their confining potentials The most interesting candidate for experimental verification is ^{194}Hg, which has low excitation energy and high confining potential.

However, shape isomers have not yet been proven to exist. If they do, their lifetimes may be immense on a nuclear scale but short in the world of practical applications. Furthermore, depending on their precise properties, the processes that inhibit their decay may also inhibit the release of energy. Finally, it may be very difficult to produce them in "commercial" quantities.

The total energy of two osmium isotopes is shown in Figure 1: ^{180}Os has an energy minimum corresponding to the nuclear ground state, but ^{210}Os also has another minimum at much larger deformation, making it a candidate for shape isomerism. Because ^{210}Os is far from the line of nuclear stability, however, it would be very difficult to produce and observe in the laboratory.

Fortunately, not all of our interesting candidates are so far from available nuclei. Figure 2 shows the excitation energy and well depth for shape isomers predicted in a sequence of mercury nuclei. Several of the most interesting candidates are nearly stable nuclei and are thus more easily accessible.

At this point, we must await confirmation of these predictions by the experimental community. During this time, we are continuing with the difficult problems of predicting the lifetimes of these states and calculating mechanisms that may be used to release energy, such as the interaction of an electron accelerated by an intense optical laser. (This work receives funding from the IR&D Program.)

Contact: M. Weiss (415) 422-4094.

Earth Sciences

We are refining our understanding of the internal structure of the earth and the causes of tectonic stress field variations. We have also made important progress in understanding fundamental fracture flow relationships.

Our research in the earth sciences ranges from geochemical modeling, to studies of rock mechanics, containment, and seismology, to investigations of new resource-recovery technologies. This work is essential to a number of Laboratory programs, including Nuclear Test, Treaty Verification, and Energy. Here we highlight two particularly interesting projects.

Tectonic Stress in the Western United States

We are studying seismic waves generated by earthquakes of moderate size to learn more about the earth's tectonic stress field. The techniques we use for analyzing these waves allow us to study remote earthquakes and are well suited to the diffuse seismicity that characterizes much of the western United States.

In the first phase of this work, we measured the wave speeds and attenuation rates of seismic waves over the many crisscrossing paths shown in Figure 1a. Using these measurements, we mapped local variations in wave speeds by standard tomographic methods (Figure 1b). In this way, we can study gross changes in the earth's internal structure and the tectonic implications of its lateral heterogeneity (variation in structure from place to place). For example, from measurements of the very low wave speeds and high attenuation rates localized in the central Basin and Range tectonic province, we estimate that the physical characteristics of this anomalous structure are consistent with models in which the cold, high-strength upper mantle was stripped away during a plate subduction event about 50 million years ago, exposing the shallow structure to the hot, partially molten mantle below.

In the second phase of our work, we use tomographic images to predict the effects of structural changes on wave propagation. Corrections for wave speeds and attenuation are made on earthquake signals to give corrected path-reduced data that depend only on source properties. We then apply source-inversion procedures to determine the orientations of tectonic stresses.

The importance of tectonic stress to our understanding of the mechanical behavior of faults and for seismic hazard assessments is demonstrated when we compare the orientations we have determined for earthquakes in northern California with the results of recent studies in central California. Studies in central California have found evidence that the tectonic stress there is oriented normal to the San Andreas Fault and not at 30-40 deg as classical faulting theory predicts, supporting the contention that the fault zone has low shear strength. However, our studies indicate that the stress field undergoes significant change north of San Francisco, where the stress-field orientation shows greater resolved-shear stresses on the San Andreas Fault, a result consistent with simple-shear faulting theory. Variations in the shear strength along segments of

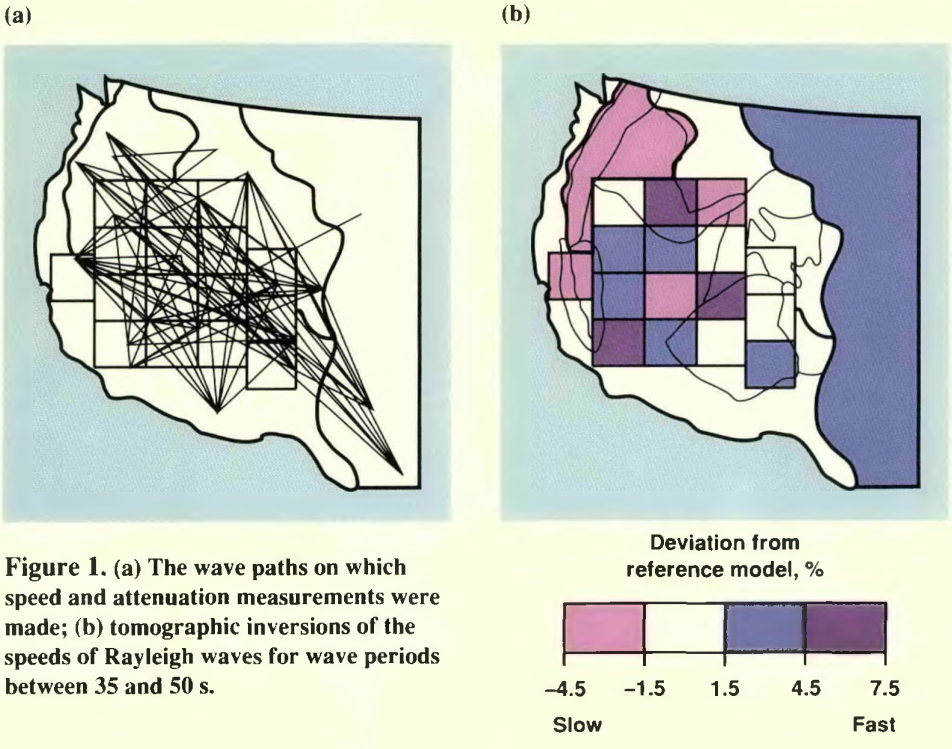

Figure 1. (a) The wave paths on which speed and attenuation measurements were made; (b) tomographic inversions of the speeds of Rayleigh waves for wave periods between 35 and 50 s.

the fault could explain these stress-field differences. With such information, seismologists can make better assessments of the seismic hazard in major populated areas.

Fluid Flow in Fractures in the Earth's Crust

Enhanced oil recovery, exploitation of geothermal heat, isolation of toxic and radioactive wastes, and mineralization of ore bodies all depend on the movement of fluids through fractures in the crust of the earth. With support from the IR&D Program, we are studying, experimentally and computationally, the physics and chemistry of fluid flow in fractured porous rock, including the effects of changes in effective pressure, dissolution, and precipitation on the flow and transport properties of fractures. The laboratory effort has emphasized saturated flow within a fracture. The computational effort, involving both numerical and analytical models, has addressed how, under unsaturated conditions, the flow fields in neighboring matrix blocks influence flow in a fracture.

We tested samples of rock with a single fracture at hydrostatic confining pressures up to 200 MPa, a pressure corresponding to the overburden at a depth of about 7 km. We determined the hydrologic characteristics of a fracture by measuring the rate of fluid flow through the sample as a function of the confining pressure. We also measured the corresponding change in aperture as sensed by cantilever gauges on the outer surfaces of the rock. We developed a profiling device that permits the precise mapping of local fracture aperture. The two surfaces that form the fracture are laid open under this device, which precisely positions the fracture surface on a movable table and measures and digitizes heights point by point as the surface is translated in steps in the horizontal plane. An image of the original fracture aperture is formed by digitally comparing the two fracture surfaces (Figure 2). With the digitized aperture distribution and permeability measurements, we can investigate the validity of the assumptions made in various fracture-flow models.

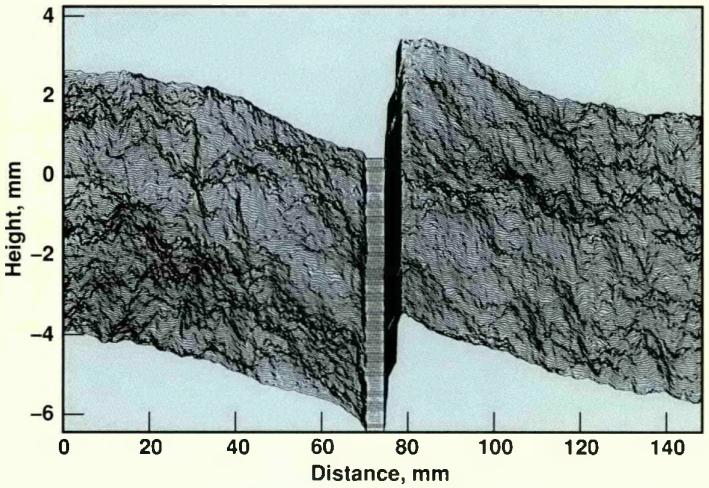

Figure 2. Digitized image of the two surfaces of a fracture.

In our computational effort, we emphasized the interaction of the flow fields in fractures and adjoining matrix blocks of unsaturated systems; this work is also applicable to unsaturated flow in heterogeneous systems where there is a sharp contrast in permeability between two material types. Using LLNL's enhanced version of the TOUGH hydrothermal flow code to model unsaturated infiltration in a fractured rock mass, we found that fracture flow is dominated by gravity, whereas matrix flow is dominated by capillary imbibition and is primarily transverse to the fracture. We also identified fundamental functional relationships between the flow fields in the fracture and matrix blocks and developed related analytical models of fracture-matrix flow for various boundary conditions.

We derived asymptotic expansions for a range of fracture inclinations, fracture spacings, and boundary conditions at the fracture entrance. We also derived a numerical solution to the related integro-differential equation for the penetration h of the liquid front in the fracture. We modeled several cases and obtained good agreement between the analytical and numerical models. When the solutions to h are plotted, the movement of the liquid front in the fracture is represented by line segments, indicating that the liquid front experiences up to five time periods, or flow regimes, characterized by physically interpretable time scales. In general, flow during any given period is dominated by the flow conditions within its corresponding flow region.

The suite of asymptotic solutions for the movement of the liquid front embodies a comprehensive theory describing the interaction of fracture and matrix flow during infiltration. We can now address such difficult problems as the fate of contaminants in unsaturated environments.

Contact: L. Younker (415) 422-0720.

Low-Weight, High-Performance Miniature Supercomputers

We are developing interconnect technology and computer components for highly reliable, low-weight, low-cost miniature supercomputers.

We are designing and building low-weight, high-performance supercomputers needed for current and future military and space applications. As part of this effort, we have used hybrid wafer-scale integration techniques to develop a set of technologies for interconnecting multiple silicon chips onto a single silicon substrate, producing extremely high-density packaging with very-high-performance interconnects.

We developed a specialized computer-controlled apparatus for laser-patterning the thin-film metal connections from the input/output (I/O) pads on the chips to the interconnection in the substrate. The computer handles the mechanical registration and controls the focus of the laser beam as it moves down the sides of the chips. These thin-film multichip hybrids offer higher packaging densities, improved reliability, and better electrical performance than the multilayer ceramic modules currently available. Hybrids produced at LLNL (Figure 1) are being used in the solid-state recorder scheduled for use on the Air Force Space Test Program.

This technology provides a fivefold volume reduction in electronic packaging for our 20-Mips (million instructions per second), 7-Mflops (million floating-point operations per second), high-performance computer. In the last two years, development has progressed through conception, prototype, and brassboard demonstration; we are now designing a more compact version that will have a 17 × 25-cm circuit board and will weigh approximately 0.5 kg. Power consumption in the processor is software-controllable; it varies between 10 and 28 W for a level of computing capability that required 100,000 W a decade ago (and would have filled a large room).

The processor, an embedded controller, uses RISC (reduced-instruction-set-computer) microprocessor architecture combined with a floating point unit (FPU). The Mips R3000 chip set operates at 25 MHz; the 32-bit CPU with an onboard memory management unit and cache contoller allows for the design of low-chip-count systems. The chip set operates a pair of caches—instruction and data—along with four write buffers to provide "cache speed" writes to memory. Eight 8-bit programmable ports are available for user-defined applications. Two DMA (direct-memory-access) channels are provided for digital video inputs. The control portion for a 16-channel analog multiplexing port is also contained within the processor hardware. The supporting analog circuitry module is a peripheral.

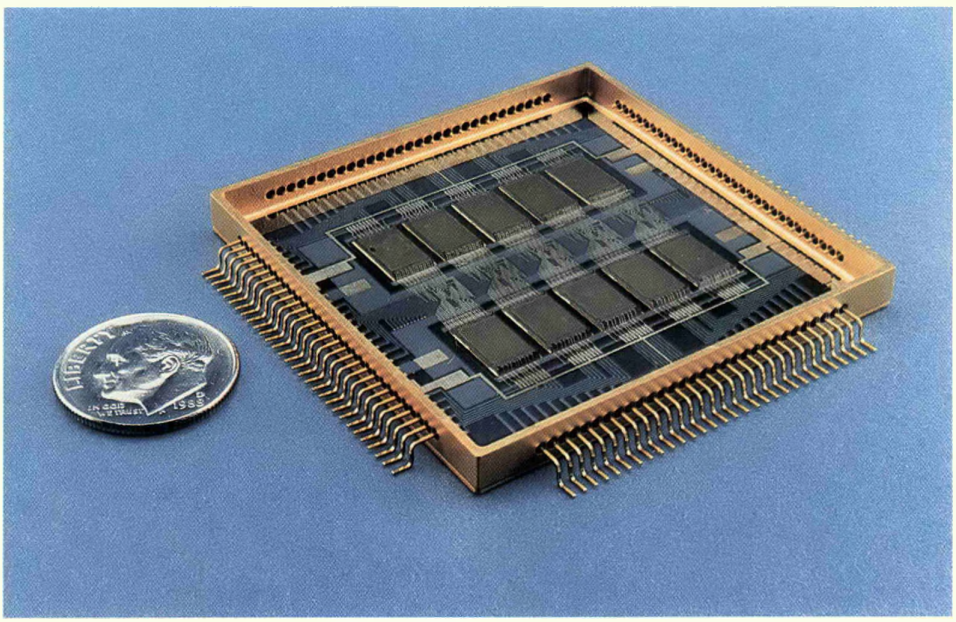

Figure 1. A completed thin-film, multichip hybrid module produced at LLNL.

The processor system consists of four unique modules: CPU (central processor unit) hybrid, cache hybrid, memory hybrid, and ROM (read-only memory) hybrid (Figure 2). The CPU hybrid contains the R3000 (CPU), the R3010 (FPU), and two gate arrays incorporating memory control, I/O, write buffers, and error detection and correction circuitry. The cache hybrid contains thirty 16-kbyte × 4-bit, 25-ns static RAMs (random-access memories) and latches to support both caches. Each cache is organized as 16 kbyte × 60 bit. The memory hybrid is organized as a 384-kbyte × 40-bit memory bank, using 128-kbyte × 8-bit, state-of-the-art static RAMs. The ROM hybrids contain five 128-kbyte × 8-bit EEPROMs (electrically erasable, programmable ROMs), providing 128 kbyte × 40 bit of onboard reprogrammable memory.

Our near-term goal is to produce a miniaturized version of this already-quite-compact processor. Such a miniaturized processor would allow us to build a supercomputer system about the size of a pocket calculator. This would not only yield large savings in terms of space but would also save weight, enabling us to put more processors in a single package.

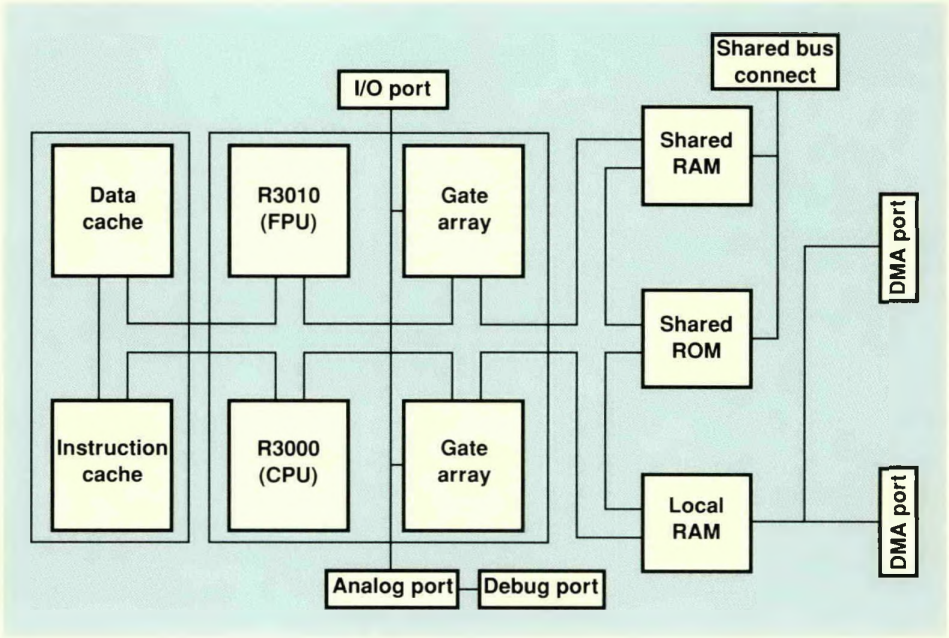

Figure 2. Architecture of the compact supercomputer.

A multiple-processor system implemented in this technology could be held in the palm of the hand and would carry more data-processing power, more memory capacity, and more I/O capability than could be purchased commercially even five years ago. This compact packaging also will allow shorter interconnection paths, improving performance and reducing electrical noise.

Contact: B. McWilliams (415) 423-4179 or A. F. Berhardt (415) 423-7801.

Meeting Pressing Environmental Challenges

Research under way at LLNL will improve our ability to clean up groundwater solvents, upgrade the Laboratory's wastewater-discharge program, improve our sampling of gas concentrations, and assess seismic safety margins at nuclear power plants.

The Laboratory has always been and remains committed to environmental protection. We take great care to ensure that current activities do not adversely affect the environment, and we are working to clean up contaminated areas from activities of previous years. Much of the contamination was discovered recently as the result of our vastly improved monitoring and detection techniques and increased knowledge about the impact of human activities on the environment. The potential environmental impacts of all LLNL activities will continue to be carefully assessed, and the quality of the Laboratory environment will be continually improved.

Cleanup of Solvents in LLNL Groundwater

The Laboratory is making progress on cleaning up organic solvents (volatile organic compounds, or VOCs) contaminating the site since it was occupied by the U.S. Navy during World War II and the early postwar years. Beginning in December 1983, when LLNL detected perchloroethylene (PCE) and trichloroethylene (TCE) in monitor wells both on site and nearby, we have drilled, logged, sampled, and hydraulically tested more than 250 monitoring wells.

The Environmental Restoration Division of the Environmental Protection Department has determined that a groundwater plume containing VOCs appears to be migrating northwestward from the southwest corner of the site at a rate of about 30 m/y (Figure 1). Three municipal supply wells located ~3 km west of the plume serve a portion of the Livermore Valley (~4000 residences). These factors led the Environmental Protection Agency to place LLNL on the Superfund National Priority List; the DOE is supporting this investigation and cleanup effort.

The amount of the contaminants is very small, even though the area is fairly large. They do not present any exposure risks to LLNL employees or Livermore residents now because they are trapped in soil and groundwater 10 to 70 m below the surface. No private or public wells exist within the plume or in its immediate path.

Restoration efforts include:

- Investigating the hydrogeology and water quality of the site, including installing monitor wells, sampling and analyzing groundwater, evaluating and closing potential vertical conduit wells, developing

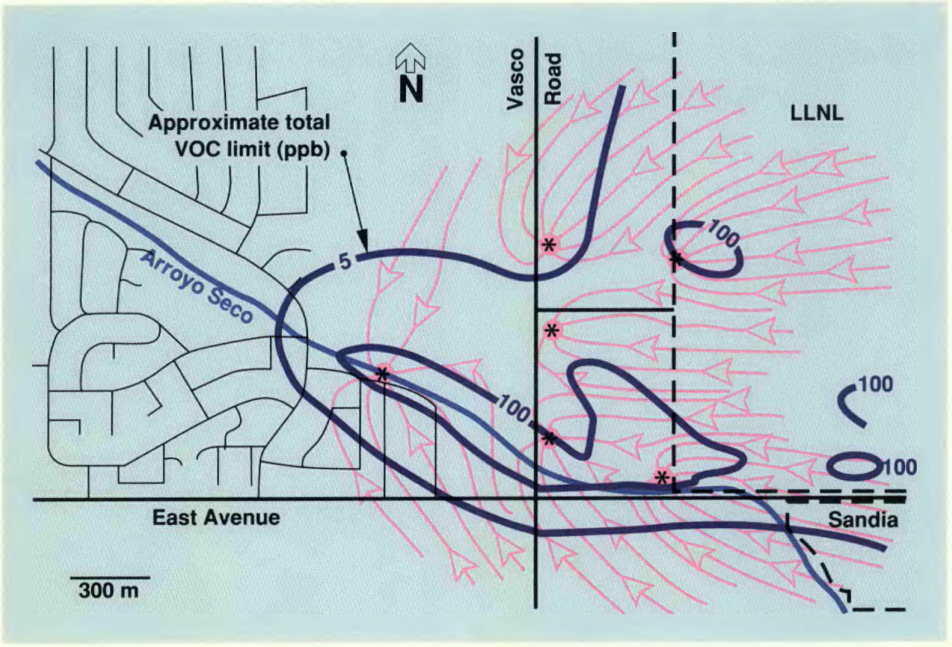

Figure 1. The groundwater plume containing VOCs (volatile organic compounds) migrating northwestward from the southwest corner of the LLNL site at a rate of about 30 m/y. Concentrations of VOCs are in parts per billion; extraction well locations are shown by the asterisks.

conceptual models of the subsurface, nd preparing a remedial nvestigation report.

- Investigating known and suspected ources of contamination, including earching historical records and nalyzing soils.
- Assessing potential risks to public ealth resulting from current onditions, determining potential pread of contaminants, and devising lternative scenarios.
- Developing and evaluating lternative remediations, including onducting pilot studies, installing xtraction wells, comparing ydrologic behavior to predictions, esting water-treatment technologies, nd preparing a feasibility study eport.
- Preparing and implementing a emedial action plan.

In 1988, LLNL began its pilot emediation study, focusing on the rea west of the traditional aboratory boundary where the lume is migrating northwestward. he "pump and treat" strategy we re testing involves pumping roundwater to the surface, treating to remove contaminants, and then eturning it to the environment. We re using computer models to etermine the optimum locations or eight extraction wells. To treat ne groundwater, we are testing a ydrogen-peroxide/ultraviolet-light ystem that destroys organic ompounds by oxidizing them to armless carbon dioxide, water, and hloride ions. Tests show excellent estruction of PCE and TCE, and e are improving the efficiency of leaning up other trace VOCs. The ffsite pilot study will include three eatment systems that will be phased n over the next two years; if they rove effective, they will be ncorporated into the final cleanup rogram.

Upgrades of the LLNL Wastewater-Discharge Control Program

All sewage from LLNL and Sandia National Laboratory is discharged through a common outfall into the Livermore community sewer system, where adequate treatment depends on the Livermore plant receiving sewage with a consistent character. LLNL waste presents two special treatment problems: the wide variety of chemicals used, and the large volume of discharge. As Laboratory waste is being discharged to the city sewer system, a portion of the flow is diverted to a monitoring and alarm system in Bldg. 196.

The Laboratory's wastewater control program incorporates five key elements. Two of these, source control and sampling, already incorporate applicable methodologies. Here we describe the other three elements of the program that are being upgraded to incorporate new technologies.

We are about to go on line with a sewer monitor upgrade (SMUG). SMUG will improve the specificity and sensitivity of the x-ray fluorescence analyzer (XRFA) metals detection, provide online identification of radioisotopes, reduce the number of false alarms, reduce instrument response times, and improve the overall reliability of the system.

To improve our metals-detection capability, we designed three new XRFA units, each of which we optimize for a particular portion of the periodic table. We can easily identify signals from the elements of interest, thus meeting our goals of improved specificity and sensitivity.

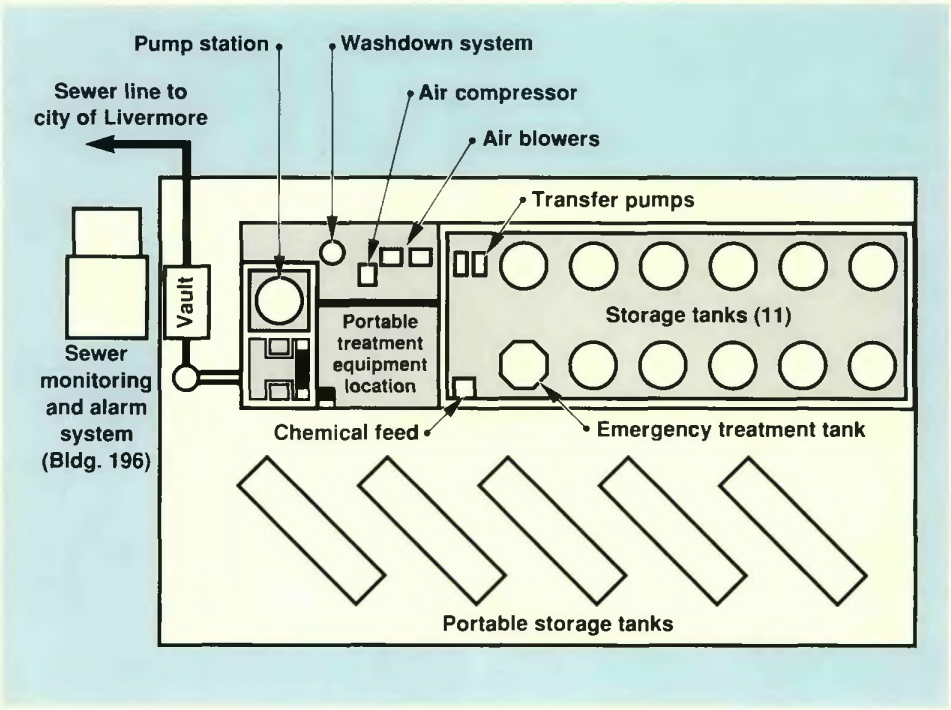

Figure 2. The proposed layout for LLNL's sewer diversion-and-containment system showing major system components.

We use a custom-built, extended-range photon detector for measuring radioisotopes. We combine rapid identification and quantification of isotopes with sensitivity to ^{239}Pu and other heavy elements. The monitoring computer receives pH and outfall volume data and then calculates total mass or curie content when there is a metals or radioisotope alarm. Raw data from all alarms are saved on disk for later detailed inspection. A "watchdog" program tests the whole system for normal operation every few seconds.

LLNL is designing a sewage diversion-and-containment system capable of containing approximately 200,000 gal of sewage. Upon receiving a signal from the monitoring system, the valve to the sewer will automatically close, and a valve to a diversion pump station will open. The principal components of the proposed system (Figure 2) are a pump station capable of handling variations in flow ranging from <100 to ~1400 gal/min, 11 tanks to contain the diverted sewage, a smaller tank for containment and possible emergency treatment, staging areas and connection fittings for tank trucks, leased emergency treatment equipment and portable storage containers, air-mixing equipment, a chemical feed tank, and transfer pumps for distributing sewage. Construction of the system should be completed by September 1990.

Locating the source of a spill is critical to prevention of future problems. LLNL will install five to nine satellite sampling stations at key locations in the sewer system. These stations should help isolate the area of the laboratory in which a spill originated. The first stations should be operational by July 1989.

An Electron-Capture Detector Diffusion Cell for Constant Gas Sampling

The Safety Science Group at LLNL often must measure the protection factors of different types of protective clothing and equipment. One method used in fit testing equipment is to challenge it in a gas-rich environment. Previous methods had two major limitations: they required the use of materials that harmed the environment, and they did not provide continuous monitoring. To overcome these limits, we have substituted the fairly inert gas sulfur hexafluoride (SF_6) and developed a real-time analyzer.

We are using a new pulse-modulated electron-capture detector (ECD) that is extremely sensitive to SF_6 and is designed for use with the Varian 3700 gas chromatograph (GC). The overall system is shown in Figure 3a. We control the amount of dilution by partially closing the sample exhaust valve, which in turn changes the pressure drop across the filter. The linear amplifier is designed to be variable with two scales, calibrated at 10× and 100× amplification. On the 10× scale, our lowest detectable limit is reduced to 0.07 ppm, and in theory we should be able to detect concentrations as low as 0.007 on the 100× scale.

(a) Overall system

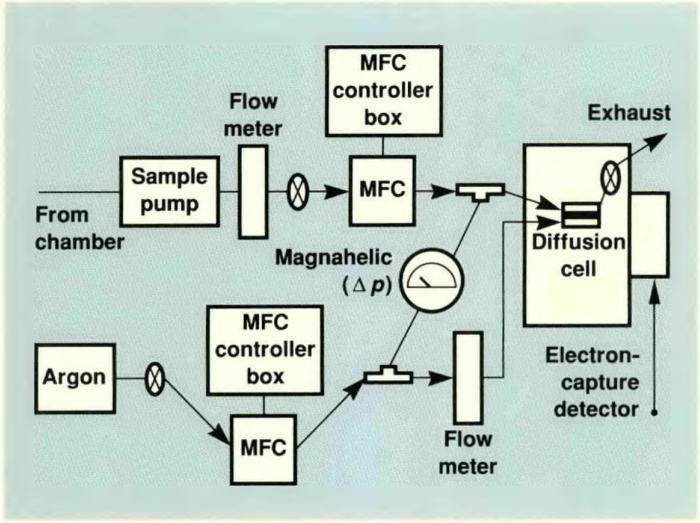

(b) Modified calibration system

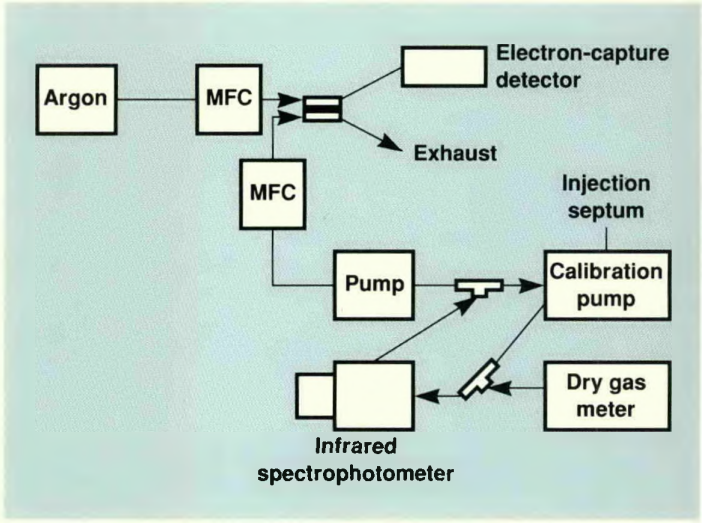

Figure 3. Our new pulse-modulated electron-capture detector that is extremely sensitive to SF_6. (a) The overall system and (b) the modified calibration system. (MFC = mass flow controller.)

We are using the exponential dilution method to calibrate the low-concentration gases. In this method, a sample is injected into a known volume, mixed thoroughly, and continuously diluted with a pure carrier gas at a constant flow. Figure 3b shows our modified calibration system.

After exploring several approaches to improve our gas-sampling technique, we developed a highly sensitive, real-time gas analyzer. We have tested our diffusion cell system extensively, and find that it meets all of our requirements. It has a dynamic range of three orders of magnitude, and we believe that we can expand this range by using the 100× amplifier, which we will test thoroughly. We have also been able to increase the flow rates and to reduce the response time to a negligible value without decreasing the dilution ratio.

By reducing the carrier gas flow to 3 ml/min during standby, we can ready the system for sampling after a 30-min warm-up time. We can easily remove any remaining signal caused by oxygen and remove any background drift with the ECD electrometer.

We have designed a diffusion cell that allows only a small fraction of our sample to mix with argon and enter the detector. We use mass-flow controllers (MFCs) to maintain the pressure drop across the diffusion cell and regulate the system flows. We can measure fit factors of 10,000 and can potentially measure 100,000. The ECD/diffusion cell system meets our requirements for a technique that gives high sensitivity, fast response, and continuous data.

Assessing the Seismic Safety Margins of Nuclear Power Plants

We have developed a method to assess seismic margins of nuclear power plants and have made a trial application to the Maine Yankee Atomic Power Station. This work was conducted within the context of U.S. Nuclear Regulatory Commission efforts to assess the safety of nuclear power plants with respect to earthquakes.

The seismic-margins method, initiated by LLNL in 1984, assesses the seismic safety margin at plants by evaluating each plant with a review-level earthquake, and thus does not depend on detailed knowledge about the specific local seismic hazards. The working definition of seismic margin is: "Seismic margin is expressed in terms of the earthquake motion level that compromises plant safety, specifically leading to melting of the reactor core. In this context, margin needs to be defined for the entire plant."

The margin-review process involves screening the components based on their importance to safety and their seismic capacity. The review products are high confidence of low probability of failure (HCLPF) capacities for components, accident sequences, and the entire plant. A typical fragility curve showing the HCLPF is given in Figure 4. The HCLPF may be thought of as the point on a lognormal distribution with 5% failure probability at 95% confidence.

We compare these HCLPF capacities, measured in terms of peak ground acceleration (pga), with the peak ground acceleration predicted for the earthquake against which the plant is to be assessed (called the review-level earthquake), which is set at a level above the design basis (safe-shutdown earthquake). We developed three ranges of capacity, stated in terms of pga: <0.3 *g*,

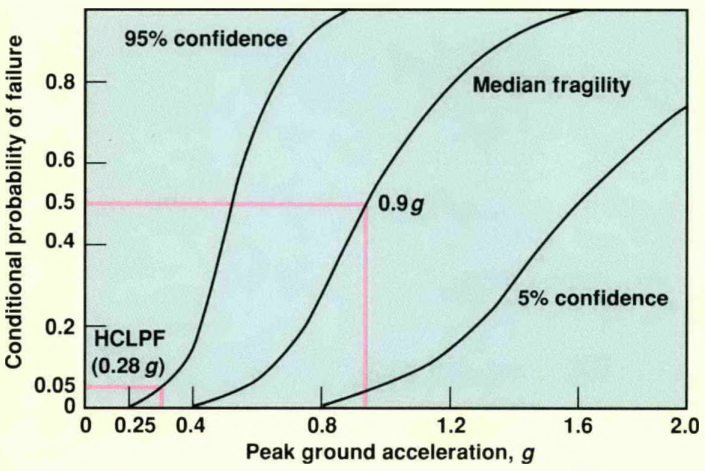

Figure 4. Sample fragility curves for a structure. We screen components based on their importance to safety and their seismic capacity, and determine high confidence of low probability of failure (HCLPF) capacities for the components, accident sequences, and the entire plant.

0.3–0.5 *g*, and >0.5 *g*. We determine which components and structures require further study for each range.

We developed criteria, based on published seismic probabilistic risk assessments, to determine which systems were important to review. For pressurized-water reactors, the dominant plant damage states result from accident sequences involving early core melt with early containment failure. Such plant damage states generally involve core damage induced by failure of plant safety functions relating to reactor subcriticality and early emergency-core cooling (injection). Thus, we must focus on the systems and components needed to perform these functions in margin reviews. For boiling-water reactors, the important plant safety functions are reactor subcriticality, emergency core cooling, and residual heat removal. In addition, with either type of plant, unique situations such as failures of upstream dams or undesired systems interactions must be assessed.

Once we have identified the components and structures requiring further study, plus those subject to systems interactions, plus plant-unique features, we subject them to a margins quantification. We calculate the HCLPF capacities for these components and structures, construct plant logic models, and arrive at accident sequence and plant-level HCLPF capacities.

After we developed the seismic-margins method, we conducted a trial review at the Maine Yankee Atomic Power Station. The plant HCLPF of Maine Yankee was found to be 0.28 *g* after certain upgrades were made. Our review helped resolve outstanding seismic issues there, pinpointed areas that needed upgrading, and proved to be cost-effective in comparison to a more formal review. Further evaluations of our method will strengthen it and expand its usefulness.

Contact: W. F. Isherwood (415) 423-5058 (groundwater cleanup), C. H. Grandfield (415) 423-1779 (wastewater-discharge control), R. A. da Roza (415) 422-5228 (gas sampler), or R. C. Murray (415) 422-0308 (seismic safety margins).

Computer Advances

Major innovations in services and security were highlights of this year's computer research.

The opening of Livermore Computer Center supercomputer resources to unclassified researchers marked the fulfillment of an important LLNL commitment. Another significant advance was the design of a stand-alone computer security monitor. We also developed a decision-support tool to aid in the strategic planning of nationwide information systems.

The Open Computing Facility

The Livermore Computer Center can now provide world-class supercomputer services to unclassified researchers at LLNL through the new Open Computing Facility (OCF). Until now, supercomputing resources were accessible only to the classified research community, although the need for large-scale scientific computing had grown in all research areas.

Creating the OCF was a major undertaking. Decisions on hardware and software requirements, consulting services, user-friendly interfaces, and portability among various supercomputer environments had to be implemented. The facility uses a Cray-XMP/48 supercomputer, already owned by LLNL, and a newly acquired 1.2-Tbyte, online robot data storage archive (Figure 1). This large-capacity, hierarchical storage system consists of 25 Gbyte of disk cache and an Amdahl 5860 computer connected to a STC 3480 tape-storage silo. Files can be automatically "migrated" between the archive system's disks and tapes. This advanced storage system allows users to store large datasets and was developed at LLNL. In 12–18 months, we will be able to provide automatic file migration between the Cray supercomputer and the OCF central storage system.

The Cray-XMP/48 runs the new NLTSS network operating system, which was also developed at LLNL. This operating system provides all the features of a traditional supercomputer operating system, but its components are available to computers distributed around a network. As a result, future

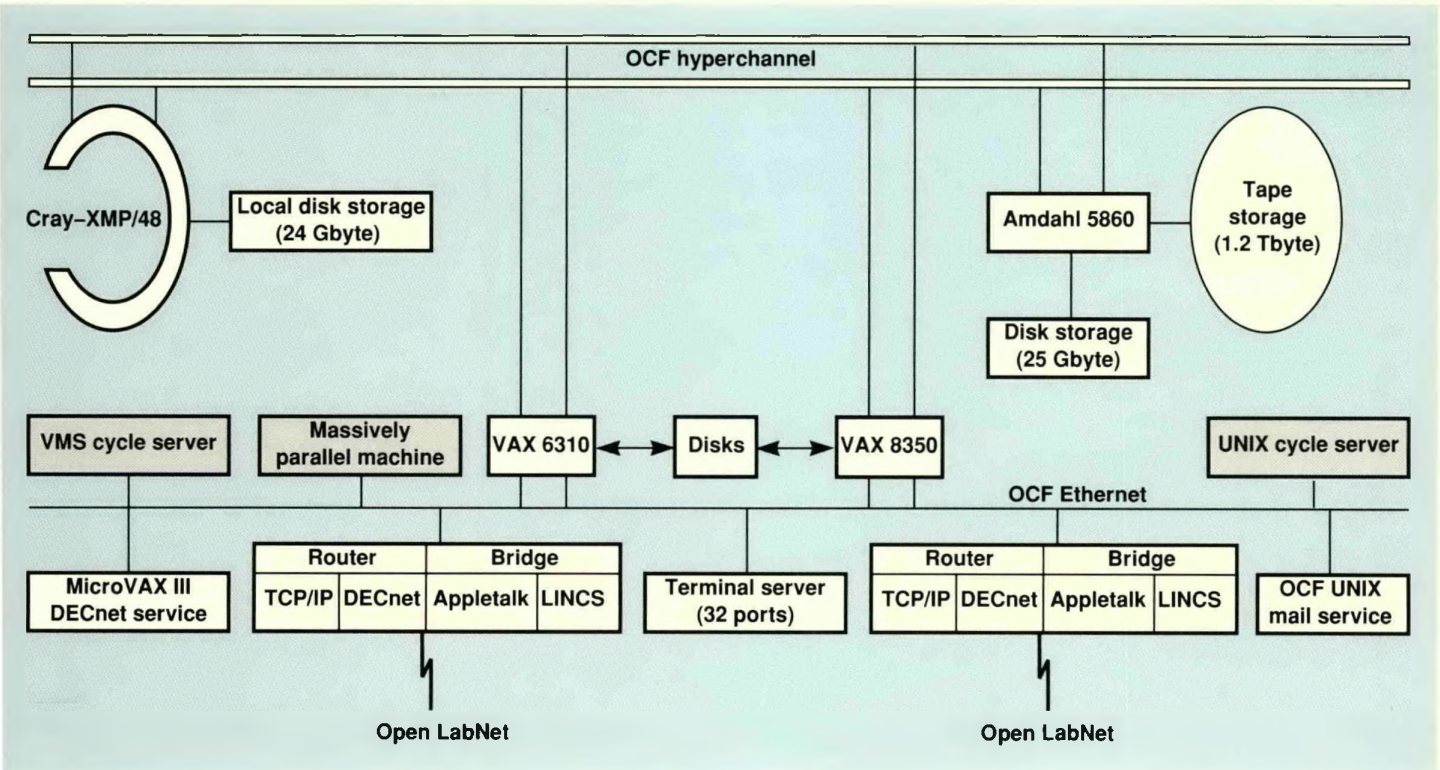

Figure 1. Configuration of the Open Computing Facility (OCF). The computers shown in gray are machines that may be added to the OCF if there is sufficient interest.

components can be added to the OCF in a modular fashion.

Physical access to the OCF is possible through the Open LabNet and dial-up, variable-speed modem lines (from 300 to 9600 baud); 32 modem lines are currently available. Open LabNet is connected to other broad-reaching networks, thus providing access to the OCF from many systems worldwide. The OCF can also be accessed through the standard Department of Defense Internet protocol suite (TCP/IP), DECnet, DEC LAT, and the LINCS protocol suite developed at LLNL. This wide selection of access methods makes it possible for users to interact readily and easily with the facility.

An OCF consulting service and documentation library operates from 8:30 a.m. to noon and from 1 to 4 p.m., Monday through Friday. Experts in OCF workstations, networking, and supercomputer software are available to assist users.

Computer Security Monitor

We have also designed and implemented a prototype Computer Security Monitor (CSM) that combines a small, stand-alone, graphics-oriented computer workstation with sophisticated monitoring software. The system is independent of hardware and operating systems and can be used with any host computer system that generates an audit trail.

Designing the CSM as an independent, stand-alone security system was an unusual step, as it is generally believed that security should be designed into an operating system. However, for various reasons, integration of computer security is not always the optimum choice: replacing old computing systems without integrated security cannot be justified economically; often, integrated security creates performance penalties in a computer or incompatibilities with an accepted interface; and the end-user education needed to enforce complicated, built-in security procedures is expensive. We believe that a reliable, tamper-proof, stand-alone CSM is the most practical solution to these situations.

The CSM incorporates characteristics of a classical intrusion-detection system, such as real-time monitoring, operating-system independence, and protection against both insider threat and data aggregation. It also contains several unique design features, including simultaneous and independent statistical and deterministic views, configurable levels of machine interdiction, severity indicators, redundancy for multilevel secure systems, and an easy-to-use interactive graphics interface.

The CSM is attached to one or more target computer systems by two dedicated communications lines; an input line transports audit records from the target host to the CSM, and an output line carries interdiction commands issued either by the system security officer (SSO) or, if so configured, automatically by the CSM. End-to-end encryption mechanisms ensure the integrity of these communications. The information auditing activities of the CSM take up few resources on the target host. Since the CSM is physically isolated from users of the target computer system, tampering is not likely to be a problem.

The CSM layout is illustrated in Figure 2. The workstation component of the CSM provides a security-monitor tool kit that allows the SSO to select and configure the interfaces, the optional system run-time parameters, and the site-specific intrusion-detection characteristics to

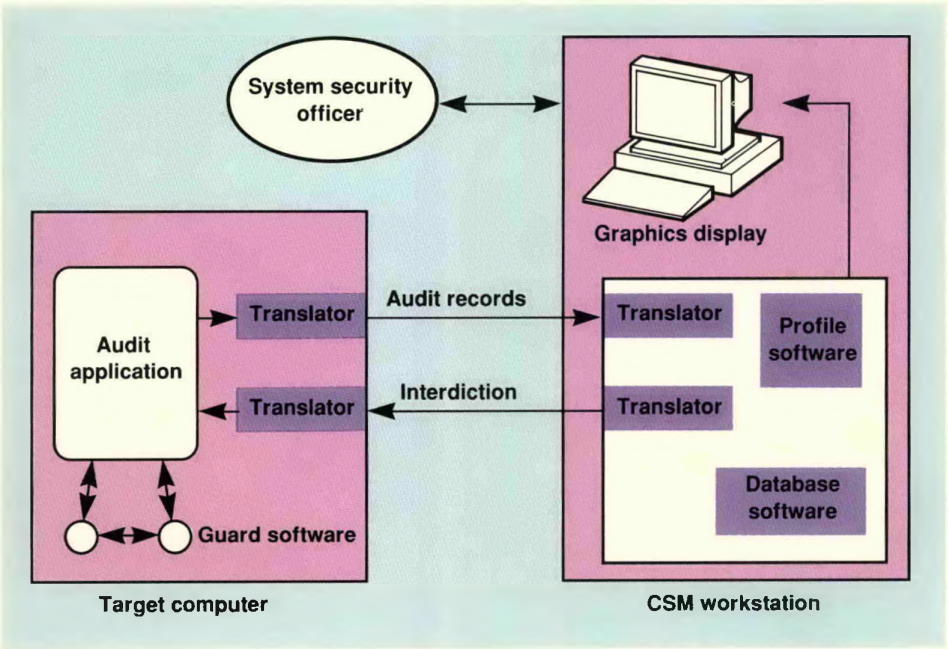

Figure 2. CSM components on the target system are largely target-system dependent. The remaining elements are largely target-system independent.

be monitored and profiled. The CSM can examine a user on the target machine against the user's statistical profile on one window while deterministic rules set up by the SSO can simultaneously and independently monitor adherence to discretionary access and critical resource controls on another window.

CSM uses a window system to view normal monitoring configurations. The Statistical Analysis Window examines user features (e.g., terminal location, time of use, and transaction frequency) to determine whether or not they fall within the permissible ranges of a user's statistical profile or signal an *abnormality*. A Reportable Events Window displays noncompliance to site-specific deterministic policies and rules. The SSO establishes critical-resource sets against which accesses (failed or successful) can be classed as either *notables* or *violations*. A *notable* occurs when the critical-resource set is of such high criticality or sensitivity that the access must be noted. A *violation* occurs when the access (or attempted access) of a resource prohibited to all but a select group is attempted by someone outside that group. A critical-resource set can be established for any set of host system objects. A System Status/Activity Window shows the status of both the monitored host system(s) and the CSM monitoring system. Other windows assist in the investigation of an anomalous user session. Windows can generate preselected queries into the CSM database, and the SSO can generate specific queries. Other functional areas of the CSM include a scrollable help window, an electronic memo window, and a system administration option window.

We are in the process of defining the requirements for an extended prototype CSM system that we hope to demonstrate next year.

Computer-Aided Planning for a Large Information-Management System

We are creating a decision-support tool to help in the strategic planning of the U.S. Defense Logistics Agency (DLA) nationwide information system. A modernization program of the DLA system, involving 23 of their major computing facilities, was begun in 1986; this modernization will cost about $2.5 billion and was one of President Reagan's top 15 Presidential Priority Systems for 1989.

Our decision-support tool is called the Distributed Open Systems Capacity Planning System (DOSCAPS). It will allow DLA system architects to manipulate hypothetically the computer resources, communication links, software applications, and databases supporting various defense business activities (e.g., soliciting proposals from vendors, awarding contracts, monitoring and evaluating contracts) to obtain the most efficient and cost-effective use of computing resources. DOSCAPS will also enable them to assess the computational consequences of these manipulations.

We developed DOSCAPS first as a proof-of-concept prototype. For this prototype, we made a generic characterization of the DLA business activities in order to calculate the computing resources required and to demonstrate the proposed user interface. We characterized and quantified the various types of work performed at particular DLA sites. We studied function, information storage, and data flow of the various workload components. Each workload component is a collection of software modules that can be characterized by transaction rate, instruction path length, and quantity of data involved.

For the computing resources to meet the requirements, we considered a small set of generic computers and communications networks, selected solely on the basis of central processing unit speed, input/output channel bandwidth, and network bandwidth. DOSCAPS calculates the computing resources required by each workload component at a given site using information obtained by analyzing performance data for existing DLA applications software, by deduction from experience with similar software at other facilities, and by predictions for software still in the design stage. DOSCAPS scales these requirements according to the relationships between the existing components and our generic computer system components.

We also developed a subsystem within DOSCAPS that can distribute, automatically or manually, the workload components across the various classes of generic computing equipment. After performing a mean-value analysis of the work as allocated to the processors at a site, this subsystem generates estimates of the throughput, response time, and queue lengths associated with each applications software module on each processor as well as the processor and network utilizations and the average processor and network response times.

Thus, using DOSCAPS, DLA system architects can hypothetically reorganize the DLA's information system and then assess the resulting computational requirements. They will be able to determine the number and size of computers and the network bandwidth required to support their hypothetical distribution of the workload components and databases at particular DLA sites and across the entire DLA network.

Contact: L. Hatfield (415) 422-8567.

LLNL's Integrated Security Systems

We have extensively upgraded our security systems for controlling access, monitoring sites, protecting facilities and materials, and gathering, processing, and communicating information.

Major improvements in LLNL's security systems are nearing completion. Funded by two Congressional line items, we are upgrading all aspects of LLNL's physical security, including access control, alarms, command and control consoles, radio communications, and physical protection of special nuclear material.

An important upgrade this year was the replacement of the older CAIN (Controlled Access by Individual Number) booths with new CAIN II booths. These new booths permit automated access control using equipment and procedures similar to those of automated bank tellers. The new CAIN II booths require the use of new badges, which have been issued to all Laboratory personnel. The new badge is slightly thicker and longer than a standard credit card; on its back, a high-coercivity magnetic strip is encoded with identification data. Each user, upon receiving the badge, is weighed and selects a four-character personal identification number that will allow use of the new booths.

To gain entry to a secured area, a user inserts the new badge and keys in his personal identification number. The booth checks the user's weight to verify that it is close to the weight recorded when the badge was issued. In case of a problem or if a user requests help, a TV camera and a hands-free telephone in the booth allow the user to contact a security officer at the central control console. Emergency exit buttons ensure that individuals can never be trapped within the booth; if the communication links to the central facility are disrupted, all CAIN II field units (booths, single-door portals, sally ports, and staffed badge-readers) maintain operation, although without the mechanisms for officer assistance. Batteries are provided to permit the field units to operate for a limited time.

The Security Department is also responsible for ensuring the protection of classified material at LLNL. More than 300 alarm stations are installed at Livermore, Site 300, and several off-site locations for this purpose. Alarm stations can be vaults, rooms, zones of a perimeter protection system, or equipment with tamper sensors. Various pathways (e.g., telephone lines, point-to-point cable, microwave) are used to carry signals from the alarm station to a central alarm point either at Livermore or at Site 300.

We are upgrading the LLNL alarm system with SILAS (Secure Interactive Livermore Alarm System), a new computer-based system developed from an industrial process controller. Except for the sensors, all new components have been designed and are being installed. A SILAS interface, located outside of each alarm station, contains a badge reader, keypad, a set of five push-buttons, and a liquid-crystal display. From this interface, authorized users can change the mode of the station from "secure," in which the door is locked and the station sensors are active, to "access," in which most station sensors are inactive. Users can also perform all normal station functions from this interface, including enrolling new users and performing inspections. These actions previously had to be done by a security officer at the central alarm station.

The user interface and SILAS station sensors communicate with a nearby computer-based controller. The controller communicates with the central computer system, which reports alarms to the security console. The central computer facility, shared with CAIN II and housed in a protected area, consists of four VAX computers with redundant data storage and redundant connections to all peripheral equipment. A large database contains all configuration information for the SILAS system. The SILAS controllers and the central computer facility are fully protected against power failures. At Site 300, the SILAS controllers also serve as the data-gathering point for the local fire alarms and equipment alarms.

The command and control consoles at Livermore and at Site 300 are the nerve centers of the Security Department. Console operators communicate with security officers ir the field and dispatch them via radio

and telephone; console operators also handle emergency paging and TV surveillance, control the emergency sirens and monitor alarm systems, and supervise the automated access-control systems. The existing consoles consist of a number of single-purpose equipment racks in close proximity, which produce a noisy environment and subject console operators to large amounts of competing information.

In the new consoles, all critical real-time security functions are integrated into modern, computer-aided workstations. Each new console consists of one or more identical, single-operator workstations that serve as the primary human–machine interfaces to all of the security systems at the site. These workstations assess and control all alarms, access-control information, communications systems (radio, telephone, intercom, paging), and surveillance television. Information is shown as icons on maps of the site displayed on the workstations' high-resolution color graphics screens.

For the upgrade of radio communications, we expanded radio coverage and added backup transmitters at both Livermore and Site 300. The encrypted channels at Livermore ensure communication between field officers. A receiver grid selects the best-quality signal, which a high-power repeater retransmits.

We also installed a microwave link between Livermore and Site 300 to carry security communications, digital data for CAIN, SILAS, and the console, and video data from Site 300 to Livermore. Security communication channels employ voice and data encryptors, redundant equipment, and uninterruptible power sources. The LLNL telephone system uses this link for nonsecurity telephone traffic.

LLNL maintains supplies of a variety of controlled special nuclear material (SNM). The protection of these materials is the highest priority of the LLNL Security Department. To this end, we are increasing the protection of the SNM storage and handling areas, called the Superblock. We are constructing a perimeter protection area around the Superblock: a double-fenced, alarmed isolation zone contains guard towers and secure pedestrian and vehicle portals. We will soon begin construction of a new office complex within the Superblock that will contain a secondary security command and control center. This center, along with the primary security control center, will monitor and assess Superblock alarms, and control responses to them.

With the completion of these upgrades, all aspects of the Laboratory's physical security will be significantly enhanced. In addition, we have been able to make these improvements with minimal impact on the job-related activities of most LLNL personnel.

Contact: E. Behrin (415) 422-6423.

1989 Laboratory Achievements Index

For further information on the activities reported in this issue, contact the individuals listed below.

Advanced Laser Applications, **32**	J. Holtz	(415) 422-4117
Compact-Torus Accelerator, **42**	C. Hartman	(415) 422-1568
Computer Advances, **105**	L. Hatfield	(415) 422-8567
Conversion of Methane to Liquid Hydrocarbons, **58**	M. Droege	(415) 422-0155
DNA Sequencing and Atomic Imaging, **64**	R. Balhorn	(415) 422-6284
Earth Sciences, **96**	L. Younker	(415) 422-0720
Experimental Facilities, Devices, and Techniques, **86**	J. C. Davis	(415) 423-1414
	L. V. Griffith	(415) 423-4209
	R. E. Marrs	(415) 422-3890
	E. H. Silver	(415) 422-2244
Fluorescence *in situ* Hybridization, **66**	J. Gray	(415) 422-5610
High-Brightness, High-Current Operation of ETA II, **48**	W. Turner	(415) 422-7976
High-Energy-Density Matter, **95**	M. Weiss	(415) 422-4094
Highly Parallel Physics Codes, **94**	P. Eltgroth	(415) 422-4096
LLNL Efforts in Arms Control, **10**	L. Ferderber	(415) 423-7789
	R. Ide	(415) 422-7378
LLNL's Integrated Security Systems, **108**	E. Behrin	(415) 422-6423
Low-Weight, High-Performance Miniature Supercomputers, **98**	A. F. Berhardt	(415) 423-7801
	B. McWilliams	(415) 423-4179
Materials Science, Technology, and Fabrication, **76**	T. W. Barbee, Jr.	(415) 423-7796
	R. M. Christensen	(415) 422-7136
	J. H. Kinney	(415) 422-6669
	H. B. Radousky	(415) 422-4478
	T. T. Saito	(415) 422-1553
	L. E. Tanner	(415) 423-2653
Mathematics of Wave Propagation, **92**	R. W. Ziolkowski	(415) 422-3889
Measuring Human Mutations, **68**	W. L. Bigbee	(415) 422-5682
Meeting Pressing Environmental Challenges, **100**	R. A. da Roza	(415) 422-5228
	C. H. Grandfield	(415) 423-1779
	W. F. Isherwood	(415) 423-5058
	R. C. Murray	(415) 422-0308
Microwave Tokamak Experiment, **40**	B. Hooper	(415) 423-1409
Military Applications: Evaluation and Planning, **6**	R. F. Perret	(415) 422-8965
Mix Modeling Experiments, **12**	W. P. Crowley	(415) 422-4667
	V. C. Rupert	(415) 422-5403
Modeling of Atmospheric Chemistry and Toxic Gas Emissions, **72**	R. Koopman	(415) 422-7381
	J. Penner	(415) 422-4140
Modeling Petroleum Generation and Expulsion, **56**	A. Burnham	(415) 422-7304
Near-Infrared Surface-Enhanced Raman Spectroscopy, **70**	S. M. Angel	(415) 423-0375
New X-Ray Diagnostics and Sources, **16**	R. Fortner	(415) 423-7374
Nonnuclear Warhead Development, **14**	M. Finger	(415) 422-6370
Paladin Optical FEL Amplifier, **46**	T. Orzechowski	(415) 422-6709
Reducing Tubing Wastage in Fluidized-Bed Coal Combustors, **54**	C. Witherell	(415) 422-8341
Relativistic Klystrons, **50**	G. Westenskow	(415) 423-6936
	S. Yu	(415) 422-7876
Special Isotope Separation Program, **24**	M. L. Spaeth	(415) 422-4116
The Human Genome Project, **62**	A. V. Carrano	(415) 422-5698
The Nova Laser, **26**	E. M. Campbell	(415) 422-5391
Uranium AVLIS Program, **22**	M. L. Spaeth	(415) 422-4116
Weapon Development, **2**	W. J. Shotts	(415) 423-8770